Metal Oxide Nanomaterials and their Application in Solar Photoelectrolysis of Water

Rantej Singh Kler

Submitted for the degree of Doctor of Philosophy

University of Sussex

September 2013

Declaration

I hereby declare that this thesis has not been and will not be submitted in whole or in part to another University for the award of any other degree.

Signature:

Rantej S Kler

UNIVERSITY OF SUSSEX

Rantej Singh Kler, Doctor of Philosophy

Metal Oxide Nanomaterials and their Application in Solar Photoelectrolysis of Water

Summary

Solar generated hydrogen as an energy source is green, sustainable, with a high energy density. One day the majority of current fossil fuel based technology could be replaced with hydrogen technology reducing CO_2 emission drastically. The goal in this research is to explore hybrid metal oxide photocatalysts in the pursuit of achieving highly efficient photoanodes for use in photoelectrochemical cells (PEC). Achieving high efficiencies of hydrogen production in photoelectrochemical cells is the key challenge for the commercialisation of PEC technology as a viable, sustainable, hydrogen source; limited only by the lifetime of the sun and the resources of the metal oxide materials.

In this research TiO_2, Fe-Ti-O, ZnO, and Zn_2TiO_4 are the photocatalysts explored. Alloys of Ti-Fe-O showed improvement over TiO_2, whilst a hybrid heterostructure of $ZnO/Zn_2TiO_4/TiO_2$ enhanced photocurrent densities significantly. A barrier layer in the photoanode achieved localised exciton separation and reduction of recombination rates by inhibiting back flow of electrons after injection into the TiO_2 layer.

Nanotubes are created by the simple electrochemical process of anodisation. The nanotube composition depends on the anode material. To control the composition of

the anode, iron and titanium are co-deposited onto a substrate using electron beam evaporation. The introduction of iron into titania nanotubes engineered the band gap, lowering the band gap energy to that of iron oxide whilst the positions of the conduction and valence bands with respect to the oxidation and reduction potentials of water remained favourable. Fe-Ti-O nanotubes showed remarkable photocurrent density improvement compared to TiO_2 nanotubes.

ZnO nanostructures deposited by vapour transport mechanisms showed variability in the morphology of the structures, as governed by the growth dynamics. Herein, it is shown that an electronically favourable situation arises by the formation of a ZnO-Zn_2TiO_4-TiO_2 heterostructure and a high photocatalytic activity is reported. The structure is composed of a large surface area ZnO nanorod photoabsorber formed on a Ti foil which forms a Zn_2TiO_4 barrier layer between ZnO and TiO_2. The Zn_2TiO_4 layer inhibits electron transport toward the surface of the photoanode whilst encouraging charge transport to the hydrogenation electrode. The heterostructure interfacial surface area is extended through the utilisation of TiO_2 nanotubes, which demonstrated a 20.22 % photoelectrochemical efficiency under UV illumination.

Surface modification of ZnO nanorods with aerosol assisted chemical vapour deposited TiO_2 nanoparticles enhanced photocurrent densities of the ZnO rods, improving charge separation of excitons created within the TiO_2 nanoparticles.

ZnO nanotubes formed *via* a novel route using chemical bath deposition of ZnO is investigated, an annulus ZnO seed layer facilitated the site specific growth of ZnO nanotubes whilst a uniform seed layer formed ZnO nanorods.

Acknowledgements

I would first of all like to thank Dr Qiao Chen for his tremendous support and encouragement whilst completing my research, his appreciation for the beauty of nature was infectious, and our long discussions were always fruitful and informative.

Thank you to all my colleagues who have made my experience in Brighton a very enjoyable one. I would like to thank Daniel Lester, with his help to navigate the chemistry world. Also Zainab Taha Al-Abdullah for her assistance in the lab. It has been a pleasure working with Ali Shahroozi.

The office would not have been the same without Giacomo Canciani, Teo Mertanen, Fang Yuanxing, and more recently Adward Lee and old man Tom Draper who have become a fruitful part of the team. I would also like to thank James Webb, Victoria Smyth and young Thomas Samuels for their invaluable assistance in our group during their MChem projects.

I have found lots of encouragement and had informative talks with the academic staff and would like to thank Dr. John Turner, Dr. Mark Osborne, Dr. Alaa Abdul-Sada and Prof. Malcolm Heggie for their support and help throughout my time at Sussex. I would also like to specifically thank Alex Burns whose assistance in our labs and speedy resolutions have been invaluable.

A big thank you to everyone who I have had the pleasure of knowing at Sussex, including Ben Day, Lauren Anthony, JK, Joe Rodway, Andy Chetwynd, Tom Macpherson, Wane Thayalan, Laura Nicholls, James Livermore, Tom Moore and Becky Joyce to just mention a few.

I would especially like to thank my family for their ongoing encouragement, and for always being there with love, support and patience. I wouldn't have half the drive if it wasn't for you. I also would like to thank my sweet Rachael, I greatly appreciate your patience and constant understanding during stressful and trying times.

Amongst my good friends in Brighton, I greatly appreciate my friendships with Will Watson and Emina Demiri and wish them the best in their future together.

Contents

List of Tables

List of Figures

List of Abbreviations

AACVD	Aerosol Assisted Chemical Vapour Deposition
AFC	Alkaline Fuel Cell
Ag/AgCl	Silver/Silver Chloride Reference Electrode
AM(X)	Air Mass (Coefficient)
CBD	Chemical Bath Deposition
CBM	Conduction Band Minimum
CIGS	Copper-Indium-Gallium-Selenide
CIS	Copper-Indium-Selenide
CNT	Carbon Nanotubes
CVD	Chemical Vapour Deposition
DR-UV-Vis	Diffuse Reflectance UV-Visible Spectrometry
DSSC	Dye Sensitised Solar Cell
EDX	Energy Dispersive X-rays
Eg	Band gap Energy
FTO	Fluorine doped Tin Oxide
HER	Hydrogen Evolution Reaction
HOMO	Highest Occupied Molecular Orbital
I_{photo}	Photocurrent

LUMO	Lowest Unoccupied Molecular Orbital
MCFC	Molten Carbon Fuel Cell
NHE	Normal Hydrogen Electrode
OER	Oxygen Evolution Reaction
PEC	Photoelectrochemical Cell
PEM	Polymer Exchange Membrane
PN	p-type/n-type Semiconductor
PV	Photovoltaic
PVD	Physical Vapour Deposition
QD	Quantum Dot
RHE	Reversible Hydrogen Electrode
SEM	Scanning Electron Microscope
SOFC	Solid Oxide Fuel Cell
TEM	Transmission Electron Microscope
UV-Vis	Ultra Violet - Visible light Spectrometry
V_{OC}	Open Circuit Potential
V_{On}	Onset Potential
VBM	Valence Band Maximum
VLS	Vapour Liquid Solid
VS	Vapour Solid
XPS	X-ray Photoelectron Spectroscopy
XRD	X-ray Diffraction
YSZ	Yttria-stabilized Zirconia

Chapter 1

Introduction

Over the next twenty years energy consumption worldwide is expected to double and fossil fuels are currently the largest supplier of energy. Fossil fuels are close to exhaustion, expensive and have a negative impact on the environment and climate. This has sparked a global effort to search for sources of energy which are not damaging to the environment and able to produce energy for the long term. Initiatives for nuclear fusion are promising, with a large scale international team constructing a nuclear fusion reactor (ITER) capable of fusing deuterium and supplying energy. However the cost of constructing a fusion plant is significant. Renewable energies could provide a long term source of energy, with feasible construction costs. For renewable energy to be considered a key energy supplier it needs to be less costly and more efficient than the current means of energy production.

The EU have created policies which aim to supply 20 % of total energy by renewable technologies by 2020,[1] cutting down global green house gas emission and stimulating the renewable energy industry. In 2011, 9.4 % of the UK's total energy production were provided by renewable sources, with a goal to fulfil 15 % of total energy production through renewable sources by 2020.[2] A goal of 50 % CO_2 emission reduction by 2020 is proposed for the EU. The UK Nuclear facilities are also in expansion to meet CO_2 reduction targets. The need for development of carbon capture, carbon reduction and renewable energy technologies is essential in meeting any of the proposed emission targets for the EU and worldwide.

1.1 Current Non-Solar Renewable Energy Technologies

Fossil fuels are finite and the CO_2 emission is damaging to the environment, while the environment itself could provide answers to sustainable energy production.

Figure 1.1 illustrates the energy produced by different renewable sources since 2008, a sharp increase in all of them is present and photovoltaic (PV) energy generation exhibits exponential growth at a current low capacity.

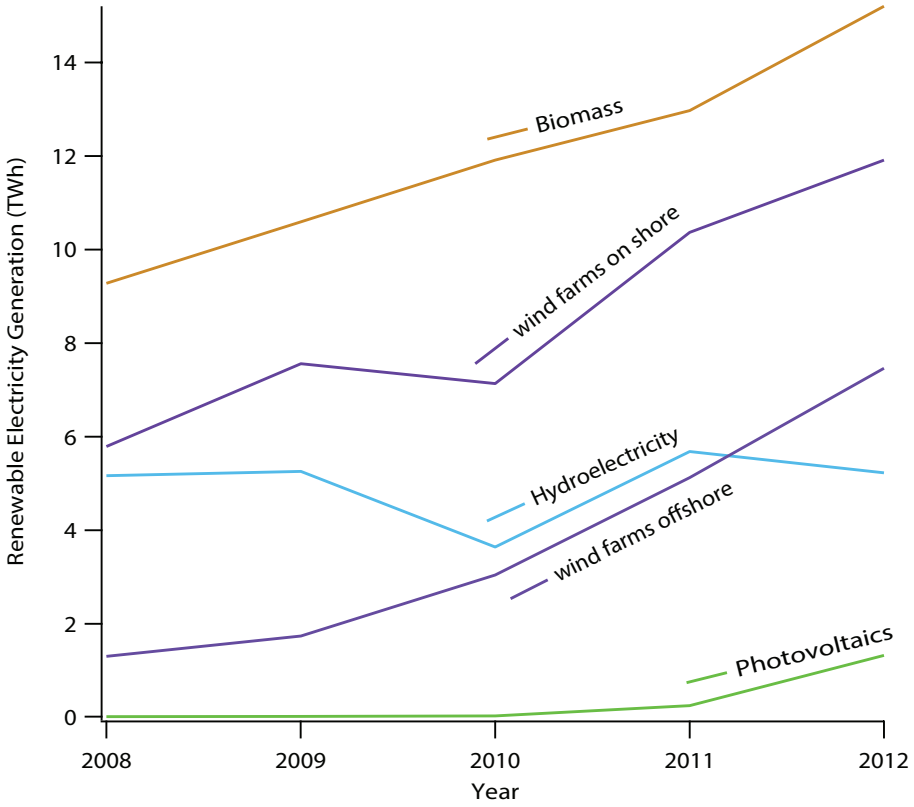

Figure 1.1: Plot of energy generated by renewable sources in the UK over the past 5 years.[3,4]

A clearer comparison between growth rates of the overall renewable electricity contribution and solar PV contribution, plotted in Figure 1.2, shows the higher growth rate of PV compared to total renewable energy produced.

This suggests that solar technologies could potentially become the dominant source of renewable energy if the trend continues. Below, I will analyse the characterisation and performance of major available renewable energy sources.

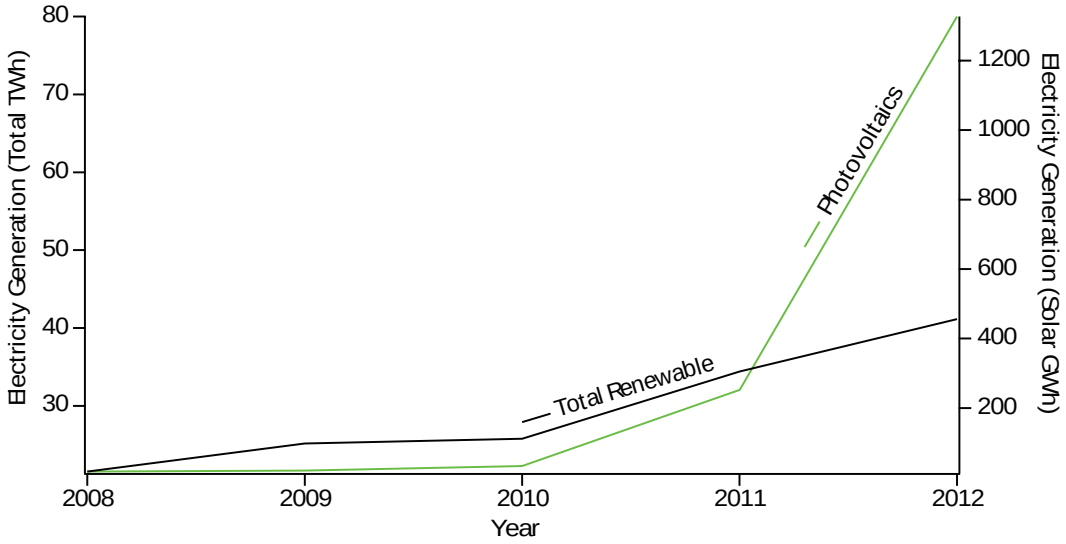

Figure 1.2: Plot showing the relative growth of energy generated by photovoltaics compared to the total renewable energy generated.

1.1.1 Biomass Energy

Biological material can be converted into fuel and release energy through combustion in which CO_2 emission is inevitable.[5,6] Agriculturally produced biomass can inhabit a large area of land, which could have otherwise been used for other forms of farming. On the other hand, biomass supplied in the form of waste products is beneficial in the context of waste management of the otherwise unused abundant waste. Biomass energy sources may be renewable but still involve carbon cycles in the environment which will have a negative impact through global warming. Biomass materials can include landfill waste, sewage sludge, biodegradable municipal solid waste, animal biomass and plant biomass. Biomass is useful in the disposal of waste but is damaging to the environment overall.

1.1.2 Wind Turbine Technologies

Wind turbine technology makes up a large fraction of the renewable energy supplied to the UK in the current green energy portfolio; it is a carbon zero energy source after installation but has disadvantages.[7] The main disadvantages of wind turbines are sound pollution caused by the rotation of the turbines on land which could be environmentally destructive for wildlife. Also manufacturing cost of turbines are significant and contribute to CO_2 emission. Energy production is dependant on weather conditions. During low wind speed periods, less energy is produced, whilst

excess wind could supply more energy than demand.

1.1.3 Hydroelectricity

Hydroelectricity is abundant, clean and safe. Water can be stored in reservoirs during periods of low demand and resupplied later. Water flows through a turbine, operating a generator and producing electricity. The Hoover Dam in Nevada supplies Las Vegas with renewable energy, with little impact to the environment. The largest issue in the construction of a hydroelectric plant is how it affects the ecology of an area and is restricted to areas with flowing water available. Small hydro power plants run off rivers and accounts for most of the hydroelectricity produced in the UK, with approximately 120 sites producing 100 MW.[8]

1.2 Solar Technologies

Solar energy is the most abundant form of renewable energy, essentially a natural nuclear fusion reactor. At high temperatures thermal radiation governed by nuclear reactions at the core of the sun follow a black body distribution. Photons carry a momentum and energy which can be utilised by thermal, photo or radiative processes. The sun provides approximately 3×10^{24} joules a year of energy to the earth; only 0.1 % of the earths surface covered with 10 % efficient solar cells would satisfy our global energy demands.[9]

The power of the sun can be harnessed in a variety of ways.[10] Thermal heat can be utilised in heating water *via* light absorption. Light can be used in solid-state and chemical processes, either a direct route to produce electricity (PV, DSSC), or by storing the energy chemically (photocatalytic water splitting or thermal chemical conversions).

Light passes through the atmosphere during passage to the surface of the earth. On entering the atmosphere of earth, light undergoes many absorption and scattering events before illuminating technology on ground level. The length of the lights path is defined as the air mass (AM) followed by a factor (AMX), where X is the number of times the light has travelled with respect to the height of the atmosphere from ground. The characterisation of the performance of solar cell technology requires

a standard spectral irradiance reference. The most commonly used is the AM1.5 spectral irradiance distribution. This is the irradiance of solar illumination after travelling an optical distance of 1.5 times through the atmosphere, after undergoing scattering and absorption events. AM1.5 corresponds to a situation where the sun is at an illumination angle of 48.19° (AM = 1/cos(48.19) = 1.5) relative to the normal of the surface of the earth. Air mass coefficient 0 is the spectral irradiance above the atmosphere, both spectra are shown in Figure 1.3. The usable power of light is less than the light above the atmosphere, and typically a value of 1000 W/m^2 or 100 mW/cm^2 is standardised in literature for an irradiance distribution of AM1.5.[11,12] Also, it is important to mention the averaged irradiance over 24 hours on an equinox is 395 W/m^2. The calculation takes into account the varying values of irradiance from dawn to dusk.

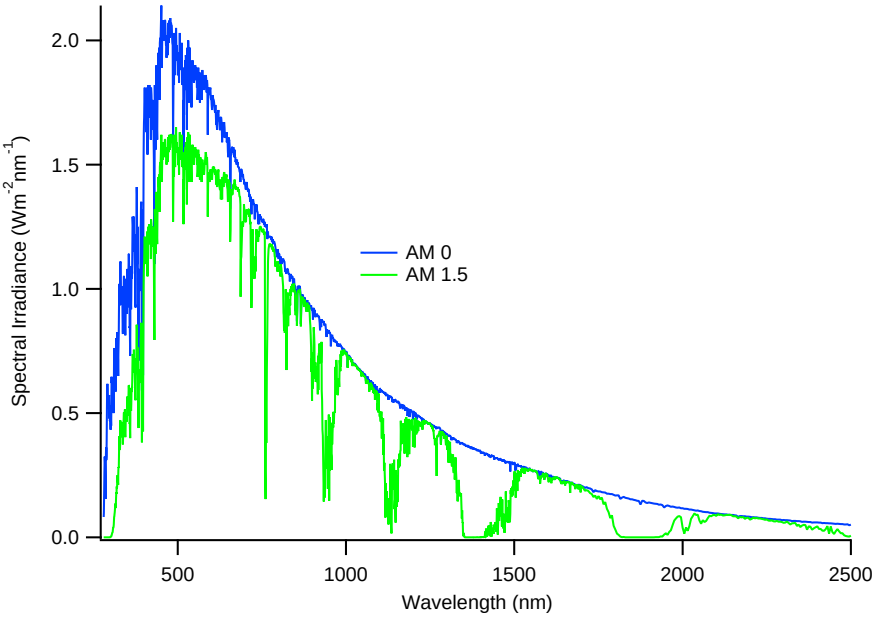

Figure 1.3: Plot of the standard terrestrial solar spectral irradiance distributions, AM 1.5 and AM 0.[13,14]

The large increase in PV technologies generating electricity in the UK is indicative of the growing interest in solar technologies, a comparison of total renewable energy output and PV technology output is shown in Figure 1.2.

Solar technologies can be classified under two categories, solid-state photovoltaic (PV) cells and photoelectrochemical (PEC) cells. Photovoltaic cells and photoelectrochemical cells both rely on semiconductor materials utilised as photosensitive

electrodes. A solid-state PV commonly consists of a bulk Si P-N diode and more recently thin film semiconductors. A dye sensitised solar cell (DSSC) contains a sensitiser which absorbs light, and a photoexcited electron is injected into the semiconductor supplying a potential and current to a load, the electrolyte redox reactions on the cathode and anode are reversed so the net reaction is zero and only electricity is generated and there is no change of the chemical environment.

A photoelectrochemical water splitting cell incorporates a semiconductor which absorbs light and the photoexcited charge carriers chemically transform the electrolyte producing chemical energy (hydrogen, energy is stored as chemical bonds). This is photoelectrolysis of water, generating hydrogen under solar illumination.

Solid-state photovoltaics have been shown to be the most efficient solar cell, but also expensive. DSSC PV solar cells are cheaper in construction and materials, but the efficiency has yet to reach that of solid-state photovoltaics. The low cost of DSSC solar cells make it an attractive avenue for new solar cell technologies. Photoelectrolysis cells produce hydrogen and is unique compared to other solar cells as the energy generated in the process is not directly formed as electricity. The energy carrier is in the form of hydrogen and can be electrochemically converted to electricity at a later time. This is advantageous over storing energy in batteries which incurs inherent losses during charging and discharging cycles (which also reduces the lifetime of a battery), and storage. Although fuel cells also incur losses, such as heat loss, fuel loss and losses due to storage, the overall longevity of a fuel cell and rapid refuelling drives the attraction of fuel cells over batteries in vehicle technology.

Understanding solar technology requires understanding the mechanism of photoexcited charge carrier creation. Semiconductors are photosensitive materials; they can conduct electricity under illumination of photons with energies higher than the band gap of the material.

Table 1.1 compares the levelised costs of various renewable technologies discussed earlier and non-renewable energy sources as of 2011. The cost of non-renewable sources are generally lower than that of renewable sources, and biomass can vary significantly in cost as well as CO_2 emission. Currently, large hydroelectricity plants are the most cost effective form of CO_2 free renewable energy, whilst solar energy is the most expensive, however the cost of solar technology is expected to drop

dramatically as technology matures.[15] This is not true for the other forms of renewable energy whose prices are in the midst of saturation as efficiencies and cost effectiveness have nearly reached optimum conditions. Thus it is expected over the next decade solar technologies could compete with fossil fuels with respect to cost effectiveness.

Technology	Price (pence/KWh)
Nuclear	8-10
Coal	10-15
Gas	5-11
Biomass	6-14
Offshore wind	12-14
Onshore wind	9-10
Hydroelectricity (5-16 MW)	7.2
Hydroelectricity (< 5 MW)	13
Solar (> 50 kW)	24

Table 1.1: Levelised costs of non-renewable and renewable energy sources, including capital costs, fixed operating costs and variable operating costs.[16,17]

1.2.1 Semiconductor Fundamentals

Crystalline materials exhibit electronic properties based on the binding nature of the atoms to the lattice. Vibrational behaviour of atoms in the crystal lattice produces a band structure, whereby certain energies are forbidden due to the creation of standing waves where group velocity vanishes (Bragg reflections) forming bands of allowed energy states and forbidden zones.[18,19]

In terms of the nearly free electron theory, the free electron potential is perturbed by a periodic lattice potential which inevitably forms standing waves. The highest occupied energy band is the valence band (electrons in this band are responsible for covalent bonding), whilst the lowest unoccupied energy band is the conduction band (electrons move freely and conduct in this band). Charge carriers near the top of the valence band and the bottom of the conduction band determine the semiconductor

properties.

For the tight binding approach, molecules bond with one and another and introduce a symmetric electron wavefunction and an antisymmetric electron wavefunction, these correspond to the bonding and antibonding energy levels (orbitals) respectively. With increasing number of atoms the number of energy levels also increase with slightly different energies due to the Paul Exclusion principle. As the number of atoms reach macroscopic levels (10^{23}) these energy levels become continuous and are no longer distinguishable from each other. The gap between the antibonding and bonding bands is associated with the band gap (E_g) of the material. The highest occupied molecular orbital (HOMO) is the valence band and the lowest unoccupied molecular orbital (LUMO) is the conduction band.

An electron excited to the conduction band will leave a positive charge in the valence band, which behaves like a particle. This is a convenient way to attribute properties of missing electrons rather than taking into account all the filled electron states in the valence band. The semiconductor is p-type if holes are the charge carrier responsible for conductivity, and n-type if electrons are the majority charge carrier.

This band structure and electron occupation of the bands determine whether a crystal is a conductor, semi-conductor or an insulator as illustrated in Figure 1.4; there are three possible scenarios;

a The valence band is filled and conduction bands partially filled by electrons; electrons are free to conduct. The material is a metal obeying free electron theory.

b The conduction band is empty and valence band full at 0K. When at ambient temperatures a small number of electrons can occupy the conduction band (and holes can occupy the valence band) according to the Fermi distribution. The material is a semiconductor since the E_g can be surpassed by thermal/optical excitations creating an exciton pair (electron-hole pair).

c The conduction band is empty and the valence band full at 0K, but the energy difference (E_g) between the bands is large (typically > 4 eV) and cannot be easily overcome. The material is an insulator in this case as there are no charge carriers free to conduct electricity.

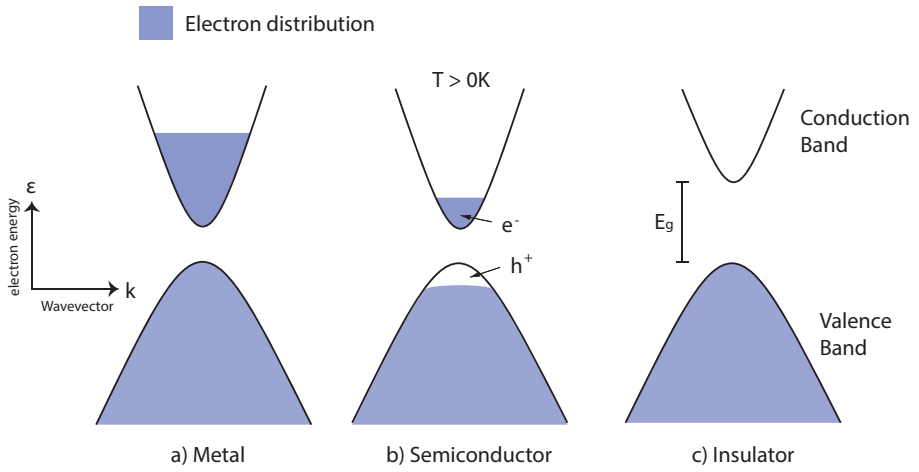

Figure 1.4: The electronic band structures of solid-state materials, (a) a material with the conduction band partially filled and valence band full is a metal, (b) a band gap under 4 eV is semiconductor and (c) a band gap larger than 4 eV is an insulator.

The energy gap and the required wavelength of light to excite electrons from the valence band the conduction band can conveniently be calculated using $\lambda = 1240/E_g$, the derivation of which is demonstrated in equations 1.1 to 1.4.

$$E(\text{joules}) = h\nu = \frac{hc}{\lambda} \tag{1.1}$$

$$E(\text{eV}) = \frac{hc}{e\lambda} \tag{1.2}$$

$$E = \frac{1.24 \times 10^{-6}}{\lambda} \tag{1.3}$$

$$\lambda(\text{nm}) = \frac{1240}{E_g(\text{eV})} \tag{1.4}$$

1.2.2 Solid-State Photovoltaics (PV)

The foremost solar technology in use today is solid-state crystalline photovoltaic semiconducting photo diodes. The p-n semiconductor diode converts sunlight directly into a potential and current.[20,21] These have limitations; the energy produced is either utilised immediately or stored in batteries. Storing energy in batteries adds to the complexity of the solar device, increasing construction costs. Single crystal/polycrystalline Si photovoltaic cells can be considered the first generation photovoltaic cells. Second generation thin film solar cells can be produced at a lower cost; as large surface areas can be achieved with limited material.[22] Semiconductors

with a direct band gap and high absorption coefficient are expensive, using thin films reduces overall cost as layers of only a micron are necessary. Greater efficiencies are achievable using Cu(In,Ga)Se_2 (CIGS) thin films,[23] with band gap values ranging from 1 eV to 1.7 eV (1240 nm to 729.4 nm) depending on gallium content. Since the peak spectral irradiance of the sun is at a wavelength of approximately 475 nm, which in terms of energy is 2.6 eV, a large portion of sunlight can be harnessed with CIGS technology. $CuInSe_2$ (CIS) thin films (no Ga) have the lowest band gap of the CIGS family.[24,25] Printable photovoltaics have been proposed in literature utilising a semiconductor ink which could in principle lead to a convenient mass manufacturing process at economically lower costs.[26] Multi-junction solar cell technology is relatively new and considered second generation photovoltaics. The construction of multi-junction solar cells involves the deposition of thin films of various semiconductor materials forming several p-n junctions, each with a different band gap/absorption energy, this allows a larger spectrum of light to be harnessed in the generation of electricity. The largest inherent loss of a single junction solar cell is the sensitivity of the cell to various wavelengths of light, by tuning the junctions to absorb different wavelengths higher efficiencies are possible with a theoretical limit of 87 % compared to 34 % for single junction cells according to the Shockley-Queisser limit. The Shockley-Queisser limit is the limit set on the maximum theoretical efficiency of a single p-n junction solar cell and is widely considered one of the most important contributions in the field. It was first calculated by William Shockley and Hans Queisser in 1961,[21] the upper limit of 33.7 % corresponds to an ideal single junction solar cell with an E_g of 1.34 eV. The Shockley-Quesser limit takes into account spectrum losses (where photons with an energy lower than the band gap cannot be utilised), radiative recombination (where electron-hole pairs recombine and cannot be used in the generation of electricity) and blackbody radiation (inherent losses due to the temperature of the solar cell).

- First Generation PV cells are capable of 25 % efficiency, but costly.

  Si crystalline/polycrystalline bulk (25 %)[27] p-n junctions. (E_g = 1.12 eV)

  GaAs (18.4 %),[28] InP (22.1 %)[29] and CdTe (16.7 %)[30] are efficient but expensive.

- Second Generation PV cells are capable of 12.7-20 % efficiency, and relatively inexpensive since thin films require less material.

  Si thin film (19.1 %)[31] and polycrystalline Si (20.4 %)[32] solar cells.

  $CuInSe_2$ (CIS - 12 %)[33] (E_g = 1 eV) and $Cu(In,Ga)Se_2$ (CIGS - 19.6 %)[25] (E_g = 1.6 eV)

- Third Generation PV cells are capable of 10-12 % efficiency, with the exception of multi-junction solar cells.

  Organic (polymer) solar technology (10 %)[34]

  Nanocrystalline solar cells (10.1 %)[35]

  Dye sensitised solar cell (not solid-state) (12 %)[36]

  Multi-junction solar cells. (41.6 %)[37]

The Fermi level is the maximum energy level filled with electrons at absolute zero as defined by the Fermi Dirac function. But since the Fermi level is a statistical measurement it is possible for it to be positioned within the band gap. The position of the Fermi level in a semiconductor defines the nature of the conductivity of the semiconductor, if the Fermi level is closer to the valence band than the conduction band, the majority charge carriers are the holes. For a semiconductor with a Fermi level closer to the conduction band the majority charge carriers are electrons.

When two semiconductors are in contact their Fermi levels align and the conduction band and valence band bend at the immediate vicinity of the junction in equilibrium due to electron and hole flow across the semiconductors, shown in Figure 1.5. This vicinity is the depletion zone, and an electric field is present in this region due to the flow of the charge carriers at the conjoining bands. The electrons combine with the holes (annihilation - indicated by the blue star) and leave behind positive ions, and negative ions on the p-type side, leaving a small width with limited charge carriers (i.e. depleted of charge carriers) creating a space charge layer.

In the practical construction of a p-n solar cell diode, a bulk boron doped p-type Si wafer and the surface of the Si wafer is doped with phosphorous or arsenic introducing an n-type Si layer, after which it is subsequently coated with a contact grid and antireflection coating. The circuit is completed with a contact on the base of

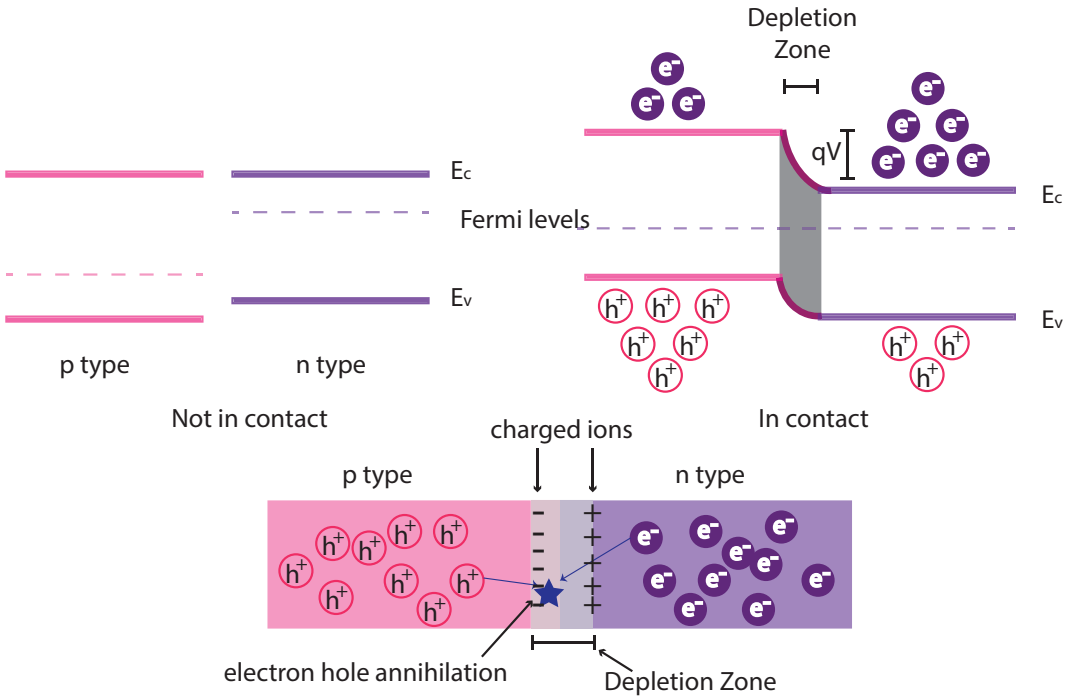

Figure 1.5: Band diagram of a p-type semiconductor in contact with an n-type semiconductor, charge carriers flow and annihilate at the vicinity of contact represented by the star. Leaving a region with few charge carriers (depletion zone) with positively charges ionised donors in the n region, and negatively charged ionised acceptors in the p region.

the p-type Si. Photons enter the material and produce an exciton pair. The electric field associated with the depletion zone separate the charges, and electricity flows through an external load. The mechanism and working of a PV diode is illustrated in Figure 1.6, electron hole pairs generated by photon absorption are influenced by the electric field in the depletion zone.

Currently solid-state crystalline silicon photovoltaics accounts for over 90 % of the solar cell market.[38] Photovoltaic systems require batteries to store energy when supply outweighs demand, this increases the size, complexity and cost of the system.

1.2.3 Photoelectrochemical Solar Cells (PEC)

Recent research has led to technological advancement allowing cheaper and abundant metal oxide semiconductor materials (TiO_2) to be incorporated into an electrochemical cell to either supply a potential and current or produce hydrogen and store energy chemically.[9]

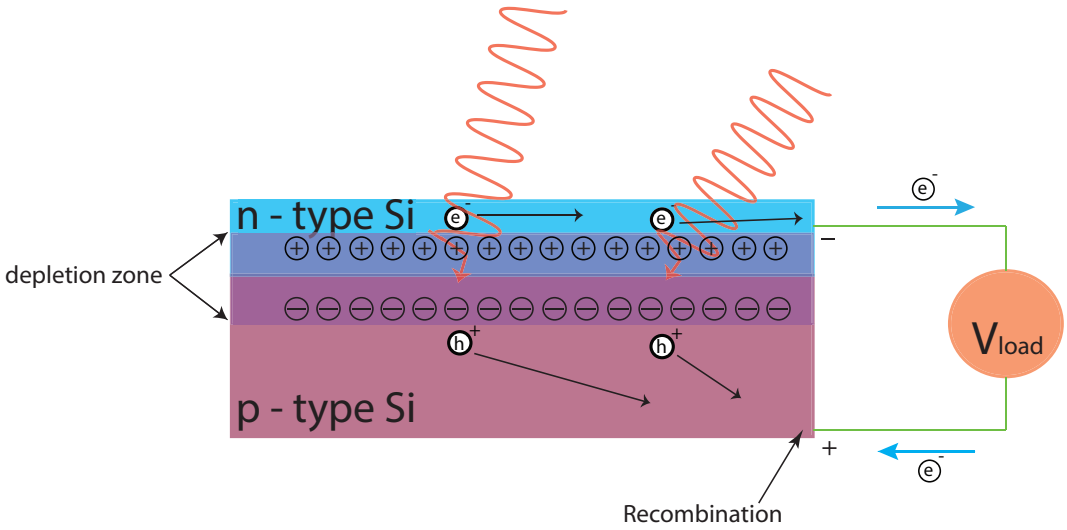

Figure 1.6: A p-n-junction diode solar cell. The depletion zone is where the electrons filling holes leaves positive ions on the n side and negative ions on p side.

Dye Sensitised Solar Cells (DSSC's)

Gratzel described the modern DSSC in 1988 along with Brian O'Reagan, and first reported a 7 % efficiency in 1991,[39] by 1993 the same group achieved a DSSC with a 10 % efficiency.[40] High efficiencies are possible due to the nanostructured TiO_2 surface, increasing the dye loading of the larger surface area of TiO_2. Additionally the liquid electrolyte is in contact with the entire surface area of the TiO_2 photoanode. Knowledge of organic dyes generating electricity under illumination has been known since the 60's, but previous attempts had been unsuccessful, due to unstable low surface area photoanodes. A nanostructured TiO_2 intermediate semiconductor solved many of the issues, yet electrolyte/sensitiser stability still poses an issue.

A photon absorbed by the dye molecule (sensitiser) promotes the molecule from the ground state to an excited state S*. In this excited state, electrons from the sensitiser are injected into the TiO_2 conduction band ($S^* \rightarrow S^+ + e^-$). The electron travels to the conductive glass and around the circuit to the platinum counter electrode. The oxidised dye molecules S^+ relax back to the ground state after receiving electrons from the iodide (I^-), the redox couple I^-/I_3^- will undergo a series of oxidations and reductions completing the circuit. A load can be placed along this circuit and provided with power, the mechanism for which is shown in Figure 1.7.

The abundancy and low cost of TiO_2 are advantageous in the construction of a DSSC, but ruthenium based dyes and platinum coatings can increase the cost

significantly. However, scientific efforts aim to reduce the need for costly dyes by exploring other sensitisers.[41]

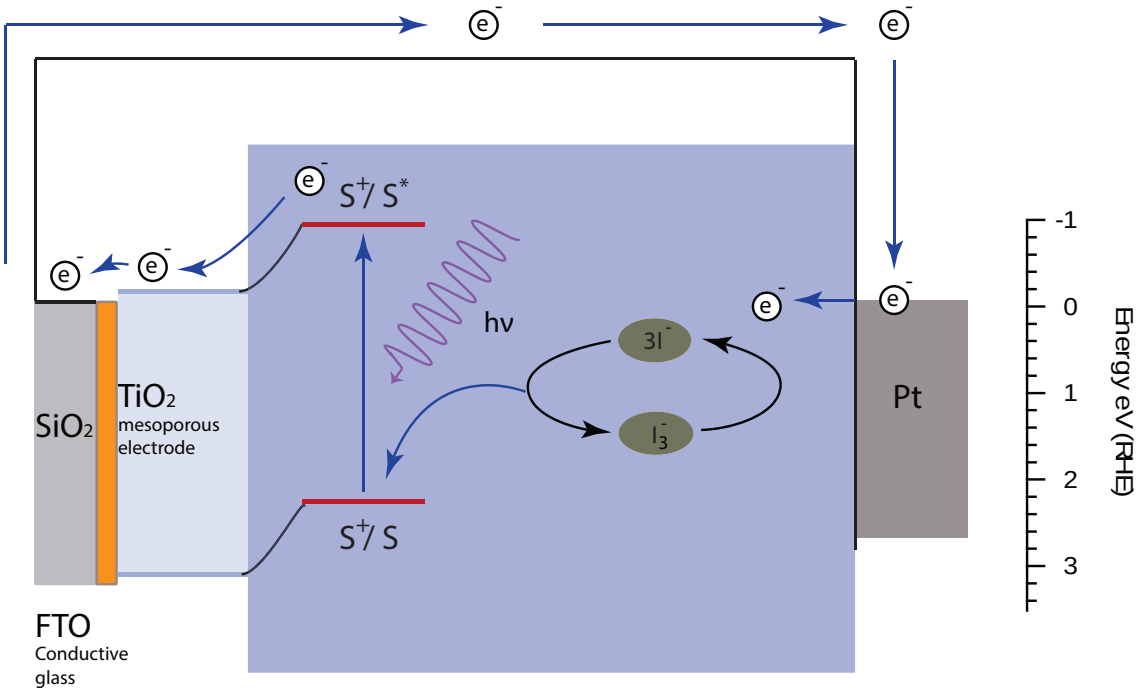

Figure 1.7: Band diagram of a dye sensitised solar cell, in this case an FTO coated with a TiO_2 mesoporous film serving as the photoanode. A simple description of the process of light absorption and charge transport in the PEC.

Photocatalytic Water Electrolysis

Michael Faraday first formulated the laws of electrolysis in 1833 and coined many of the terms still in use today, these laws led to electrochemistry becoming a subject in it's own right.[42,43] Although decades earlier electrolysis of water was discovered to produce hydrogen in 1789 by Jan Rudolph Deiman and Adriaan Paets van Troostwijk.[44,45] The process was improved by William Nicholson and Anthony Carlisle using a voltaic pile as a DC power source supplying electrons to the cathode with a certain potential.[46,47]

Photoelectrochemistry was first discovered by Becquerel in 1839 in the form of the 'Becquerel effect',[48] whereby two electrodes immersed in an electrolyte produced an electrical current under illumination. Much later, the understanding of photoelectrochemistry was cemented by Brattain and Garret in 1954; through the study of chemical reactions on the surface of a germanium semiconductor electrode under

illumination. Brattain and Garret showed that the chemical reactions are influenced by controlling the semiconductor properties and exposing the electrode to illumination.[49]

The first experimental confirmation of photoelectrochemical decomposition of water was observed by Fujishima and Honda in 1972, using a TiO_2 photoanode.[50] The solar photoelectrochemical decomposition of water has emerged as a widely studied area of research. Advancement in nanotechnology has allowed the observation of smaller features as well as the ability to create nanostructured photoanodes, thereby increasing the surface area of the photoanode. This has led photoelectrochemical water splitting research to achieve higher efficiencies, and a possible solution to the storage of energy produced by the sun.[51]

The work in this thesis concentrates on nanostructured photoanode design for PEC solar hydrogen production. The sun provides photons for absorption by a material (semiconductor) which creates electron-hole pairs, these electron-hole pairs aid in the decomposition of a H_2O molecule, separating hydrogen and oxygen. The reaction taking place at each of the electrodes is shown in equations 1.5 to 1.7 for highly acidic electrolytes. In an alkaline solution, reactions are facilitated by OH^- ions rather than protons. These reactions are shown in equations 1.8 to 1.10. The redox potentials are given in both the reversible hydrogen electrode (RHE) scale and the normal hydrogen electrode (NHE) scale. The hydrogen generated can then be transported to a storage medium for later use as a fuel.

$$2\,h\nu = 2\,e^- + 2\,h^+ \quad \text{Acidic conditions (pH 0)} \tag{1.5}$$

$$2\,h^+ + H_2O_{(l)} = \frac{1}{2}O_{2(g)} + 2\,H^+_{aq} \quad \text{1.23 V RHE/NHE} \tag{1.6}$$

$$2\,H^+ + 2\,e^- = H_{2(g)} \quad \text{0 V RHE/NHE} \tag{1.7}$$

$$2\,h\nu = 2\,e^- + 2\,h^+ \quad \text{Basic conditions (pH 14)} \tag{1.8}$$

$$2\,OH^-_{aq} + 2\,h^+ = \frac{1}{2}O_{2(g)} + H_2O_{(l)} \quad \text{1.23 V RHE (0.43 V NHE)} \tag{1.9}$$

$$2\,H_2O_{(l)} + 2\,e^- = 2\,OH^- + H_{2(g)} \quad \text{0 V RHE (-0.8 V NHE)} \tag{1.10}$$

The charge carriers need to have an energy difference greater then 1.23 eV in an ideal PEC, which is the minimum energy required to split water into hydrogen and oxygen determined by the Gibbs free energy of the reaction.[52,53]

The Gibbs free energy is a measure of the free energy of the evolution of a chemical system and the spontaneity of the reaction; if the change in G is negative, $\Delta G = \Delta H - T\Delta S$, a spontaneous reaction can occur and produce a voltage during the reaction, i.e a battery. If the change in Gibbs free energy is positive the reaction is not spontaneous, and in this case the electrochemical cell is said to be electrolytic and requires a voltage for the reaction to take place, this is the case in photoelectrolytic water splitting. The relationship between voltage and the change in Gibbs free energy is described by equation 1.11.

$$\Delta G_{T,P} = -w_{electrical} = QV = -nFE \tag{1.11}$$

The rate of hydrogen generation can be expressed as $R(H_2) = \frac{I_{photo}}{nF}$ where F is the Faraday constant (9.6485×10^4 C/mol), n is the number of moles of electrons it takes to produce one mol of hydrogen, I_{photo} is the photocurrent, E is the electrode potential and $w_{electrical}$ is the electrical work done.

The conversion of one molecule of H_2O to H_2 and $\frac{1}{2}O_2$ is $\Delta G = 237.2$ kJ/mol. This is equivalent to 1.23 eV per electron transferred according to equation 1.11 where the number of moles of electrons is two for generating 1 mol of hydrogen. The sun radiates 1000 W/m^2 on the surface of the earth at a penetration depth of 1.5 times the atmosphere. A 10 % efficient ideal PEC cell coverage of 1 m^2 (with a photopower output density of 100 W/m^2, at half of 1.23 V gives a photocurrent of 162 A) can generate 3 g / 34 L (standard temperature and pressure - STP) of hydrogen per hour, this is an equivalent of 0.432 MJ energy content (120 Wh).

The process of water photoelectrolysis is depicted in Figure 1.8, the photosensitive anode absorbs light creating an exciton pair. The photoanode (working electrode) is the electrode where the oxygen evolution reaction occurs (OER) and the hydrogen evolution reaction (HER) occurs on the Pt counter electrode (cathode). The quality of the photoanode determines the OER rate and is the electrode of interest. The photoexcited electron traverses the circuit and is injected into the electrolyte to be utilised in the reduction of water, generating hydrogen. On the

photoanode surface, a hole is injected into the electrolyte oxidising the water and bubbling oxygen.

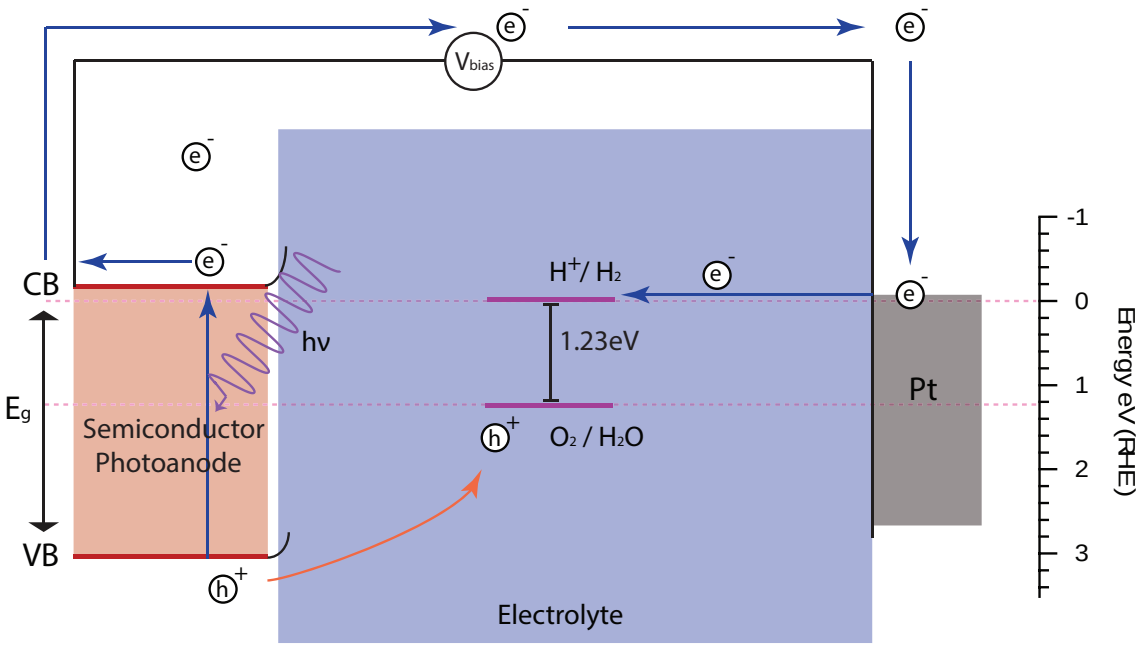

Figure 1.8: Band diagram of the fundamental mechanism of water electrolysis.

In practice about 2 eV is required to overcome the energy losses relating to reaction kinetics and charge transfer through electrical leads and the electrolyte i.e. the electrode overpotentials and ohmic potentials. The electrode overpotential results from low activity of the electrodes in the electrolyte, which is also known as the activation overpotential. The ohmic loss is due to resistive losses in the cell. The overpotential must be minimised to obtain high efficiency. For example, the use of co-catalysts can assist in reducing the overpotential for a given redox reaction to take place.

1.3 Utilising Nanostructured Metal Oxides

Photoanode Fundamentals

The metal oxide semiconductor used as a photoanode must satisfy a number of conditions to be considered applicable for PEC water splitting applications. Firstly, the band edges must straddle the water reduction and oxidation potentials; secondly, the band gap energy should be such that a large portion of the solar spectrum can

be harvested. Only photons with a high enough energy (hν) to surmount the band gap of the photoanode can be absorbed to create an exciton pair.

Unfortunately, the most stable metal oxide semiconductors have a band gap energy in the UV range.[54] For example, TiO_2 has a band gap energy of 3.2 eV (λ (nm) = $1240/E_g$) which is the equivalent of a photon with a wavelength of 387 nm. The UV range of the solar spectrum is only a fraction to the whole spectrum, ideally the semiconductor should have a band gap in the 2 eV range thereby utilising the visible part of the spectrum. Recent attempts have been driven toward doping and surface modification to improve electronic properties of the photoanodes or engineering band gaps including the introduction of donor and acceptor levels to the band structure.[55–61]

Band bending occurs at the interface between the semiconductor and liquid electrolyte in the photo electrochemical cell when the Fermi levels of the semiconductor and the chemical potential of the redox couple of the electrolyte are in equilibrium.[62] A potential can reduce the band bending until the conduction band minimum (CBM) and valence band maximum (VBM) are unbent, and an accumulation layer is no longer present (no space charge layer) at the interface, the potential when this situation arises is called the flat band potential (V_{fb}).

The electrolyte Fermi level (chemical potential) is between the O_2 and H_2 redox couple and is dependent on the concentration of the ions in the electrolyte. The chemical potential is a function of the Gaussian type distribution of redox states.

A space charge layer forms at the semiconductor/electrolyte interface, if the chemical potential of the electrolyte is lower than the Fermi level of the semiconductor, electrons flow from the semiconductor into the electrolyte under illumination and equilibrium after contact. This leaves positive ions on the surface of the semiconductor. Negatively charged ions congregate on the electrolyte side of the interface, and this space charge double layer region at the interface is known as the Helmholtz layer. The band bending is due to the congregation of charges at the interface similar to the mechanism of a p-n junction.

By applying a positive bias to the photoanode the photoexcited electrons flow from the semiconductor to the counter electrode. This charge flow raises the Fermi level of the Pt counter electrode (charge carrier density increases in the Pt). Thereby,

simultaneously increasing band bending and encouraging charge separation. Also, if the conduction band is lower than the proton reduction potential, raising the Pt counter electrode Fermi level supplies the electrons with enough energy to reduce water.

If the PEC cell is based on a single n-type semiconductor material, the band gap must straddle the reduction and oxidation potentials and the Fermi level of the semiconductor must be above the electrolyte redox couple Fermi level for the reduction reaction to take place. The CBM must be more negative than the proton reduction potential (0 V vs RHE) and the VBM must be more positive than the oxidation potential (+1.23 eV). TiO_2, ZnO and zinc titanate all satisfy this requirement. Iron oxide does not, Fe_2O_3 has a high oxidative power due to the lower position of the valence band edge (2.4 V_{RHE}, over a volt larger than the oxidation potential) yet the conduction band is not high enough for reduction to occur. However applying an external voltage raises the Fermi level of the counter electrode (the bulk Fermi level) and consequently lowers the CBM/VBM edges with respect to the electrolyte redox couple, it is then possible for the electron to traverse the circuit with enough energy to reduce the water.

The conduction band and valence band edges are affected by the pH of the electrolyte, and shift with 59 mV×pH with respect to the vacuum energy.[63] Increasing the pH of the electrolyte raises the band edges. Unfortunately this is also true for the reduction and oxidation potentials. The band edges therefore remain fixed with the reduction and oxidation potentials. Hence, positioning the band edges into a more favourable straddling position is not possible by solely altering the pH of the system.

Typically most metal oxide semiconductors are n-type due to the non-stoichiometric nature under typical synthesis conditions,[65–67] the crystal structure can be metal rich or oxygen deficient which raises the Fermi level. Some metal oxides are oxygen rich or deficient of metal under synthesis conditions, these non stoichiometric conditions results in p-type behaviour.

Some metal oxide band positions are shown in Figure 1.9, versus energy (eV vs RHE) and the reduction and oxidation potentials are plotted in dashed lines. The first few are relevant to this work, the others are useful for future work. The values

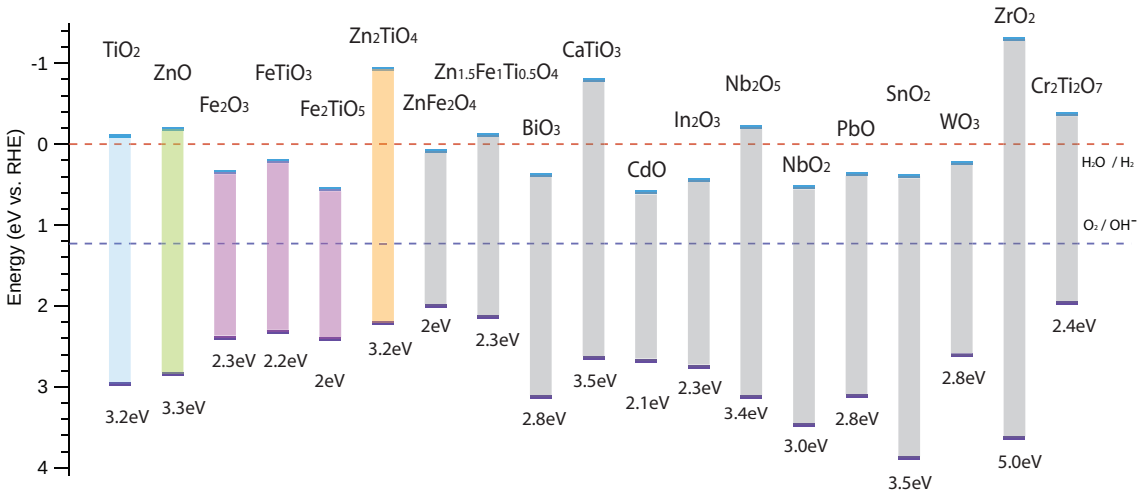

Figure 1.9: Band positions of a selection of metal oxides and metal oxide alloys, illustrating their position with respect to H_2O oxidation and H_2 reduction potentials.[64]

of the band positions and band gaps are summarised in Table 1.2.[64]

For metal oxides, the valence band maximum (VBM) is determined by the 2p orbital of oxygen, whilst the conduction band minimum (CBM) is determined by the cation electronic structure and empty orbitals. The fluctuation of the VBM is due to the symmetry of the crystal, and the electronic structure of the neighbouring cations. In the case of ZnO, the filled 2p levels of O^{2-} and empty 4s levels of Zn^{2+} are seperated when the ions are bought together to form a solid. Reading from the energy diagram in Figure 1.9, chromium titanate ($Cr_2Ti_2O_7$), for example, is a suitable candidate for unassisted water splitting, the CBM and VBM straddles the redox couple potentials and the band gap allows photoexcitation in the visible light range (2.3 eV is 540 nm, green absorbtion) utilising a significant portion of the solar spectrum. The only practical issue whether chromium titanate is sufficient for water splitting, is if the VBM position provides enough overpotential to facilitate oxidation reactions (OER) on the surface of the photoanode and charge carrier mobility within the chromium titanate crystal.

Advantages of Nanomaterial Photoanodes

Nanostructuring materials can significantly enhance the surface area of the material and will subsequently increase the electrolyte/semiconductor contact surface area. A larger surface area of the electrolyte/semiconductor junction can facilitate a larger

Metal Oxide	CBM (eV vs RHE) ± 0.1 V	VBM (eV vs RHE) ± 0.1 V	Band gap Eg (eV)
TiO_2	-0.1	3.1	3.2
ZnO	-0.2	3.1	3.3
Fe_2O_3	0.4	2.7	2.3
$FeTiO_3$	0.2	2.4	2.2
Fe_2TiO_5	0.6	2.6	2.0
Zn_2TiO_4	-1	2.2	3.2
$ZnFe_2O_4$	0	2	2
$Zn_{1.5}$ $Fe_1Ti_{0.5}O_4$	-0.1	2.2	2.3
BiO_3	0.4	3.2	2.8
$CaTiO_3$	-0.8	2.7	3.5
CdO	0.6	2.7	2.1
In_2O_3	0.5	2.8	2.3
Nb_2O_5	-0.2	3.2	3.4
NbO_2	0.5	3.5	3.0
PbO	0.4	3.2	2.8
SnO_2	0.4	3.9	3.5
WO_3	0.2	2.6	2.8
ZrO_2	-1.3	3.7	5.0
Cr_2Ti_2O	-0.4	2	2.4

Table 1.2: Band edges and band gaps of the various metal oxides plotted in Figure 1.9.

number of oxidation evolution reactions.

Ordered nanomaterial semiconductors provide advantageous charge transport routes. Also, 1D wires and tubes can act as optical waveguides if the dimensions are in the order of the wavelength of the illumination of interest. 1D alloy nanomaterials can create an array of tunable properties, controlling band gaps by alloying semiconductors and controlling structure based optoelectronic properties.[68]

Metal oxides play a crucial role in physics, chemistry and material science, metal elements are able to form a wide variety of oxide compounds. The ease of processing metal oxides is a great advantage in the development of devices, which is versatile and cost effective. A challenge in finding materials for photoanodes is discovering hybrid metal oxides with superior stability in electrolytes, whilst retaining beneficial band positions i.e. absorption greater than 1.23 eV and straddling the redox poten-

tials. Nanostructured materials further reduce costs compared to bulk materials, if expensive elements are used, a large surface area is achievable with limited material.

Research into heterostructure metal oxides provides the opportunity of engineering band gaps and electronic properties. Alloying metal oxides and creating a hybrid oxide with a preferential band gap has been extensively researched. Heterostructure junctions utilise surface electronic state dynamics,[69] improving charge transport in the structure. A variety of scenarios are possible which are illustrated in Figure 1.10.

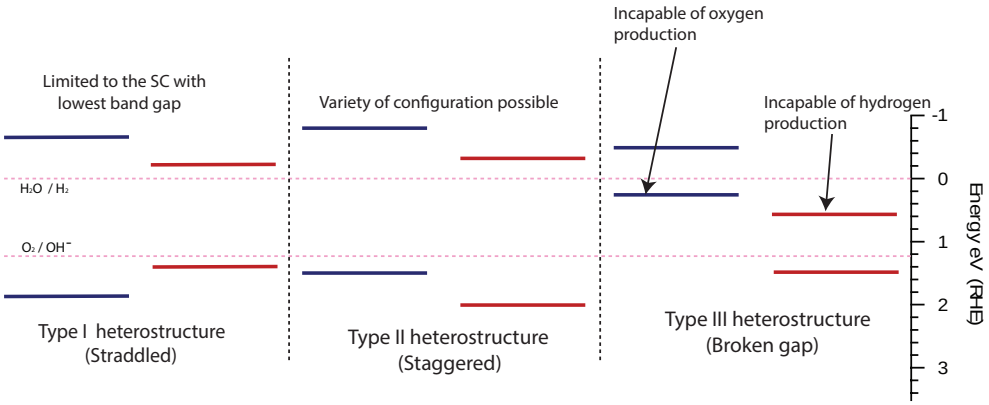

Figure 1.10: Three types of heterostructure semiconductors are classified according to their position between each other. Type I and type II can be utilised as a photoanode material, whilst type III is not useful for photocatalytic water splitting.

For a Type I heterojunction, a wide and narrow band gap material are in contact. One could be UV sensitive and the other could be sensitive to visible light. The redox power is determined by the narrow band material. A Type II heterojunction is a junction between materials with different Fermi levels and work functions but similar band gaps. A typical situation is a p-n junction, electron energy will be determined by the CBM of the n-type material and hole energy is determined by the VBM of the p-type material. A broken gap heterostructure is a type III heterojunction where the band positions of either material do not straddle the redox potentials. Oxidation and reduction reactions will be stunted in a type III heterostructure serving as a photoanode. Therefore it is essential to enable precise control of the electronic structure to maximise the light absorption and determine appropriate positions for the CBM and VBM.

1.4 Hydrogen, Fuel of the Future?

Amongst the benefits of hydrogen is the versatility in direct energy conversions; thermal, mechanical and electrical energy conversions are all possibilities.[70]

Hydrogen is a lightweight fuel and is the richest in energy per unit mass of any fuel. Hydrogen as a fuel for a combustion engine has an optimum thermodynamic efficiency of 38 % and is 8 % higher than that of petrol.[71,72] Hydrogen is also a carbon zero fuel, since oxidation (combustion) of hydrogen produces only water as a by-product. However, at the high temperatures involved in the combustion of hydrogen, harmful nitrogen oxides may be produced. An efficient way of using hydrogen as a clean gas fuel is to use it in a fuel cell. Hydrogen has an energy density of 120 MJ/kg, whilst petrol has an energy density of 44.4 MJ/kg.[73] Hydrogen has a much higher energy density, which coupled with the zero carbon emission, makes it an ideal candidate as a clean fuel for the future. The detailed structure and mechanism of a hydrogen fuel cell will be discussed later in section 1.4.

Current methods of hydrogen production are costly, non-renewable and CO_2 emissive, limiting the development of a mainstream hydrogen economy.

The key challenges of progressing to an oil-free hydrogen economy are achieving low mass to weight ratio hydrogen storage methods,[74] and renewable methods of hydrogen production with higher efficiencies. If these challenges are tackled, a future powered simply by the sun and water will significantly change our way of life as a society.

Current Methods (CO_2 Emissive) of Hydrogen Production

Currently the major production of hydrogen is chemically extracting hydrogen from fossil fuels (96 %), which inevitably still contributes to CO_2 emission.[75]

The methods of extracting hydrogen are;

- Steam reforming of natural gas or methane (hydrocarbons)[76–80]

  $$CH_4 + H_2O \rightarrow CO + 3H_2$$

  $$CO + H_2O \rightarrow CO_2 + H_2$$

- Partial oxidation of methane[81–83]

$$CH_4 + \tfrac{1}{2}O_2 \rightarrow CO + 2H_2$$

$$CO + H_2O \rightarrow CO_2 + H_2$$

- Autothermal reforming of hydrocarbons[84–87]

$$2CH_4 + O_2 + CO_2 \rightarrow 3H_2 + 3CO + H_2O \text{ (exothermic due to oxidation)}$$

$$CO + H_2O \rightarrow CO_2 + H_2$$

- Gasification of coal[88–92]

$$3C + O_2 + H_2O \rightarrow H_2 + 3CO$$

$$CO + H_2O \rightarrow CO_2 + H_2$$

In all of the above processes carbon plays a significant role and the final products are H_2 and by-product of CO_2. Ultimately hydrogen produced this way is not beneficial to the environment and if used in transport will contribute to CO_2 emission unless an effective way to either store or convert CO_2 back into hydrocarbons are developed. Cleaner methods of hydrogen production are required before it can be considered as a renewable, CO_2 neutral fuel.

CO_2 Neutral Methods of Hydrogen Production

Alternatively the four key green solar hydrogen generation systems include:

- Photoelectrochemical cells (PEC)
  - Electrolytes in a cell undergo photocatalytic reaction due to a light sensitive anode, facilitating water electrolysis.[93]
- Photovoltaic (PV) cells as an electrolyser
  - A DC current supplied *via* photovoltaics facilitate water electrolysis.[94]
- Photobiological systems
  - Living organisms produce hydrogen under illumination (photosynthesis of algae or cyanobacteria).[95]
- Thermal decomposition of a metal oxide (thermochemical cycles).

- Sunlight can be focused to create a high temperature beam. The heat associated with the beam decomposes a metal oxide, which in turn is oxidised in the presence of water, and generates H_2.[96]
- $ZnO \rightarrow Zn + \frac{1}{2}O_2$ (2300 K Δ H = 557 kJ/mol)
- $Zn + H_2O \rightarrow ZnO + H_2$ (700 K Δ H = -63 kJ/mol)

A PV and an electrolyser system is a two part configuration, a solid-state photovoltaic provides the electrons under illumination. The electrons are utilised in the decomposition of water. The choice of photovoltaic diode dictates the range of light absorbed. Thus, by employing a PV semiconductor with a band gap of approximately 2.4 eV a large portion of the solar spectrum can be harnessed. However, there is extra energy cost which is lost in overcoming the overpotentials of the redox reactions. Additionally, the storage of the water splitting module increases the complexity of the system.[97] A high photocurrent may be possible but a significant amount of this electric output is wasted to drive the overpotential, this is not true for a PEC where the band bending of the semiconductor-liquid interface actually decreases the overpotential. Less energy is wasted in a PEC, and a larger portion of the suns irradiance can be utilised in directly splitting water.

Water splitting can also occur by photobiological processes.[98,99] For example, when algae are deprived of sulphur they start producing hydrogen rather than oxygen through photosynthesis. A hybrid biophotoanode has recently been shown to produce hydrogen at double the efficiency of iron oxide photoanodes, the photoanodes are created by cross coupling iron oxide with phycocyanin.[100] Phycocyanin is a light harvesting protein and when integrated with a hematite film enhances light absorption.

Thermochemical cycles utilise the decomposition of metal oxides in the presence of water, splitting water as the chemical reactions occur.[101–104] Iron oxide,[105,106] copper oxide[107] and zinc oxide[108–110] are just a few of the metal oxides that can undergo the cyclical process of decomposition and oxidation at reasonable temperatures, producing hydrogen as the by-product. This method of hydrogen production is useful when heat is available as a waste product of a process, or under magnified solar illumination. The work in heating the metal oxide is the major influence in overall output efficiency.

This work will concentrate on photoelectrode designed for photoelectrochemical cells.[9] A PEC has many advantages over the other hydrogen production methods described, the simple design of a PEC results in lower energy losses compared to an electrolyser-electrolyte configuration, and far less energy waste than a thermocyclical process which outputs inherent wasted heat. While, photobiological systems seem promising, the research is not as well grounded as photoelectrochemical cells and not as flexible when it comes to choice of biological materials for the construction of the generators. The materials in the construction of a PEC primarily consist of the semiconductor photoanode, of which a countless number of metal oxide/nitride alloys can be explored.

Hydrogen Storage

Once hydrogen is generated, it will immediately require effective storage. This is essential for the practicality and portability of the technology. The DOE target for the volumetric capacity storage of hydrogen was 28 g H_2/L in 2010 and 40 g H_2/L in 2015.[111]

Current efforts are geared toward incorporating hydrogen into solid matrices,[112] which can adsorb hydrogen effectively for storage and easily extracted for later use.[113] Hydrogen stored on graphene pillars was predicted to store hydrogen with a high mass/weight ratio, storing up to a volumetric capacity of 41 g H_2/L.[114]

Along with carbon based storage (graphene/CNT/bucky balls), metal hydrides and metal oxides such as ZnO[115] and TiO_2[113] have all garnered considerable interest.

Metal organic frameworks (MOFs), metal oxide frameworks and activated carbon bind molecular hydrogen to the surfaces *via* Van der Waals interactions (physisorption). Metal/chemical hydrides trap atomic hydrogen *via* a strong chemical bond which consequently requires high temperatures (150-200 °C) to release hydrogen.[116]

Metal decorated polymers could provide a lightweight matrix to store hydrogen, with short molecular adsorption and desorption times.[117] Interestingly in the inverse scenario a polymer outer layer can protect hydride nanocomposites from O_2 and H_2O,[118] allowing a selective gas permeability for hydrogen adsorption and desorption.

Fuel Cells

The generated hydrogen can release its energy through an efficient fuel cell operated at a relatively low temperature and pressure, these conditions are essential for the safety and longevity of commercial technology. Here I will discuss some technical details of a modern hydrogen fuel cell.

Fuel cells work in the opposite sense of water electrolysis and were first developed practically by Francis Thomas Bacon in 1959, whilst the principle was first demonstrated much earlier by Sir William Grove in 1839.[119] The principle is illustrated in Figure 1.11 for two types of fuel cell, (a) the polymer exchange membrane fuel cell and (b) a solid oxide fuel cell. The conversion of hydrogen to water through reverse electrolysis allows an obtainable work of 237 kJ/mol (H_2O Gibbs free energy) and can reach high theoretical efficiencies. Whilst chemically converting hydrogen to water (combustion) inherently produces heat and is approximately 50 % efficient, thereby obtaining only 143 kJ/mol of work from the 286 kJ/mol available (enthalpy of combustion).[120]

Fuel cells are classified according to the materials used as the electrolyte. A list of a few types of fuel cells include:

- Polymer exchange membrane fuel cell (PEMFC)[121,122]
  - A PEMFC operates at low temperatures, ranging from 30-100 °C. The ionic flow of charge is facilitated by hydrogen ions, the reaction is shown in Figure 1.11(a). The electrodes are decorated with Pt catalysts to assist in the electrochemical reaction.
- Solid oxide fuel cell (SOFC)[123]
  - Oxygen ions are the charge carriers in an SOFC, the ionic flow in the solid oxide electrolyte is a thermally activated process and require temperatures ranging from 500-1000 °C. A variety of materials are utilised in the electrode material of an SOFC. The construction of an SOFC is illustrated in Figure 1.11(b).
- Alkaline fuel cell (AFC)

  - OH^- is the charge mediator in the aqueous electrolyte and operates in a temperature range from 50 °C to 200 °C, the alkaline fuel cell has the highest efficiency of 60 % whilst the efficiency of a PEMFC is between 25-58 % and an SOFC is below 43 %. A key issue of the AFC is the formation of potassium carbonate which blocks the pores of the cathode and reduces the ionic conductivity of the electrolyte.

- Molten carbon fuel cell (MCFC)

  - CO_3^{2-} is the charge carrier and operates at 650 °C, the molten electrolyte is composed of lithium-potassium carbonate salt heated to high temperatures. A significant advantage of an MCFC is that non-noble metal electrodes can be used, for example a nickel anode and nickel oxide cathode are able to facilitate the electrochemical reaction.

A solid electrolyte enables a simple construction of the cell. A solid polymer membrane serves as the electrolyte in PEM fuel cells and platinum incorporated porous carbon electrodes serve as anode and cathode. The platinum is the catalyst in the electrodes which react with hydrogen removing electrons from the atoms. The hydrogen ions can conduct through the polymer membrane and react with oxygen at the cathode forming water. The PEM cell is illustrated in Figure 1.11(a).

Solid-state electrochemistry is not new; Faraday discovered PbF_2 and Ag_2S can conduct electricity through the motion of ions,[124–126] and can either have negligible electron transport or can conduct both ions and electrons (intercalation electrode). A key advantage of using a solid electrolyte in a fuel cell is the reduced complication in construction, where all constituent electrodes and electrolyte can be deposited layer by layer and form a convenient cell, without the need for membranes and liquid (requiring seals). Metal oxide electrolytes have been known since 1884 when Warburg demonstrated Na^+ ions can be transported through glass (SiO_2).[127] Later Nernst found ZrO_2 doped with Y_2O_3 can conduct oxide ions; an ionic current passing through the crystal oxide produces white light and was proposed as a unique form of electric light.[128,129]

Solid oxide fuel cells on the other hand require high operating temperatures (1000 °C), with the high operating temperatures the choice of materials used in the

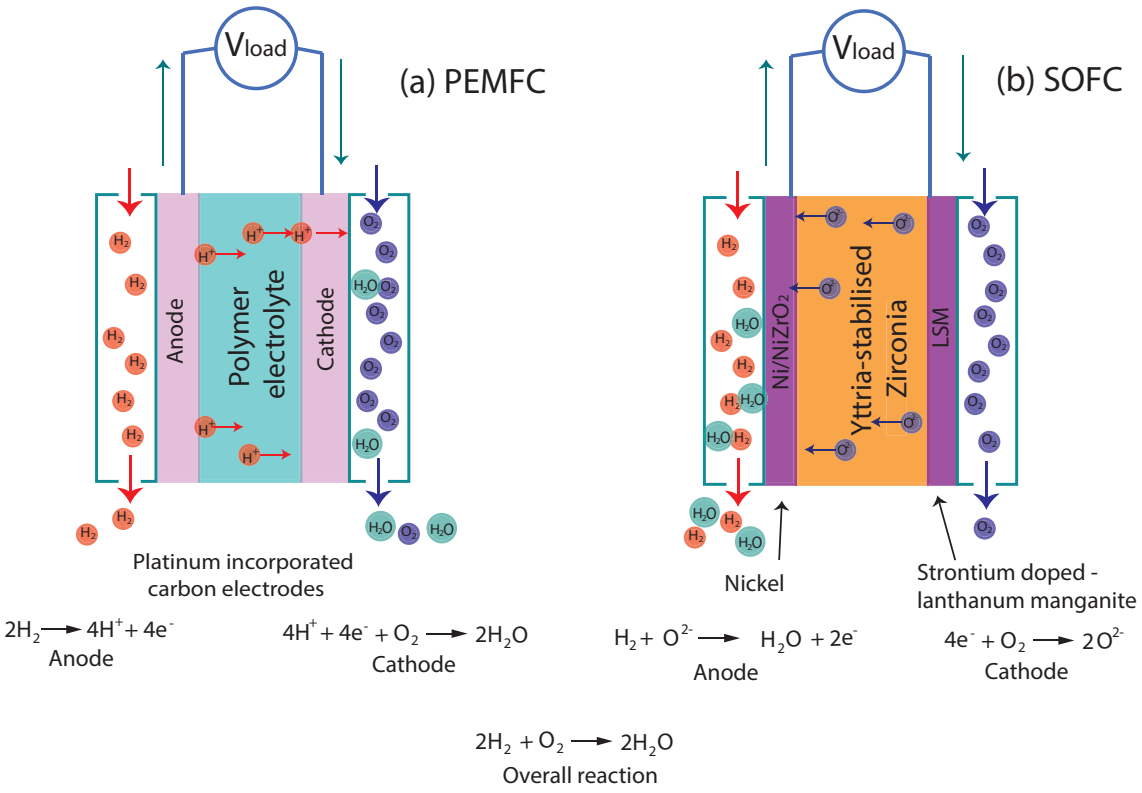

Figure 1.11: Illustration of the mechanisms of a PEMFC (a) and an SOFC (b), conducting H^+ and O^{2-} ions respectively.

construction of the fuel cell are limited and poses problems for long term stability of the cell. The three most commonly used electrolytes are yttria-stablised zirconia (YSZ), doped ceria (CeO_2) and lanthanum gallate ($LaGaO_3$).[130] In the case of a metal oxide electrolyte the charge carriers are negatively charged oxygen ions. Oxygen is supplied at the cathode and reacts with electrons, the oxygen ions migrate through the metal oxide and react with hydrogen at the anode forming water. The cathode material determines the oxidation reaction and determines efficiency of the cell. Lanthanum manganites and lanthanum cobaltites are metal oxide semiconductors which show good catalytic properties at high temperatures. Recent progress has shown a material composed of strontium doped lanthanum manganites (LSM)[131,132] possesses good properties as a cathode material, i.e. good electronic conductivity and matching heat expansion coefficient with YSZ. It is also less prone to chromium poisoning and demonstrates lower power losses at lower temperatures. For the anode, nickel is a cheap high performing material in catalysing the oxidation of hydrogen and can be alloyed with the electrolyte material to form a better epitaxial junction. Generally both electrodes are porous to allow easy and dispersed access

of gas to the electrode/electrolyte interface.

Solid oxide fuel cells can operate using other hydrogen compounds as the fuel at the anode, since oxygen ions are the charge carriers and can react with other hydrogen based fuels. At the high temperatures required, an *in situ* steam reforming process can provide the electrode with hydrogen.

1.5 Thesis Overview

The thesis is devised of 7 chapters, the first 3 of which aim to provide the reader with the theory of methods used in the research reported herein.

Chapter 2 outlines the analytical tools used in the course of this research; a scanning electron microscope is an essential tool in the analysis of morphology of nanostructures, whilst X-ray diffraction gives insight to the crystallography and composition of materials synthesised. The purpose of controlling morphology and composition of nanomaterial photoanodes is to improve the performance of the photoanode for the purpose of photocatalytic water splitting. The photoelectrochemical testing utilising the photoanodes in photocatalytic water splitting gives a direct insight into the properties and performance of the materials.

The synthesis of the unique architecture nanostructure metal oxides took several forms, as described in chapter 3, each of which have benefits and drawbacks. The fabrication of thin films of transition metals by electron beam evaporation provides a versatility of choice for the thin film material.

Syntheses routes of structures took many forms including; vapour transport synthesis, anodisation, aerosol assisted chemical vapour deposition and chemical bath deposition.

The work is focused on three transition metals, Ti, Fe, and Zn, and their oxide counter parts. Chapter 4 concentrates on the synthesis of Fe-Ti-O nanotubes. Employing e-beam evaporation to form a thin film metal substrate, the thin film undergoes electrochemical anodisation which produces nanotubes through an oxidation/dissolution process. The purpose of employing two transition metals in the photoanode material is to engineer the band gaps and utilise a greater spectrum of light than is possible with TiO_2 alone. The band gap of TiO_2 is UV sensitive whilst

Fe_2O_3 is sensitive to visible light encompassing more of the usable solar spectrum, the Fe_2O_3 CBM position is less favourable than the TiO_2 CBM, where the CBM is more positive than the reduction potential of water. Through the alloying of the materials it is possible to achieve a smaller band gap than TiO_2 and maintain favourable band positions. It is successfully shown that with the introduction of iron to the titanium nanotube structure, the photoelectrochemical performance of the nanotubes as a photoanode improves and the H_2 generation rate doubles compared to bare TiO_2 nanotubes.

Vapour transport methods proved insightful and versatile, as highlighted in chapter 5 which explores ZnO synthesis by vapour transport mechanisms. It is possible to synthesise a multitude of structures by controlling synthesis conditions. ZnO rods formed on a Ti foil proved an efficient photoanode, we have established a thin TiO_2 layer forms on the Ti foil initially, and a Zn_2TiO_4 layer forms at the interface between this TiO_2 layer and the ZnO rods, this introduced a heterostructure capable of increased photoefficiency due to better charge separation at the interface.

This improvement was insightful for the architectural design explored in chapter 6 to improve efficiency by creating a 3D electronically favourable structure; ZnO rods created within TiO_2 nanotubes increased the surface area of the heterostructure junction improving light absorption and charge separation significantly, hence enhancing photopower density output significantly compared to TiO_2 nanotubes or ZnO rods alone.

Novel photoanodes created by AACVD, VS and CBD are explored in chapter 7. TiO_2 coated ZnO rods showed improvement in photopower density ouput, though is limited to a sparse coverage of the rods. A mesopourous ZnO film created by AACVD showed significant photocurrent but not as high as the crystalline counterparts, crystallinity plays a crucial role in the high photocurrents attributed to the $ZnO/Zn_2TiO_4/TiO_2$ heterostructure. Chemical bath deposition of ZnO structures created a one step nanotubular array of ZnO. An initial ZnO annulus seed layer instigated the site specific growth of ZnO, forming a nanotubular structure from the initial ring framework.

Chapter 2

Analytical Methods

The materials produced in this work are novel in structure and composition. Morphological information of materials created are obtained using a scanning electron microscope with a resolution of only a few nm. The composition of materials can be analysed by energy dispersive X-rays which supply elemental analysis information, whilst a deeper characterisation of the crystal structure and composition is carried out with X-ray diffraction. X-ray diffraction provides important details of the fundamental structures created, including crystallinity and crystal orientation.

Photoelectrochemical testing is an important characterisation technique of the materials for use as a photoanode, that is the efficiency of hydrogen production under illumination and recording the current-potential relationship. This allows the photopower density output of the solar cell to be calculated and the quality of the material as a photoanode assessed.

2.1 Scanning Electron Microscope (SEM)

The scanning electron microscope[133] is a critical analytical tool in the analysis of nanostructures. The SEM provides a method to observe morphology and characterise composition of materials. Optical microscopes are limited by the Abbe diffraction limit ($\sim d = \lambda/2.8$ for modern optics where d is the resolvable feature size); with a limited resolution of approximately 180 nm for green light, well above the resolution required to image structures as small as 50 nm. A scanning electron microscope is not limited to this resolution and can achieve a few nm resolution.

The fundamental mechanism behind the electron microscope is the observation of electron interaction with a material rather than photon (optical) interaction, an electron has a smaller de Broglie wavelength. The derivation of the de Broglie wavelength of an electron under a bias is shown in equation 2.2 to 2.4 and the relativistic form is shown in equation 2.5 where p is momentum, h is Planck's constant, λ is the de Broglie wavelength, eV is the electron voltage and m_e is the electron mass. The diffraction limit is reached when the wavelength of the electron beam is similar to the dimensions of the material under study. For an electron microscope, the typical electron energy ranges from 5 to 30 keV, which corresponds to a de Broglie wavelength range of 0.017 nm to 0.007 nm respectively. Therefore, the diffraction limit will be less than 0.02 nm for a transmission electron microscope (TEM). For an SEM the resolution is determined by the electron beam profile.

$$\lambda = \frac{h}{p} \tag{2.1}$$

$$eV = \frac{1}{2} m_e v^2 \tag{2.2}$$

$$p = m_e v = \sqrt{2eVm_e} \tag{2.3}$$

$$\lambda = \frac{h}{\sqrt{2eVm_e}} \tag{2.4}$$

$$\lambda = \frac{h}{\sqrt{2m_e eV + \frac{eV}{c^2}}} \tag{2.5}$$

An electron source accelerates a stream of high energy electrons toward a sample surface which are decelerated upon striking the surface where a number of scattering events take place. Secondary electrons are released, after bombardment, from the atoms close to the surface. In such cases, the resolution is limited to 2-5 nm due to the beam profile and the electron mean free path. These secondary electrons are detected, and a morphological image is built-up. Characteristic X-ray's produced by relaxation of electrons to lower orbitals in atoms close to the surface can give compositional information.

2.1.1 Electron Source

Electrons are ejected from a metal filament through thermionic emission.[134] A current is applied across a tungsten filament at the top of the column of an electron microscope, Figure 2.1. The current heats the filament *via* resistive heating, and the electrons in the filament gain enough kinetic energy to overcome the work function of the material. A high positive voltage of +5-20 kV is applied to the extraction anode near the filament of the electron gun, this bias provides the electrons with a high kinetic energy; accelerating electrons through the column. The SEM requires a vacuum environment to avoid scattering inside the column as well as to allow thermionic emission to occur. The vacuum is maintained by a diffusion pump backed by a roughing rotary pump.

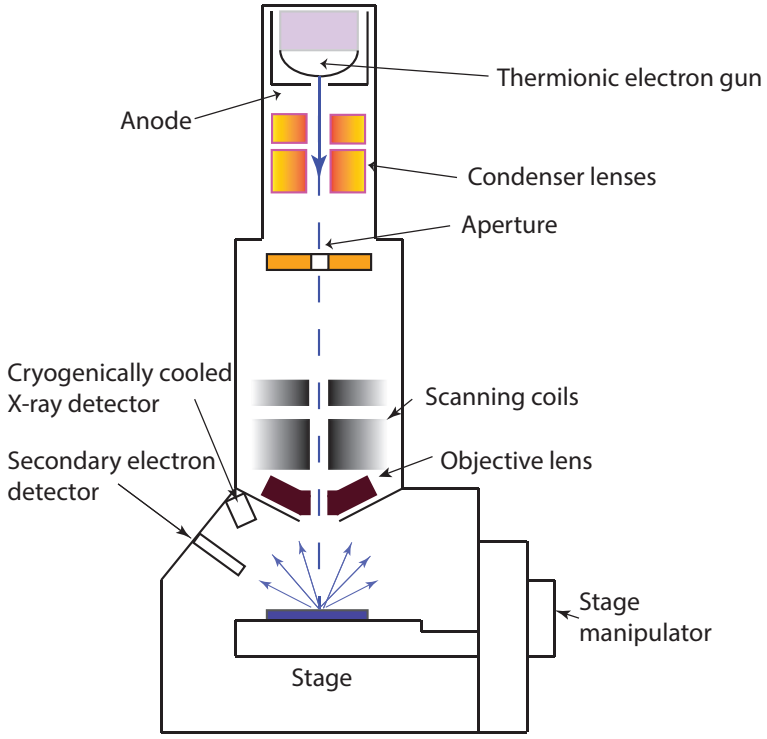

Figure 2.1: Schematic of a scanning electron microscope.

The stream of electrons passes through a series of magnetic fields which controls size, shape and position of the electron beam. In Figure 2.1, the column is shown and pathway of the electron beam. The electrons traverse the first magnetic field, the condenser lenses, which confines the e-beam reducing the beam size and adjusting the shape. The aperture removes any unwanted stray electrons.

The second set of lenses determine the position of the beam on the sample surface

and are controlled to image the surface in a scanning mode, similar to a CRT screen, raster scanning the material. The final sets of lenses converges the electron beam into a fine and focused beam; these are the objective lenses. Inside the objective lenses is the stigmator, the stigmator is a set of coils that have two dimensional control (x-y) of the beam and corrects any astigmatism of the beam, forming a round sharp electron beam focusing on the object (the scanning and stigmator are inside of the objective lenses).

2.1.2 Morphology Imaging

Secondary electrons are the most commonly detected electrons for topological analysis in an SEM; these are low energy electrons ejected from an atom, due to the incident electron beam. The electrons typically have energies below 50 eV and are emitted a few nanometres from the surface. Secondary electrons are generated through an Auger process by a high energy electron scattering process, the incidence of the high energy electrons causes the ionisation of the core electron of the sample, which leaves a core hole in it's absence. The upper level electrons will relax into the core level and release the binding energy in the form of photons. The photon energy is strong enough to cause ejection of other electrons (secondary electron) in the upper level, loosely bound to the nuclei. The advantage of using secondary electrons to image the surface, is that the distinctive low energy of the electrons allows it to be separated from the primary electrons (beam) in the background, achieving a good image contrast. In addition to the high contrast, the low energy secondary electrons also have a small mean free path, which restricts the probe depth; and guarantees a high resolution. The combination of high contrast and high resolution gives the ultimate quality of the topographical surface image.

Backscattered electrons (BSE) are high energy incident electrons elastically deflected within the sample material; under the influence of the nuclei of the atoms in the material. The BSE detector (not installed in our SEM) is usually positioned as close to the normal of the target surface as possible; usually very close to the e-beam. Heavy atoms (high atomic number) have a larger positive charge of the nucleus, and a higher chance of electrons deflecting in the direction of the detector at high energies. Therefore the contrast of the backscattered electron image is dom-

inated by the atomic weight and it can be used to distinguish between plastic and metal containing domains. The electrons penetrate a few microns depth from the surface of the sample material before deflecting either once or several times (before it reaches close enough to the radius of a nucleus), which is dissimilar to secondary electrons where electrons are ejected very close to the surface (a few nm) due to a limited electron mean free path. The backscattered detection can reveal compositional information as materials with a higher atomic mass appear brighter; a larger flux of back scattered electrons are observed with a heavier/larger nucleus.

Evehard-Thornley Detector

Our SEM has a secondary electron detector installed, which obtains the topological information of the sample under investigation. The Everhart-Thornley detector,[135] illustrated in Figure 2.2, enhances the secondary electron signal after an electron undergoes an avalanching process. A few electrons enter the detector and are amplified into millions of electrons detected as a signal. The signal is too weak without an avalanching process.

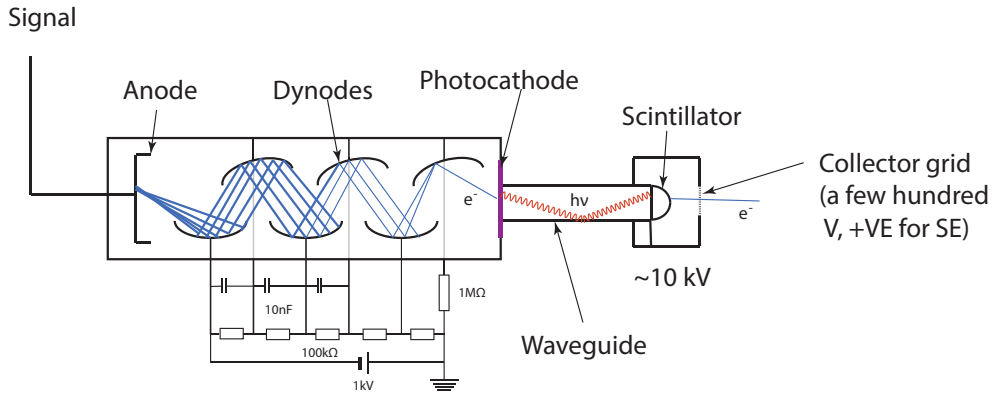

Figure 2.2: Secondary electron detector. The collector grid is positive to attract low energy secondary electrons..

In order to eliminate the high energy primary and backscattered electrons, the SE detector is mounted horizontally, parallel to the sample surface. The detector (Everhart-Thornley detector) consists of a Faraday cage which is positively charged (tens to hundreds of volts) to attract low energy electrons which are then amplified by an electron multiplier (dynodes). The electron will then be accelerated further towards the phosphor coated screen at the front of the photomultiplier tube. The emitted photons propagate through a waveguide into the photomultiplier tube. The

photons travel through the wave guide and strike a photoanode, producing electrons. The electrons travel through the photomultiplier cavity striking dynodes (at a bias of +100 V); these photoelectrons generate secondary electrons at the dynodes giving off excess electrons. An avalanching effect of multiplying electrons results in millions of electrons produced from a single electron; to allow detection at the anode. The signal produced at the anode is amplified and registered on a cathode ray tube (CRT) screen synchronised as a function of beam position on the sample.

2.1.3 Compositional Analysis - EDX

An X-ray detector can also be installed in the SEM to detect the X-ray fluorescence generated in the electron scattering process and used to analyse the composition of the sample under investigation. The energy dispersive X-ray (EDX) detector measures the energy of the X-rays created *via* the bombardment of electrons striking a sample surface. These X-rays are emitted after a core electron is ejected and an upper electron relaxes to the core level. The energy of the X-ray corresponds to the binding energy difference between the core level and upper level. Thus each element has it's own distinctive X-ray emission, independent of the kinetic energy of the primary electron. The primary signals are due to an electron relaxing *via* the Kα transitions, where an electron in the L shell replaces a missing electron in the K shell. Other transitions can also generate X-ray fluorescence but at a lower energy. Together with the Kα emission, it is possible not only to identify the elements in the sample, but also quantify their relative concentration. Figure 2.3 illustrates the premise.

The detector is a solid-state device, a few mm thick. The p-i-n (PIN) diode detector is a p-type material and n-type material sandwiched between an insulator. A -1 kV bias is applied to the contacts and as a high energy photon (X-ray) passes through the device a cascade of electron-hole pairs form creating a voltage pulse across the device. The device is cooled using liquid nitrogen (LN) to reduce the conductivity of the excitons (silicon and lithium are typically used as the semiconductor and insulator respectively).

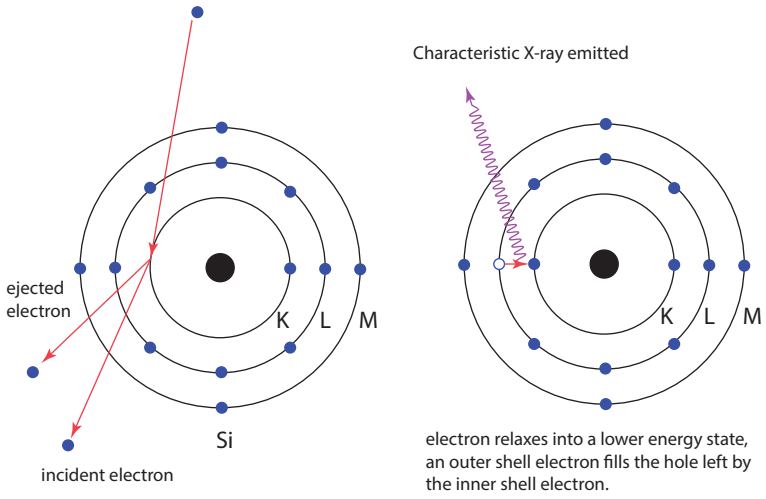

Figure 2.3: X-ray emission *via* a k_α transition.

2.2 X-ray Diffraction (XRD)

Our lab is also equipped with a SIEMENS D500 X-ray Diffractometer. The Cu target X-ray source (electrons bombard Cu, producing X-rays) emits X-rays at a characteristic $Cu_{K\alpha 1}$ wavelength of 1.54 Å, other wavelengths are too weak or are cut off by a filter. A Bragg-Brentano configuration is adopted, in which the sample is attached to a rotating stage and the detector is attached to a secondary rotating stage. The detector rotates at twice the angle of the sample holder.[136]

The X-rays enter crystal structures and are reflected by the atoms in the lattice, causing constructive and destructive interference of the reflected waves at certain angles. The angle at which constructive interference occurs is defined by the spacings of the lattice and the wavelength of the X-ray; following Bragg's Law.[137] The deflection geometry is illustrated in Figure 2.4.

Figure 2.4 shows that the X-ray has travelled an extra length between consecutive planes of the lattice. Constructive interference occurs when the X-ray's are reflected at consecutive planes in phase, this happens when the extra length travelled by an X-ray is a multiple of the wavelength. This is only possible because X-ray wavelengths are comparable to lattice spacings. The material will have many of these consecutive planes, and the cumulative effect produces narrow fringes or Bragg peaks at the angles corresponding to the separation of particular sets of planes.

$$n\lambda = 2d_{hkl}\sin\theta \tag{2.6}$$

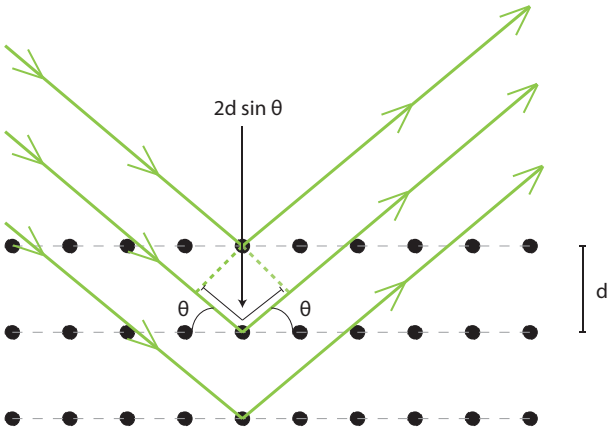

Figure 2.4: Illustration of Bragg's law, if the spacing between planes of atoms is close to the wavelength of the photons the constructive interference can be easily detected.

The detector arm rotates by 2θ as the sample rotates by θ. This is convenient as it is possible to keep the X-ray source stationary, and the detector is always in the line of sight of the reflected X-ray beam.

In glancing angle mode, the X-ray source strikes the sample at a set angle, and the detector arm rotates by theta. In this case, the signal pattern is localised to the illuminated spot and the angle of sample entry. This is usually used for loose samples, but can also be used to analyse a specific depth or part of the sample under investigation. The reflected beam is weaker compared to the theta/2-theta mode.

To analyse the X-ray diffraction spectra, Igor pro software suite was primarily used for data analysis and technical graphing whilst X-ray diffraction software packages powderx and X'Pert HighScore Plus are used for the quantification of the patterns. Diffraction peak fitting is analysed using open source algorithms.[138]

The XRD pattern produced, consists of a series of diffraction peaks. The position of which are determined by the lattice spacings of the material under inspection. The Bragg equation relates angle of constructive interference and the consecutive spacings of planes. The full width half maximum width (FWHM) of the peaks is determined by the crystallite domain size following the Scherrer equation (equation 2.7) published in 1918.[139] Where $B(2\Theta)$ is the FWHM, λ is the wavelength of the X-rays, θ is half the 2θ value of the peak, L is the crystallite domain size and K is the Scherrer constant/shape factor. The FWHM is measured in radians.

$$B(2\Theta) = \frac{K\lambda}{L\cos\theta} \tag{2.7}$$

The Scherrer equation shows the peak width is inversely proportional to the crystallite size; large single crystals will have a narrow full width half maximum. The Scherrer constant can range from 0.8 to 1.2 in powder samples according to the geometry of the crystallite, it is also known as the shape factor. Scherrer reported a value of 0.93 for the Scherrer constant for crystals with cubic symmetry. In this thesis the crystallite size is used qualitatively, as an indication of the magnitude of single phase crystallite sizes and the geometry of crystals.

In other words, as the number of diffracting planes in well defined spacings increases the brighter and more well defined the constructive interference peaks becomes.

Peak widths get broader with decreasing crystallite size, the crystallite size broadens at larger 2θ values due to the instrumental profile and optical configuration, better results are gained from peaks between 30° and 50° (2θ).

The peak height is an approximation of the peak intensity, and the peak area is the real measure of the peak intensity. The peak height depends on the number of crystallites diffracting X-rays, and can be used to determine the composition of the sample. If the material exhibits a preferred orientation the peak height will be intense at the Bragg angle corresponding to the preferred orientation.

Typical XRD spectra recorded from ZnO powder, TiO_2 powder and a Ti foil are shown in Figure 2.5. For the majority of materials created in this work, a Ti foil served as a substrate for growth of materials and it is useful to differentiate these peaks. TiO_2 is the staple metal oxide studied in the work herein, knowledge of the crystal structure of the powder helps ascertain a background profile for the materials. ZnO is extensively studied through chapters 5-7 and a background profile of randomly orientated powder crystallites is fundamental in illustrating the alignment of ZnO formed in later chapters.

Tables 2.1 to 2.3 contain the data of diffraction peaks collected from the samples in Figure 2.5. These materials will be dominant in the XRD patterns in the following chapters. Standard P25 TiO_2 powder is purchased from Sigma Aldrich, with a particle size of 21 nm. Values of crystallite size in Table 2.2 can be averaged as a

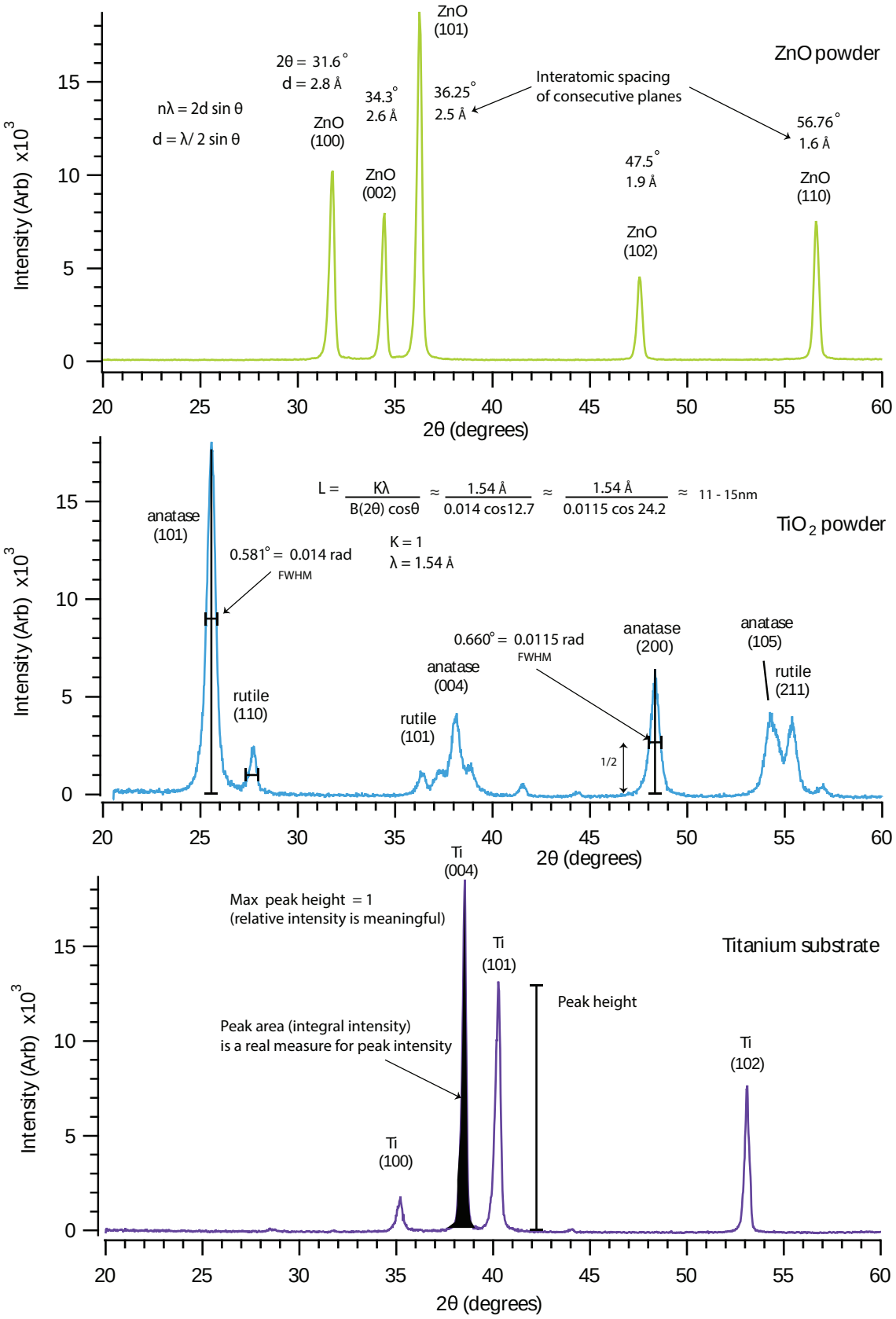

Figure 2.5: Peak patterns for ZnO powder, TiO_2 (P25) powder, and a Ti foil. The important characteristics of the peaks for analysis are highlighted; interatomic distances, crystalline size and contents of the unit cell can be characterised by peak analysis.

ZnO (hkl)	2θ (°)	Peak height (counts)	Peak area (counts°)	Crystallite size (nm)	d (Å)
(100)	31.80	10155.60	3243.09	30.62	2.81
(002)	34.45	7888.57	2519.14	30.83	2.60
(101)	36.25	18683.40	5966.36	30.98	2.48
(102)	47.55	4482.95	1670.18	27.58	1.91
(110)	56.60	7462.68	2383.13	33.44	1.63

Table 2.1: XRD analysis of ZnO powder. Average crystallite size of 30.69 nm.

TiO_2 (hkl)	2θ (°)	Peak height (counts)	Peak area (counts°)	Crystallite size (nm)	d (Å)
(101)a	25.06	18339.5	10151.3	17.40	3.55
(110)r	27.24	2739.08	1399.52	18.94	3.27
(101)r	35.78	1471.63	751.91	19.34	2.51
(004)a	37.64	4427.84	2827.97	15.55	2.39
(200)a	47.82	6703.55	3710.57	18.58	1.90
(105)a	53.72	4489.62	4492.31	10.53	1.71
(211)a	54.86	4197.31	2502.03	17.77	1.67

Table 2.2: XRD analysis of TiO_2 powder. Average crystallite size of 16.87 nm. Anatase is represented by a and rutile by r.

whole obtaining a value of 16.87 nm or averaging between 30°-50° which can be more accurate. The average crystallite size is 17.82 nm between 30°-50°. The crystallite size is only 3-4 nm smaller than the particle size. Therefore P25 powder is almost made up of single crystals.

ZnO powder has larger crystallites than p25, the data is given in Table 2.1. Average crystallite size is 29.68 nm between 30° and 50°, and 30.69 nm for all the peaks. The lattice parameters of ZnO are c = 5.2 Å and a = b = 3.25 Å and the volume of a ZnO wurtzite unit cell is 23.83$Å^2$.[140] To gain some perspective, a single crystallite contains over half a million unit cells of wurtize ZnO.

Titanium foil serves as a substrate for a variety of the hybrid photoanode constructed in this work. These peaks serve merely for reference when they are present

Ti (hkl)	2θ (°)	Peak height (counts)	Peak area (counts°)	Crystallite size (nm)	d (Å)
(100)	35.22	1958.51	708.82	27.26	2.55
(004)	38.54	18703.80	4778.30	38.99	2.34
(101)	40.26	13322.60	4254.44	31.36	2.24
(002)	53.12	7821.07	2164.57	37.99	1.72

Table 2.3: XRD analysis of a Ti foil. Average crystallite size of 33.9 nm.

in an XRD pattern. Present Ti peaks give insight into the X-ray penetration depths in to a sample where titanium serves as a substrate, if they are present we know that the X-rays are diffracting from the substrate as well as structures in close proximity to the surface. This allows determination of the spatial composition of the roots of ZnO rods or roots of titania nanotubes.

2.3 Photo-Electrochemistry Overview

Electrochemistry is a subject with many useful applications that are fundamental to modern science and technology. These include batteries, fuel cells, electrochromic displays, electrophoresis and electro plating (galvanising). In the most basic form, electrochemistry is the study of chemical reactions at the surface of two electrodes (metal conductor/semiconductor/carbon) in contact with an electrolyte. An electrolyte is a conducting medium where the charge carriers are ions. The electrolyte is typically a liquid containing an ionic species but can also be of the form of a solid/non aqueous based electrolyte, i.e. ionically conductive polymers, metal oxides and fused salts. Liquid electrolytes have the advantage of forming a complete electronic junction by direct contact with the whole surface area of an electrode, providing a large ionic conductivity.

Two different metals have two different Fermi levels, and in contact the Fermi levels (chemical potential) of the system must be the same (in equilibrium) as there is electron flow between one and the other. Thus when two metals are in contact the work function of one metal raises as the Fermi levels equilibrate, this shift results in a potential difference when the two metals are in contact. Figure 2.6 illustrates the

energy and potential difference caused by a shift of the work function of a metal as it reaches equilibrium, the work function is the energy required to remove a bound electron from a material. The contact potential is the difference between the work functions of the materials when the Fermi levels are equal, divided by the electronic charge. This is the Volta effect.

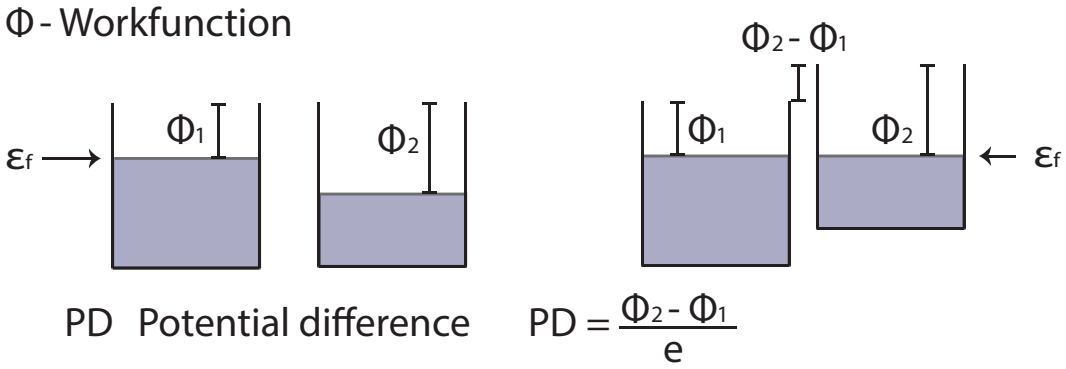

Figure 2.6: Illustration of electron states of two metals in contact, a contact potential difference equal to the shift of the work function divided by charge forms.

An electrochemical cell requires at least two electrodes, and usually only one electrode reaction is of interest. The reactions taking place at each of the electrodes can be considered two half-cell reactions. The electrode of interest is the working electrode, and the electrode which completes the circuit is the counter electrode. Characterisation of a half reaction requires a well understood reference electrode. A reference electrode is self-contained within an electrolyte of constant composition. The behaviour is well documented, and the potential of the reaction is known to a precise degree.

The reference electrode I have chosen to adopt is the silver-silver chloride electrode (Ag/AgCl), which is a silver wire coated with silver chloride contained in a saturated KCl solution (0.197 V vs. NHE). A saturated KCl solution is used, as the potential is known to a precise degree through measurements. Measuring the behaviour of a half cell reaction requires measuring the potential of the working electrode with respect to the reference electrode, whilst a counter electrode completes the cell.

There are several scales with which the potential can be compared, the most convenient form is the reversible hydrogen electrode (RHE) because the oxidation and reduction potentials of water remain fixed at any pH. The pH of the electrolyte shifts the oxidation and reduction potentials of water with respect to the normal

hydrogen electrode (NHE) and vacuum energy according to the Nernst relation given in equation 2.8. In this work, an Ag/AgCl reference electrode is adopted, which is fixed with NHE. 0 V vs Ag/AgCl ($E^0_{\mathrm{Ag/AgCl}}$) is equivalent to a potential of 0.197 V vs NHE. The relationship between potential scales in acidic and alkaline electrolytes are shown in Figure 2.7.

$$\mathrm{E_{RHE}}=\mathrm{E_{Ag/AgCl}} + 0.059\,\mathrm{pH} + \mathrm{E^0_{Ag/AgCl}} \tag{2.8}$$

E_{RHE} is the potential vs RHE and $E_{\mathrm{Ag/AgCl}}$ is the potential vs an Ag/AgCl reference electrode.

It's important to note that in an alkaline electrolyte (pH = 14) 0 V vs RHE is equivalent to -1.023 V vs Ag/AgCl, and 1.23 V vs RHE is equivalent to 0.207 V vs Ag/AgCl. These values allow us to calculate the onset potential and optimal photocurrent at 1.23 V (RHE). All photoelectrochemical measurements in this work are conducted in an electrolyte solution of 1 M KOH (purchased from Sigma Aldrich) in deionised water with a pH value of 14.

For a two electrode electrochemical setup, the potential is measured as the reversible hydrogen electrode. At approximately 0.4 V (RHE) the oxygen evolution reaction begins, this indicates the overpotential for the oxygen evolution full cell reaction is 0.4 V (RHE) which is partially due to the flat band potential between the photoanode and electrolyte, and recombination in the space charge layer, hole trapping or hole accumulation at the surface of the photoanode.[141,142]

2.3.1 Experimental setup of a solar water splitting cell

Developing efficient solar hydrogen generation is the goal of this work, providing chemical energy (H) from abundant sources. Increasing efficiency to 10 % could allow commercialisation of PEC water splitting.

A photoelectrode serves as the anode, and a platinum counter electrode as the cathode. The potential is measured in respect with the reference electrode and the working electrode (photoanode). The current is measured between the photoanode and counter electrode (A platinum (Pt) foil is used in our experiment). A semiconductor, upon illumination with an energy greater than the band gap, excite electrons

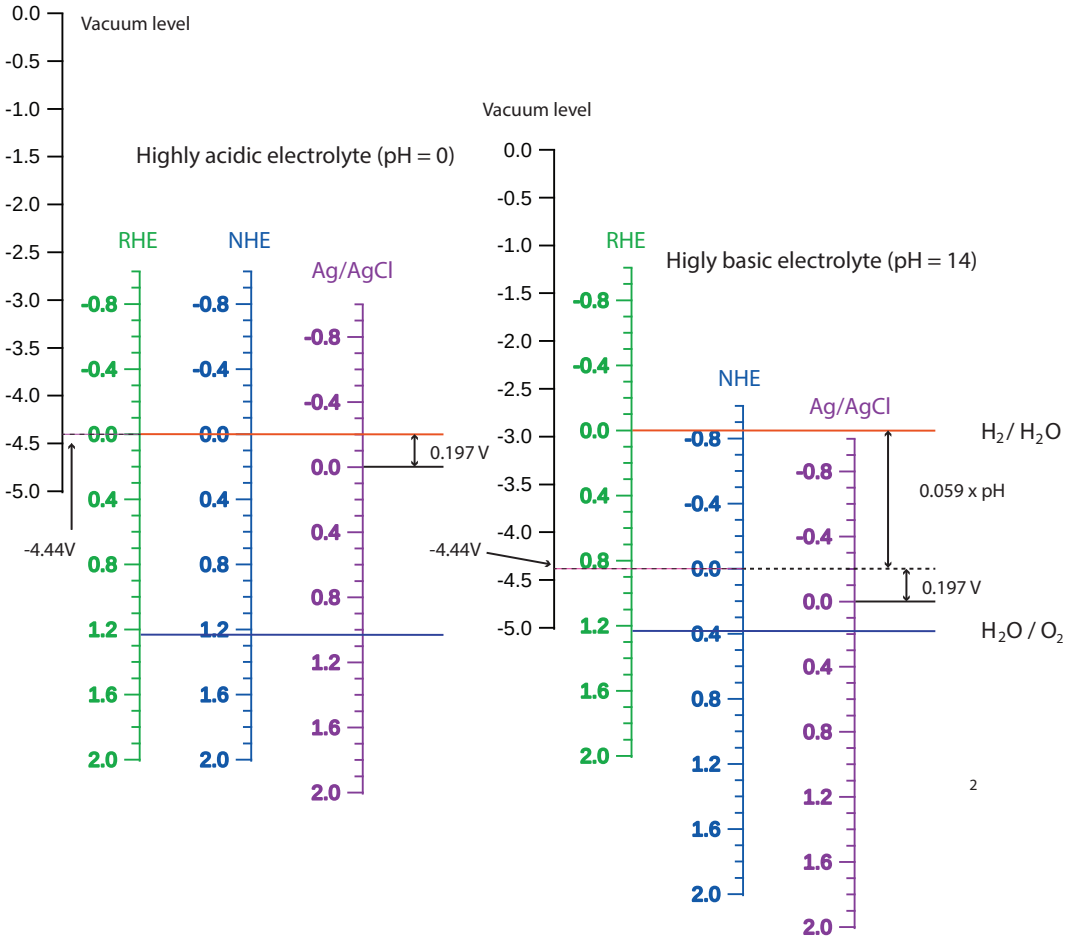

Figure 2.7: Potential scales of the reversible hydrogen electrode (RHE), normal hydrogen electrode (NHE) and silver/silver chloride electrode (Ag/AgCl) for acidic and basic conditions. NHE and Ag/AgCl are both fixed with vacuum, and the redox potentials of all three are pH dependant. RHE is pH independent, and the hydrogen redox potential remains at 0 V_{RHE} for any pH.

from the VBM into the CBM. The electrons commute the circuit of the electrochemical cell to the platinum counter electrode where hydrogen evolution occurs. Oxygen evolution occurs at the photoanode surface, the hole counter part is injected into the electrolyte; oxidising the water. Figure 2.8 shows the experimental setup of the glass photo-electrochemical cell specially constructed by the University of Sussex glass blower workshop. The three sectioned cell contain compartments for each of the electrodes and the connectors between the compartments can be fitted with a semi-permeable membrane which would allow accurate measurements of hydrogen evolution.

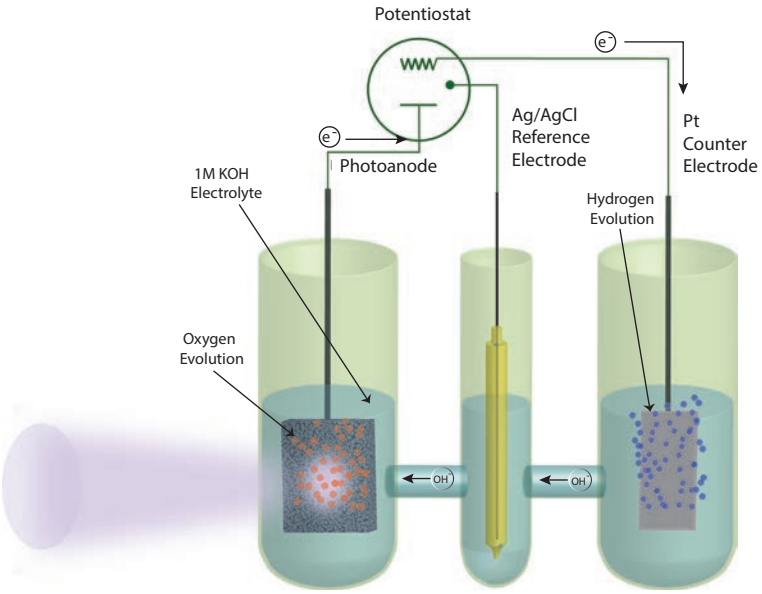

Figure 2.8: Three electrode photo-electrochemical setup. The electrolyte consists of a 1 M KOH solution, and a saturated Ag/AgCl reference electrode is utilised in measuring the potential.

2.3.2 Light Sources

Xenon Lamp

A 300 watt xenon lamp (Compact Illuminator 6000CI, ORC) provided the illumination for the majority of the photoelectrochemical investigations. The spectrum of the xenon lamp, Figure 2.9, closely matches the solar spectrum which suggests that the xenon arc lamp is an excellent choice to simulate solar energy. The spectrum was recorded on a USB UV-Visible spectrometer (Ocean Optics). The light intensity is dominated by the visible portion of the spectrum with a small amount of UV. The slightly oscillating part of the spectrum intensity close to the peak wavelength is due to interference effects of the CCD array detector, this is indicated by the matching positions of the maxima of the interference effects for both the solar and the xenon lamp spectra and therefore the oscillation present is light source independent.

The solar spectrum has a larger intensity in the UV range between 350 nm and 400 nm (3.54 eV to 3.1 eV) compared to the xenon lamp, unfortunately this is in the energy range of absorption of the band gaps of the materials explored in this work. Thus, the xenon light source encompasses a large range of unusable wavelengths and it is undemonstrative to calculate efficiency using the xenon light source alone. To calculate photoefficiency, it is convenient to measure the UV response under a set

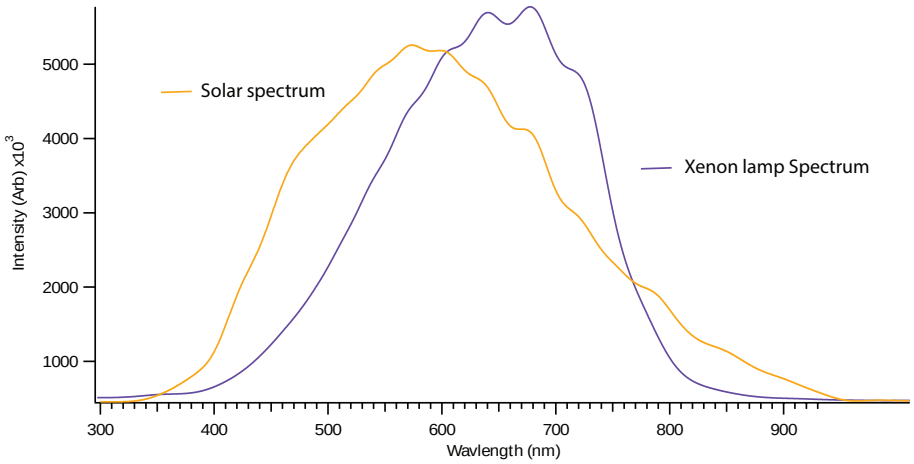

Figure 2.9: Output spectrum of xenon light source, and natural sunlight. The golden curve is the solar spectrum and the purple curve is the spectrum of a xenon lamp. During measurement of the spectrum the intensity of the beam is reduced as to avoid damaging the CCD sensor of the UV-visible spectrometer.

illumination intensity, which will give us the UV photoefficiency.

Xenon Lamp, with a UV Transmitting Filter Installed

The xenon light source is fitted with a transmission filter allowing only UV light to pass; i.e. opaque to other wavelengths. The Hoya U-340 lens spectrum in Figure 2.10 shows the UV intensity peak, ranging from 300 nm to 400 nm. This allows the UV response of the photoanode to be measured and the photoefficiency in the UV range to be calculated. The intensity output of the xenon lamp with the filter fitted is 35 mW/cm^2, and the area under illumination of the sample is 1 cm^2. Comparatively, at sea level, approximately 6 % of the sun's radiation energy is within the UV spectrum, this is approximately 6 mW/cm^2. Taking this into account, the UV efficiencies can be divided by 6 to find an approximate value for the efficiency under AM1.5 irradiance.

The UV output of the xenon lamp with the filter fitted is less intense than the UV output of the whole beam of the xenon lamp, as the filter lens has a maximum transmittance of 75 % $\pm$ 5 %. The photopower output densities of the photoanode material under investigation will reduce accordingly, by approximately 25 % than the same material under xenon light illumination excluding the filter.

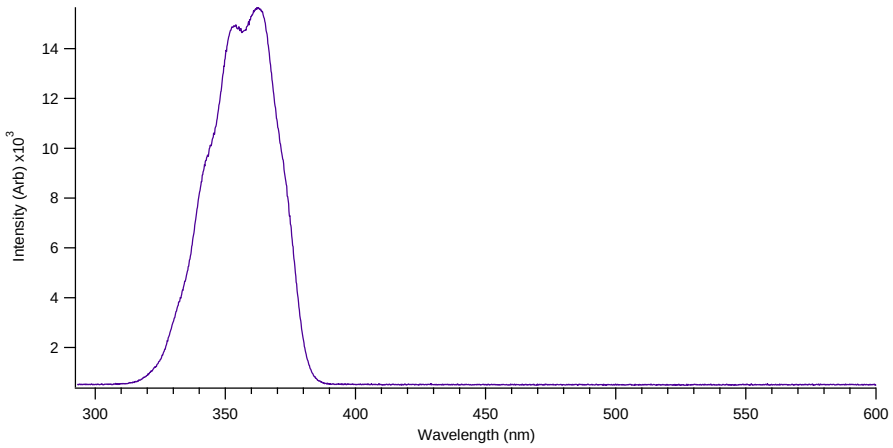

Figure 2.10: Output spectrum of xenon light source (300 W) with a UV transmission filter in place (Hoya U-340).

Cold Cathode Fluorescent Lamp light source

The cold cathode light source is a low wattage bulb, the power density output of which is a 800 μW/cm^2. A mercury vapour discharge causes a fluorescent coating to emit visible light, with photon energies close to the band gap of the materials under study (3-3.2 eV). The spectrum in Figure 2.11 shows the high intensity peak at various wavelengths, notably, the peak at 370 nm is ideal for the materials under investigation ($\gamma_\epsilon = 3.35$ eV).

The CCFL is an inexpensive solution to long term stability studies of materials, as the bulbs can be replaced easily and the photoanode under investigation can be illuminated for days. The intensity output is far less than the xenon lamp, which also increases the bulb lifetime compared to a xenon lamp. Although frequent switching reduced the lifetime significantly resulting in the replacement of 3 bulbs over 48 hours.

2.3.3 Efficiency Analysis of the Photoanodes

In this research, an *EA160 Potentiostat* (eDAQ solutions) is used to control potential and measure current, and the majority of I-V scans were conducted at a rate of 10 mV/s from -1.2 V to 1.5 V. Igor WaveMetrics software is utilised in the analysis of the I-V data to calculate efficiencies and plot photocurrent densities.

The performance of the photoelectrochemical cell (PEC) is determined by the solar conversion efficiency.[93]

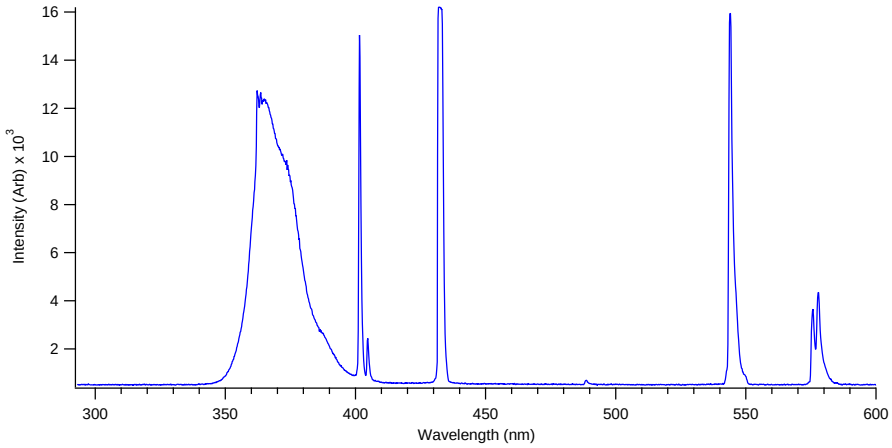

Figure 2.11: Output spectrum of a cold cathode fluorescent lamp (CCFL) light source.

$$\eta_c = \frac{\Delta G^0(H_2O)R(H_2) - V_{Bias}I_{photo}}{I_{rad}A} \tag{2.9}$$

$$\eta_c = \frac{\text{Power stored in hydrogen - Power input from power supply}}{\text{Power from the light source}} \tag{2.10}$$

Where η_c is the cell efficiency, ΔG^0 is the standard Gibbs energy of water splitting ($\Delta G = -nFE$, $E = 1.23V$), $R(H_2)$ is the rate of hydrogen generation ($R(H_2) = \frac{I_{photo}}{nF}$), V_{Bias} is the bias applied to the PEC, I_{photo} is the photocurrent of the cell and I_{rad}A is the illumination energy density. The efficiency is calculated using equation 2.11.

$$\eta_c = \frac{(1.23V - V_{\text{RHE}})I_{photo}}{P_{Input}} \tag{2.11}$$

Where $P_{Input} = I_{rad}A$, V_{RHE} is the reversible hydrogen electrode potential calculated from the measured bias (Ag/AgCl). Equation 2.11 assumes a perfect PEC, with no overpotential losses and ideal counter electrode. This will give an underestimate as it will not take into account the flat band potential or losses. The open circuit potential can be used to calculate efficiency neglecting overpotential losses and the flat band potential. This is shown in equation 2.12, where η_p is the photoanode efficiency, V_{Meas} is the measured potential and V_{OC} is the open circuit potential.[143]

$$\eta_p = \frac{(1.23 - (V_{Meas} - V_{OC}))I_{photo}}{P_{input}} \tag{2.12}$$

Chapter 3

Synthetic Methods

Nanomaterials are materials which have features with dimensions ranging from 1 nm to 100nm; controlling features of structures at this scale can increase the surface area of the structures by orders of magnitude. Control of the 3D architecture of materials of interest not only benefit from increased photocatalytic activity but can vastly improve optical and electronic properties of the material. This work will focus on the development of technologies to create sophisticated 3D architectures of metals and metal oxides in order to maximise the photoefficiency of nanostructured photoanodes in a watersplitting PEC. Techniques utilised include simple PVD techniques, vapour transport methods, electrochemical anodisation and chemical bath deposition.

3.1 Electron Beam Evaporation

Electron beam (e-beam) evaporation allows the deposition of thin metal films, these metal films will serve as the precursor metal in the anodisation process to create nanotubes. It is possible to control layer by layer deposition, creating a 3D nanotube architecture and forming a multi-junction metal oxide structure with varying band gaps along the length of the nanotubular array, allowing a broader absorption energy range of the solar spectrum. E-beam evaporation is a useful tool for doping which is highly controllable with a guaranteed homogeneous distribution.

In order to create thin films of metals *via* physical vapour deposition (PVD), a high temperature is needed. A versatile way to deposit a controllable thickness and composition of metals is through direct evaporation of a slug of the target metal.

Most metals require a high temperature to evaporate material from the surface ($>$ 1300 °C), it is difficult to achieve these temperatures with convection heating equipment (such as furnaces or convection ovens). Electron beam evaporation is an effective physical vapour deposition technique; where electrons are propelled *via* thermionic emission and a bias voltage to then bombard a crucible. The advantage of e-beam heating is that the heat is focused and directed by the emission current and bias voltage, heating only the crucible and material contained. So the environment is relatively cold and only a small heating power is required to achieve high temperatures. As such it is relatively simple to construct the e-beam facility and maintain a highly stable evaporation process.

Thermionic emission and e-beam evaporation both require high vacuum conditions to avoid scattering by impurities, oxidation of the thin film and sacrificing the heating filament. In this work I designed and assembled a PVD system for developing 3D nanomaterials. The e-beam evaporator is installed in a high vacuum chamber shown in Figure 3.1(a), the setup consists of:

1. Electron Beam Evaporator
2. Vacuum Chamber
3. High Voltage Supply
4. Current Supply
5. Backing Rotary Pump
6. A Turbo Molecular Pump
7. An Ion Pump
8. Pirani Gauge/meter
9. Ionisation Gauge
10. Ionisation Gauge Controller
11. Stage/Sample Manipulator (with heating coils)

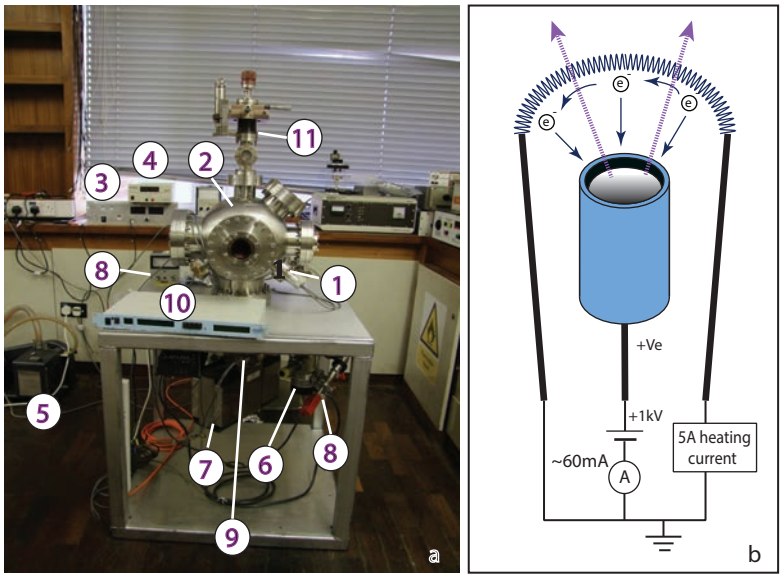

Figure 3.1: Electron beam evaporator experimental setup, the evaporator operates in high vacuum conditions and the chamber is shown in the photo in Figure (a). Figure (b) illustrates the basic premise of e-beam evaporation, and the crucible and filament circuit.

The electron beam evaporator (inset) consists of either a graphite (inner diameter of 8 mm, 13 mm long) or a molybdenum (Mo) (inner diameter of 4 mm, 10 mm long) crucible surrounded by a 0.15 mm diameter tungsten wire. Graphite has a high sublimation temperature (3652 K) making it an ideal container for high temperature processes exhibiting limited damage over repeated heating cycles. Mo also has a high melting temperature (2900 K) with the ability to withstand high temperature processes that also doesn't change shape or soften the material, the cyclical heating treatment did however damage the structure of the crucible. An advantage of using Mo is the ease of which repairs can be carried out using spot welding. Tungsten (W) is the most commonly used metal in the construction of resistive heating filaments, including traditional vacuum light bulbs and the SEM's electron gun. The main reason for this is the high temperatures that W can withstand, with a melting temperature of 3683 K/3410 °C, the other reasons include the strength, workability and the conductivity of the material which allows the ability to spot weld tungsten for repairs when the filament 'burns out'. The tungsten wire serves as the thermionic electron source; current passes through the tungsten filament causing resistive

heating thus increasing the energy of the electrons to overcome the work function of tungsten. The +ve high voltage (∼1 kV) between the crucible and tungsten attracts the electrons towards the crucible. This bombardment heats the crucible kinetically. The heating mechanism and structure of the e-beam heating configuration is shown in Figure 3.1(b). The current collected by the crucible to the earth is the emission current (I_e).

The temperature of the crucible and precursor is proportional to the heating power supplied by the electrons bombardment. Heating power is determined by equation 3.1, where P_h is the heating power, I_e is the emission current and V_B is the bias voltage between the filament and crucible. The heating power relates directly to the number of electrons striking the crucible and the kinetic energy the electrons impart with each collision. Typical bias voltages range from 800 V to 1 kV and emission currents range from 50 mA to 80 mA, for iron and titanium respectively. The heating powers range from 28 W to 70 W.

$$P_h = I_e \times V_B \tag{3.1}$$

At high temperatures the source material evaporates at a controlled rate, with the rate of evaporation dependent on the vapour pressure and temperature of the precursor. The crucible position is optimised with respect to the line of sight with the substrate, i.e. the substrate faces the crucibles aperture. During the deposition, the substrate temperature can be independently controlled with heating filaments installed to the holding plate. The deposition rate can be controlled to the nm scale, and significant deposition rates are achievable allowing thick films to grow (microns).

3.1.1 Maintaining a High Vacuum Environment

A series of vacuum pumps maintain the high vacuum environment required for evaporation of the metal anode and to avoid oxidation of the thin film. The high vacuum environment also prevents scattering of the electron beam and the metal source beam, providing a direct path of the electron beam and evaporated metal vapour as well as increasing the lifetime of the heating filament. The system is

'pumped' down by multiple vacuum pumps at a variety of stages towards reaching a high vacuum. I used a rotary pump, a turbo molecular pump, a titanium sublimation pump and an ion pump. The stainless steel chamber is customised with a selection of ports, and it is possible to utilise several e-beam evaporators simultaneously. The pressure of the chamber is monitored with two pressure gauges. One is a Pirani gauge for readings from atmosphere to 1.10^{-4} mbar, and the second is an ion gauge with a range from 1.10^{-3} mbar to 1.10^{-12} mbar, the sensitivity to low pressure is limited by photoelectric noise created by electrons striking the grid of the ion gauge and emitting X-rays.

Rough Rotary Pump

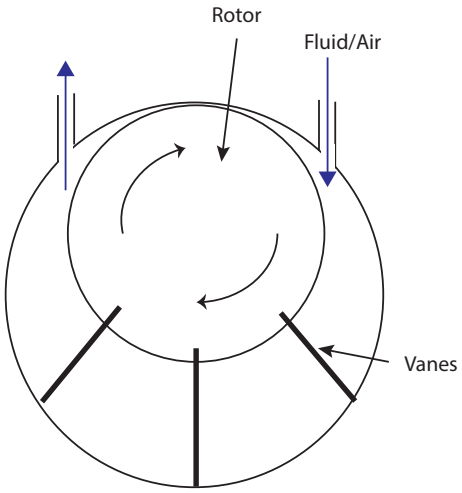

Figure 3.2: Illustration of the mechanism of pumping by a rotary vane pump, the air is driven through to the outlet by vanes attached to a rotor.

The chamber environment achieves a rough vacuum using a rotary vane pump, a common tool found in most chemistry labs. Vanes are attached to a rotor which is eccentrically supported on a cycloidal cam. The rotor and vanes sweep the gas from the inlet to the outlet. The space between the rotor and the cavity is limited between ports to restrict gas return, Figure 3.2 illustrates the basic mechanism. The purpose of the rotary pump is to achieve pressures down to 1.10^{-4} mbar. This prevents damage of the turbo molecular pump once in operation.

Turbo Molecular Pump

The turbo molecular pump achieves a high vacuum range from 1.10^{-4} mbar to 1.10^{-9} mbar. The pump consists of a series of turbine rotors with multiple blades; molecules bombard the series of blades and flow through the outlet to the rotary pump and exhaust, shown in Figure 3.3. The high vacuum is achieved by the high speed of the blade rotation rate, ranging from 20,000 - 90,000 revolutions per minute. In practical design, a rotor is followed by a stator (a stationary set of blades) consecutively, the molecules collide with the rotor and strike the stator and then continue to the next set.

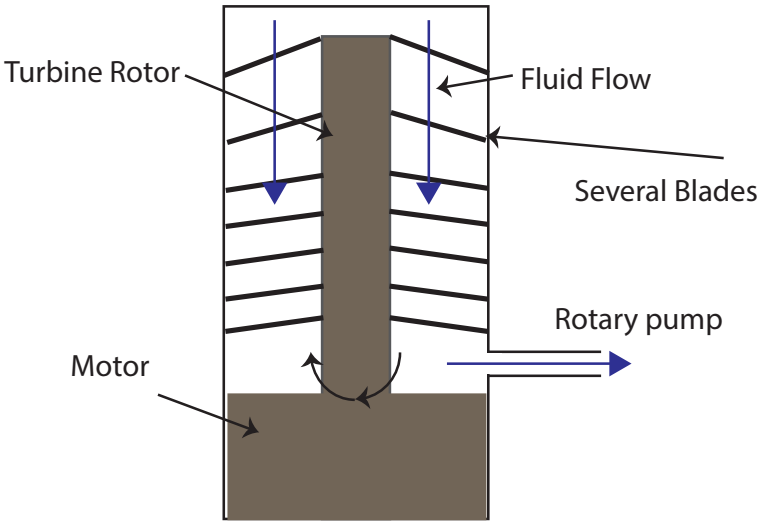

Figure 3.3: Basic mechanism of a turbo molecular pump, the rotors have multiple angles blades and the rotation pushes molecules from the top set of blades to the lower sets and travel through to the rotary backing pump.

Titanium Sublimation Pump

The titanium sublimation pump (TSP) consists of a titanium filament. The titanium filament is heated by a large current (40 amps), reaching the titanium sublimation temperature through resistive heating. The highly reactive Ti vapour coats the inner surface of the vacuum chamber, residual gas in the chamber will react with the clean Ti film on the chamber walls and form a solid product. In conjunction with the Ti evaporated through e-beam evaporation, a dual pumping process occurs.

Ion Pump

An ion pump is attached to the base of the vacuum chamber, and can reach pressures of 10^{-5} to 10^{-11} mbar. An ion pump has no moving parts and doesn't require oil or produce vibrations, thus is a low maintenance piece of equipment. The basic premise of an ion pump is illustrated in Figure 3.4.

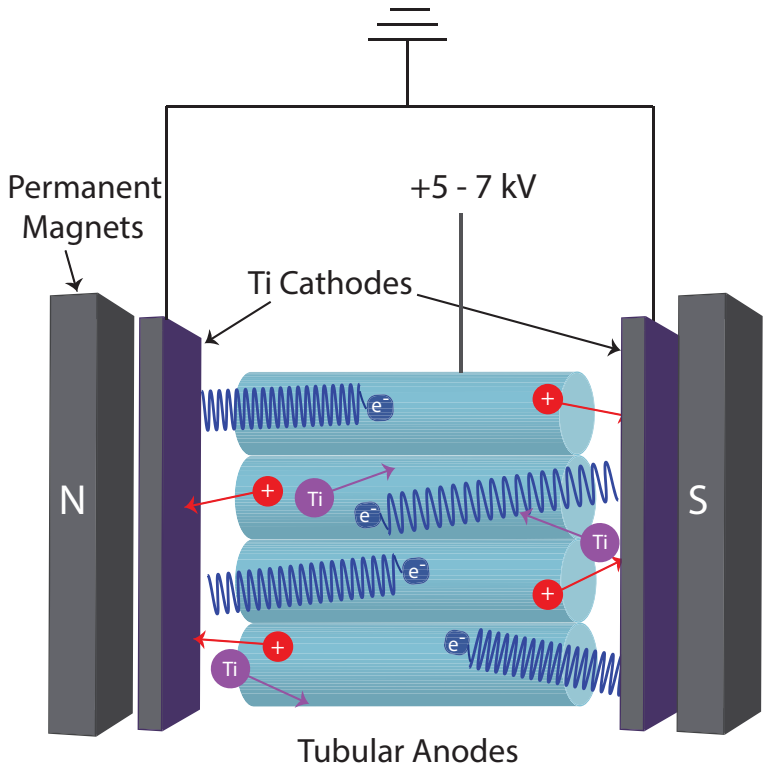

Figure 3.4: Illustration of a sputter ion pump. Tubular anodes and magnetic field form multiple penning traps in parallel. Electrons in the penning trap move in helical patterns under an axial magnetic field of 0.1 T, ionising a higher density of neutral atoms. Ionised atoms sputter Ti, which reacts with gas and coats the internal cavity with fresh Ti.

An ion pump can be composed of multiple penning traps which confines electrons. Electrons (and secondary electrons after ion impact) are emitted from the cathode under an electric field (+5-7 kV) and move in a helical trajectory due to the axial magnetic field along the tubular anodes. The electron cloud in turn ionises neutral atoms of the gas, the ions are accelerated to the Ti cathodes (the magnetic field has negligible effect on heavy ions). The ion impacts the Ti cathode and releases Ti atoms, sputtered inside the cavity. The sputtered Ti atoms react with chemically reactive gases thereby pumping the cavity. The impacting ions have significant energy (a few keV) and penetrate deeply into the Ti cathode surface tens of atoms

deep. This is useful for pumping non-reactive gas atoms which would otherwise be unaffected by the sputtered Ti atoms.

3.1.2 Deposition Conditions and Rates

The deposition rate directly relates to the temperature and vapour pressure of the metal precursor, the distance between the source and substrate and the quality of the vacuum. Evaporation from a liquid surface was experimentally confirmed to be proportional to $(P_v - P)$ by Heinrich Hertz where P_v is the vapour pressure and P is the pressure acting on the surface.[144] Rate of evaporation cannot be increased by additional heat without increasing the equilibrium vapour pressure of the liquid. Knudsen[145] modified the Hertz relation with an additional term (α_v) to take into account of evaporant vapour molecules reflected back to the surface, which do not contribute to the evaporant flux. This is known as the sticking coefficient.

Equation 3.2 shows the Hertz-Knudsen relation including sticking coefficient. N_e is the number of evaporant molecules, A_e is the area of the evaporation source, m is the molecular mass of the evaporant, k_B is Boltzmann's constant, T is the absolute temperature, $P_e(T)$ is the vapour pressure of the evaporant and P is the hydrostatic pressure acting on the surface.

$$\frac{dN_e}{A_e dt} = \alpha_v \left(\frac{1}{2\pi m k_B T}\right)^{\frac{1}{2}} \frac{1}{r^2}(P_e(T) - P) \tag{3.2}$$

Langmuir showed in 1913 that the Hertz-Knudsen relation also applies to evaporation from free solid surfaces (Langmuir evaporation) and is independent of the residual gas pressure as the resistance due to the residual gas pressure is negligible. The Langmuir-Knudsen relation (equation 3.3) shows the quantitative relationship between the various factors and mass deposition rate per unit area of source surface.[146]

$$R_m = C_m \left(\frac{M}{T}\right)^{\frac{1}{2}} \frac{1}{r^2} P_e(T) \tag{3.3}$$

Where R_m $(kg/m^2 s)$ is the mass deposition rate, $C_m = \left(\frac{1}{2\pi \times k_B}\right)^{\frac{1}{2}}$, M is the molecular mass and r is the distance between the precursor and substrate. The $1/r^2$ term takes into account the inverse square law due to the material beam radiating radially in 3d space from a point source.

Taking into account angular dependance of the substrate with respect to the crucible, the Langmuir-Knudsen relation can be expressed as in equation 3.4.

$$R_m = C_m \left(\frac{M}{T}\right)^{\frac{1}{2}} \cos\theta \cos\varphi \frac{1}{r^2} P_e(T) \tag{3.4}$$

Where θ and φ are the angles of the crucible aperture surface normal and the position of the substrate, and the angle of the substrate normal with respect to the crucible position respectively, these are illustrated in Figure 3.5. A manipulator shaft accommodates the substrate where the thin film is formed, centred in the vacuum chamber. The manipulator shaft allows the growth to be halted by adjusting the substrate position out of the line of sight of the crucible $\varphi = 90$ according to Figure 3.5. At large θ and φ the mass deposition rate is significantly limited, The maximum rate of deposition can be achieved when θ and φ approach 0°.

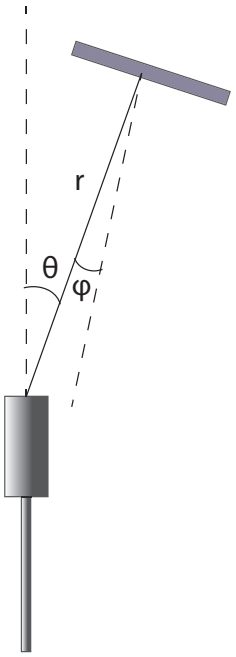

Figure 3.5: Illustration of the substrate position and angular dependence with respect to the crucible.

The thickness deposition rate $\frac{dh}{dt}$ can be expressed by equation 3.5.

$$\frac{dh}{dt} = \frac{R_m}{\rho} \tag{3.5}$$

Where ρ is the precursor density. Combining equations 3.3 & 3.5 and assuming $\theta = \varphi = 0$, we can simplify the equations to equation 3.6.

$$\frac{dh}{dt} = \frac{C_m}{\rho}\left(\frac{M}{T}\right)^{\frac{1}{2}} \frac{1}{r^2} P_e(T) \tag{3.6}$$

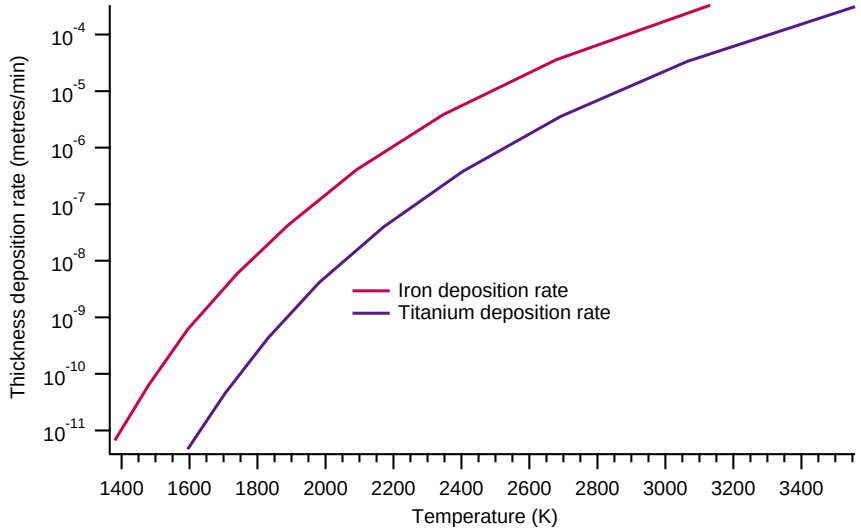

Figure 3.6: The maximum thin film deposition thickness rate of the e-beam evaporator (P=0). The y-axis is logarithmic, illustrating the sensitivity of evaporation rate with respect to temperature.

The precursor vapour pressure is temperature dependent, a comparison of Fe and Ti deposition rates depending on temperatures are shown in Figure 3.6. Fe requires a lower temperature to maintain the same rate of deposition as Ti due to the higher vapour pressure of iron, the P_e of iron at 2091 K being ten times larger than the P_e of Ti at 2171 K. The vapour pressures Ti and Fe are obtained[147] and substituted into the Langmuir-Knudsen relation to plot the evaporation rate. The evaporation rate increases exponentially with crucible temperature as the vapour pressure is related to temperature by $P_e = P_0 e^{-\frac{L}{RT}}$ where L is the latent heat of vapourisation and R is the molar gas constant.

3.2 Anodisation

Anodisation is an electrolytic passivation process, where the metal undergoing oxidation is placed into an electrolyte bath as the anode. For example to develop TiO_2 nanotubes, a Ti substrate serves as the anode in the electrolyte bath. The electrolyte controls the chemical oxidation and dissolution of the metal substrate and to assist in ion transportation. The electrolyte composition includes water to assist

in oxidation of the surface of the metal substrate. For creating nanostructures the anodisation is normally accompanied by a dissolution process facilitated by an acid and fluoride. The dissolution process is essential for generating a porous structure and to maintain the anodisation rate.

An electric field is applied to direct the oxidation and oxide dissolution process, and encourage vertical nanotubular growth. The concentrations of the various parts of the electrolyte are dependent on the metal used in the anodisation process. Oxidation and dissolution rates are metal and metal oxide specific.

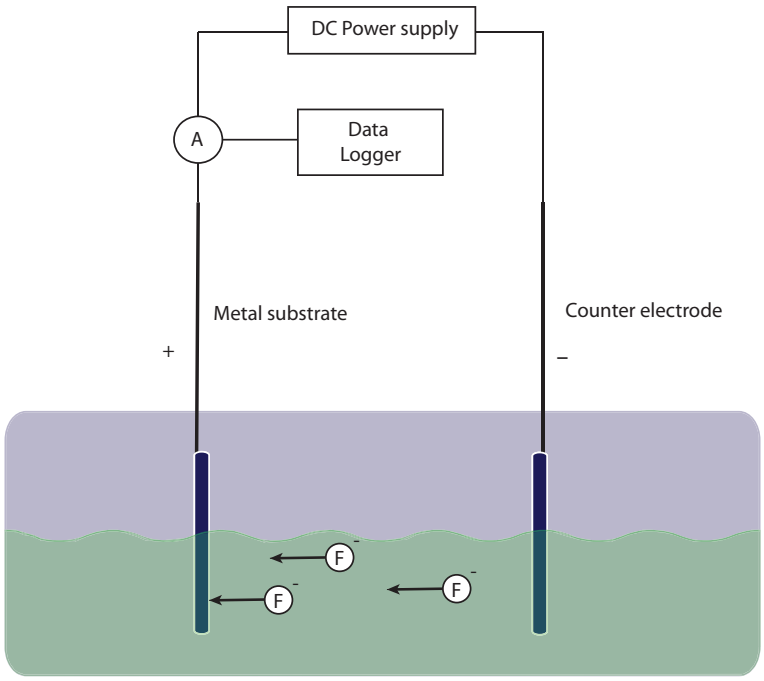

Figure 3.7: Anodisation experimental setup, an electrolyte bath containing two electrodes (one is the substrate) are connected to a computer *via* a data acquisition module and a voltage is applied across the two electrodes.

Figure 3.7 shows the electrochemical bath in which anodisation takes place, usually a DC bias of 60 V is applied between a counter electrode (Ti) and the target metal substrate serving as the anode. Equation 3.7 and 3.8 represent the oxidation reaction occurring at the surface of titanium and iron in electrolyte containing water. These are the metals specific to the hybrid nanostructures synthesised in this work. Equations 3.9 & 3.10 illustrate the chemical dissolution process occurring on the TiO_2 and Fe_2O_3 surfaces respectively.

$$Ti + 2\,H_2O \rightarrow TiO_2 + 2\,H_2 \tag{3.7}$$

$$2\,Fe + 3\,H_2O \rightarrow Fe_2O_3 + 3\,H_2 \tag{3.8}$$

$$TiO_2 + 6\,F^- + 4\,H^+ \rightarrow [TiF_6]^{2-} + 2\,H_2O \tag{3.9}$$

$$Fe_2O_3 + 12\,F^- + 6\,H^+ \rightarrow 2\,[FeF_6]^{3-} + 3\,H_2O \tag{3.10}$$

Initially oxide pores are formed within the first 5 mins, thereafter, electric-field driven F^- ions dissolve the oxide pores and oxidation occurs within the pores simultaneously with dissolution. The dissolution will thin the oxides at the bottom of the pores which allows further anodisation. This continuous process creates a nanotubular structure when the oxidation and dissolution rates are balanced. If the anodisation rate is too fast, a thick layer of oxide will form at the bottom of the nanotubes which will limit the anodisation current and in some cases only a densely packed thin film of oxide is formed instead of nanotubes. If dissolution rate is too fast; fragmented, short nanotubes will form and the overall length of the nanotubes is limited by the dissolution rate.

Figure 3.8 illustrates the anodisation current as a function of anodisation time in the process of anodising a titanium plate to form TiO_2 nanotubes. Figure 3.8(a) represents the anodisation of titanium pre-treated with acidic solution; partially covering the surface with hydroxide islands. In this case the hydroxide islands was created by exposing Ti to HF solution before anodisation. The anodisation current drops rapidly as the hydroxide islands behave as surface catalytic centres. The quick formation of an oxide layer is represented by a quick reduction in the anodisation current. Figure 3.8(b) is a typical current-time curve (clean surface) where oxygen evolution occurs in the initial stages of anodisation, through the electrolysis of water as indicated by the initial high anodisation current. In this case the sample was mechanically polished with diamond paste to remove residual oxides and defects. Therefore at the initial stage, the electrochemical potential is directly applied through the electrolyte promoting the water hydrolysis reaction. Following the anodisation process, eventually both samples form an oxide layer which is attributed to the initial exponential decay of the curve.

The growth process is clearer from Figure 3.8(a) showing the pore and tube formation in steps labelled as D2, D3 and D4. The initial decay represents the formation of an oxide layer, followed by the formation of a porous structure indicated

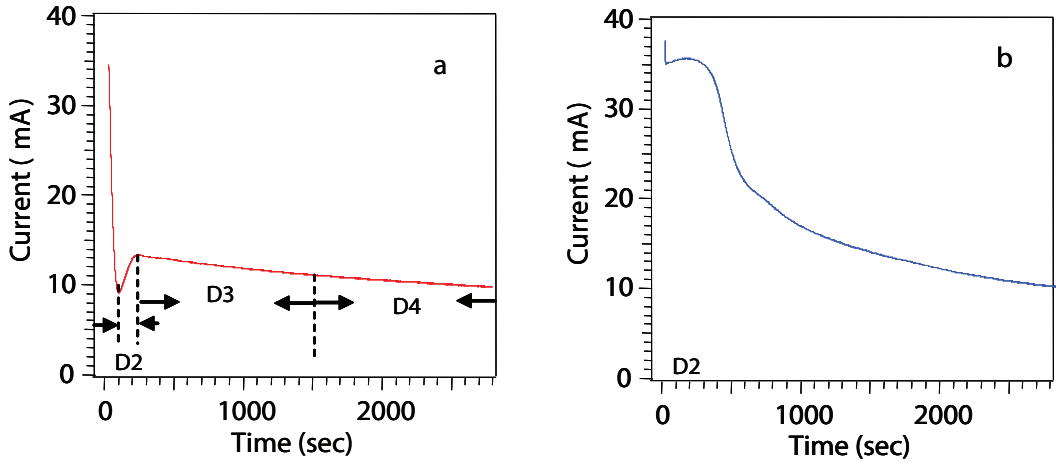

Figure 3.8: Current-Voltage (I-V) curves illustrating the formation of nanotubes, current is directly related to the electrochemical oxidation process and is indicative of surface area of the anode. (a) is the anodisation current-voltage curve for a pretreated Ti foil to form hydroxide islands on the surface, and (b) is the anodisation current-voltage relationship of a mechanically polished Ti plate.

by a rapid decrease of the anodisation current in the D1 region (not labelled). This increases the surface area of the titanium anode, thereby increasing the current density in the D2 region. From D3 to D4 the porous structure extends into a tubular array during a dissolution process. As the tubes become longer the ion conductance in and out of the tube becomes smaller, which results in a steady current density.

3.3 Vapour Transport Synthesis

Vapour liquid solid (VLS) and vapour solid (VS) synthesis of nanostructures are are forms of vapour transport synthesis in a chemical vapour deposition (CVD) process.[148] The deciding factors in the formation of metal oxide nanostructures are the surface reactions and condensation of the vapour. The condensation and surface reactions are dependant on the vapour partial pressures of the metal and oxygen, the temperature of the reaction zone and the flow rate of the carrier gas.

Vapour processing techniques are an actively and widely researched topic,[149] creating unique nanostructures with useful applications.[150]

For the growth of ZnO materials Zn vapour is carried into the reaction zone, where it is oxidised on the substrate. The carrier gas can consist of oxygen if growth temperatures are below 500 °C; at high temperatures oxygen is diluted with an inert carrier gas.

Zn vapour is introduced by two different methods in this work. The first method to create Zn vapour is through the carbothermal decomposition of ZnO with graphite, where the reaction is shown in equation 3.11. The powders are mixed at a 1:1 ratio by mass with a weight of 0.15 g each and finely mixed with a pestle and mortar. The temperature of the furnace is ramped to 1100 °C for synthesis and the crucible containing the precursor is placed into the centre of the furnace with the substrate placed above the precursor, followed by the introduction of Ar as the carrier gas.

$$2\,\mathrm{ZnO} + \mathrm{C} \rightarrow 2\,\mathrm{Zn} + \mathrm{CO_2} \tag{3.11}$$

The second method of introducing Zn vapour to the reactor is by direct evaporation of Zn powder. Vapour produced from a pure Zn powder requires lower temperatures, the Zn oxidises and then solidifies on the surface of the substrates during condensation. Temperatures can range from 450 °C to 750 °C (> 420 °C, higher than the melting point of Zn) and the consequence of changing temperatures results in change of morphology due to the varying partial pressures of Zn vapour and O_2. Which also effects the growth rate. The low temperatures required for the vapourisation of Zn allows a wider choice for substrate to be used in the reaction.

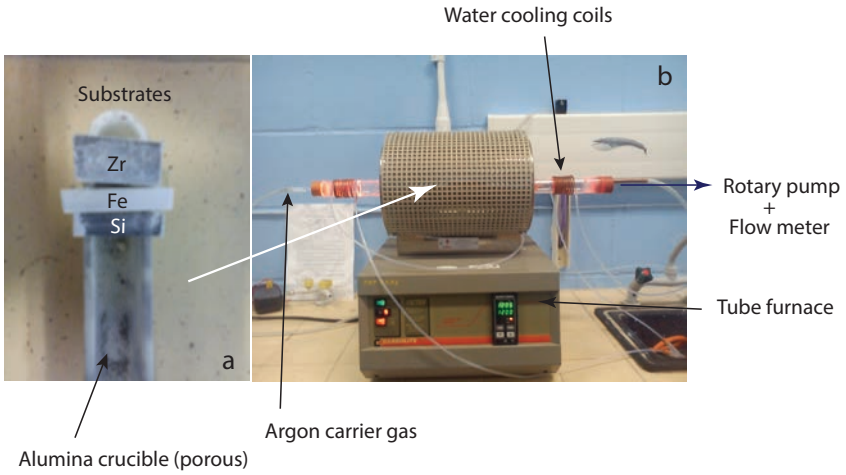

Figure 3.9: Vapour transport deposition setup. Figure (a) shows the placement of the various substrates with respect to the crucible; Zn powder is placed directly under the substrates. Figure (b) is a photo of the horizontal tube furnace (Eurotherm) where vapour transport reactions are carried out.

Figure 3.9 shows a photo of the setup used for the vapour transport synthesis, and Figure 3.10 illustrates the position of the substrate with respect to the precursor under deposition synthesis conditions. The reactor is made up of a quartz tube

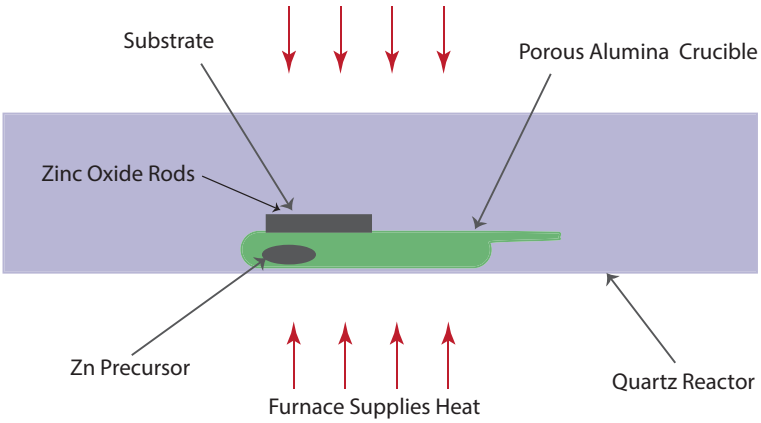

Figure 3.10: The substrate rests on the lips of the crucible, above the Zn precursor.

inserted into a horizontal tube furnance (Eurotherm), thus, the vapour production technique is restricted to temperatures below 1200 °C. As this temperature is below the softening point of quartz. In the case of direct metal vapourisation, the melting point of the precursor must be below this value. Carbothermal decomposition of ZnO requires temperatures above 800 °C, whilst vapourisation of Zn only requires temperatures above 420 °C.

The size of structures grown depends largely on the Zn and O vapour partial pressures and concentrations, as well as the occupation time in condensation region of the reactor. The reaction temperature dictates the vapour pressures. Whilst the flow rate of Ar (carrier gas) effects the time the vapour spends in the condensation zone (occupation time) as well as the oxygen concentration introduced into the reactor. At lower concentrations, an increase in mean free path of the oxide monomers reduces the size of the nanoparticles. These parameters are manipulated to achieve a variety of shapes and forms of ZnO nanostructures.

3.3.1 Vapour Liquid Solid Growth & Vapour Solid Growth

Vapour Liquid Solid (VLS) growth was first described by Wagner. VLS is the mechanism of crystal growth by precipitation from a liquid seed supersaturated with the vapour material, at the liquid-solid interface. The solid crystal solidifies from the root and the liquid remains at the top. VLS was first demonstrated using silicon as the precursor to form Si whiskers up to a micron in diameter, gold was utilised as the catalytic seed with a reaction temperature of 1050 °C.[151]

Temperatures required for VLS growth are determined by the precursor vapour-

isation temperature and the melting point of the catalytic seeds utilised as growth sites. Nanoparticles are typically used for seeding, reducing the size of the initial nucleation sites as well as having a lower melting temperature than their bulk counterpart. A eutectic melting point of the seed and substrate further reduces the temperatures required.

Vapour Solid (VS) growth temperatures are dependent on the precursor vapourisation temperature alone. A number of transition metals can be used as the seed and ordered growth is possible if the lattice of the substrate closely matches that of ZnO (i.e. GaN, sapphire etc). The Zn vapour is partially oxidised on the surface of the catalyst during vapour transport, raising the melting point temperature and is further oxidised by the oxygen in the environment forming solid ZnO structures.

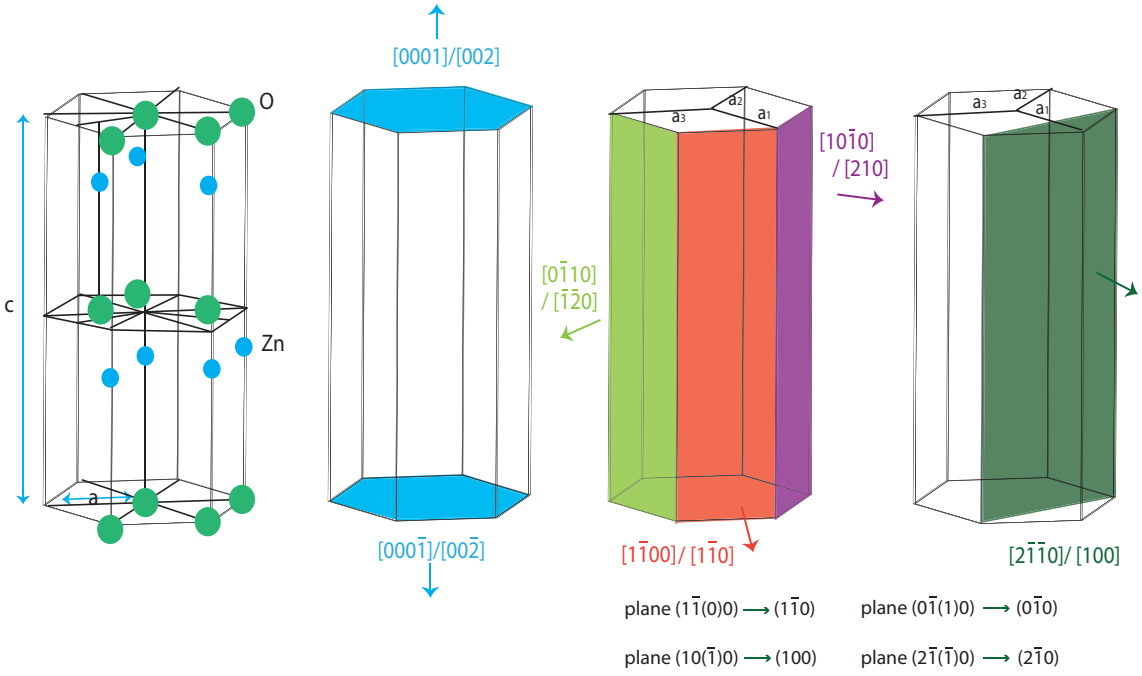

Figure 3.11: Illustration of the ZnO wurtzite structure. The miller indices of directions and faces are highlighted.

It is convenient to describe the miller indices of a hexagonal structure using a 4 index scheme, this takes into account the 3 directions of symmetry in the x-y plane. Figure 3.11 illustrates the respective planes and directions of a ZnO wurtzite crystal structure and their 3 index scheme counterparts. For a set of planes it is convenient to use the notation {hkil}, for example, the set of planes of $\{01\bar{1}0\}$ include $(01\bar{1}0)$, $(0\bar{1}10)$, $(\bar{1}010)$, $(10\bar{1}0)$, $(1\bar{1}00)$ and $(\bar{1}100)$. Similarly a set of directions are represented by <hkil>, whilst a singular direction is represented by [hkil].

In both cases the ZnO solidifies and grows preferentially in the c-axis [0001]. The ZnO wurtzite structure can be described as alternating planes of tetrahedrally coordinated Zn^{2+} and O^{2-} ions. These are stacked along the c-axis. The oppositely charged ions results in positively charged (0001) planes and negatively charged $(000\bar{1})$ planes, this results in a large surface energy for these polar surfaces. The wurtzite ZnO therefore has a normal dipole moment along the c-axis. During vapour transport the initial ZnO nucleus exposes a high energy polar surface, the incoming vapour favourably adsorbs on the polar surface exposing a polar surface, this process is repeated over time thereby forming 1D ZnO structures (nanowires/nanorods). The next fastest growth directions are in the lateral directions, such that the $\{2\bar{1}\bar{1}0\}$ and $\{01\bar{1}0\}$ sets of surfaces are the most commonly observed surfaces, this facilitates the radial growth of the ZnO nanorodular structures, as well as forming unique structures.

Since high temperatures are required (1000-1350 °C) to carbothermally reduce ZnO, the seed can also be at high enough temperatures to be in a liquid phase, depending on the position of the substrate in the reactor and can thus be classified as VLS growth. Silicon is used as a substrate; as it can withstand high temperatures. A variety of seeds can be used, with the temperatures required to melt these seeds varying significantly and thus changing the growth dynamics. Alumina seeded Si demonstrated bunching of ZnO rods, while a gold seeded surface creates a homogenous array of ZnO rods.

The versatility of VLS growth allows a variety of nanostructures to be made up of different elements, for example TiC,[152] Si,[153,154] MgO,[155] CdS,[156,157] ZnCdS[158] and ZnS[159] nanowires have all been realised.

VS growth is different to VLS in that the growth of the crystal does not involve a liquid catalyst. Nucleation sites are determined by the defects on the surface of the substrates and impurities or aberrations on the surface where metal vapour adheres and begins a self-seeding process. It constitutes a direct nanostructure growth method onto a substrate. TiO_2 nanowires form at a temperature of 1050 °C,[160] and the formation of such 1D structures are well documented[161] and but not completely understood. Solid seeds can be utilised as nucleation sites, and even in high temperature conditions the Zn/seed alloy may not undergo melting and a

vapour solid reaction may be erroneously identified as a vapour liquid solid reaction (VLS). Heterostructures such as TiO_2/SiO_2 core/shell co-axial tube arrays have been created using VS deposition.[162]

3.3.2 AACVD

Aerosol assisted chemical vapour deposition (AACVD) is a convenient technique for creating homogenous films with a high deposition rate.[163,164] The choice of precursor used for the deposition is countless, as the solvent containing the metal precursor does not undergo thermal evaporation to create a vapour.[165] However, it is required that the precursor is soluble in a solvent, since the solution is ultrasonically vapourised and carried to a heated substrate. The vapour will adhere to the hot surface and is decomposed/oxidised forming an oxide of the chosen material. Carbon nanotubes formed *via* AACVD has been realised[166] as well as polymer deposition[167] demonstrating the range of possible materials that can be deposited by AACVD.

In the AACVD process an ultra sonic transducer vibrates at a high frequency causing the liquid to vibrate quickly, cavitation occurs in the solution creating small vacuum pockets. Any liquid close to the pocket evaporates as the vacuum pockets bursts (in the case of ultra sonic bath cleansers, these tiny pockets are formed on a surface and the bursting action is accompanied by a force, pulling off contaminants from the surface). The gas particles are fine, in the micrometre diameter range, which are airborne and can be transported by gas flow to deposit homogenously onto a substrate.

The substrate can be heated either by a horizontal bed or a furnace. Furnace heating inherently coats the quartz reactor tube. If the thin film material required is a metal oxide, the heat assists in the oxidation of the metal precursor vapour on the surface to form the nanostructures or thin films.

The AACVD deposition setup is illustrated in Figure 3.12, this shows the hot bed cold wall reactor configuration. The bed consisted of an aluminium block with a heater cartridge inserted into the centre, the cartridge is controlled with a power supply. This configuration will have a higher deposition rate compared to using a furnace (hot wall reactor) to heat the substrate, as the heat is concentrated on a small surface and vapour decomposes/oxidises solely on the substrate. A cold trap

is connected to the outlet if the solvents pose a health and safety risk.

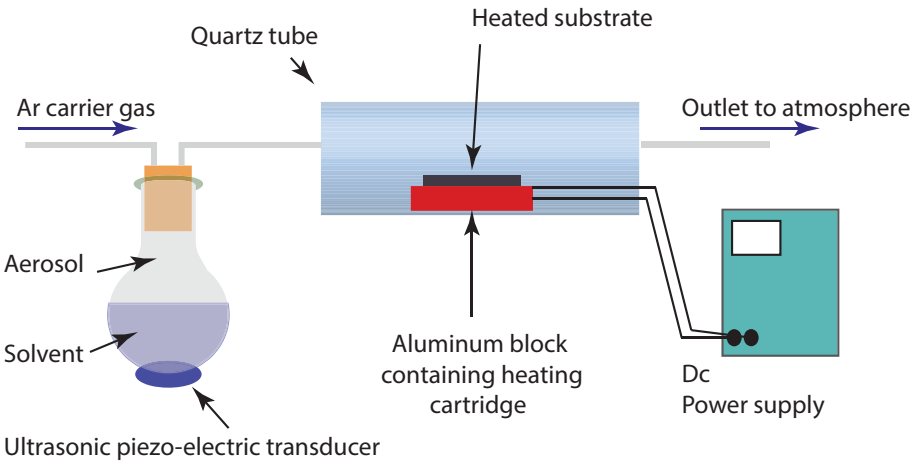

Figure 3.12: Illustration of the AACVD deposition setup, an aluminium block (heating cartridge inserted within) is heated with substrate in contact with the block. The heating block and substrate are contained within a quartz tube reactor.

For developing hybrid oxide materials, I developed a CVD growth apparatus with the ability to use a combination of AACVD and vapour transport (VS) deposition. In-situ AACVD deposition can assist in doping a ZnO structure during VS growth, which combined with the versatility of precursor choice increases the freedom to create heterostructures with various concentrations of transition metal oxides. The combined setup is shown in Figure 3.13. AACVD growth can be conducted immediately after a VS reaction, thereby surface coating the ZnO structure with a material which could benefit the photocatalytic properties of the structure. In this work I have demonstrated enhanced photoelectrochemical behaviour of ZnO rods by decorating the rods with titania nanoparticles.

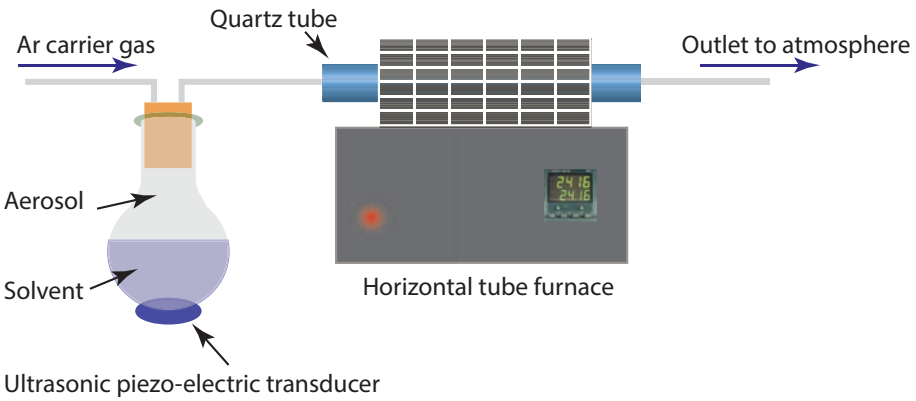

Figure 3.13: Combined AACVD and vapour transport deposition setup, the quartz tube is heated in the furnace where vapour transport growth takes place and a subsequent AACVD deposition is carried out.

The independent control of the feeding rate of a precursor during a vapour transport growth is highly attractive, as usually the system is closed and the precursor can only be controlled by placement in the reactor and mass of the precursor. Additional precursor can be fed with multiple elements during the growth, controlling the concentration ratio. The key issue is whether the VS growth temperatures match the specific temperature of the AACVD deposition of the precursor under investigation.

3.4 Chemical Bath Deposition (ZnO)

In the case the substrate cannot be heated to high temperatures, such as plastic, chemical bath deposition (CBD) can be utilised in the formation of ZnO nanostructures. CBD is a form of wet chemical growth which can be conducted at much lower temperatures than the methods previously described.[168] This allows a high degree of freedom for the substrate employed as temperatures only range from 50 °C to 95 °C depending on the solvent used in the chemical transformation.

Chemicals with a base nature decompose the Zn precursor, and create hydroxide ions which in turn form zinc hydroxide. The hydroxide undergoes condensation into ZnO, the adsorption sites are dependent on how chemically active the seed is and are preferential on the polar faces $(0001)/(000\bar{1})$ of the ZnO wurtzite structure. Growth is preferential in the $[\pm 0001]$ direction due to the polar surfaces of the $(0001)/(000\bar{1})$ planes, similar to the process of rodular growth under vapour transport conditions. This is the fundamental mechanism in the formation of arrayed ZnO nanorods and nanowires in aqueous solution.[169]

A seeded substrate is required, and a convenient way of coating a thin film of the seed layer is to use a spin coater. Our home built system allows fast spin rates which dry the solution containing the seed precursor and the centrifugal forces spread the film evenly. The substrate is then heated to convert the precursor into a thin film of ZnO seeding crystals. The annealing temperature is dependent on the substrate used for the CBD reaction. Zinc acetate dihydrate is usually used as the seed precursor $Zn(O_2CCH_3)_2(H_2O)_2$ (Purchased from Sigma-Aldrich - CAS 5970-45-6), which is dissolved in a solvent.

For the growth solution, typically a 1:1 ratio of either Zinc acetate (ZnAc) or Zinc

nitrate ($Zn(NO_3)_2$) and Hexamethylenetetramine (HMTA) (the latter two chemicals are also purchased from Sigma-Aldrich - CAS 10196-18-8 and CAS 100-97-0 respectively) are dissolved in a solvent (deionised water). The solution is kept under heated conditions from several hours to days. The chemical reactions proceed to form nanostructures of ZnO which are dependent on seeding, growth temperature, and duration of growth. HMTA decomposes into NH_3 and ultimately OH^- ions thereby increasing the solutions pH gradually. These OH^- ions react with Zn^{2+} and form solid ZnO, reducing the pH in the process. The chemical reaction during the growth is shown in equations 3.12 to 3.15. Nanorods grow as the crystal forms in a preferential orientation from the initial adsorption sites and the lateral growth is restricted by orientation of the crystal faces and the size of the ZnO seed.

$$(CH_2)_6N_4 + 6\,H_2O \longleftrightarrow 4NH_3 + 6\,HCHO \tag{3.12}$$

$$NH_3 + H_2O \longleftrightarrow NH_4^+ + OH^- \tag{3.13}$$

$$Zn^{2+} + 2\,OH^- \longleftrightarrow Zn(OH)_2 \tag{3.14}$$

$$Zn(OH)_2 \longleftrightarrow ZnO + H_2O \tag{3.15}$$

Chapter 4

Fe-Ti-O Nanotube Composite Formation *via* Anodisation.

The first photoanode to be utilised in the photoelectrochemical decomposition of water by Fujishima and Honda in 1972 was a TiO_2 anode, under UV light illumination.[50] Since then many semiconductors have been investigated and TiO_2 remains one of the best candidates as a photoelectrode for water splitting due to its charge transfer properties and stability in an electrolyte.[170–176] TiO_2 has a large band gap and requires photons of energy greater than 3.2 eV. Photons with an energy of 3.2 eV have a wavelength in the UV range (387 nm). Efforts are concentrated to decrease the band gap energy of TiO_2, to encompass visible light absorption; for example carbon[177,178] and nitrogen doping[179] have shown to reduce the band gap of titania. Transition metal doping of titania have also shown promising photocatalytic properties, extending the normal absorption edges of anatase and rutile to longer wavelengths.[180] TiO_2 mesoporous structures used in dye sensitised solar cells is a less costly promising route in the construction of a photoanode, the abundant material has been shown to reach solar efficiencies of 7 %.[181]

Fe_2O_3 nanostructures have recently been reported to exhibit good qualities as a photoelectrode in the use of water splitting.[182–184] The valence band minimum is significantly below the oxidation potential of water (> 1 V), and holes have sufficient energy for the water redox reaction. Another advantage is the low value of the band gap energy, which is not limited to the UV, and can absorb visible wavelengths less than 560 nm (2.2 eV). A key concern is the poor minority charge mobility

($0.2\ cm^2V^{-1}s^{-1}$)[185] of iron oxide which results in shorter diffusion lengths (2-4 nm) and increased rate of recombination. Heterostructures of metal oxides have demonstrated improvements over single component photoelectrodes.[186,187] Heterostructure counterparts of the iron electrode can assist in increasing charge mobility, either by creating a junction where field assisted separation of excitons can take place, or charge is injected into the secondary semiconductor thereby reducing recombination rates.

Titanium dioxide production starts with the mining of naturally occurring ilmenite ($FeTiO_3$), which poses a question whether an iron titanate material can be produced close to the initial manufacturing process of TiO_2 at a considerably lower cost. It is shown in this work iron titanate performs better as a water splitting photoelectrode and could be produced at an industrial scale at a lower cost. A mining facility could produce TiO_2 as well as water splitting photoanodes simultaneously through the use of furnaces and appropriate materials possibly creating nanorods, which can be produced through high temperature growth.

It has been demonstrated by Hussain and Siddiqa that doping of TiO_2 nanotubes with Fe and Cr can drastically effect the band gap of the material. Reducing the bare titania nanotubes band gap from 3.25 eV to 1.85 eV with Cr and Fe doping.[188] Yet preferential band positions remain. Fe-Ti-O could be ideal for water splitting, utilising visible light absorption in the process of photocatalytic water reduction.

4.1 TiO_2 Nanotube Formation

A variety of methods of TiO_2 nanotube formation have been reported. The most common methods are template synthesis and anodisation.[189] Other methods of nanotube synthesis are well documented including hydrothermal methods,[190] and low temperature self-assembling chemical growth methods.[191] It is possible to grow TiO_2 nanowires using VS reactions,[160] electrospinning,[192,193] radio frequency evaporation[194] and hydrothermal techniques.[195] A variety of other TiO_2 nanostructures have been demonstrated experimentally, amongst these are nanorods and nanowalls created *via* metal-organic chemical vapour deposition (MOCVD),[196] as well as titania nanofibers (electrospinning).[197] TiO_2 is a well researched material in literature,

and the catalytic behaviour of TiO_2 is well understood.[170]

Anodisation is a convenient templateless technique which allows a high level of control in the synthesis of titania nanotubes.[198–200] The titania nanotube dimensions are determined by the synthesis conditions. Hydrothermal and chemical routes are notoriously difficult in the control of the morphologies of the titania nanotubes. Also, template based synthesis require further steps in the synthesis procedure, which is costly and time consuming. The anodisation process creates a vertically aligned tubular array which are advantageously utilised as a photoanode. The morphology allows effective charge transport and provides a large surface area of the semiconductor/electrolyte interface for the redox reactions to take place.

The material serving as the anode in the anodisation process will dictate the metal oxide formed, either a metal foil or a thin film of the metal can serve as the anode. I will show that in both cases ordered nanotubes are formed, creating titanium dioxide nanotubes by utilising a Ti foil or a Ti thin film on conductive glass, and creating iron oxide nanotubes utilising a Fe foil or a thin film of Fe deposited on conductive glass.

Figure 6.4 shows a well-ordered TiO_2 NT array created on a Ti foil substrate, the anodisation potential is potentiostatically set at 60 V. The electrolyte is composed of 2 % water and 0.3 % NH_4F in an ethylene glycol solution. The anodisation is conducted for one hour, achieving a nanotube length of 10 μm with an inner diameter 109.2 nm $\pm$ 13.3 nm and outer diameter of 166.7 nm $\pm$ 15.5 nm.

4.2 Fe_2O_3 Nanotube Formation

Fe_2O_3 has recently attracted a renewed interest. The encouraging optical, semiconducting and magnetic properties of Fe_2O_3 has resulted in an increase of volume of research conducted in its use for a variety of material applications from drug delivery[201] and pigments[202] to optical devices. Fe_2O_3 nanotubes can be formed through the use of a variety of methods including sol gel,[203] hydrothermal, CVD, surfactant assisted synthesis,[204] as well as template synthesis[205] as discussed earlier and finally, electrochemical synthesis (anodisation).[206] The availability and durability of Fe_2O_3, as well as non-toxicity, makes Fe_2O_3 highly attractive as a cost effective

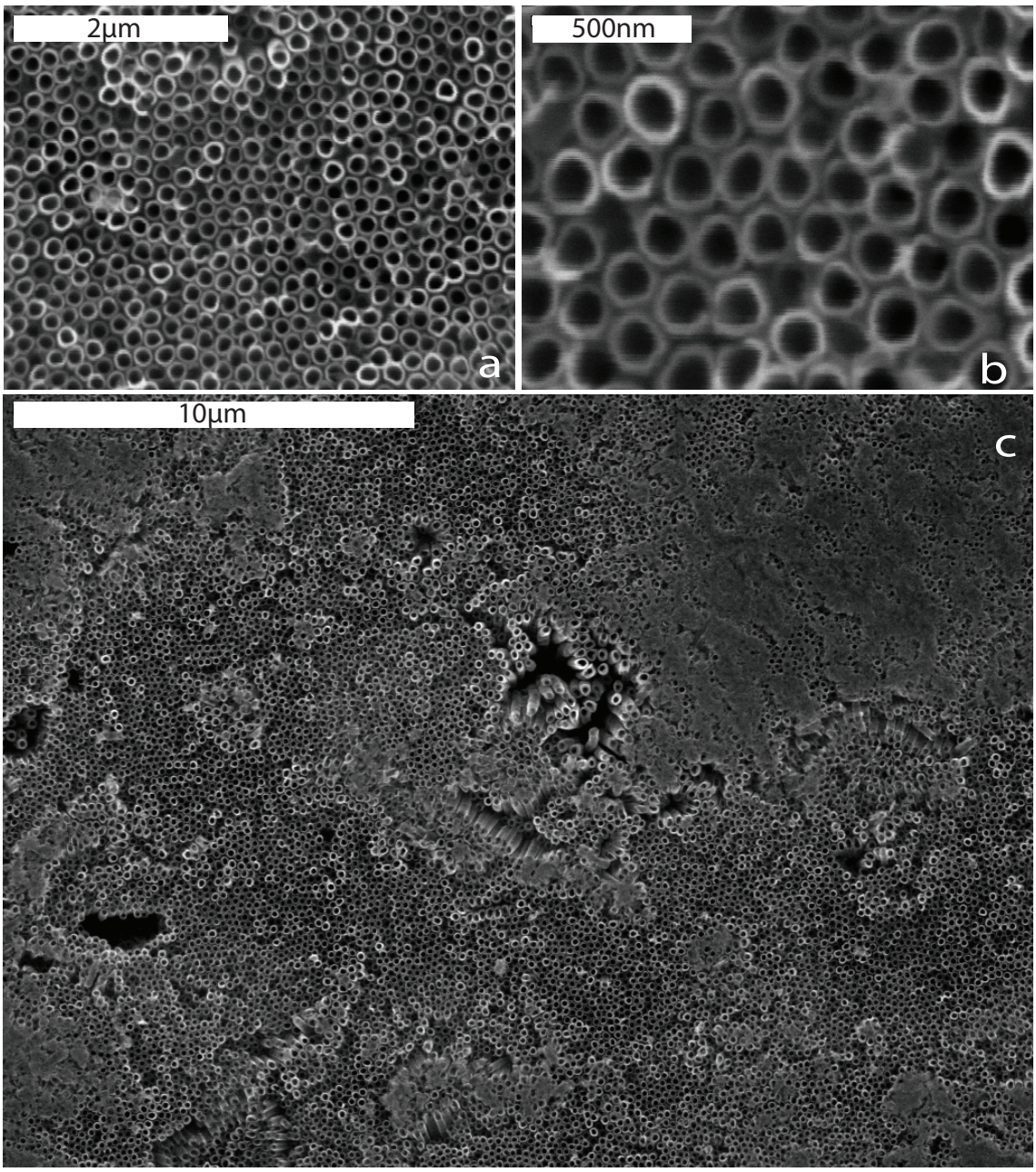

Figure 4.1: SEM micrograph of TiO_2 nanotubes of varying magnification (a) ×15,000 (b) ×45,000 and (c) ×5,600, grown using a Ti foil serving as the substrate anode.

material for photoelectrochemical cells. Gratzel et al reported a high performing silicon doped Fe_2O_3 photoanode[207] and Ingler and Khan have reported a self-biased tandem photoelectrochemical cell based on p-n Fe_2O_3 photoanodes.[208]

The band gap of Fe_2O_3 is 1 eV smaller than TiO_2, photons with energies greater than 2.2 eV can create an exciton pair. This makes Fe_2O_3 an ideal candidate for visible light absorption, unfortunately the conduction band (CBM) is lower than the H^+/H_2 redox potential (more positive). The electrons created *via* excitation require additional energy to overcome the potential difference between the redox potential and CBM, therefore unassisted water splitting cannot occur using an Fe_2O_3 photoanode without significant alterations to the band structure. The flat band potential is much greater for an Fe_2O_3 anode compared to TiO_2 where both band edges straddle both redox potentials. On the otherhand the valence band minimum (VBM) of Fe_2O_3 is much lower (more positive) than the O_2 /H_2O redox potential, and holes have sufficient energy to assist in the oxidation of water, for the reactions to be balanced a bias is required to increase the energy of the electrons in the Fe_2O_3 to overcome the difference between the CBM and H^+/H_2 redox potential.

In this work I developed an anodisation method to create vertically aligned Fe_2O_3 nanotubular arrays. The nanotube array is directly synthesised on an iron foil which can serve as the photoanode in a photoelectrochemical cell, the nanotubular structure shows effective charge transport along the ordered tubes, enhancing photoelectrochemical properties. The semiconductor/electrolyte contact surface area of a nanotubular array is increased drastically compared to a planar surface, resulting in a larger area for the redox reaction to take place and immediate charge separation close to the surface of the tubes.

The high solubility of iron oxide was found to raise the dissolution rate. To counter the high dissolution rate the concentration of ammonium fluoride dissolved in the electrolyte is reduced in accordance. The dissolution is directly affected by the concentration of the F^- ions and the pH of the electrolyte. The electrolyte in which the anodisation is carried out is composed of 2 % H_2O and 0.15 % NH_4F in ethylene glycol.

At the beginning of the anodisation process, a passivation oxide layer is immediately formed under the influence of an applied potential, oxidising iron to form a

thin layer of Fe_2O_3, the reaction is shown equation 3.8.[206,209,210] The fluoride ion is released from the NH_4F and propagates through the electrolyte (under bias) towards the anode, dissolving Fe_2O_3 as shown in reaction 3.10. This field assisted dissolution process is directionalised, which results in an initial porous structure forming and then creating a nanotubular array; as with TiO_2. Nanotube formation continues until there is an equilibrium between the oxidation rate and chemical dissolution rate; this is repassivation.[211]

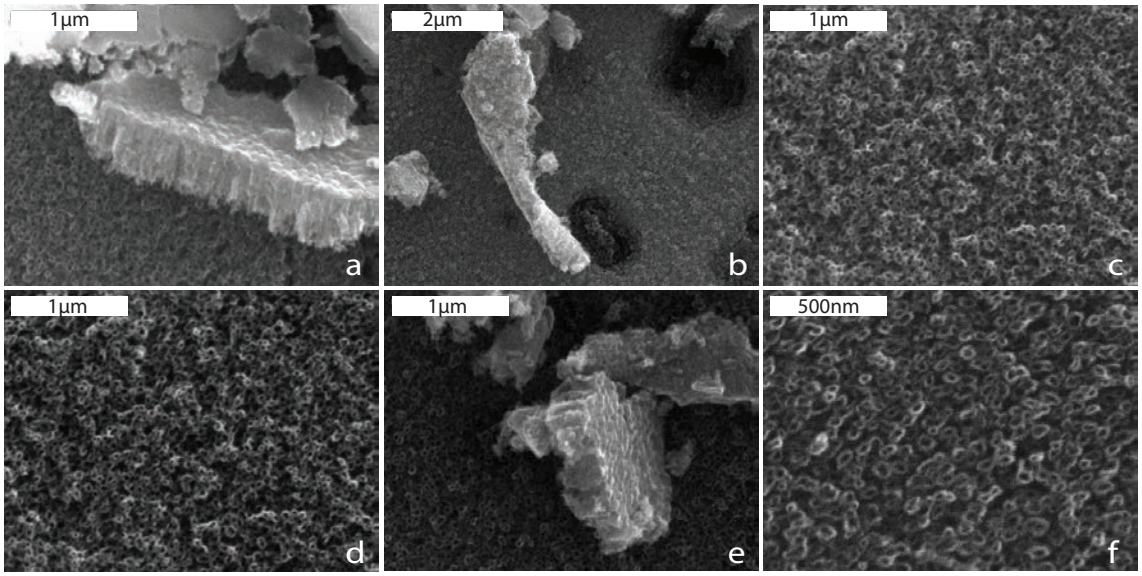

Figure 4.2: SEM micrographs of Fe_2O_3 nanotubes, grown using a Fe foil serving as the substrate at the magnifications of (a) ×15,000, (b) ×9500, (c) to (e) ×15000, and (f) ×30,000.

The thickness after 40 mins anodisation at 60 V with electrodes 4 cm apart is 385 nm ± 44 nm with an inner diameter of 29.4 nm ± 6.6 nm and outer diameter of 67 nm ± 9 nm as shown in Figure 4.2(a) to (f). This is much smaller than the TiO_2 nanotubes formed and is possibly due to a higher solubility of iron oxide and a faster oxidation rate, which has directionalised the dissolution process further. The fluorine ions dissolute with a larger ratio toward the Fe foil anode than laterally.

4.2.1 Ti Thin Film PVD on to a FTO Substrate

Here, I will present the fabrication of a semiconductor nanostructure formed on conducting glass, this provides the possibility of creating a transparent photoanode. Fabricating the photosensitive material onto a transparent substrate increases the photoefficiency of the photoelectrochemical cell as it allows multiple passes of light

through the photoanode. Also on a transparent substrate light can be illuminated from behind the nanotubes close to the Ti/TiO_2 interface. Electron-hole pairs created close to the metal/metal oxide interface have shorter distances to travel within the oxide and is not limited to the nanotube film thickness. The difficulty remains in the durability of the conductive film in deposition environments. Fluorine doped tin oxide coated glass is commonly used as a conducting glass and is economically viable due to the low cost of manufacture.[212,213] In this work the anodisation is performed in identical conditions as discussed earlier in the creation of titania nanotubes. Anodisation is performed until the film becomes transparent, the Ti film remaining on the substrate will be of the order of a few hundred nanometres and the TiO_2 nanotubes are vertically aligned above the film. SEM micrographs of the nanotubes formed are shown in Figure 4.3(a) to (f) at various magnifications and areas of the sample, which illustrates the homogeneity of the nanotube film.

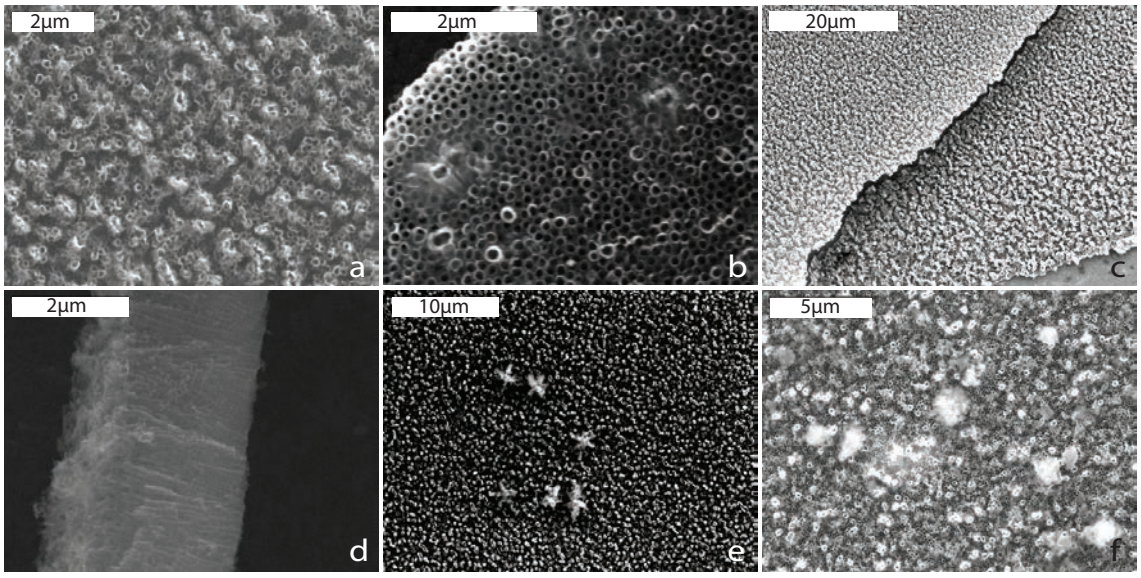

Figure 4.3: SEM micrograph of TiO_2 nanotubes formed using a thin film of Ti evaporated onto FTO (fluorine tin oxide) glass at various magnifications, (a) ×5000, (b) ×9000 (c) ×850, (d) ×7500 (e) ×1400 and (f) ×2600.

Initially a thin film of titanium is deposited on a FTO substrate, a titanium slug serves as the Ti precursor, using an e-beam evaporator constructed in a high vacuum chamber; discussed in chapter 3.1. The high vacuum chamber is evacuated to a pressure of 2.10^{-6} mbar *via* a turbo molecular pump, assisted by a backing rotary pump. The crucible consisted of a molybdenum cup, surrounded by a tungsten filament. The tungsten filament is heated *via* resistive heating by supplying the

filament with a current of 4.6 A utilising a current supply. This is sufficient enough to activate thermionic emission of electrons. The bias between the crucible and the filament is 900 V. Adjustments are made to sustain a suitable heating power (emission current × bias). The high melting temperature of Ti (1668 °C) required a heating power close to 70 W and above (emission current ranged from 70 mA to 80 mA). Deposition rates depend on the heating power of the system; at 70 W, approximately 100 nm/hr of Ti is deposited onto the substrate in the centre of the chamber, as calibrated by SEM thickness measurements. Deposition rate could be increased by moving the substrate closer to the electron beam evaporator, or increasing heating power.

The FTO/thin film substrate is placed into the anodisation bath using a special holder which has conductive foils to maintain a closed circuit between the titanium film and cathode, the film was anodised for 40 mins at a bias of 60 V in an electrolyte of 3 % H_2O and 0.3 % NH_4F in ethylene glycol. The increase in water and F^- ion concentration compared with the electrolyte used in the anodisation of iron, is adjusted to reflect the lower rate of dissolution of TiO_2. The anode and cathode are separated by 4 cm. This created nanotubes 2.5 μm ± 0.1 μm long with a 99.7 nm ± 12.4 nm inner diameter and 140 nm ± 18 nm outer diameter, shown at various magnifications in the SEM micrographs presented in Figure 4.3(a) to (f).

4.3 Co-Evaporated Fe/Ti Thin Film, and the Formation of Nanotubes

The e-beam evaporator I constructed in this work can deposit up to 4 metals simultaneously, allowing a two dimensional architecture of varying compositions of four metals. This freedom of compositional structure of the thin film can be advantageously controlled to construct multiple band gap nanotubes *via* anodisation. In this work I will concentrate on two transition metals, namely Ti and Fe and control the composition of Fe-Ti-O nanotubes forming a three dimensional architecture. The evaporation of transition metals require crucibles (the container of the precursor) with high melting points and durability at high temperatures. I utilised molybdenum (m.p. 2623 °C) for Iron evaporation and graphite (m.p.$_{sublimes}$ 3652 °C)

for Ti evaporation. The degradation of molybdenum after multiples evaporations proved expensive and wasteful. Graphite crucibles are cheaper, more convenient and proved durable compared to the Mo crucible. The less conductive properties, meant graphite required higher bias and heating current to achieve similar heating powers as before with the Mo crucible. A 1 kV bias is applied between the crucible and filament. The multiple evaporations or simultaneous evaporations lasted several hours or in some cases multiple sessions. The heating power for the Fe evaporator is maintained at 50 W and Ti evaporator at 100 W, a thick layer of Ti is initially deposited to improve lattice match of the thin film and Ti foil. This reduces strain once the metal has cooled. Iron is slowly added as not to mismatch the lattice of the thin films significantly. Once the thickness of the film is sufficient to avoid interfacial stress, the mixture of Fe-Ti can be deposited.

The samples are rinsed with ethanol, then water and sonicated for 3 mins before undergoing anodisation. A variety of Fe-Ti-O nanotubes are shown in the SEM micrographs in Figure 4.4(a) to (c), each with a varying elemental Fe content.

The dimensional data is for the Fe-Ti-O nanotubes (Figure 4.4) with varying composition as summarised in Table 4.1. The values are compared with pure TiO_2 and Fe_2O_3 nanotubes. Energy dispersive X-ray (EDX) measurements are carried out on the nanotubular array to determine the composition of the material.

Composition of Fe-Ti-O NT's	Length (μm)	Inner Diameter (nm)	Outer Diameter (nm)	Wall Thickness (nm)	Figure
TiO_2	10	109 ± 13	167 ± 16	29 ± 7	4.1
2 % Fe	10	77 ± 10	123 ± 8	23 ± 5	4.4 (c)
7 % Fe	11	51 ± 6	102 ± 17	25 ± 6	4.4 (b)
10 % Fe	16.2	47 ± 13	87 ± 17	20 ± 8	4.4 (a)
Fe_2O_3	0.385	29 ± 7	67 ± 9	19 ± 4	4.2

Table 4.1: Dimensions of Fe-Ti-O nanotubes with varying Fe content.

The TiO_2 nanotubes discussed in Chapter 4.1 were synthesised in an electrolyte with higher F^- ion concentration (2 % H_2O and 0.3 % NH_4F in ethylene glycol) than for the Fe doped nanotube samples (2 % H_2O and 0.15 % NH_4F in ethylene glycol) in Table 4.1. With increasing Fe content the nanotubes inner and outer diameters reduce, the size has reduced by more than half from 2 % Fe content to

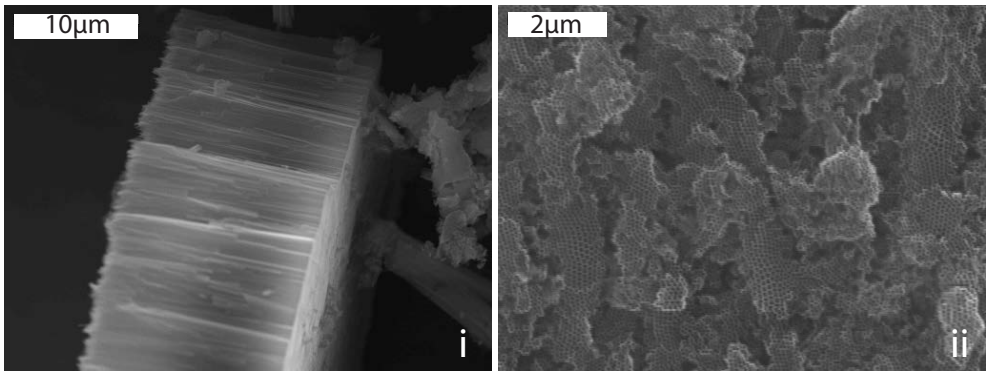

(a) 10% Fe content on Ti plate

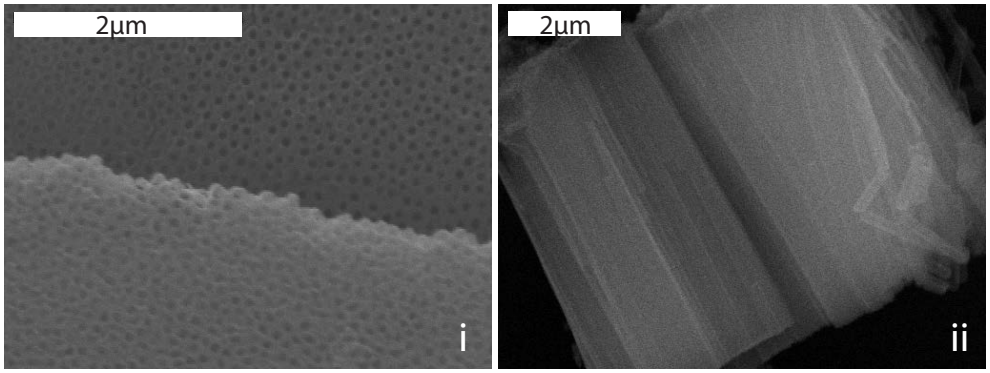

(b) 7% Fe content on Ti plate

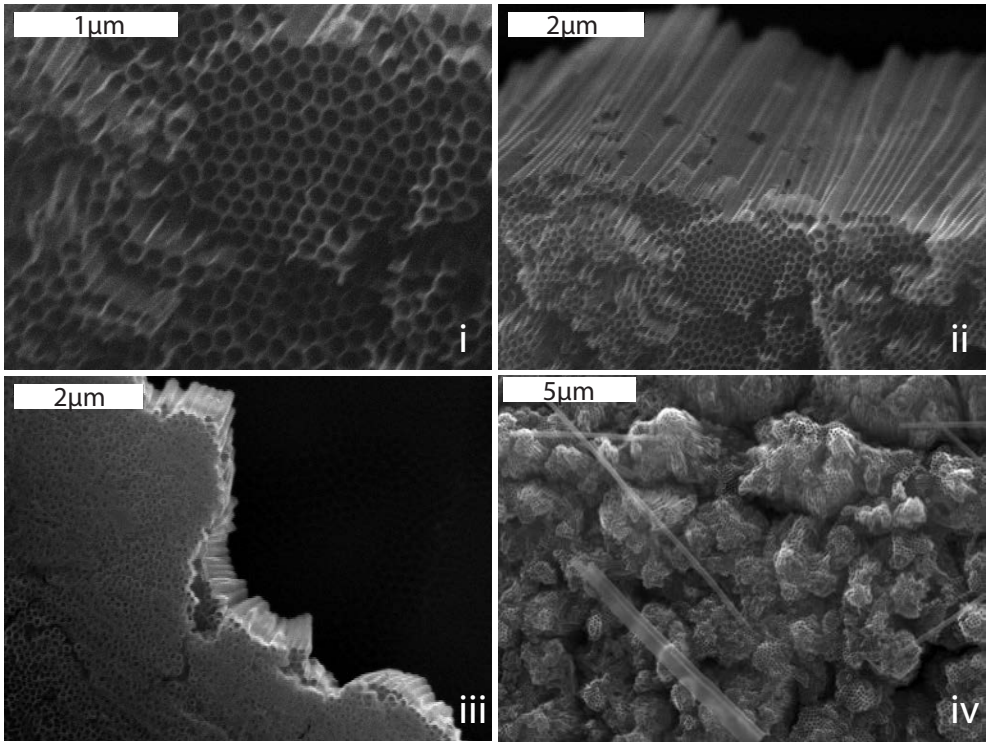

(c) 2% Fe content on Ti plate

Figure 4.4: SEM micrographs of Fe-Ti-O nanotubes formed on a Ti foil, with various ratios of Fe-Ti content. (a) shows nanotubes with a 10 % content with varying magnification, i-×1500 and ii-×6250. (b) shows a 7 % content concentration nanotubular array, i-×14,500 and ii-×7500 and (c) is a sample with the lowest concentration of Fe at magnifications of i-×20,000 ii-×6,000 iii-×8,000 and iv-×3500.

10 % Fe content. The thickness of the nanotube walls also decrease with increasing Fe content. It is possible, by increasing iron content the solubility of the thin film increases, increasing the dissolution rate as more iron is added to the composition of the thin film. If this is the case, the formation of the initial pores of the tubes would be smaller in diameter and the oxidation and dissolution will be guided by the initial pore size. The length of the nanotubes are all of the same order with the exception of the iron oxide nanotubular array, which could be due to the cracking of the tubular array and the entire array could not be distinguished.

4.4 TiO_2 and Fe_2O_3 Nanotube Formation on Complementary Substrates

The e-beam evaporator I constructed in this work allows the evaporation of multiple metals simultaneously. Evaporating varying concentrations of Ti and Fe to create nanotubes with varying band gaps along the length of the nanotubes can enhance the absorption properties of the nanotubular array. The tips of the tubular array can be composed of a higher Ti concentration forming a UV absorbing material closer to the illumination source, longer wavelengths penetrate further into the material where they can be absorbed by the higher iron content nanotubes where the band gap approaches that of iron oxide (2.2 eV), closer to the thin film metal contact.

The deposition of Fe onto a substrate required less heating power than Ti, due to the higher vapour pressure of Fe and lower melting temperature (1538 °C compared to the Ti melting point of 1668 °C). The heating power is controlled to be kept at 28 W, which is under half of the heating power for a similar deposition rate of Ti. The filament current depends on the morphology of the tungsten (length) and is controlled according to target emission current at a fixed bias voltage. The bias is maintained at 700 V with a filament current of 9.5 A, the emission current is 40 mA. Figure 3.6 illustrates the rate of deposition in m/min for iron and titanium under perfect vacuum conditions. For a deposition rate of 1 nm/min, Ti (1900 K) requires an additional 300 K compared to Fe (1600 K). Figure 4.5(a) are SEM micrographs of TiO_2 nanotubes formed by anodising a thin film of Ti, which was evaporated on a Fe foil. Figure 4.5(b) are the SEM micrographs of a Fe-Ti mixture thin film

evaporated and anodised on a Ti foil. The electrolyte in which the anodisation is carried out is composed of; 2 % H_2O and 0.15 % NH_4F in ethylene glycol.

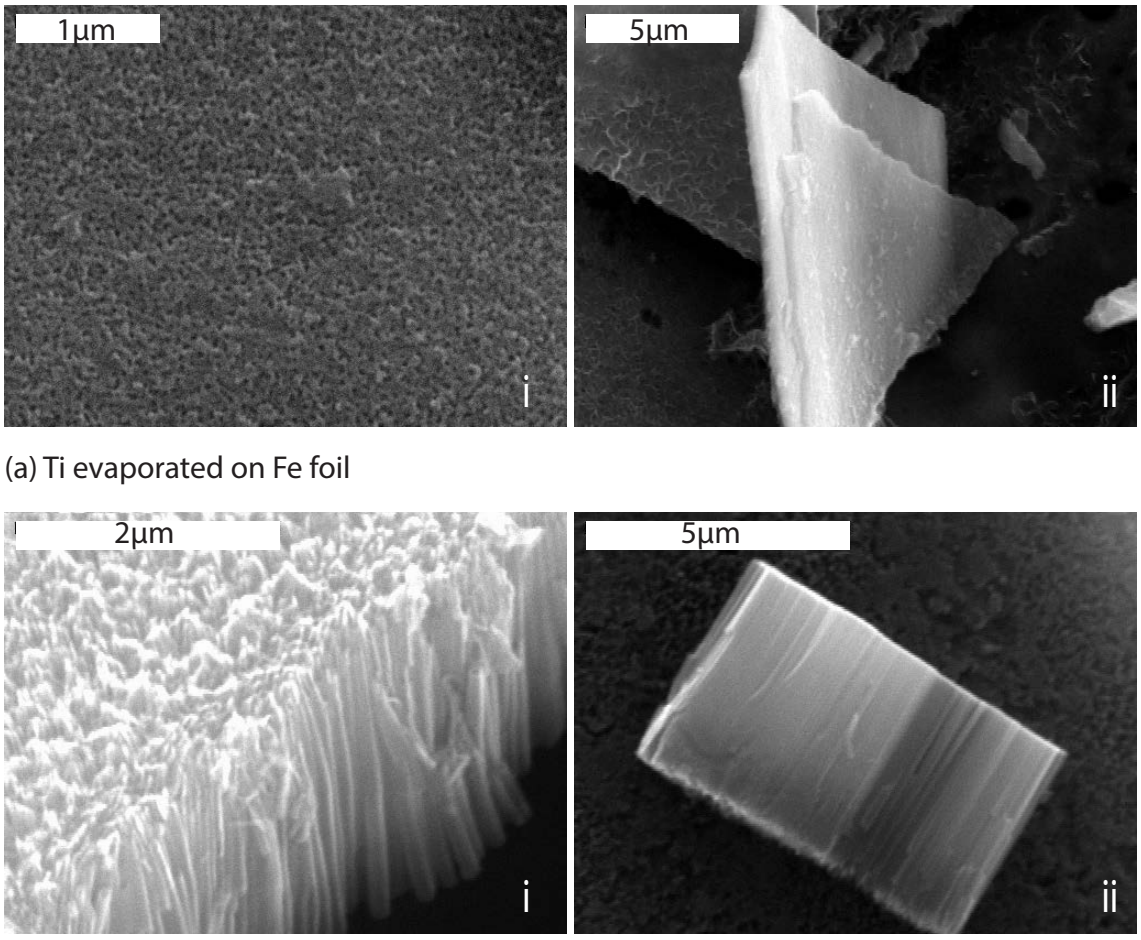

Figure 4.5: Examples of a thin film evaporated onto a substrate and anodised, (a) TiO_2 nanotubes formed using a thin film of Ti evaporated on a Fe foil with magnifications of i-×17,500 and ii-×4000, (b) Fe with Ti evaporated on a Ti foil, and nanotubes formed of the Fe-Ti-O thin film with magnifications of i-×16,250 and ii-×7000.

The TiO_2 nanotubes formed by anodisation of Ti evaporated onto a Fe substrate formed a porous structure and the tubes are masked by debris. The inner pore diameter is 33.5 nm ± 8.3 nm, the smaller diameter compared to TiO_2 nanotubes formed on a Ti plate could be a result of the increased conductivity of the iron electrode, the same potential used in the anodisation process results in a higher anodisation current and rate of dissolution. Also the low concentration of F^- ions and water reduced the lateral oxidation and dissolution process. The thickness of the Ti layer is unclear, two layers are present, each approximately 400 nm thick.

These two layers could be composed of a TiO_2 nanotube array and a Fe_2O_3 nanotube array, or two layers of TiO_2 nanotube arrays. The Ti/Fe oxide nanotubes formed on a Ti plate are more distinguishable and have an inner diameter of 44 nm ± 8 nm, an outer diameter of 73.3 nm ± 7 nm and are approximately 4.3 μm long. The electrolyte used is identical in the synthesis of both nanotube arrays.

4.4.1 Titanium and Iron stacked Thin Film on Conductive Glass

In this work I created Fe-Ti-O nanotubes on conductive glass in an identical process of forming TiO_2 nanotubes on FTO described in Chapter 4.2.1, with the addition of Fe in the deposition process. Forming the tubes on conductive glass has the same advantages as described with TiO_2 on FTO, and an additional optical absorption enhancement due to the reduction of the band gap of the nanotubes by the incorporation of iron in the nanotubular array. A problem with using FTO glass is the sensitivity of adhesion of the thin films directly after evaporation; the initial instability of the film is caused by the attack of moisture at the interface between the metal and FTO glass. The hydroxide formed is super hydrophilic whilst the metal surface is normally hydrophobic. Therefore, high interface tension exists between the FTO and metal, which is released through the peeling of the thin film from the substrate. This can be overcome by evaporating a thin film of Ti before the mixtures are evaporated. The high reactivity of freshly evaporated titanium will help in the adhesion of the thin film on the FTO glass substrate. The Ti layer is initially evaporated for one hour, followed by a Fe-Ti mixture for another hour. This process is repeated to form layered deposition of the two metals with varying Fe content in a stacking fashion. In the hope to distinguish the varying iron content along the nanotubular array using EDX elemental mapping.

Anodisation is performed in an electrochemical bath. The FTO/thin film is fitted into a substrate holder and contact is made from the top of the thin film. A 40 mins anodisation is carried out at a potentiostatic potential of 60 V using the same electrolytes used to create Fe_2O_3 nanotubes.

During the anodisation the film undergoes a variety of colour changes, from purple (1 min), silver (2 min) to yellow gold in the first 5 mins. The thin film then

becomes darker, and eventually becomes gold after going through several colour stages (maroon after 10 mins, green after 13 mins and turquoise after 15 mins, reaching gold with a dark purple layer at the bottom of the substrate after 30 mins). This is indicative of the varying wavelengths of absorption of the thin film (the complementary colour of the reflecting colour) as iron content changes through the nanotubular film. A darker film indicates a larger spectrum range of visible light absorption due to varying Fe concentration as nanotubes form, which will enhance the light harnessing properties of the material over TiO_2 alone (during TiO_2 anodisation the film turns gold from silver). The nanotubes themselves are transparent (as seen with TiO_2 nanotubes formed on FTO), so the metal oxide film layer on the thin film must be the material which undergoes the colour changes at various concentrations.

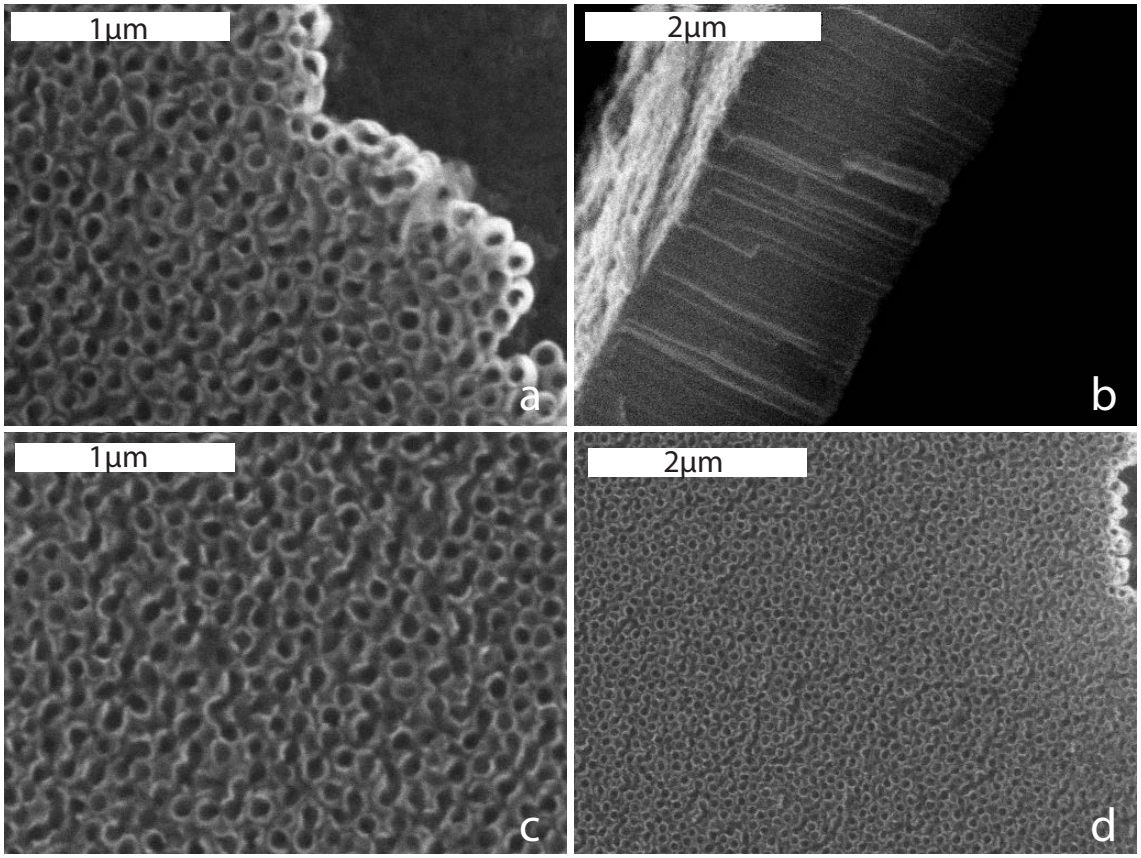

Figure 4.6: SEM micrographs of Fe-Ti-O nanotubes with 26 % Fe content on FTO substrate, with magnification of (a) ×27,500, (b) ×15,000, (c) ×27,500 and (d) ×14,000.

The mixtures were similar to the form discussed earlier, with varying thicknesses and Fe-Ti ratios. Figure 4.6(a) to (d) shows the SEM micrographs of ordered Fe-

Ti-O nanotubes with an overall 26 % Fe content synthesised on FTO glass, the associated EDX spectrum is shown in Figure 4.7.

The tubes formed have an inner diameter of 67.2 nm ± 12.5 nm, and an outer diameter of 118.8 nm ± 12.3 nm, the walls of the tubes are significantly larger (25.8 nm ± 6.2 nm) than the 10 % Fe content nanotubes formed on a Ti foil when it should be smaller with increasing Fe content. This indicates the FTO conductive glass affects the dissolution process, and conductivity of the electrochemical anodisation circuit. Generally good quality nanotubes are formed, although some of the walls of the nanotubes are fragmented, possibly due to the fast dissolution rate of iron oxide. The tubes are straight without kinks and defects with a length of approximately 2 μm (1.94 μm ± 0.04 μm).

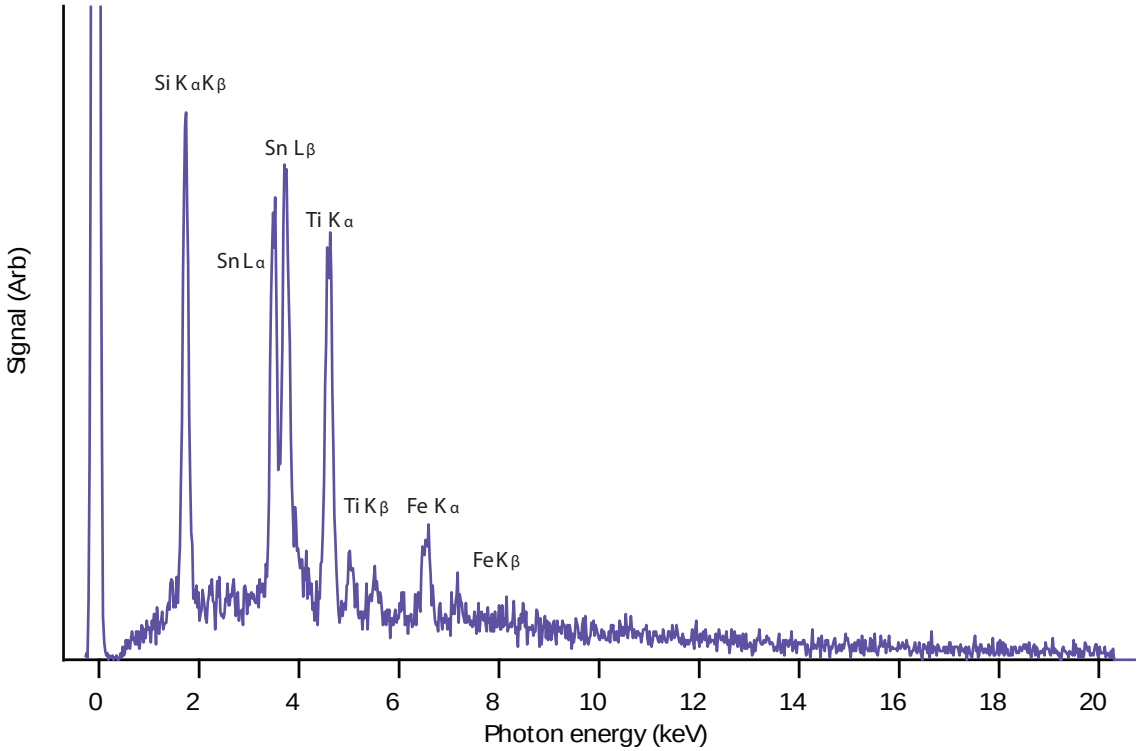

Figure 4.7: EDX spectrum of 26 % Fe content Fe-Ti-O nanotubes on FTO substrate.

In Figure 4.7, the Si signal is contributed from the glass substrate and the Sn signal originates from the FTO thin film on the glass substrate. Thus it is expected that the FTO thin film underneath the Fe-Ti-O nanotubes is maintained after performing e-beam evaporation and anodisation on the substrate. There are two Ti peaks resolvable in the spectrum, the K_α transition at 4.5 keV and the K_β at 4.93 keV. The peaks at 6.4 keV and 7 keV are contributed from the Fe K_α and K_β trans-

itions, respectively. The detector installed on our SEM is not sensitive to oxygen. Quantitative analysis shows that 26 % of Fe is present in the Fe-Ti-O nanotube film. The nanotubes formed consistently, though stacking was not clear in the elemental mapping mode of the SEM. This could be due to the sensitivity or dynamic range of the SiLi XRF detector in the X-ray range, or due to migration of the iron during anodisation.

4.5 Photoelectrochemical Analysis

The photoelectrochemical properties of the Fe-Ti-O nanotubes are analysed using a three electrode electrochemical cell discussed in chapter 3. The electrolyte solution is 1 M KOH deionised water. The reference electrode used is an Ag/AgCl electrode and a Pt foil serves as the counter electrode. In an alkaline solution, the Nernst equation (equation 2.8) is used to calculate the reversible hydrogen electrode (RHE) potential to measure optimum operating conditions, as the redox potentials of water are fixed with potential *vs* RHE.

A potential sweep from -1 V to +1 V, across the reference electrode and working electrode (photoanode), is controlled using a potentiostat. The current is measured across the platinum counter electrode and working electrode. The excitons created in the photoanode material during illumination (full beam of the xenon lamp, not filters were employed) are separated under the influence of the potential and the electron traverses the circuit reducing water on the platinum electrode surface. Meanwhile, holes created close to the surface of the photoactive material can travel into the electrolyte solution and oxidise the water generating oxygen on the surface of the photoanode.

The Fe-Ti-O nanotubes formed directly after anodisation are partly amorphous; resulting in high recombination rates under illumination. The charge mobility in the metal oxide is highly dependant on the crystal quality. High quality crystals form perfect band structure and channels for charge transport, whilst for an amorphous sample the high density of defects and their associated charge will result in exciton trapping and increased rates of recombination, thereby reducing the photoefficiency of the photoanode. In order to improve the charge mobility the crystal quality of the

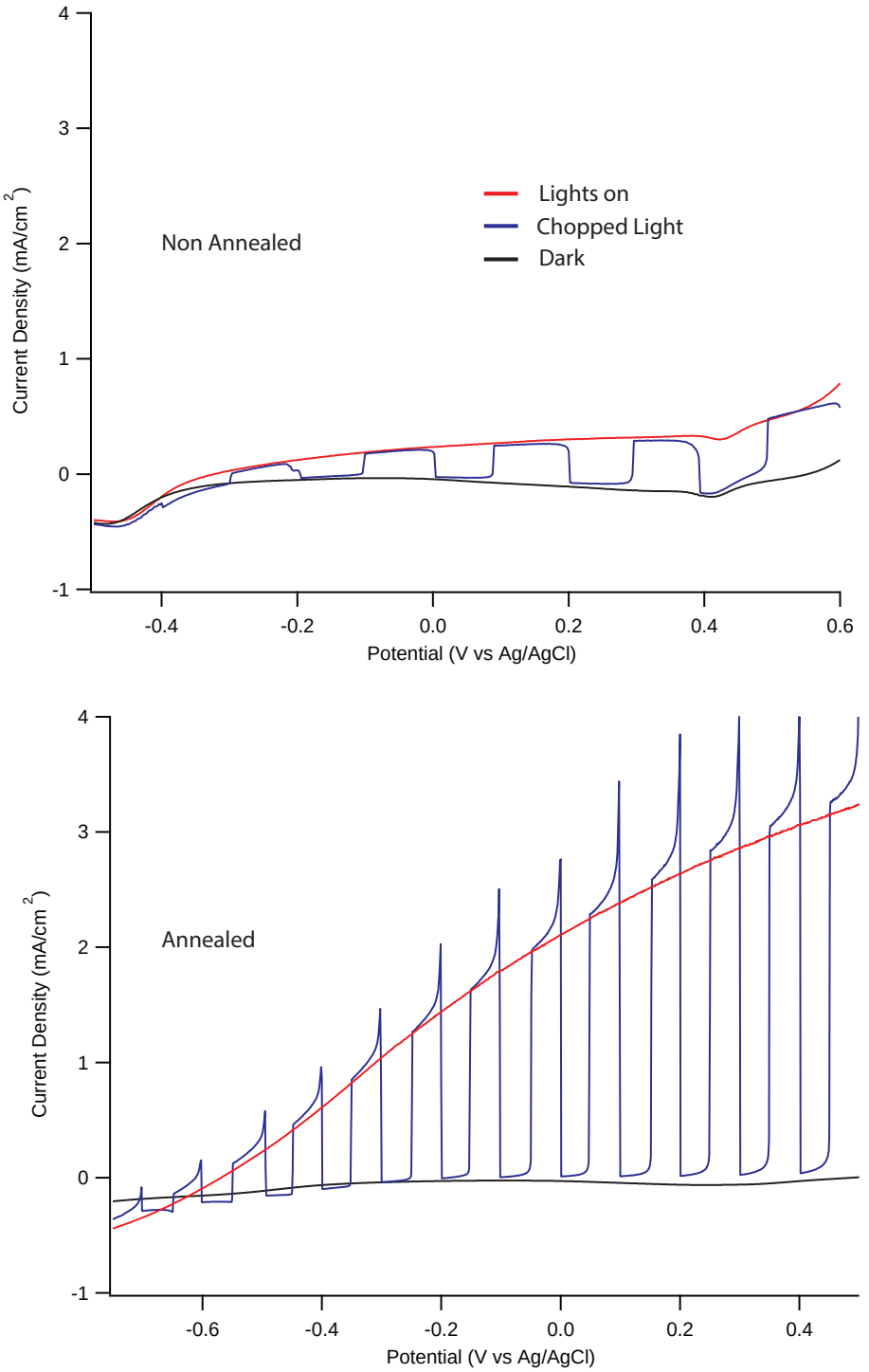

Figure 4.8: Photocurrents I-V plots of Fe-Ti-O comparing a non-annealed (amorphous) sample with the same sample annealed (higher crystallinity). The spiking and chopped light profiles are artefacts of the electronic switching of the xenon light source, rather than a property of the photoanode. The onset potential of -0.56 $V_{Ag/AgCl}$ is the equivalent of 0.43 V_{RHE}, which would be the potential required in a two electrode electrochemical cell.

nanotubes has to be improved by thermal annealing. Here, I annealed the samples in air ramping up to a temperature of 550 °C. This resulted in a dramatic increase of the crystal quality accompanied by the significant increase in the photocurrent, the effects of annealing and crystallinity were studied once the X-ray diffractometer was installed in our laboratory. Higher crystallinity results in fast pathways for electron transport. Annealing could also transforms the rutile into anatase throughout the surface of the TiO_2 nanotubes, the iron oxide into haematite or form a mixture of iron titanates through-out the nanotubular structure.

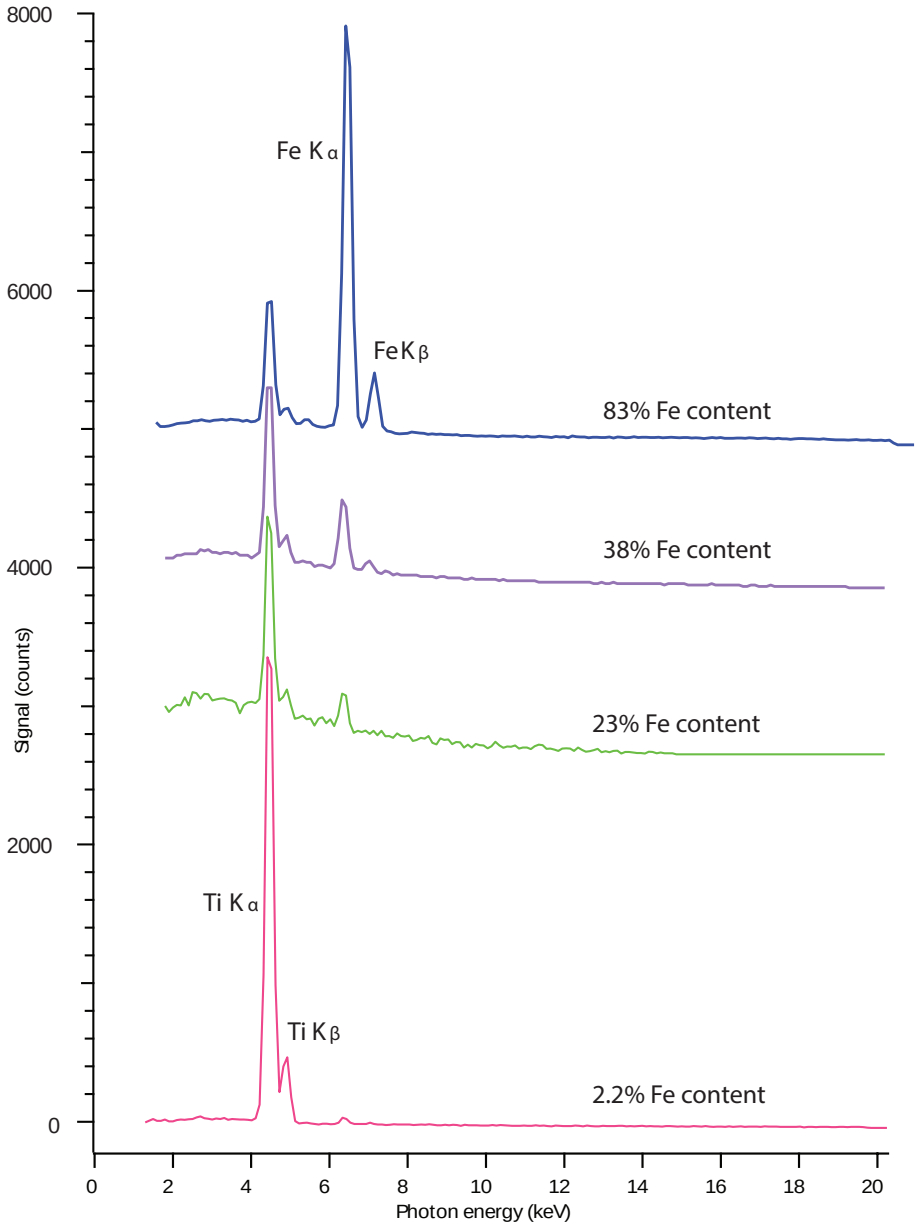

Figure 4.9: EDX spectrum of Fe-Ti-O nanotubes grown on a Ti foil with varying Fe content.

In an amorphous material, there are many more opportunities for charge carriers to scatter and recombine; the diffusion length of the electron will be very limited. In an ordered structure, the electron has a greater chance of travelling further without scattering thereby allowing a more effective separation of the charge carrier (e^- & h^+). Figure 4.8 shows the significant difference in quality of the photoanode depending on whether the material is annealed or not. Annealed samples achieve a much greater photocurrent density. For comparison, a mobile phone battery outputs on average a current of 120 mA, this could be provided by a watersplitting module with a photoanode area of 6 cm by 10 cm ($\frac{120mA}{2mA/cm^2}$) under illumination and a bias of 1.025 V_{RHE}.

The chemical composition of the Fe-Ti-O nanotubes was determined using EDX analysis. The EDX spectra are shown in Figure 4.9, and the varying content of Fe and Ti relative to one and another is clearly resolved, quantitative analysis of the spectra determined the relative concentrations of Fe and Ti. The samples were photoelectrochemically tested, Figure 4.10 shows the photocurrent densities of 5 samples examined with various concentrations of Fe. Inset are the photopower density curves of each of the materials.

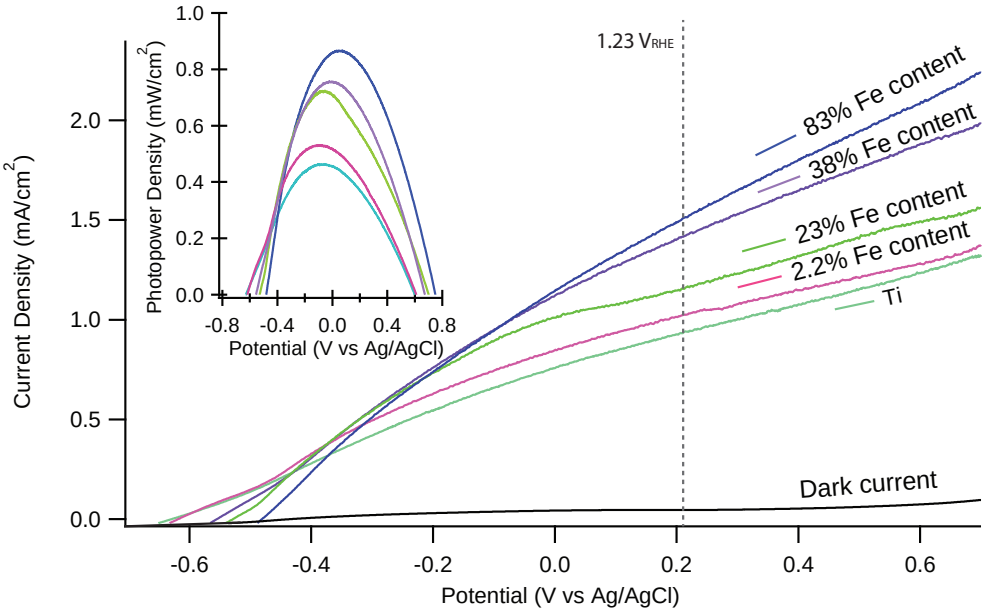

Figure 4.10: Photocurrents I-V plots of Fe-Ti-O nanotubes grown on a Ti foil of varying Fe content. Inset are the photopower density curves for these materials.

The onset potential increases with iron content, this could be a consequence of the band structure alteration of the iron titanate nanotubes. Lowering the band

Iron content	P_{max} (mW/cm^2)	$I_{1.23V_{RHE}}$ (mA/cm^2)	$V_{0_{mA/cm^2}}$ ($V_{Ag/AgCl}$)	V_{onset} (V_{RHE})
0 %	0.463	0.952	-0.63	0.394
2.20 %	0.531	1.019	-0.619	0.405
23 %	0.724	1.152	-0.529	0.495
38 %	0.757	1.411	-0.556	0.468
83 %	0.867	1.499	-0.48	0.544

Table 4.2: Photoelectrochemical data for various compositions of Fe-Ti-O nanotubes. Potentials are measured *vs* Ag/AgCl unless stated otherwise.

edges with respect to the redox potential. This would consequently require a higher potential for an upward bending of the band to occur close to the surface of the photoanode. Also, if the conduction band is below the reduction potential, extra energy is required for the electron to facilitate the hydrogen evolution reaction.

Onset potential can also increase if there is an increase of hole accumulation close to the nanotube/electrolyte interface due to the structural and electronic properties of the Fe-Ti-O nanotubular structure as well as defects.

The $FeTiO_3$ CBM position is 0.2 V_{RHE} below the proton reduction potential (0 V_{RHE}), yet Fe_2TiO_5 is significantly lower at 0.6 V_{RHE}. Iron oxide has a CBM position of 0.4 V_{RHE}, and titanium dioxide is the most favourable at -0.1 V_{RHE}, 0.1 V above the proton reduction potential, these positions are shown in Figure 1.9.

Another possibility is that titanium dioxide and iron oxide form independently throughout the nanotubular structure and the titania conduction band remains above the proton reduction potential. A charge injection process could provide the titania conduction band with electrons excited from iron oxide, a bias then assists in the flow of the charge carrier to complete the electrical circuit.

Figure 4.10 shows a comparison of current-voltage behaviour of the various Fe-Ti-O nanotubes investigated, and Figure 4.11 shows the respective maximum photopower output densities for varying composition. For Pure TiO_2 nanotubes the output photopower density is 0.46 mW/cm^2, which is the lowest value amongst the samples, and with a small amount of elemental Fe present in the nanotubular array structure the power output density increases by 15 %. With almost a quarter of Fe

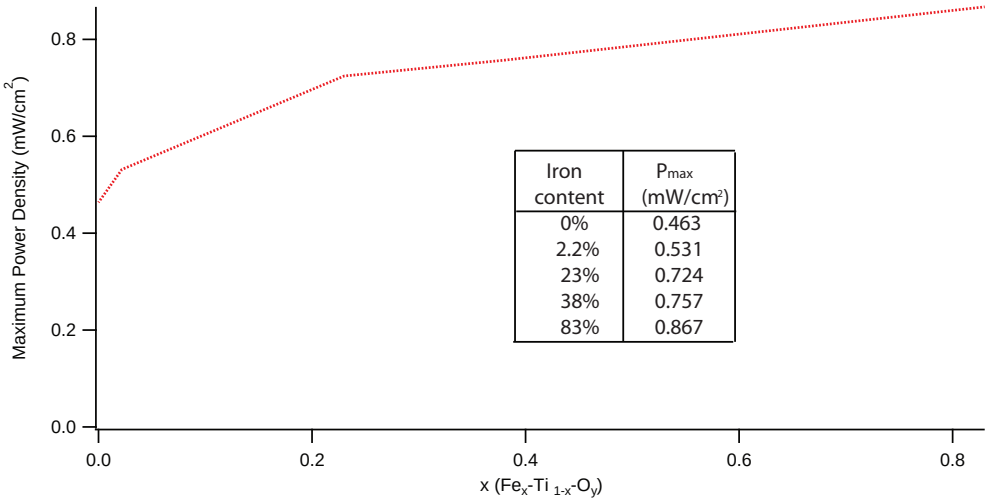

Figure 4.11: Maximum photopower density of Fe-Ti-O nanotubes with varying content of iron.

present in the Fe-Ti-O nanotubes, the maximum power density has nearly doubled to 0.72 mW/cm^2, and with 38 % Fe content the power output density is almost the same with a value of 0.76 mW/cm^2. The best power density output produced with a photoanode is a photoanode of a composition consisting mostly of iron, 83 % Fe content shows double the photo power density output (0.87 mW/cm^2) compared to pure titania nanotubes. The increase in photocurrent and power density is attributed to engineering of the band gap of the material. The band gap decreases with increasing Fe content in the Fe-Ti-O structure and the value of the band gap saturates once the concentration of Fe content reaches 50 %.[214] The band gap will approach that of Fe_2O_3 as more Fe is incorporated into the nanotubular array (2.2 eV is well within the visible range). Allowing a much larger portion of the spectrum of the xenon light source to be utilised into the photoelectrochemical conversion of water into hydrogen.

4.6 Conclusion

In this work, I have demonstrated the ability to control the 3D architecture of iron-titanium-oxide composite nanotubes. Physical vapour deposition by electron beam evaporation proved effective in creating thin films of titanium and iron with varying concentrations. These thin films were anodised to form a highly ordered nanotube array, which demonstrated improved photocurrents and photoefficiencies through

the engineering of the band gaps of the nanotubular array photoanode. Increasing iron content in the composite nanotubes reduced the band gap, whilst the band edges of the material remained in favourable positions with respect to the redox couple potentials.

The e-beam evaporator constructed herein can be utilised further to create a multi layered semiconducting black leaf structure. For which UV wavelengths are absorbed closer to the light source and the wavelengths being absorbed widen along the length of the tubes, allowing visible light to be absorbed close to the roots of the nanotubular array.

Chapter 5

Zinc Oxide Nanostructures formed by Vapour Transport Processing

Zinc oxide is a wide direct band gap semiconductor; the band gap is 3.3 eV and is comparable to that of TiO_2. However, ZnO tends to have a higher conductivity than TiO_2. The wurtzite crystal structure of ZnO has noncentrical symmetry and high energy polar surfaces. The hexagonal crystal structure promotes higher electron mobility in crystalline samples of ZnO. The crystal structure is illustrated in Figure 3.11 with associated miller indices of directions and planes of the wurtzite crystal structure. The possibility of creating high quality large bulk single crystals with favourable electronic and optical properties has revived interest in ZnO as a semiconductor. The electron mobility of ZnO is high at 200 cm^2/Vs with a low effective mass (0.24 m_e).[215,216]

1D ZnO nanostructures are the most commonly synthesised ZnO structures. The natural crystal dynamics of growth assists in the preferential growth in one direction, creating nanorods,[217,218] and nanowires.[115] A fast growth rate in the [0001] direction of the wurtzite structure is due to high energy polar surfaces on this face, where the precursor preferably adsorbs to this high energy surface. There is also relatively fast growth along the lateral faces, but not as much as they are lower energy non polar faces. With high Zn vapour partial pressures growth in the c-axis and the lateral faces balance to form rods.[219]

ZnO can be utilised in a variety of applications making it a highly attractive semiconductor to research. The exceptional electrical and optical properties, as

well as the self-forming crystal dynamics means ZnO is advantageous as a semiconductor material. ZnO nanorods and nanowires are relatively easy to produce, and have good charge carrier transport properties and high crystalline quality which open up possibilities of utilising ZnO in gas sensing applications[220–222] and field effect transistors (FETs).[223] The tetrahedrally bonded oxygen atoms and zinc atoms which forms a ZnO crystal, results in a non-centrosymmetric structure, such that the crystal undergoes a lattice distortion under applied pressure, resulting in local dipole moments. This piezoelectric property and the large electromechanical coupling properties of ZnO make it an attractive material in the design of piezoelectric generators. The piezoelectric effect can be enhanced by controlling the nanostructure morphology, i.e. nanobelts demonstrate large piezoelectric coefficients.[224] The optoelectronic properties of ZnO make it a promising photosensitive material, which can be applied to dye sensitised solar cells.[225] Altering the structure can enhance the photosensitivity; by reducing the band gap or creating heterostructures capable of enhanced optoelectronic properties. For example, doping ZnO with nitrogen,[226] QD sensitisation of ZnO structures[227] or creating a CIGS/ZnO heterostructure.[25] These examples either engineer the band gap to enhance absorption or create electronically favourable situations. In this work I demonstrate a ZnO-Zn_2TiO_4-TiO_2 heterostructure enhances the electronic properties at the interface of the junctions, which improves charge transport in the photoelectrochemical cell.

P-type ZnO is notoriously difficult to synthesise but recent reports have suggested doping ZnO with Sn to achieve this feat.[228] The p-n ZnO material has been utilised in the construction of solid-state p-n-junction nanolasers.[229,230] A p-n junction ZnO structure created in one step will have far reaching possibilities, especially in the advancement of ZnO self-driven devices. The electric field associated with the p-n junction will separate excitons close to the junctions, which in turn can drive the water splitting reaction.

5.1 Vapour Transport Nanostructure Synthesis

To reiterate synthetic methods, VLS (vapour liquid solid) occurs when a eutectic alloy liquid droplet forms and provides site specific nucleation sites. ZnO nucleates

at these sites and grows following the supersaturation of the liquid droplet with the Zn vapour, incremental nanowire growth proceeds thereafter pushing the seed upward (the seed remains at the top of the nanowire).

VS (Vapour solid) is similar to that of VLS, with the exclusion of liquid seed catalytic growth sites. Instead, a self-catalysing process occurs on the surface of the substrate,[231,232] or a solid seed serves as a nucleation site. The choice of seed and the temperature of the seed determines which reaction is driving the growth process.

In the VLS method, the growth temperature has to be higher than the melting point of the eutectic seed. Whilst for the VS method, the growth temperatures can be lower.

5.1.1 Carbothermal ZnO decomposition

Vapour transport synthesis of decomposed ZnO is conducted in a quartz tube inserted inside a horizontal tube furnace (Eurotherm) the setup is shown diagrammatically in Figure 3.9 in chapter 3. High temperatures are required for the reductive decomposition of ZnO (∼2000 °C), the presence of graphite reduces the decomposition temperature to approximately 1000 °C *via* a carbothermic reaction route shown in equation 5.1. The Zn vapour and residual oxygen later react to form ZnO crystals. Graphite reduces ZnO into Zn, which has a low melting point (m.p. ∼420 °C) and the reactor temperature is higher than the boiling point of Zn (b.p. 907 °C). Thus, the Zn immediately forms vapour and is carried by the Ar gas with flow rates between 100 to 200 standard cubic centimetres per minute (SCCM) (the reactor is initially evacuated to 1.10^{-3} mbar). The growth rate is determined by the reductive decomposition reaction. The growth temperature dictates the vapour partial pressures of the Zn vapour and O_2 and accordingly changes the morphology of the zinc oxide structures grown.[233,234]

$$2\,\mathrm{ZnO} + \mathrm{C} \rightarrow 2\,\mathrm{Zn} + \mathrm{CO_2} \tag{5.1}$$

In order to investigate the effects of seeding on morphology of the nanostructures, I used VLS and VS methods with Zn generated by reduction of ZnO with graphite. I chose Au (Figure 5.1), Al_2O_3 (Figure 5.2), and TiO_2 (Figure 5.3) nanoparticles as

seeds deposited on a Si substrate. Most of these seeds are inert and stable at high temperatures, the only difference is that gold is a metallic non-polar seed, whilst metal oxides are polar for certain crystal faces.

Gold is frequently used as a seed in literature and is easy to deposit.[235] A gold sputterer is composed of an evacuated chamber filled with Ar and a gold target that is negatively biased by 5 kV, which will discharge the Ar gas and form a plasma and Ar^+ ions in the chamber. The positively charged Ar cation bombards the negatively charged gold target, releasing Au clusters from the surface of the target. The Au clusters generated will then be deposited onto the substrate.

Spin coating of TiO_2 is conducted on a Si wafer, the spin solution consisted of 5 % wt TTIP (titanium tetra isopropoxide is purchased from Sigma-Aldrich CAS-546-68-9) and 7 % wt PVA (polyvinyl alcohol is purchased from Sigma-Aldrich CAS-9003-20-7) in deionised water. PVA is added to the solution to increase viscosity and achieve faster spin rates (800 RPM). Ti compounds are extremely sensitive to moisture and a slow spin rate could cause an inhomogeneous coating. The coated Si is heated to 500 °C to thermally oxidise the titanium compound, achieving nanoparticle seeding (50-200 nm) homogenously coating the surface of the Si wafer.

Aluminium oxide seeding is achieved *via* dip coating a Si wafer in a 0.5 M solution of $Al(NO_3)_3$ (aluminium nitrate is purchased from Sigma-Aldrich CAS-7784-27-2) in deionised water, and annealed at 450 °C for 30 mins to form alumina.

Si wafers are used as substrates as they can withstand the high temperatures required and do not deform, Si has a melting point of 1,414 °C. The size of the particulate seeding is critical for lower temperatures as the size can dictate the melting temperature of the seed. The seed should also be a good catalyst for growth as a nucleation site. The gold nanoparticles are liquid by the time 1000 °C has been reached. The liquid undergoes supersaturation by the Zn vapour and precipitates solid ZnO crystals, condensing into ZnO rods if VLS is the driving mechanism. If the Zn/seed alloy remains solid at reaction temperatures, a VS mechanism takes place and oxidation of Zn on the solid nucleation sites initiates a ZnO seed and the formation of ZnO structures.

The reaction conditions are as follows, the ZnO and graphite powders are finely mixed with a pestle and mortar and placed in an alumina crucible. The crucible is

placed in the centre of a quartz reactor positioned inside a horizontal furnace, the reactor is evacuated to 1.10^{-3} mbar and Ar is introduced with a flow rate of 100 SCCM. The samples are placed 5-8 cm from the centre of the furnace and a heating ramp rate of 50 °C/min is maintained until 1050 °C is reached, and the reaction takes place for one hour.

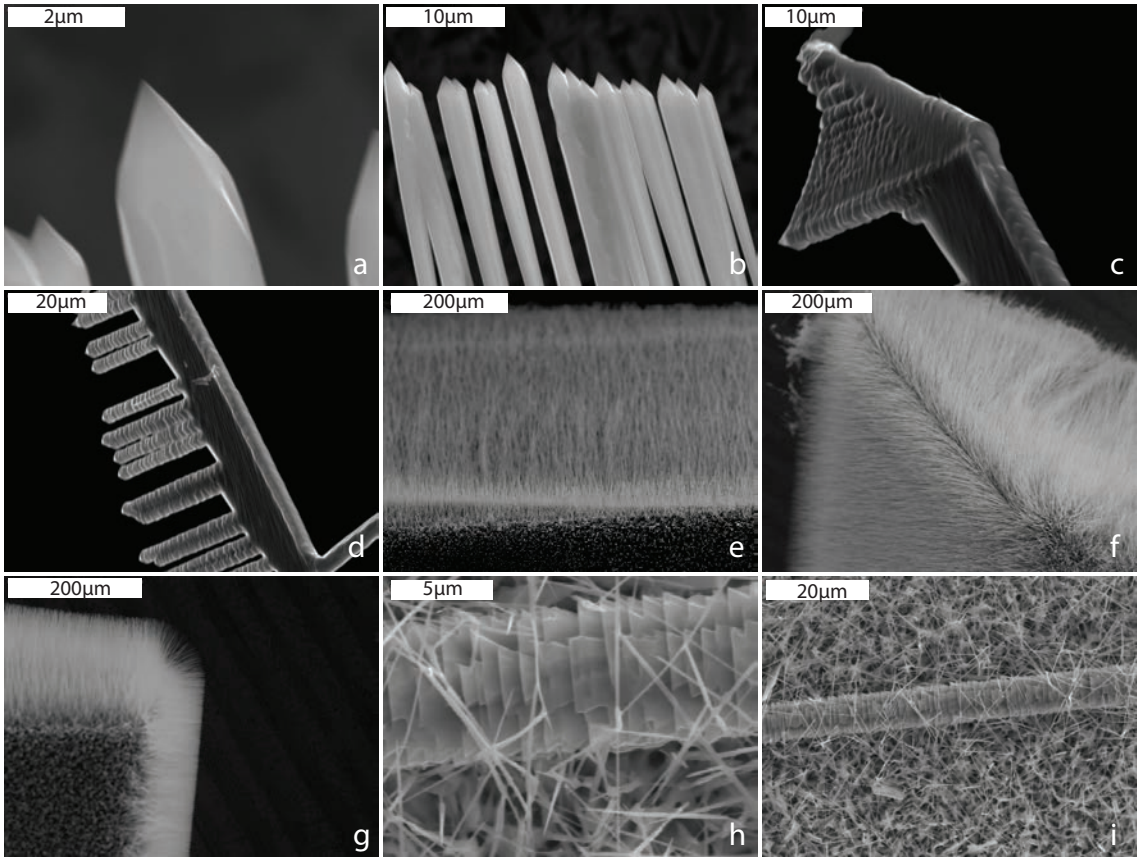

Figure 5.1: SEM micrographs of ZnO structures grown *via* a vapour transport reaction (1050 °C) on a sputter coated Au seeded Si wafer substrate. (a) and (b) show the ZnO nanorods formed at the edges of the Si substrate, with sharp terminated ends and organised growth at ×7,500 and ×1,500 magnifications. (c) and (d) show some of the larger structures formed on the Si wafer, where accelerated growth has formed combs with features greater than 10 μm. (e) to (g) show the ordered array of nanorods at low magnifications (×75 to ×100) to illustrate the density of the forest of ZnO nanorods. (h) and (i) shows a unique sheet like formation of ZnO (×2000 and ×750 respectively).

Figure 5.1(a) to (i) shows a few examples of the ZnO structures formed on a gold seeded Si wafer, the rods formed have a large diameter of 1.55 μm ± 0.28 μm and are highly ordered. The sharp tip seen in Figure 5.1(a) and (b) show the tip to be terminated at an angle of 30°, exposing the $\{01\bar{1}2\}$ set of planes. Figure 5.1d shows a large ZnO comb, the teeth are hexagonally formed in layers orientated in the

[0001] direction. The length of the teeth are 17.7 μm $\pm$ 1.336 μm with a diameter of 2.55 μm $\pm$ 0.3 μm. The base of the comb is a planar lateral surface of ZnO which is 7.67 μm $\pm$ 0.8 μm wide. The lengths of the rods/whiskers measured in Figure 5.1(g), is 71.79 μm $\pm$ 11.3 μm. The growth is very organised in Figure 5.1(a) to (g), and the Au liquid seed and Zn vapour likely underwent supersaturation at these temperatures, though it is not clear whether gold is present at the top of the structures. It is uncertain whether the reaction underwent a VLS or VS process. Figure 5.1(h) and (i) show connective growth between the long whiskers of ZnO, forming tripod morphologies. These morphologies were present at the edge of the sample and could possibly be due to sparse seeding on these areas.

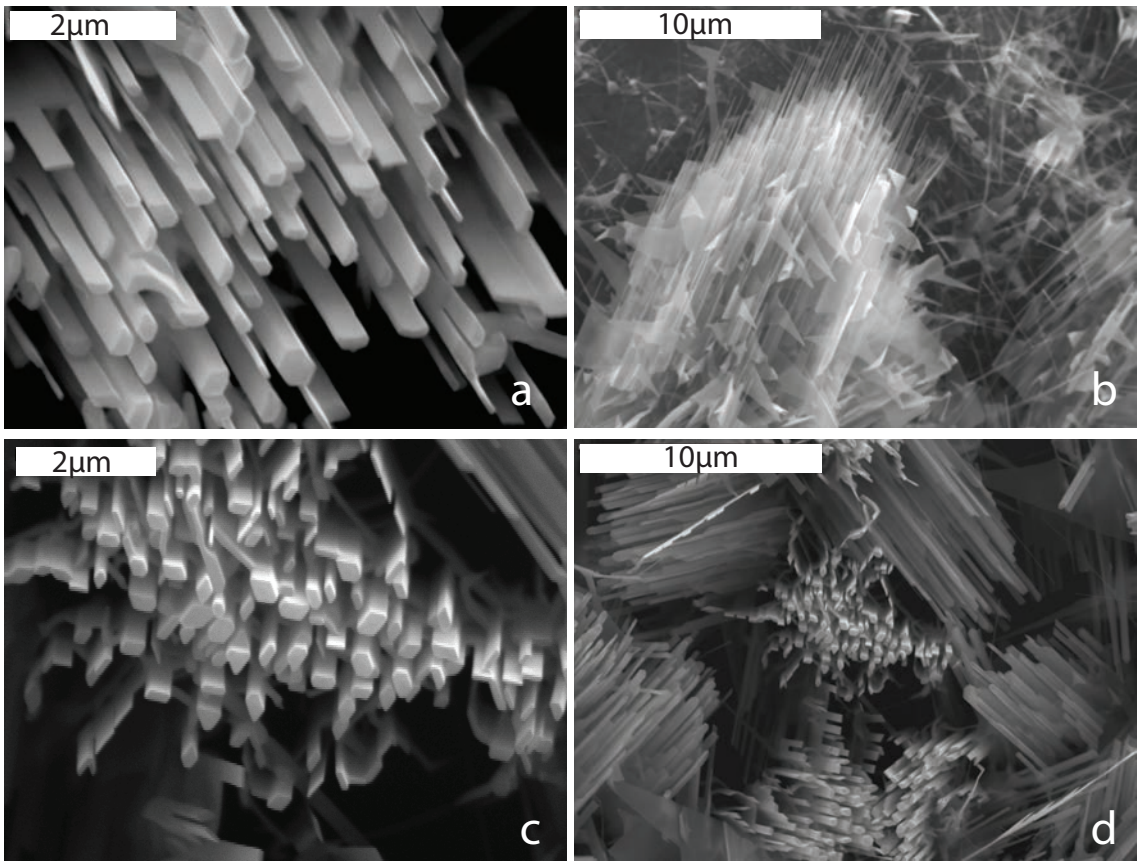

Figure 5.2: SEM micrographs of ZnO structures grown *via* vapour transport deposition of alumina seeded Si wafer substrates. (a) shows a high magnification (×11,000) SEM micrograph of the bunched ZnO rods formed at an angle to the surface, whilst (b) shows large bunched rods formed laterally on the surface (×3,000). (c) shows a top down view of the rectangular ZnO rod array (×9,000), illustrating the varying dimensions of the rectangular rods. (d) is a low magnification (×3000) micrograph of a selected area of the substrate.

Figure 5.2(a) to (d) shows SEM micrographs at various magnifications, of bunching of rectangular ZnO rods on an Al_2O_3 seeded Si substrate. The rods lay on the surface rather than precipitate between the substrate and seed. The aluminium oxide seed provides nucleation sites on the surface of the alumina particle, by taking into consideration the high melting point of alumina it is likely the ZnO condensed on the surface rather than supersaturating a liquid seed and precipitating solid ZnO. The ZnO structure have an average width of 286 nm ± 35.5 nm and a length of 9.5 μm, which is significantly smaller than the gold seeded Si. The bunching could be possibly due to the lattice structure of aluminium oxide. The Zn vapour condenses in epitaxially favourable lattice positions on the alumina rectangular lattice, gradually forming multiple rectangular rods. The Sapphire (Al_2O_3) c-axis and ZnO a-axis have almost no lattice mismatch ($4[01\bar{1}0]_{ZnO}$ = 12.996 Å & $[0001]_{Al_2O_3}$ = 12.99 Å), so the ZnO preferably adsorbs to the lattice in this orientation growing along the c-axis. Restrained by the rectangular lattice of the $(11\bar{2}0)_{Al_2O_3}$ plane, the ZnO rods form in a rectangular tilted ZnO form dominated by the initial lattice strain determined by the alumina.[236]

Similar structures are observed in the literature, in an Al doped ZnO vapour solid reaction, where Zn and Al powder are alloyed under high pressure and temperature and then serve as the vapour source for the reaction. It was demonstrated a rectangular array of ZnO rods form, synthesised in the c-axis on a Si substrate, with the side facets of the rods belonging to the $(2\bar{1}\bar{1}0)$ and $(10\bar{1}0)$ planes.[237] The varying rectangular dimensions were explained by the formation of an initial ZnO belt in the $[01\bar{1}0]$ direction with periodic thickness due to Al redistribution, followed by rodular growth along the c-axis out of the sheets to form a rectangular array of ZnO rods. In our case, there is two dimensional growth in the $[01\bar{1}0]$ and $[2\bar{1}\bar{1}0]$ directions, followed by c-axis growth of rectangular rods.

Figure 5.3 shows SEM micrographs of vapour transport deposition of ZnO on a TiO_2 nanoparticle seeded silicon wafer. The temperature of the substrate was controlled to be approximately 700 °C; controlling the substrate temperature can alter the condensation rate and growth rate. Here I investigate the influence of growth rate on the crystal morphology and explore the possibility of developing a variety of structures in order to optimise for different applications. Dendritic

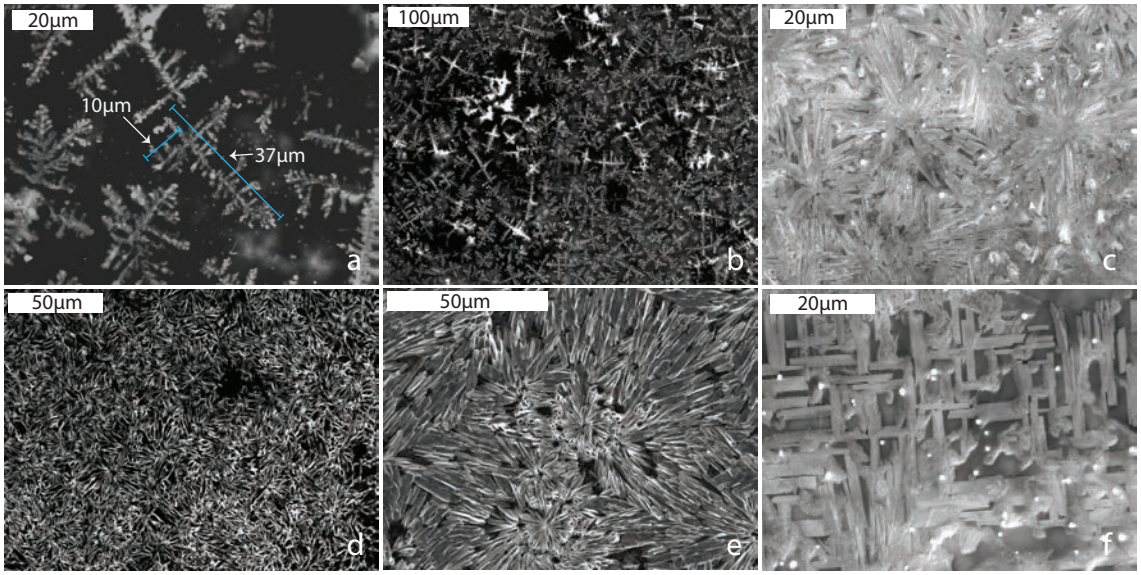

Figure 5.3: SEM micrograph of ZnO structures grown *via* VLS with a spin coated TiO_2 seeded Si wafer substrate. (a) and (b) are SEM micrographs of structures formed in the low temperature zone (×400 and ×100 magnification respectively), and (c)-f) are formed in the high temperature zone, with low magnifications (c) ×500, (d) ×250 (e) ×400 and (f) ×750.

structures form across the surface of the substrate when growth rate is restricted and Zn vapour solidifies rapidly on the surface at a low flow rate, with low seeding density; shown in Figure 5.3 (a) & (b). The dendrimer shapes have a unique 90 degree symmetry. In other words the features may be either folded or rotated by 90 degrees. This is indicative of growth along the $(\bar{2}110)$, $(2\bar{1}\bar{1}0)$, $(0\bar{1}10)$ and $(01\bar{1}0)$ faces, and exposing the top of the structure with the (0001) face with limited vertical growth. The dimensions of the dentritic ZnO structures range from 500 nm to 40 μm, one of the structures is labelled in Figure 5.3(a). The TiO_2 seeding density dictates the density of ZnO structures formed, with sparse seeding, limited nucleation sites dictate the initial growth and interconnecting ZnO structures. Figure 5.3 (c)-(f) are SEM micrographs of ZnO webbed nanobelt/flower mats formed in the hot zone of the furnace on TiO_2 seeded silicon. The substrate is at a temperature of 1050 °C and zinc vapour attaches to the TiO_2 nanoparticulate surfaces and undergoes self-catalysing condensation after initiating growth on the lateral crystal faces forming horizontal belts with an average length of 7.35 μm ± 1.5 μm and a width of 858 nm ± 200 nm. The coverage of TiO_2 is a factor in the morphology of the ZnO webbed mats. Figure 5.3(d) shows a dense forest of horizontal belts formed on a dense seeding layer and with high growth rates, while magnified portions are

shown in the SEM micrographs in Figure 5.3(e) and (f). ZnO grown *via* chemical bath deposition have shown similar morphology where lateral growth is dominant compared to the [0001] direction,[238] in which lowered concentrations of zinc acetate and Hexamethylenetetramine were used during the chemical bath growth process.

5.1.2 Direct Zn Powder Evaporation

Here, I demonstrate the formation of ZnO nanorods through direct Zn evaporation of pure Zn powder. This has the advantage of requiring lower temperatures (450 °C and above) than is needed to decompose ZnO/graphite into Zn vapour. This opens up the possibility for a greater choice of substrates which can be used in the reaction. More importantly, it opens up a wider window of experimental temperatures and better control of the growth dynamics. To investigate the effect of seeding and substrate on the growth process of ZnO, vapour transport deposition was conducted on Si with three types of seeds, shown in Figure 5.4, and on three different substrates, shown in Figure 5.5.

In this experimental work, 1 g of Zn powder (purchased from Sigma-Aldrich CAS 7440-66-6) is placed in a porous alumina boat and the substrates placed over the Zn powder. The alumina boat is placed into the centre of the quartz reactor within a horizontal furnace. The quartz reactor is evacuated using a rotary pump and Ar with varying flow rates is introduced into the reactor. The temperature was raised by 50 °C/min up to 650 °C, and this temperature was maintained for 20 mins. All experiments are conducted in this fashion, with Ar flow rate ranging from 50 SCCM to 1000 SCCM depending on the ZnO structure desired. The Ar gas carries oxygen from the environment into the reactor.

Figure 5.4(a) shows SEM micrographs of a direct Zn vapour transport deposition of ZnO on a bare Si surface with a flow rate of 80 SCCM, i shows a high magnification portions, whilst ii-iii show the low magnification SEM micrographs of the substrate, illustrating the ZnO rod density on the surface . The diameter of the ZnO rods are 426 nm ± 58 nm, with a length of 5.145 μm ± 0.76 μm.

During the same reaction, a gold seeded silicon wafer produced very similar rodular structures with larger lengths. Figure 5.4(b) i and ii show high magnification SEM micrographs of the rods created and iii shows the coverage of the rods on the

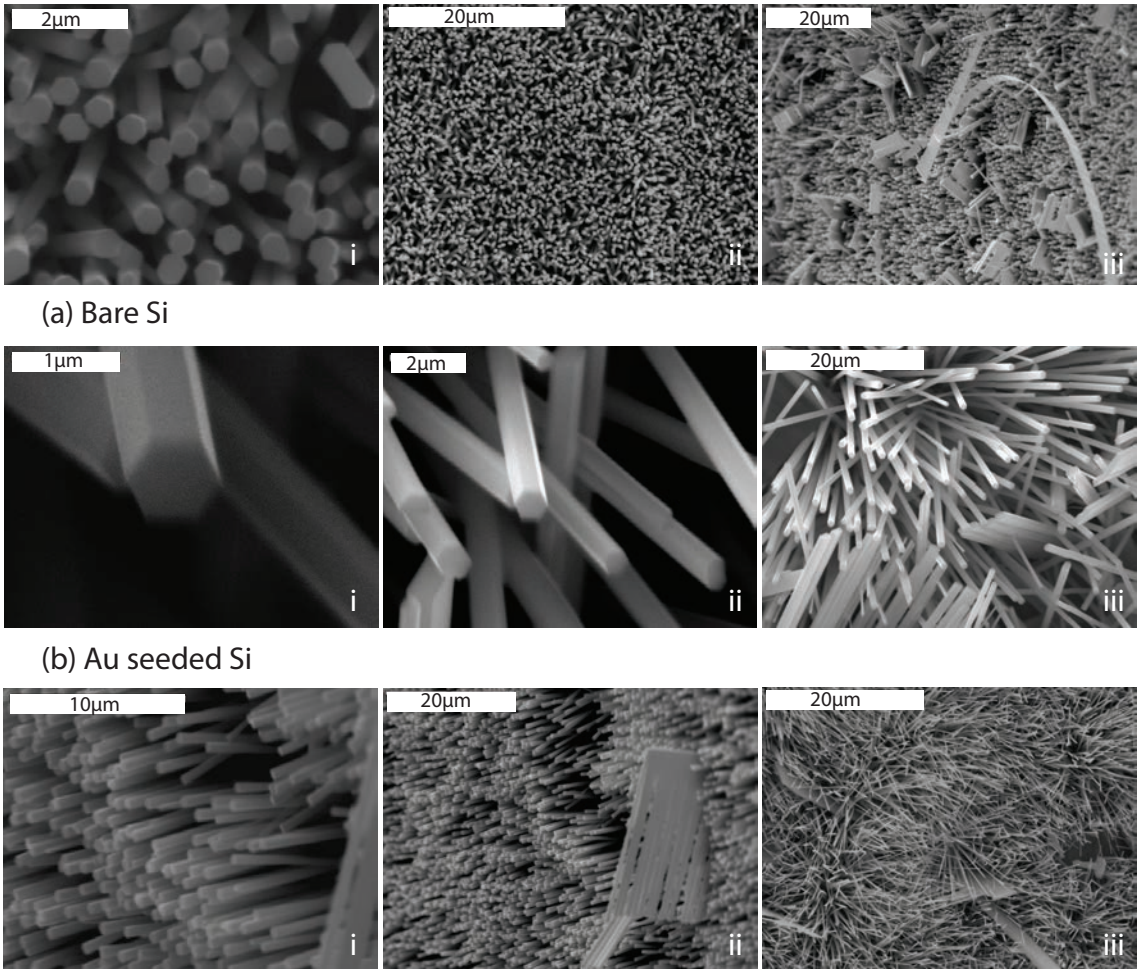

Figure 5.4: SEM micrograph of ZnO rods grown *via* a vapour transport reaction on a bare (a) i-×7,500, ii-×1,125, iii-×625, Au (b)i-×15,000, ii-×5,000, iii-×1000, and ZnO (c)i-×2,200, ii-×850, iii-×1000 seeded Si wafer substrate.

substrate, with a diameter of 810 nm ± 123 nm and a length of 22.81 μm ± 1.5 μm.

Figure 5.4(c) i to iii shows SEM micrographs of ZnO rods grown on ZnO seeded Si at different magnifications, with a smaller diameter (426 nm ± 58 nm) and a longer length (31.76 μm ± 2.9 μm) than the ZnO nanorods formed on a gold seeded silicon wafer. The increase in aspect ratio could possibly be due to the size of the initial ZnO seed, and the diameter could be restricted by the size of the seed. Thus, growth along the length of the rod is enhanced due to the lateral restriction. In all cases the growth is directed in the c-axis, exposing the (0001) face on the top of the rod and the $\pm(01\bar{1}0)$, $\pm$ $(10\bar{1}0)$ and $\pm(1\bar{1}00)$ planes on the sides of the rods. The hexagonal shape of the ZnO rods is evident in the SEM micrographs.

Three substrates are placed in the quartz reactor, and ZnO rods are grown under

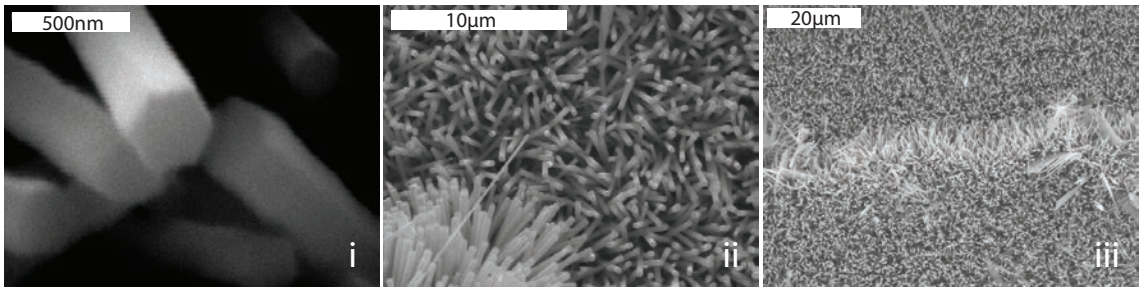

(a) Zr substrate

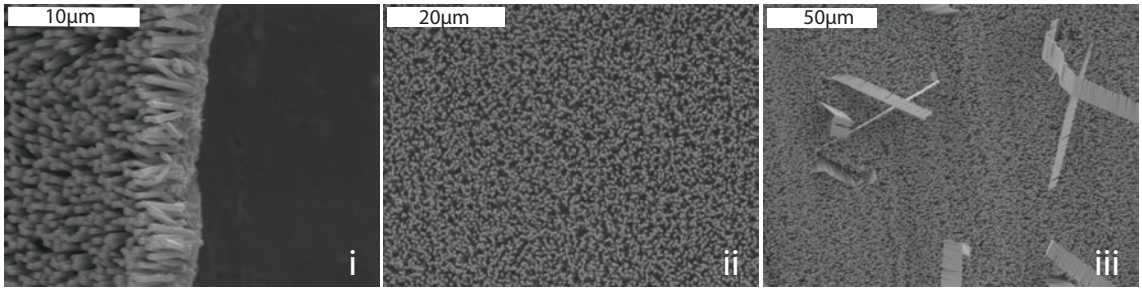

(b) Ni substrate

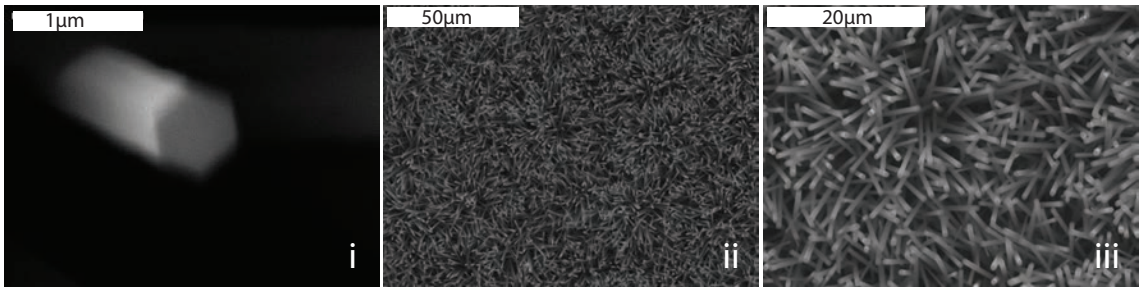

(c) Fe substrate

Figure 5.5: SEM micrograph of ZnO rods grown *via* a vapour transport reaction on a Zr substrate (a)i-×30,000, ii-×2,200, iii-×600, Ni substrate (b)i-×2,000 ii-×750, iii-×300, and Fe substrate (c)i-×15,000, ii-×350, iii-×1000.

a vapour transport reaction under identical conditions as the seeded substrates. In Figure 5.5(a) ZnO rods formed on a zirconium substrate were the longest of the rods formed in the reaction, having a diameter of 288 nm ± 43 nm and length of 11.18 μm ± 1.6 μm. ZnO grown on a nickel substrate were larger in diameter (431 nm ± 43 nm), but under a third the length (3.83 μm ± 0.08 μm) of the rods formed on Zr; a cross section of the array of ZnO rods can be seen in Figure 5.5(b) i. At lower magnifications, ii to iii, the ordered ZnO rodular array is densely spread across the substrate. The Ni substrate may form an oxide layer by thermal oxidation during the temperature ramp, NiO has been shown to have good catalytic properties for

the growth of well aligned nanowires[239] with similar dimensions to the structures reported here.

The ZnO condensation on an Fe substrate formed ZnO rods with a diameter of 675 nm ± 93 nm and length of 9.014 μm ± 1.34 μm, shown in Figure 5.5c i to iii at different magnifications. The rods have a larger diameter than the other ZnO rods formed on the Zr and Ni substrates under the same conditions, which could possibly be due to the higher reactivity of Fe. It is also possible that Fe_2O_3 formed on the surface of the Fe foil by thermal oxidation and the Fe_2O_3 layer catalysed the ZnO vapour condensation reaction more effectively. It has been suggested ZnO can undergo VLS reaction routes catalysed by a liquid Fe_2O_3/Si nanoparticle alloy.[240]

It has been shown that ZnO rods form on a variety of substrates and seeds with similar morphology. The dimensions do not vary much between one and another, indicating seed and substrate do not contribute to the growth process after growth is initiated. ZnO rods with a hexagonal morphology has formed on all of the samples. The ZnO growth through the condensation of Zn vapour, produced by the evaporation of Zn powder, is a self-catalysed process, and it is possible to choose a variety of substrates to form ZnO rods.

5.1.3 Morphology Control

Environmental conditions dictate the morphology of ZnO structures during the vapour-solid growth. Local temperature and vapour pressures change according to position, further from the centre of the furnace substrates are cooler, changing the condensation dynamics. Also occupation time of Zn vapour in the growth zone of ZnO can determine the size and morphology of the structures produced. A variety of morphologies are represented in Figure 5.6 with notable planes identified. Figure 5.6(a) shows the morphology of a nanorod or nanowire the definition of which depends on the aspect ratio, for a small aspect ratio (i.e. 1:50) it is the former and for a large aspect ratio (i.e $1{:}1.10^4$) it is the latter. Figure 5.6(b) shows a nanoneedle which is generally a rod with gradually decreasing radii of the (0001) plane toward the tip of the rod. If the upper planes are at an angle of 30° with respect to the length of the needle then we can assign these planes to the $\{0\bar{1}\bar{1}2\}$ set of planes. Figure 5.6(c) is a nanonail structure, where the diameter of the rod increases toward

the tip of the rod; the opposite process of the nanoneedle.

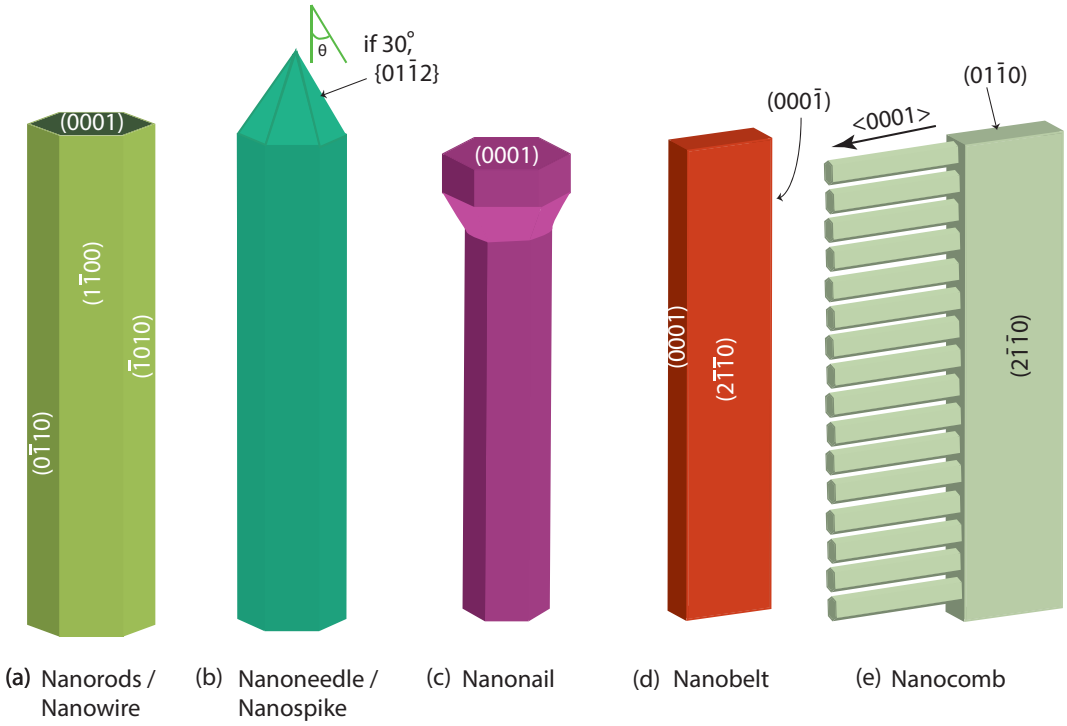

Figure 5.6: A variety of possible morphologies of ZnO, (a) is a simple nanorod or nanowire, (b) is a nanoneedle, (c) is a nanonail and (d) is a nanobelt, on which a nanocomb (e) can form.

It is possible to change the dimensions of ZnO rods by controlling the vapour pressures of oxygen and zinc; this is achieved by controlling temperature or carrier gas flow. At higher vapour pressures growth is enhanced in all directions.

Nanoribbons[241–243] shown in the SEM micrographs in Figure 5.7(a) to (d) are formed at a growth temperature of 650 °C for 20 mins under an Ar flow rate of 150 SCCM on a Ti foil substrate. In this case, a primary ribbon grows along the [2$\bar{1}\bar{1}$0] direction with a width of 1.3 μm ± 0.2 μm; illustrated in Figure 5.6(d). Teeth of the comb form in the c-axis direction [0001] and have grown to a length of 3.372 μm ± 0.22 μm with an average diameter of 400 nm ± 64 nm; illustrated in Figure 5.6(e).[244,245] ZnO forms a ribbon as the [2$\bar{1}\bar{1}$0] growth rate is enhanced, on which further rod/wires grow in the c-axis along the ribbon. The formation of the ribbon could be due to an increased Ar flow in the condensation area, which increases the oxygen concentration close to the growth sites, thereby increasing the oxidation rate of the Zn and accelerating growth. The side surfaces of the combs are the ±(01$\bar{1}$0) faces. Double sided combs also can grow if the growth in the [000$\bar{1}$]

direction becomes as preferential as the [0001] directions growth.[243] Nanobelts have a useful morphology for piezoelectric applications[246,247] allowing a crystal lattice distortion with a favourable bending modulus, and due to the non-centrosymmetric structure of ZnO induces a voltage by inducing electric dipole moments in the crystal structure.

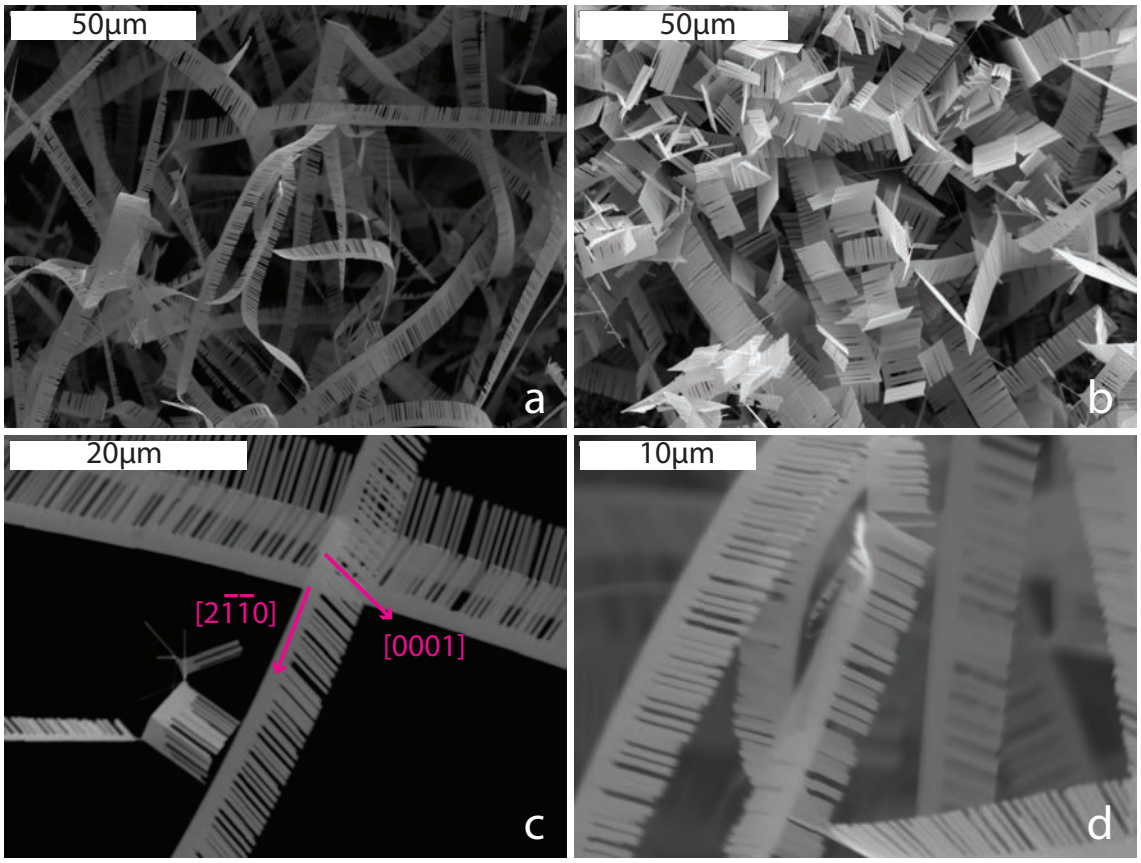

Figure 5.7: SEM micrographs of ZnO structures on a Ti foil substrate, forming ribbons and comb structures grown *via* VS at a growth temperature of 650 °C. The combs are close together on the substrate, shown at varying magnifications (a) ×500, (b) ×550, (c) ×1500, and (d) ×2250 .

The growth of nanonails is similar to earlier examples of nanorod growth, the SEM micrographs are shown in Figure 5.8 (a) to (d). The reaction temperature, 550 °C, and Ar flow rate (50 SCCM) determined the morphology. The average diameter of the rods is 450 nm ± 140 nm, whilst the head of the nail has a diameter of 1.57 μm ± 0.18 μm and an overall length of 10.6 μm ± 1.2 μm. At lower growth temperatures, compared with the carbothermal method of Zn vapour generation, the vapourisation of zinc off the growth site is reduced. Under such conditions the overall growth rate is controlled by the oxygen partial pressure, which controls the

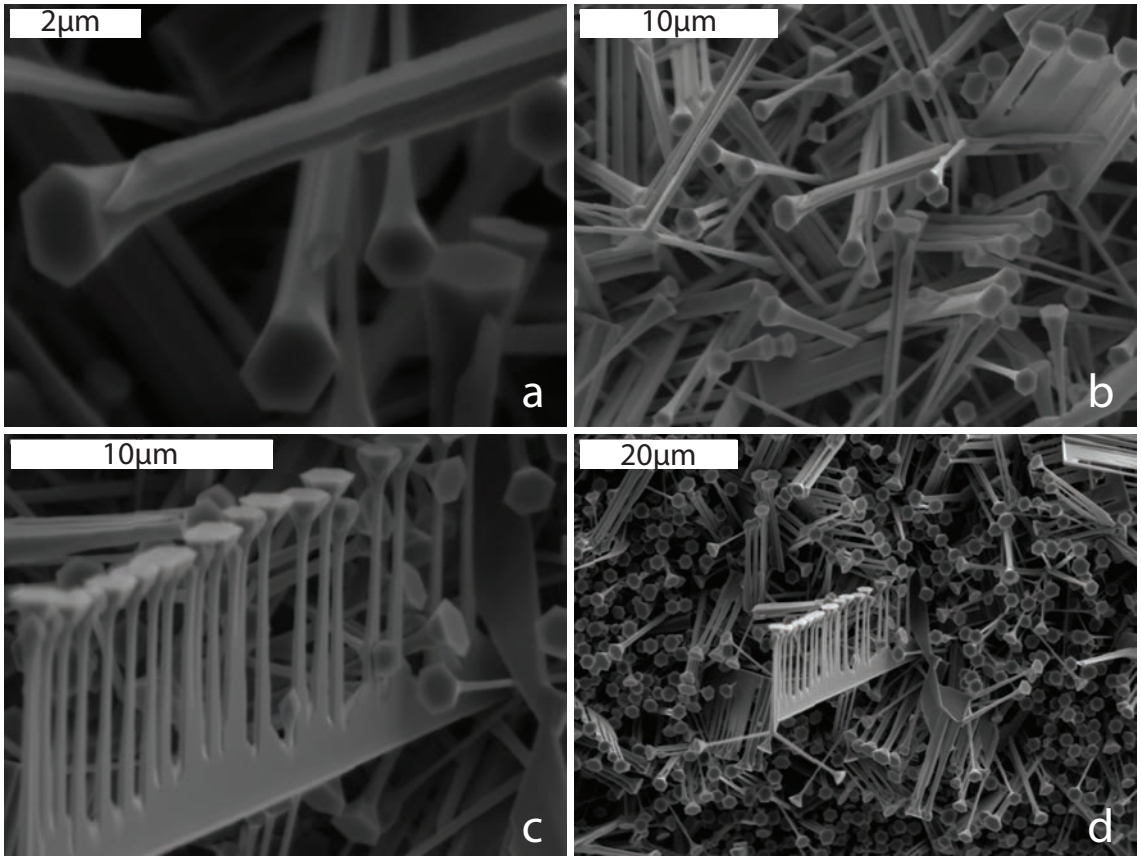

Figure 5.8: SEM micrographs of ZnO nanonail structures grown *via* VS using a Ti substrate. Nanonails which have formed in the centre of the substrate, shown at varying magnification, (a) ×8750, b ×2500 (c) ×3500, (d) ×1000.

zinc oxidation rate. At the interface between the top of the seed and Zn vapour, the growth rate is controlled by the fine balance of the Zn vapourisation rate and Zn oxidation rate. The former is controlled by the growth temperature and the latter is controlled by both growth temperature as well as the oxygen partial pressure. As temperature increases, the oxygen vapour partial pressure raises which subsequently increases growth in the lateral faces forming the head of the nail.

Nanoneedles form at even lower growth temperatures, 450 °C. Figure 5.9(a) to (c) show SEM micrographs at various magnifications of ZnO nanoneedles formed with an average diameter of 400 nm ± 85 nm and length of 4.5 μm ± 0.6 μm. This suggests that if the growth temperature is further reduced, the supply of Zn vapour is reduced to the level that controls the overall growth rate. The deficit of Zn vapour will cause the reduction of lateral growth resulting in a smaller rod diameter. The reduced overall growth rate results in the ZnO structure slowly forming in the [0001] direction, and lateral faces build up gradually forming a sharp tip as the ZnO

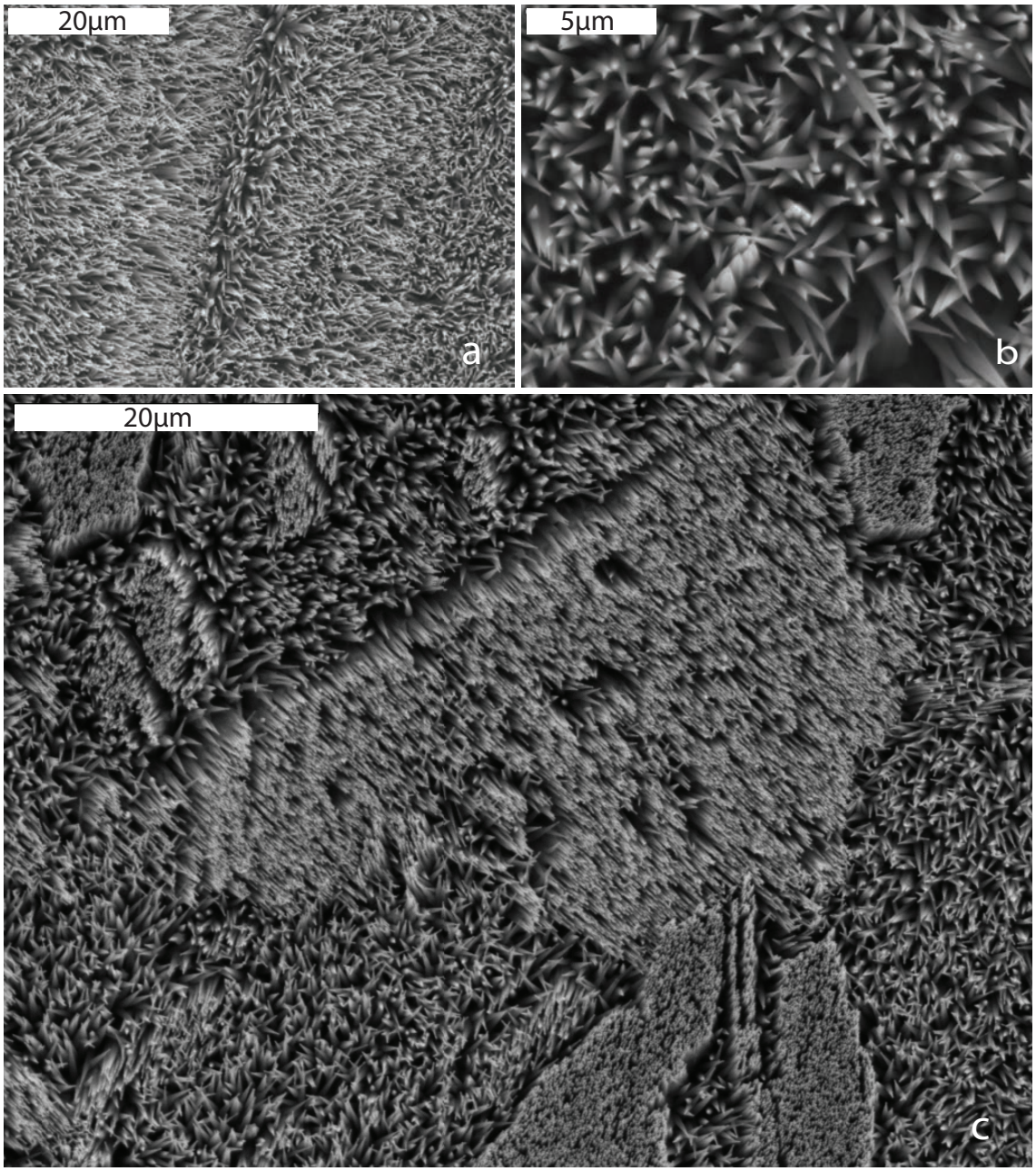

Figure 5.9: SEM micrographs of ZnO needle structures grown *via* VS using a Ti substrate, at a low reaction temperature (450 °C). (a) shows a dense forest of the ZnO needles (×1000), whilst (b) is a high magnification SEM micrograph of the needles (×3500). (c) shows the density and homogeneity of the needles of a large sampled area at a magnification of ×2000.

nanoneedle forms.

Tetrapods can be synthesised by vapourising Zn in a precursor mix of Zn/TiO_2 in ambient atmosphere[248] at temperatures reaching 1000 °C. The legs of the multipods are aligned in the c-axis.[249] Initially a ZnO nucleus condenses which is not a single crystal and has no particular alignment with several polar faces. Growth is initiated on the polar faces and legs form along the [0001] direction with a crystalline nature. Tetrapods tend to grow in atmospheric pressures.[250,251] Although this is not the case in Figure 5.10 where the reaction chamber is evacuated and Ar is introduced at a rate of 200 SCCM.

Figure 5.10(a)-(c) show SEM micrographs of multi-legged ZnO structures densely packed formed on a mechanically polished Ti foil with a growth temperature of 550 °C for 20 mins; the foil is sanded and then polished with 0.5 μm diamond paste, reducing aberrations on the surface thereby reduces nucleation points on the surface. The hot surface of the substrate is ideal for the ZnO to attach and adhere after initial growth. The nucleation initiates above the surface of the substrate[252] *via* a self-nucleation process. Tetrapods have been shown to form in ambient atmosphere, with nitrogen or impurities in the air acting as nucleation sites. The self-nucleation occurs above the plate which has been treated to remove dirt and as much aberration as possible. The average diameter of the centre of the leg is 1.97 μm $\pm$ 0.26 μm, and the average length is 8.5 μm $\pm$ 1.5 μm. The large diameter of the multipods compared to rodular structures indicate the growth rate is higher, a different seeding process is taking place where Zn vapour self-catalyses and ZnO rapidly condenses on the initial Zn seed.

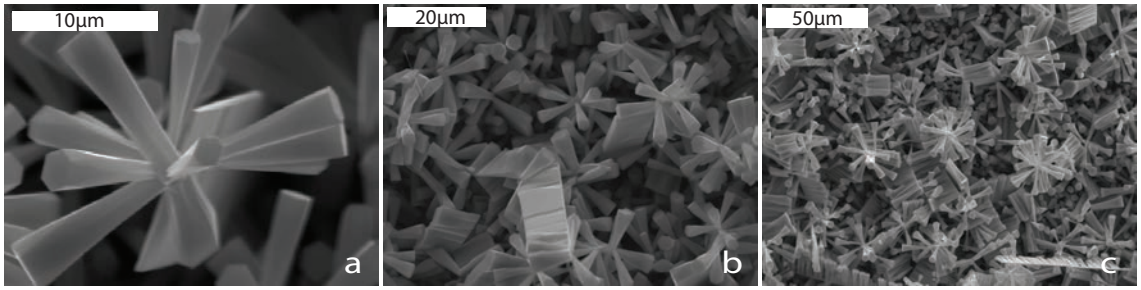

Figure 5.10: SEM micrographs of ZnO multipod structures grown *via* VS on a polished Ti substrate, shown here at various magnifications of (a) ×2000, (b) ×625 and (c) ×250.

Under low temperature growth conditions it is possible to grow ZnO hierarchical

structures.[253] In Figure 5.11 (a) & (b), an initial ZnO rod is formed in the [0001] direction and ZnO grows on the sides of the rods. This was completed on a Zr substrate at 450 °C, for 20 mins with an Ar flow rate of 200 SCCM. Lao et al used indium oxide to grow a nanorod core where the ZnO grew hierarchical from the sides with various degrees of symmetry.[253] In our case, the ZnO rods self-seed the hierarchically growth. It is doubtful the Zr created a core rod. Another group, Wang et al,[244] used tin oxide and zinc oxide as source materials to create hierarchical structures. The tin is used to initiate nucleation for the initial ZnO rod growth which continues on the sides of the hexagonal rods. Let's assume the middle core is the ZnO rod terminated with the (0001) face, the side of the rods will be the $\pm(01\bar{1}0)$, $\pm(10\bar{1}0)$ and $\pm(1\bar{1}00)$ faces. An increase in growth rate on these lateral faces extend into arms in the corresponding direction, exposing the (0001) face on the top of the arms. The average length of the arms of the hierarchical ZnO structures are 1.76 μm $\pm$ 0.2 μm with a diameter of 452 nm $\pm$ 37 nm.

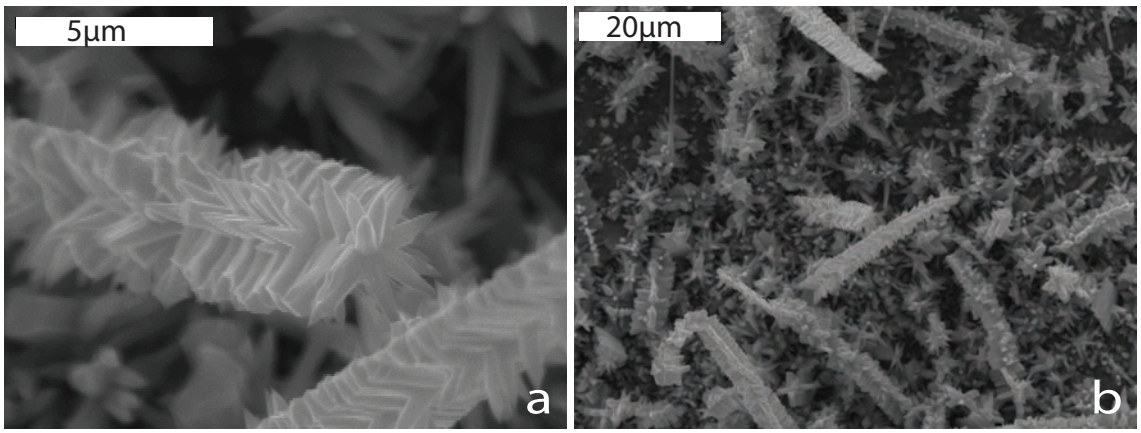

Figure 5.11: SEM micrographs of ZnO spinal structures grown *via* VS using a Ti substrate, hierarchical ZnO structures are formed at low temperatures and vapour pressures. (a) is a high magnification SEM micrograph of the structure (×5000), and (b) shows a large area containing multiple spinal structures at low magnification (×900).

The growth kinetics and the nanostructure morphology can be manipulated by control of the Ar gas flow, which introduces a higher concentration of oxygen into the reactor with higher flow rates. The larger flux of oxygen carried by the argon increases the oxidation rate of the Zn vapour, enhancing growth rates. Thus, a stepped control of the Ar flow produces smaller rods onto larger rods. The growth is conducted at a temperature of 650 °C and initially a high flow rate of Ar is set to

1 l/min (1000 SCCM) and midway through the reaction is reduced to 100 SCCM, Figure 5.12(a) & (b) shows the ZnO structures created under these conditions. The initial rods have a diameter of 3 μm $\pm$ 0.27 μm and upon this rod, 696 nm $\pm$ 194 nm diameter rods continue to grow. Complex 3D structures can be designed and created by altering the gas flow rate during the growth process.

Similarly, if the reaction temperature is changed during ZnO rod growth the oxygen and zinc partial vapour pressure are effected, reducing or increasing growth of the ZnO rods. Figure 5.12 (c) & (d) show rods initially ramped to 650 °C at a high rate of 100 °C/min. The Ar carrier gas flow is set to zero, stunting further growth. The reactor cools down to 600 °C and the Ar carrier gas is reintroduced. At a lower temperature the O_2 and Zn partial vapour pressure are lower, thereby reducing condensation and oxidation rates of Zn, reducing the size of the rod. The initial rod has diameter of 2.1 μm and the upper rod is 1.1 μm, illustrating the sensitivity of the growth rate with Zn and O_2 partial pressures.

Staged Ar carrier gas flow during the growth process varies the oxygen concentration in the reactor. The growth begins with a low carrier gas flow (100 SSCM) and is increased to 1 l/min (1000 SSCM) after 5 mins, an increase of carried oxygen from atmosphere is introduced into the quartz reactor. Instead of growing larger diameter rods onto smaller diameter rods, growth is initiated on the side faces of the rod. Figure 5.13 shows the branched structures formed when this situation arises.

ZnO rods have formed on a cross platform, as shown in Figure 5.13(a), the arms of the cross are 10 μm long with a width of 0.5 μm. ZnO rods have formed on the surface of the cross, the 90° symmetry indicates the arms of the platform have formed in the $\pm(2\bar{1}\bar{1}0)$ and $\pm(0\bar{1}10)$ planes, exposing the (0001) and $(000\bar{1})$ faces at the top and bottom. The growth on the top of the surface, (0001), is initiated and forms smaller rods on the cross. The smaller rods have a diameter of 317 nm $\pm$ 50 nm and a length of 4.9 μm $\pm$ 0.4 μm.

Figure 5.13(b) shows an inner core rod, with branched ZnO rods formed on the sides of the rod. The smaller rods have a diameter of 293 nm $\pm$ 44 nm and a length of 3.4 μm $\pm$ 0.3 μm. and the inner core has a diameter of 1.44 μm $\pm$ 0.23 μm and a length of approximately 10 μm. The smaller rods have formed at an angle of 120° with respect to the long axis of the large ZnO inner rod.

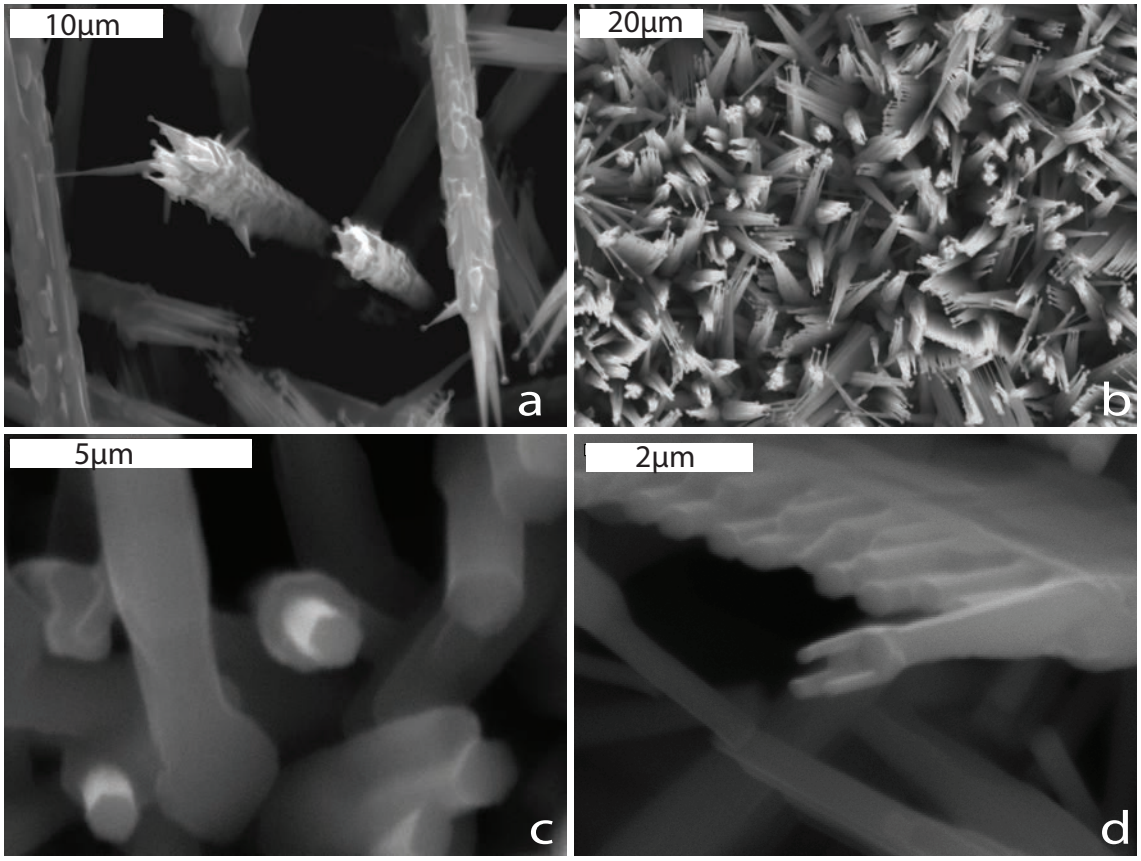

Figure 5.12: SEM micrographs of diameter controlled ZnO rodular growth, an example of rods of a smaller diameter extended from rods with a large diameter, (a) and (b) are formed by lowering Ar flow in the reaction chamber with magnifications of ×2,000 and ×750, (c) and (d) are formed by reducing the temperature during growth at magnifications of ×6,000 and ×10,000 respectively.

Growth of flowering ZnO structures were also present, very large structures and long rods formed on the ends of the leafs of the ZnO nanoflower. In Figure 5.13(c) the diameter of the flower is 40 μm whilst in (d) the diameter is 100 μm. In both cases, the centre of the flower has an increase of lateral growth of the ZnO structure and the side facets are visibly larger. The diameter of the smaller rods are on average 701 nm ± 316 nm for both of the structures. The increase of oxygen concentration, by increasing Ar flow, has accelerated growth in the c-axis forming very fine rods on a larger ZnO structure.

A summary of the various morphologies and conditions of growth are given in Table 5.1. The growth temperature and the flow rate of Ar are the key parameters, and in the table other conditions such as position on substrate and treatment of substrate are also outlined.

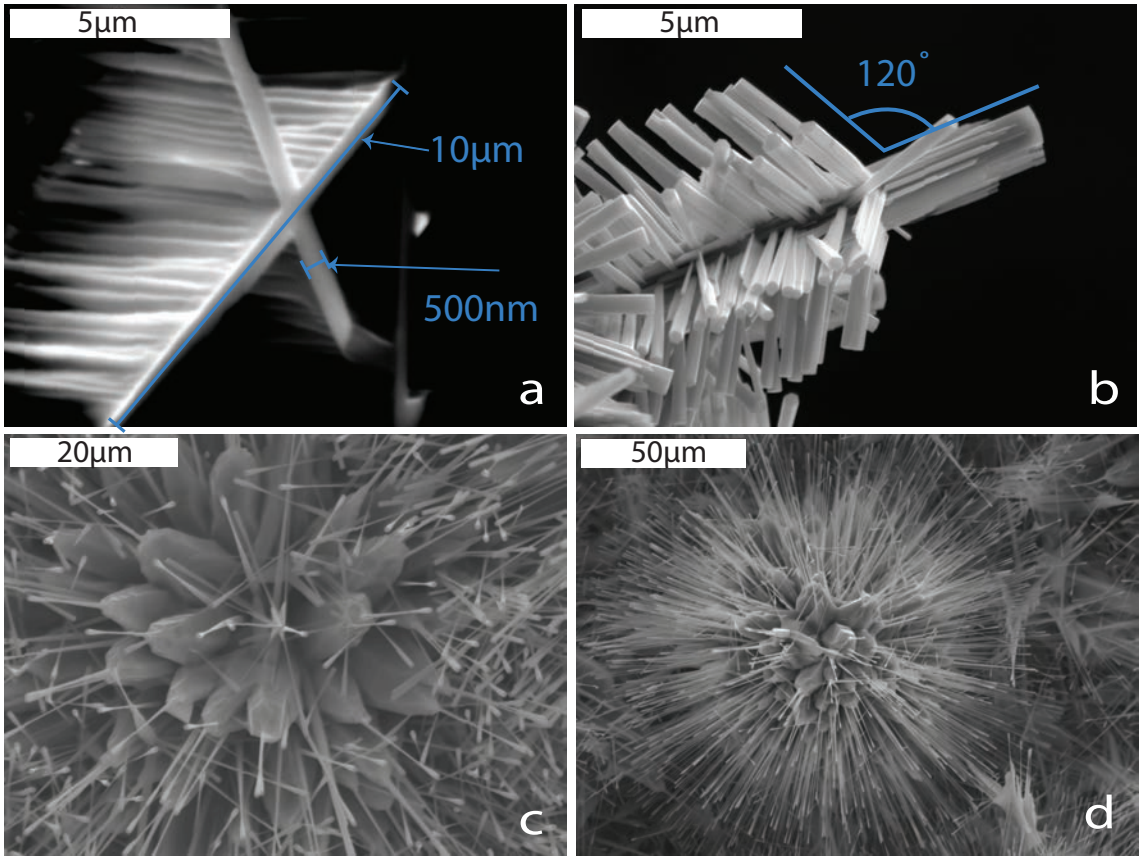

Figure 5.13: SEM micrographs of ZnO structures nucleated from a variety of crystal faces *in situ*, multi-nucleation sites create branched structures. (a) and (b) show rods formed on various planes of ZnO at magnifications of ×4000 for both. Whilst, (c) and (d) show ZnO flowers with long rods formed on the petals at a low magnification of ×750 and ×300 respectively.

Morphology	Temperature (°C)	Ar Flow Rate (SCCM)	Extra Conditions	Figure
Rods/Wires	650	80-1000	centre	5.5 & 5.6
Belts/Combs	650	150	largely on edges	5.7
Nails	550	50	everywhere	5.8
Needles	450	80	everywhere	5.9
Multipods	550	200	polished surface	5.10
Hierarchical	450	200	Zr substrate	5.11
Small rods	650	1000 down to 100	10 mins each	5.12(a)-(b)
on Large rods	650 to 600	100	10 mins each	5.12(c)-(d)
Flowers/Branched	650	100 up to 1000	5 mins low and 15 mins high	5.13

Table 5.1: Conditions for selective ZnO nanostructure morphologies.

5.2 XRD Analysis of the Crystal Structure of ZnO Nanorods Formed on a Ti Foil

In this work I have investigated the photoelectrochemical properties of ZnO rods formed on a Ti foil substrate. The reaction temperature is 650 °C, and the temperature is ramped from room temperature to the reaction temperature at a rate of 50 °C/min. The vapour transport reaction takes place for 20 mins. The ZnO nanorod thin film formed under these conditions are shown in the SEM micrographs in Figure 5.14(a) to (d) at varying magnifications.

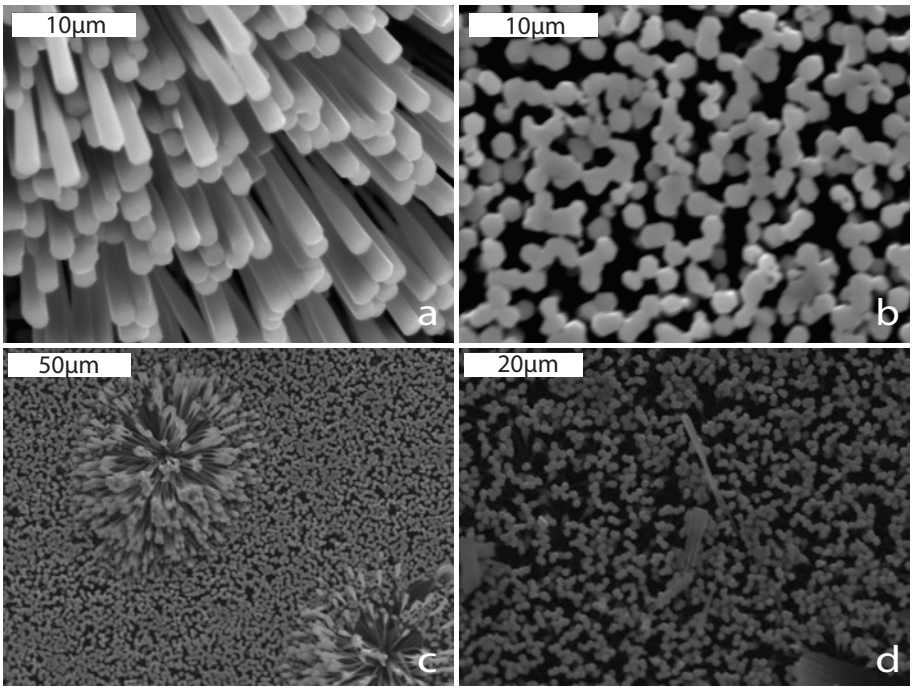

Figure 5.14: SEM micrograph of ZnO rods grown *via* VS on a Ti foil substrate at different magnifications, (a) and (b) high magnification (×1500 & ×1750 respectively) and (c) and (d) at low magnification (×300 and ×750 respectively), under investigation using XRD and photoelectrochemical analysis.

X-ray diffraction of the samples, Figure 5.15, shows the presence of a predominant sharp ZnO (light green fill) c axis (0001) peak, and significant ZnO (100), (101) and (102) peaks at the corresponding 2θ values of 34.44°, 31.84°, 36.28° and 47.56° respectively. The (002)/(0001) phase is the most dominant peak (highest relative intensity), indicating the growth of the rods have a preferred [002]/[0001] orientation. The average crystallite domain size is 37.21 nm as determined from equation 2.7, which is 21 % larger than the crystallite size of randomly orientated

ZnO powder (30.69 nm). This indicates ZnO rods have larger coherent diffraction domains. Hence, a longer range order compared to powder samples. Lattice constants for the ZnO rods are a = 3.2503 Å and c = 5.208 Å.

The ZnO peaks are much larger than other crystal structures present, and inset of Figure 5.15 are magnified portions of the spectrum. On the left is a 40× magnification of the spectrum, and on the right is a 20× magnification of the plot. TiO_2 (cyan fill) can now be identified in the sample, and mostly of a rutile crystal structure, with peaks of (110), (111), (210) and (211) planes at the corresponding 2θ values of 27.5°, 40.1°, 42.14°, and 43.26°. The TiO_2 peaks have a much lower intensity compared to ZnO, and is formed on the surface of the Ti foil. The crystallite size varied drastically from 18 nm to 59 nm, the comparable physical size of the film of TiO_2 is likely the cause of the variation in crystallite size. The Ti foil (purple fill) can be clearly identified within the XRD spectrum with peak intensities over 500 counts, indicating the X-rays are sampling the substrate.

The thin film of TiO_2 must be formed by the thermal oxidation of the Ti foil surface, and rutile is the most thermodynamically stable phase of TiO_2 at high temperatures. The size of the initial particles determine formation of TiO_2 crystal phases, anatase is thermodynamically stable for small particles (< 10 nm), and above 35 nm rutile is the most stable phase. Intermediately to these is brookite which is thermodynamically stable for moderately sized particles. In our case, the Ti foil is a bulk material and rutile is the likeliest phase formed by thermal oxidation. An anatase (004) peak at 38.38° is present, the formation of which could be due to the smaller sized granular features on the Ti surface undergoing thermal oxidation, and abberations which are below 10 nm.

Interestingly, Zn_2TiO_4 has formed on the material. This can only have been formed between the TiO_2 thin film and the roots of the ZnO rods. The mass transportation limit sets the maximum size of the Zn_2TiO_4 film beneath the ZnO rods. The two peaks present at 29.78° (220) and 35.1° (311) have a small crystallite phase domain of 7.25 nm and 12.87 nm. The crystallite domain size might be restricted by the physical dimensions of the Zn_2TiO_4 film between the rods and TiO_2 film, and if so, the thickness of the film will be in the order of 10 nm. The XRD data of the ZnO rods formed on a Ti foil is summarised in Table 5.2 as analysed

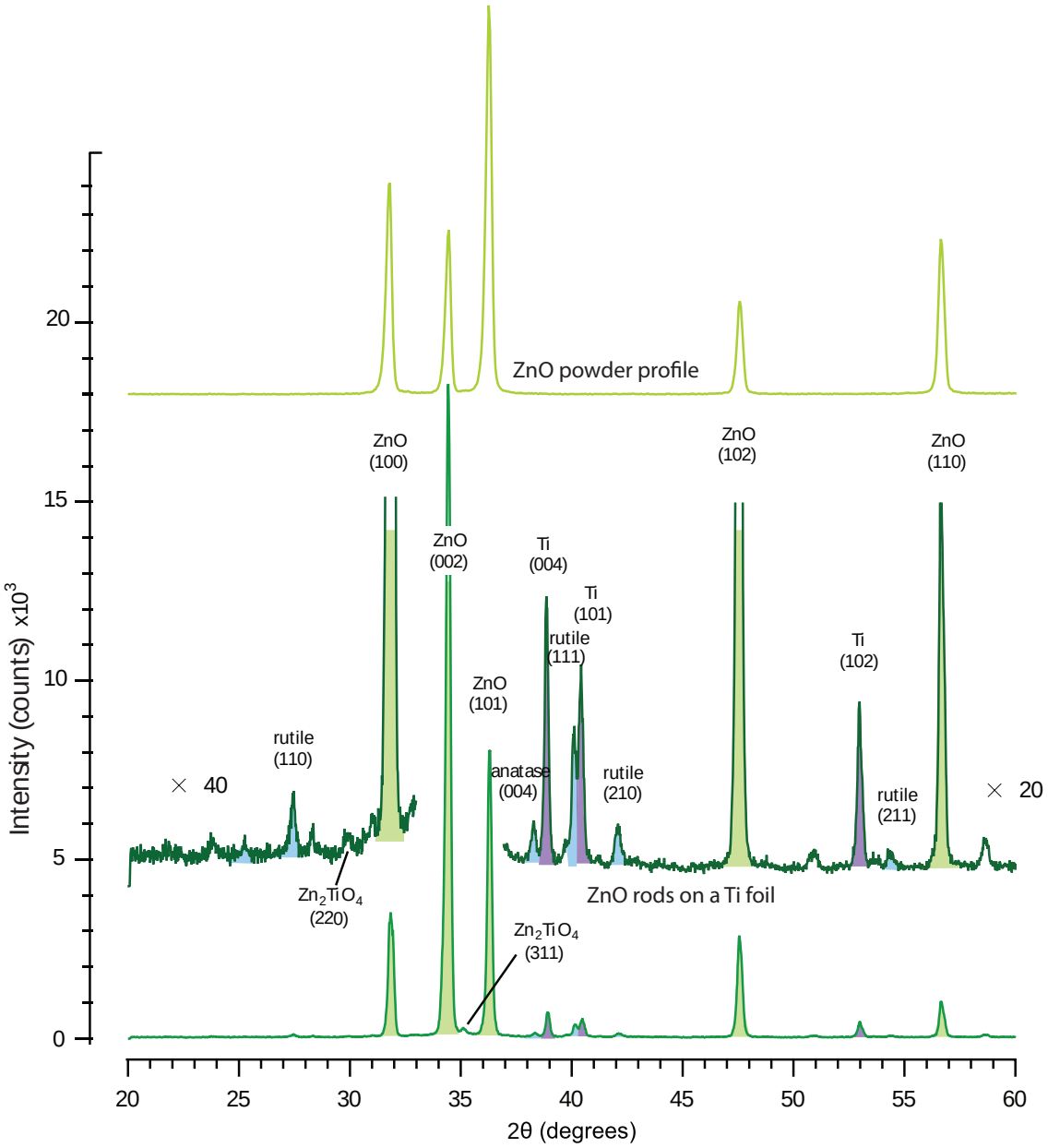

Figure 5.15: The top spectrum shows the ZnO standard, and the bottom XRD plot is the ZnO rods grown *via* VS on a Ti foil substrate. The middle plots are magnified (40× on left and 20× on right)in order to show the low intensity peaks. The presence of Zn_2TiO_4 is clear in the middle magnified plots.

using the Igor software suite.

Material	(hkl)	2θ (°)	2θ ref. (°)	Peak height	Peak area	Crystallite size (nm)	d (Å)
ZnO	(100)	31.84	31.77	3559	1060.8	32.81	2.8105
	(002)	34.44	34.42	18476	4720.1	38.54	2.6040
	(101)	36.28	36.25	8142	1906.7	42.25	2.4761
	(102)	47.56	47.54	2907	804.5	37.13	1.9118
	(110)	56.64	56.60	1049	312.7	35.84	1.6250
Zn_2TiO_4	(220)	29.78	29.83	73	97.9	7.25	3.0003
	(311)	35.1	35.14	317	242.9	12.87	2.5566
TiO_2	(110)r	27.5	27.91	122	62.3	18.95	3.2434
	(004)a	38.36	37.84	164	76.8	21.26	2.3465
	(111)r	40.10	41.72	225.4	38.4	58.77	2.2486
	(210)r	42.14	44.83	155	85.8	18.21	2.1443
	(211)r	54.26	55.11	90	153.3	6.20	1.6905
Ti	(002)	38.92	38.42	753	160.3	46.85	2.314
	(101)	40.48	40.17	574	317.7	18.11	2.2283
	(102)	53.00	53.01	476	131.7	37.97	1.7277

Table 5.2: XRD data of ZnO rods formed on a Ti foil. The crystallite size is determined from the FWHM using equation 2.7 and the lattice spacing is determined using equation 2.6. The reference values are taken from the International Centre for Diffraction Data, JCPDS numbers: ZnO - 36-1451, Zn_2TiO_4 - 25-1164, TiO_2 (a-anatase) - 21-1272, TiO_2 (r-rutile) - 21-1276 and Ti - 44-1294.

Figure 5.16 shows the structure proposed in accordance with the diffraction peaks observed. A TiO_2 thin film forms at high temperatures (650 °C) on the surface of a Ti foil due to thermal oxidation, the TiO_2 acts as a seeding layer for the growth of ZnO, and Zn vapour attaches to the seed and partially oxidises. The first few layers of deposited ZnO is in direct contact with TiO_2, and reacts with the TiO_2 thin film forming Zn_2TiO_4. The chemical transformation can be expressed as equation 5.2. The ZnO vapour facilitates further growth on the zinc titanate complex, dominated by the c-axis growth direction of the crystal, forming ZnO nanorods. The reac-

tion between the TiO_2 and ZnO at the nanorod/substrate interface create Zn_2TiO_4 through a unilateral diffusion process, limited by the mass transportation limit, i.e. the Zn_2TiO_4 forms solely at the roots of the ZnO nanorods.

$$TiO_2 + 2\,(ZnO) \rightarrow Zn_2TiO_4 \tag{5.2}$$

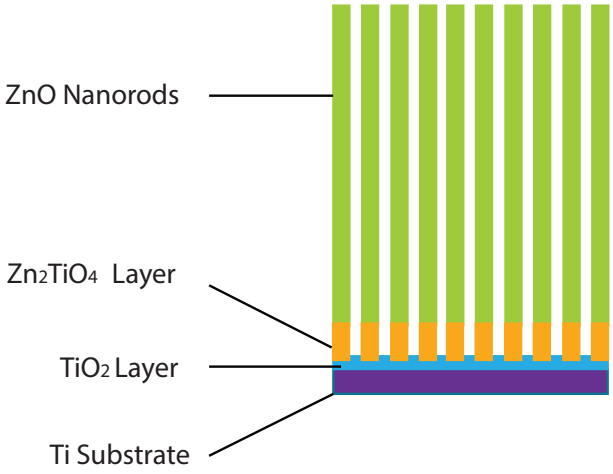

Figure 5.16: Initially an oxide film forms at temperatures above 500 °C on the titanium surface, thereafter ZnO begins growth at self-nucleation sites on the surface and growth occurs in the c-axis, whilst migration occurs at the roots of the rods and the oxide film and zinc titanate forms. Due to the mass transportation limit, Zn_2TiO_4 can only be formed at the interface of TiO_2 and ZnO.

5.3 Photoelectrochemical Tests

The main application and motivation for developing the nanostructured metal oxide semiconductors are for the harvesting of solar energy through water splitting. The advantage of the nanorod structure is that it allows the mass transportation of the electrolyte between the rods whilst maintaining a large surface area to facilitate the surface electrochemical reactions. Photoelectrochemical tests are performed in the setup as shown in Chapter 3, the electrolyte consisted of 1 M KOH in water; with a pH of 14. A xenon lamp simulates the solar spectrum and a surface area of 1 cm^2 is illuminated. A potentiostat scans the potential and measures the current using a three electrode configuration, the potential is measured between a saturated Ag/AgCl reference electrode and working electrode. The current is measured between the Pt counter electrode (cathode) and working electrode (photoanode) and

is directly proportional to hydrogen generation at the cathode surface.

A typical I-V curve is shown in Figure 5.17, corresponding to the sample in the SEM micrographs shown in Figure 5.14, which show good quality well ordered rods with an average diameter of 1.664 μm $\pm$ 0.141 μm and a length of 15.5 μm $\pm$ 2.3 μm. The staggered curve (blue) recorded the current as the illumination was chopped during the potential sweep, the chopper consisted of an opaque card which intermittently covered the xenon lamps beam rather than electronic switching of the lamp, which was the method utilised in the previous chapter. The curve demonstrates a fast response rate between successive switching, which indicates a true photo response in the electrochemical scanning process. A sharp response rate is indicative of high electron mobility in the photoanode structure. The current curve when the illumination is absent is represented by the black curve (dark current), the near zero value of the dark current illustrates the large red curve is solely a photoinduced current. The purple curve represents the power density output of the photoanode, calculated using the onset potential and ignoring overpotential losses using equation 5.3. Where, P_p is the output power density of the photoanode provided by the electrical energy generated by photons used to generate hydrogen at the counter electrode. V_{Meas} is the measured potential, V_{OC} is the open circuit potential when the photocurrent is zero, 1.23 V is the standard potential of water electrolysis, and can be considered the short circuit potential in terms of solar cell analysis, i.e V_{SC} = 1.23 - V_{OC}. I_{photo} is the photocurrent measured from the structures under illumination. The onset potential (V_{On}) is the open circuit potential measured relative to the RHE potential scale (0 $V_{\mathrm{RHE}} \equiv$ -1.023 $V_{\mathrm{Ag/AgCl}}$ pH=14) and gives a quantitative value for the flat band potential if there are no other overpotential losses or hole accumulation/recombination at the photoanode surface.

$$P_p = (1.23 - (V_{Meas} - V_{OC}))I_{photo} \tag{5.3}$$

$$V_{On}^{\mathrm{RHE}} = V_{OC}^{\mathrm{Ag/AgCl}} - (-1.023) \tag{5.4}$$

A direct comparison of the photoelectrochemical efficiency between TiO_2 nanotubes and ZnO nanorods is presented in Figure 5.18. The TiO_2 nanotubular array

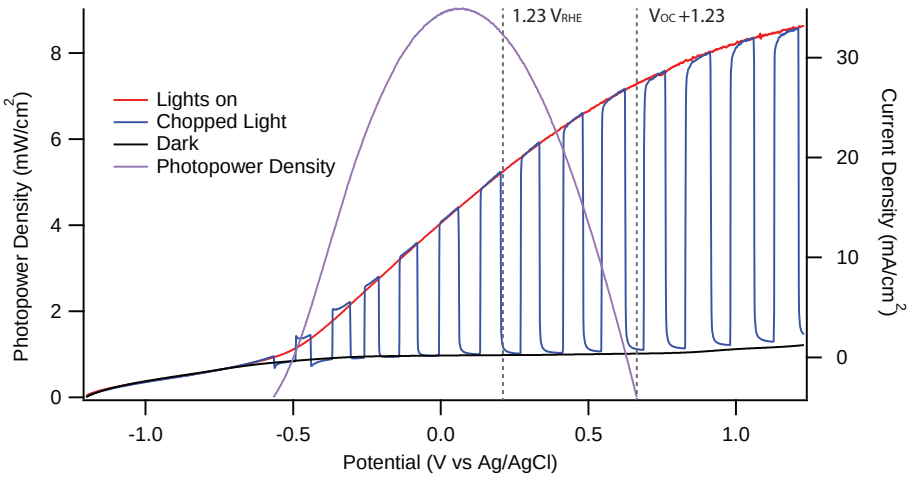

Figure 5.17: Photocurrent (Right axis) measurements under xenon lamp illumination (no filters), I-V plot, of ZnO rods grown on a Ti foil plate, with Zn_2TiO_4 at the interface between TiO_2 and ZnO. Left axis corresponds to the photopower density output.

is 2 μm thick, and the outer diameter of the nanotubes is 133 nm, with an inner diameter of 83 nm. Whilst the ZnO rods are 15.6 μm long with a diameter of 1.66 μm. The TiO_2 nanotube array should out perform the ZnO rods, due to the larger surface area of the TiO_2 nanotubes as well as shorter distance required for charge transport to the metal film contact. The surface area of one rod is approximately 80 μm^2, whilst the surface area of TiO_2 nanotubes closely packed in a hexagonal area of the same size is 140 μm^2. Thus, the surface area and morphology are similar enough to compare the two materials. The photocurrent for the TiO_2 nanotubular array reaches 20 mA/cm^2 at 1 V vs Ag/AgCl, whilst ZnO rods on a Ti foil reach 30 mA/cm^2 at 1 V vs Ag/AgCl. ZnO has a maximum power density output of 8.2 mW, whilst the TiO_2 nanotubes have a maximum power density of 6.4 mW, the ZnO rodular array on a Ti foil with a Zn_2TiO_4 barrier layer is 22 % more photoefficient than the TiO_2 nanotubular array. The onset potential for both materials are very close to one and another, for TiO_2 the V_{On} is 0.36 V_{RHE} and for ZnO the V_{On} is 0.4 V_{RHE}, this indicates that the band edge positions for the two materials are similar.

The high photocurrent density of ZnO rods could not only be attributed to the high electron mobility within ZnO (200 $cm^2V^{-1}s^{-1}$ for ZnO compared to 30 $cm^2V^{-1}s^{-1}$ for TiO_2), but due to a staggered interfacial semiconductor heterostructure at the root of the ZnO rods. The interfacial heterostructure is formed by ZnO on top of a TiO_2 thin film, with Zn_2TiO_4 in between which provides a charge barrier

layer, effectively separating exciton pairs.

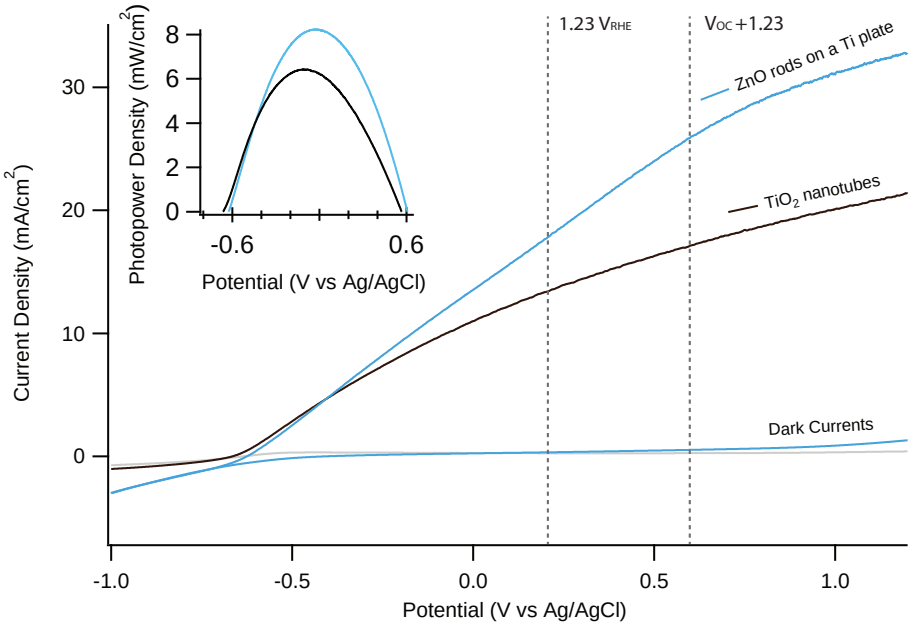

Figure 5.18: Photocurrent density of TiO_2 nanotubes compared to ZnO rods grown on a Ti foil, with Zn_2TiO_4 at the interface between TiO_2 and ZnO. Inset: power densities of both photoanodes have a similar peak power output.

Figure 5.19 shows the photocurrent density of a ZnO nanorod array formed on a Ti foil substrate over a period of 48 hours at a potentiostatic potential of 1.5 V. The potential is applied between the photoanode and Pt cathode in a two electrode cell configuration using a 1 M KOH electrolyte. The sample was under bias and illumination for 2 days to illustrate the stability of the photoanode, with a 7 % reduction in the photocurrent. The photoanode is highly durable, and a large photocurrent is maintained. The light source used is a 36 W cold cathode fluorescent lamp CCFL with a UV wavelength range with a peak at 365 nm (Figure 2.11 shows the spectrum, with an intensity of 800 μW), classified as UVA, rather than the more powerful 300 W xenon lamp. A CCFL lamp has the advantage of time and thermal stability, so it is suitable for the longevity test. The light source was intermittently switched on and off, which demonstrates the current is photoinduced and to observe photoresponse of the structure. The slow decay of the photocurrent is partly due to the degradation of the bulbs of the light source, due to frequent switching.

Hydrogen generation was measured using a bubble flow meter, the three electrode configuration was utilised and a potential of 1 $V_{Ag/AgCl}$ is applied between the photoanode and reference electrode. The current measured between the photoanode

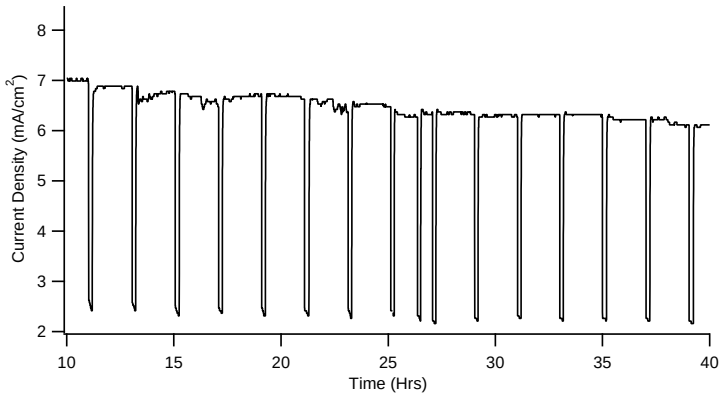

Figure 5.19: Photocurrent density plotted at a potentiostatic potential (1.2 V) over two days in a two electrode electrochemical setup. A potential is applied between the photoanode and a Pt foil counter electrode.

and Pt counter electrode was 22 mA/cm^2. The hydrogen collected from the Pt foil cathode compartment of the cell was directed through a 6 mm_{OD} (3 mm_{ID}) glass tube containing a bubble, the distance the bubble moves in a given time directly relates to the flow rate of the gas. The generation of hydrogen was measured to be 1.018 cm^3/hr. According to $R(H_2) = \frac{I}{nF}$, a photocurrent of 22 mA should produce 6.9×10^{16} molecules of hydrogen, i.e. 0.41 mmol/hour or 4.6 ml per hour (same as cm^3/hr). This value is larger than the measured value, which is possibly due to the movement of hydrogen within the electrolyte. This could be avoided by employing a semi permeable membrane between compartments of the photoelectrochemical cell.

Most metal oxides are non-stoichiometric under typical laboratory/synthesis conditions, which changes the electrical properties of the material. TiO_2 and ZnO are both n-type with a Fermi level close to the conduction band due to the excess of metal in the materials (raising the Fermi level). The metal rich nature of these materials means the semiconductors are more likely to contain oxygen vacancies and metal interstitials. Oxygen deficient materials are n-type in nature, whilst oxygen rich and metal deficient materials are p-type oxides (CoO, NiO, FeO, MnO, Cu_2O Cu_2O UO_2).[65–67]

A (upward) flatband potential is introduced when the semiconductor and electrolyte are in galvanic contact. The lower work function of the n-type semiconductor and higher work function electrolyte allows electron transfer events when in contact raising or lowering the bands close to the junction, Figure 5.20. Sandwiched between the zinc oxide and titanium dioxide is a zinc titanate layer which has a

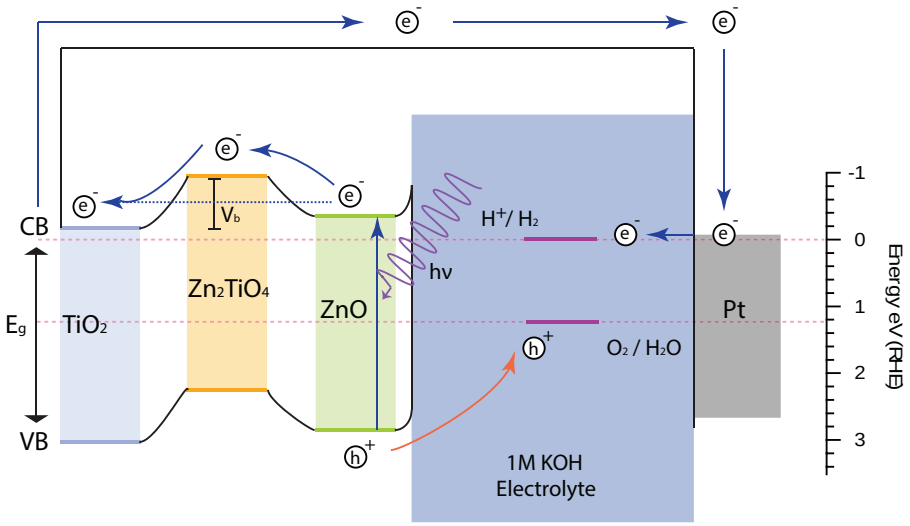

Figure 5.20: Schematic of band positions of solid/solid interfaces as well as solid/liquid interface. The ZnO acts as a photoabsorber and the Zn_2TiO_4 acts as a barrier layer effectively seprating electrons and holes.

conduction band higher than either of the other conduction bands. This creates an additional barrier potential; from Figure 5.20 it is possible to see a spatial pathway for the electron, from creation in any of the semiconductor materials and effectively being separated, where energy is needed to overcome the potential barrier for recombination to occur. The voltage is such that electrons traverse through the circuit to the Pt electrode and reduces water on the surface of the Pt electrode; meanwhile the holes facilitate oxygen evolution reactions (OER) at the surface of the nanostructured photoanode and electrolyte interface.

The energy levels of the three oxides[64, 254] composing the heterostructure is shown in Figure 5.21. In contact, the conduction and valence bands bend toward each other forming a staggered multibarrier heterostructure. Holes and electrons are separated at the interfaces of the type II staggered heterostructure.

5.4 Thickness Controlled Rods and Photocurrents

The thickness of the ZnO nanorod thin film can be controlled by the overall growth time at fixed conditions. Through a number of reactions under identical vapour conditions, differing only in reaction time and Zn precursor, a range of ZnO nanorods/nanowires were examined photoelectrochemically to determine the quality of

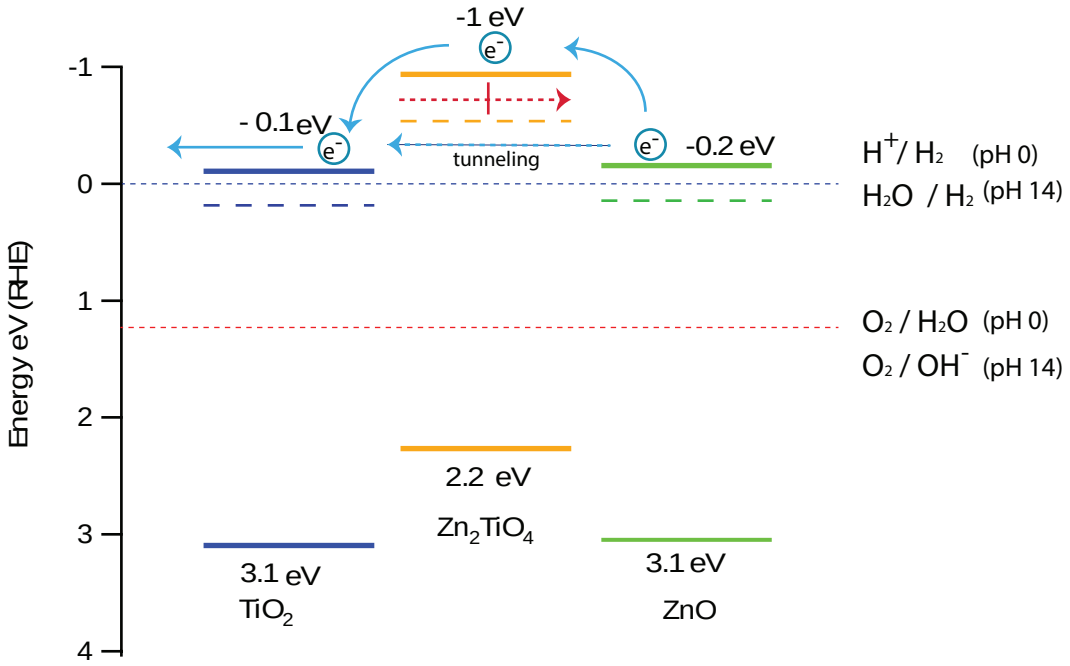

Figure 5.21: The three energy levels of the oxide semiconductors. All have a similar Fermi level and the CB/VB bands lay outside the water oxidation/reduction potentials, thereby allowing them to be candidates for water-splitting photoelectrode material.

performance in relation to the length of ZnO nanorods. The thickness of the films were measured using the cross sectional view of the sample in the SEM. Examples of cross-sectional SEM micrographs used to measure the thickness of the ZnO nanorod film are shown in Figure 5.22, with thicknesses of (a) 10.8 μm, (b) 7.6 μm and (c) 30 μm. The effect of the film thickness on the maximum photopower density output is plotted in Figure 5.23.

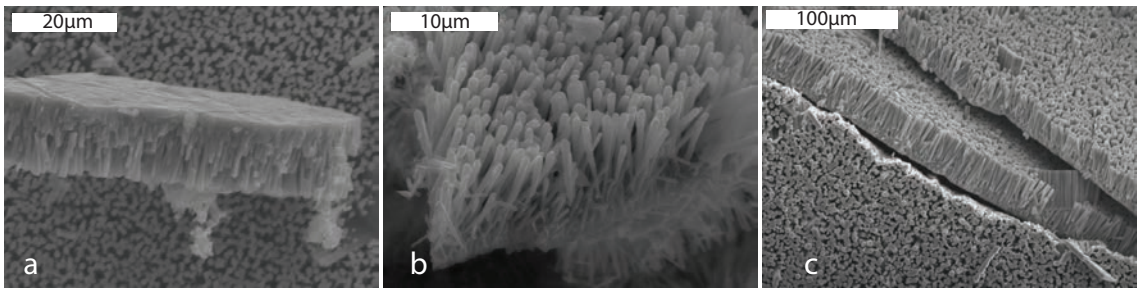

Figure 5.22: SEM micrographs of series of typical cross-sectional measurements carried out to measure the thickness of ZnO nanorod thin films grown on a Ti foil substrate. (a) Average thickness of 10.8 μm $\pm$ 0.9 μm, (b) average thickness of 7.6 μm $\pm$ 0.2 μm and lastly (c) average thickness of 30 μm $\pm$ 3 μm.

Longer nanorods have a larger surface area in contact with the electrolyte and

have a higher probability of photon capture under illumination, but also could suffer a higher rate of exciton recombination. Increasing the thickness of the ZnO nanorod thin film is expected to contribute to an increase in photoefficiency, but as shown in Figure 5.23 the photoefficiency saturates after a thickness of 10 μm is reached. This is attributed to the length and density of rods which inhibit the path of photons which could have otherwise been utilised in electron generation close to the metal contact, where recombination rates would be reduced.

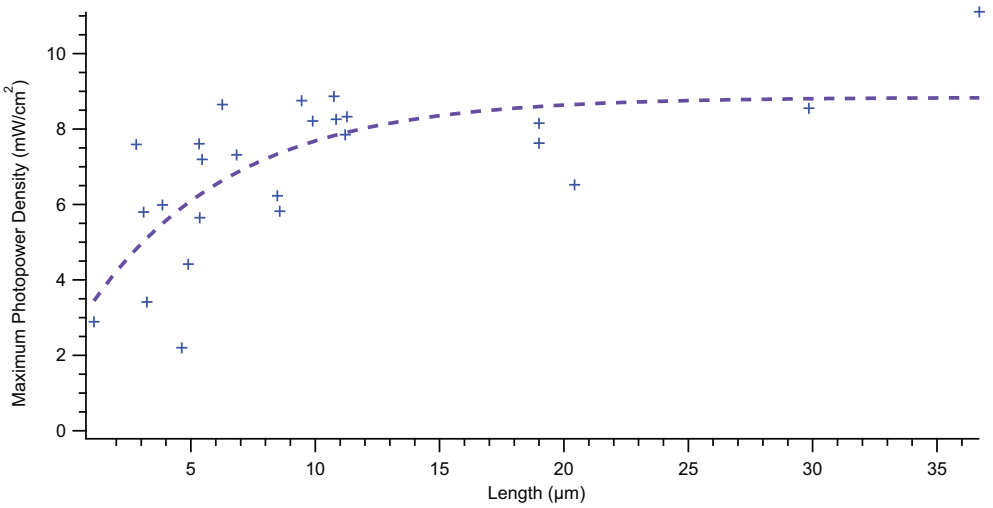

Figure 5.23: Plot of peak photopower density output of a variety of lengths of ZnO rods, all rods are grown *via* VS reaction at a reaction temperature of 650 °C.

The diameters of the ZnO rods varied only slightly for different samples. Thus, the largest factor contributing to the efficiency of the photoanode would be the length. The diameter of the nanorods are expected to have less of an effect, if the overall surface area is constant. The increased charge pathways to the circuit will largely effect recombination of electron hole pairs and the number of electrons which can be harnessed for the water splitting process. For thick films, the efficiency reaches a steady value as the increasing photocatalytic surface area and probability of photons capture begin to compete with the losses of usable charge carriers *via* exciton recombination and obstructed photon path.

5.5 Growth of ZnO Structures in a KOH Rich Environment

The morphology and photoefficiency of ZnO nanostructures could also be affected by subtle changes in the chemistry of the growth environment. Here I examine the effects of adding KOH into the growth environment on the thin film structure and properties. 0.5 ml of 1 M KOH solution is added to the precursor and a boat containing 5 ml of 1 M KOH is placed upstream from the substrate. Growth is conducted under typical VS conditions with a temperature ramp rate of 50 °C/min reaching the growth temperature of 650 °C and maintaining the growth temperature for 20 mins. The results are surprising; photoelectrochemical properties of the material have enhanced significantly. The increase in photocatalytic behaviour could be due to defects or doping of ZnO. The defects in the crystal lattice could be caused by *in situ* dissolution process, this or the K doping of the ZnO structure could introduce new donor and acceptor levels between the valence band and conduction band.[216]

The morphology has changed significantly with the inclusion of KOH compared to the rods formed under identical conditions without KOH; the structures are multi-faceted cup-like structures and pyramid shaped gems. Figure 5.24(a) shows a low magnification SEM micrograph of the surface of the substrate. The average diameter of the gems are 4 μm, with a range of diameters from 1.9 μm to 7.3 μm. Figure 5.24(b) shows an SEM micrograph of a cup like structure which is almost a complementary form of the gems, rather than pyramid facets directed outward they are imposed into the structure. Figure 5.24(c) shows the relative positions of cups and gems, the density of gems are greater than that of the cups.

With added KOH, when Zn is vapourised, nanosized clusters of KOH particles form and are transported to the substrate. The addition of the KOH in the ZnO crystal could form defects which will affect the growth of ZnO rods and possibly improve band structure properties of the material. The local defects could be in the form of potassium zincate, as described in equations 5.5 & 5.6. Such defects could interfere with the growth of the normal rods.

$$ZnO + 2\,KOH + H_2O{=}K_2Zn(OH)_4 \tag{5.5}$$

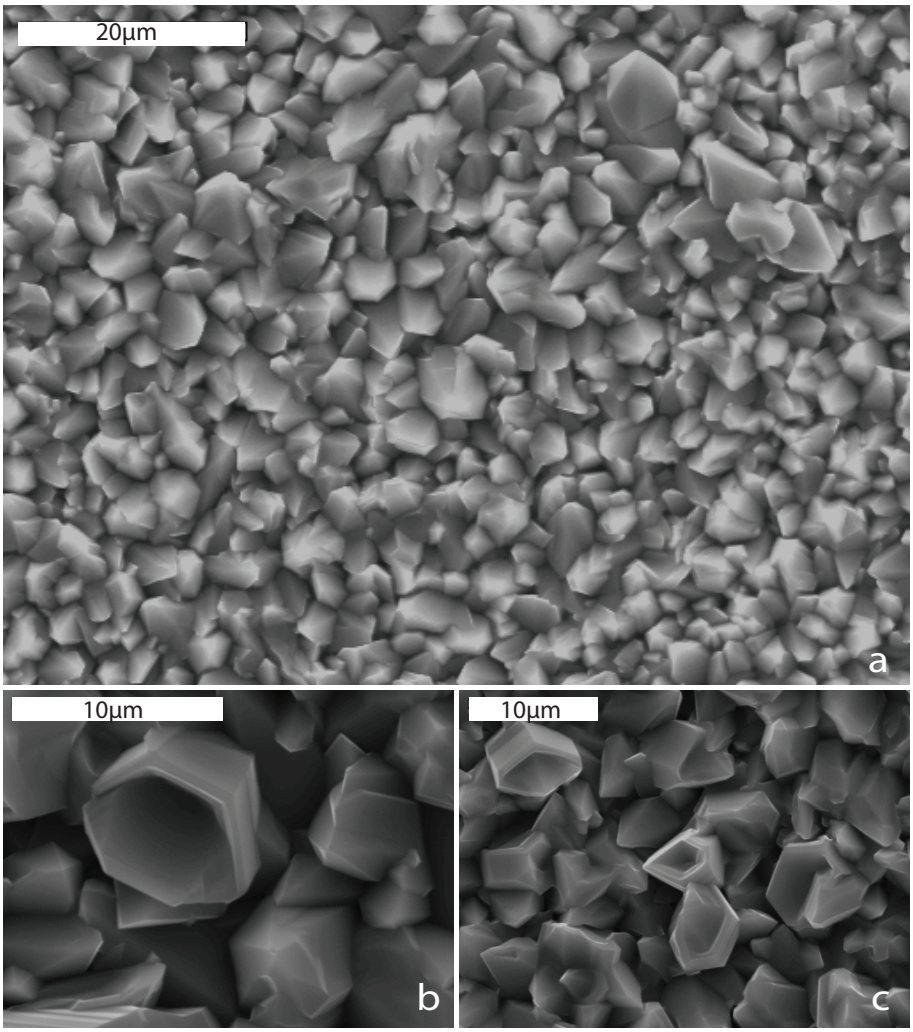

Figure 5.24: SEM micrograph of unique multi-faceted micro-structures of ZnO gems, growth *via* VS at a temperature of 650 °C on a Ti foil substrate. 1 M KOH is mixed with the Zn powder precursor and additionally placed in a crucible upstream from the Ar flow.

$$K_2Zn(OH)_4 = K_2ZnO_2 + 2\,H_2O \tag{5.6}$$

On the same sample, growth is accelerated closer to the boat containing the KOH upstream of the carrier gas and rods are 20 times larger than the nanorods formed without KOH present. At this size the dynamics of growth is unclear, the structures are formed with interesting selective growth faces with a 6 fold symmetry. The 6 fold symmetry indicates the faces experiencing selective growth are the $\{10\bar{1}0\}$ faces, i.e. the lateral faces of the hexagonal wurtzite crystal structure. In Figure 5.25(a) the 6 fold symmetry is clear and the rod has a diameter of 20 μm with the $\{1\bar{1}02\}$ faces exposed creating an hexagonal pyramid tip (these faces are semipolar), Figure 5.25(b) shows branched growth from the micro sized rods, with a core diameter of

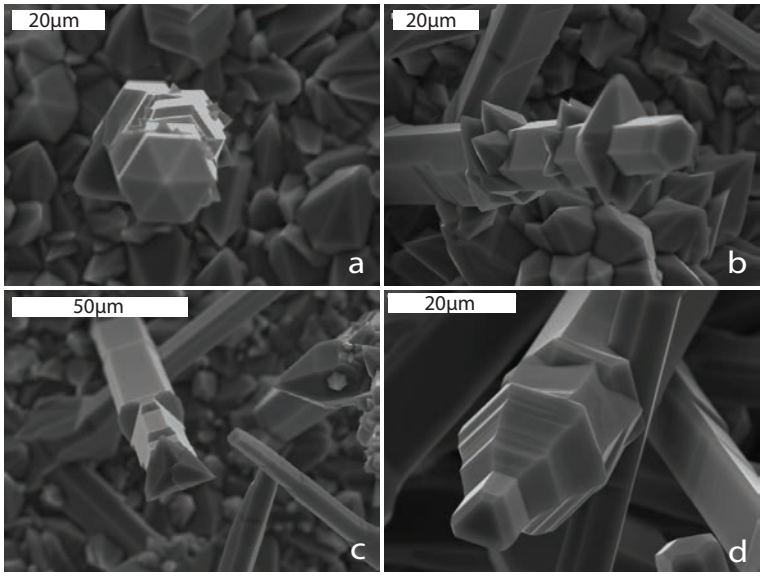

Figure 5.25: SEM micrograph of unique micro-structures of ZnO rods, growth *via* VS at a temperature of 650 °C on a Ti foil substrate. ZnO undergoes accelerated growth and form Multi faceted rodular shapes, with 6 fold symmetry.

10 μm with the branches extending the diameter to 30 μm. The latter two SEM micrographs, (c) & (d), show a mix of 3 fold symmetry with the 6 fold symmetry, in the 3 fold symmetry the $(11\bar{2}0)$, $(\bar{2}110)$ and $(1\bar{2}10)$ faces have a faster growth rate. The diameter of both core rods are 20 μm. The structural growth is possibly due to the potassium ions substituting Zn sites and interstitial sites resulting in higher reactivity on surface faces.

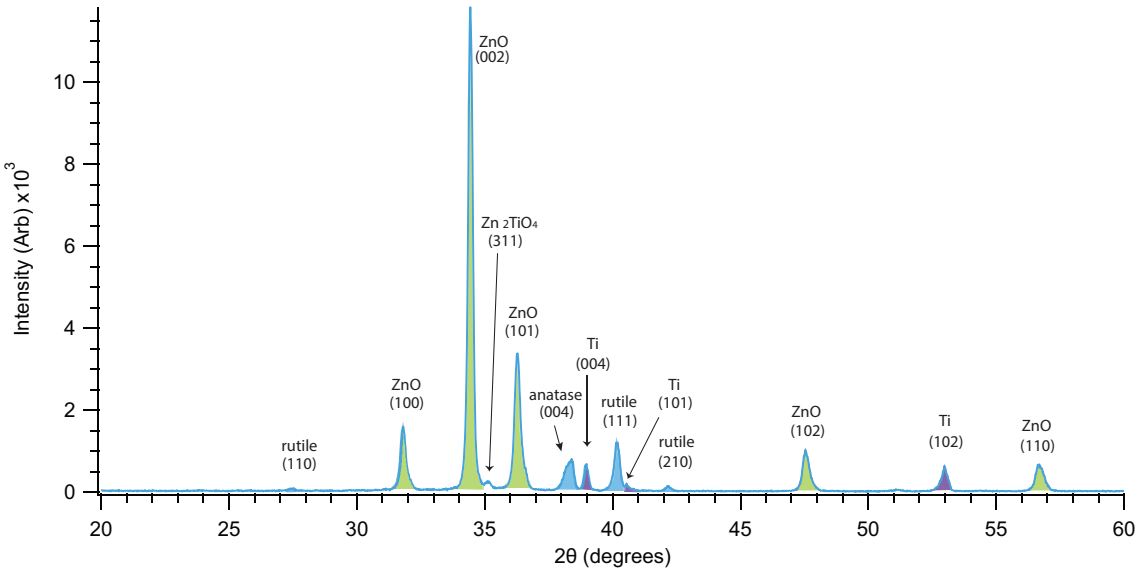

Figure 5.26: XRD plot of ZnO structures formed on a Ti foil in a KOH rich environment.

The crystal characterisation of the structure created was analysed utilising X-ray

diffraction. The XRD peak spectrum is shown in Figure 5.26, the peaks are very similar to the growth of ZnO without KOH. Indicating growth is preferential in the c-axis as it is with nanorods. The ZnO peaks have half the intensity than that of ZnO rods grown excluding KOH, the peak area magnitude of ZnO microstructure of the (0001) peak is 2770 arb. units compared to 4720 arb. units for the ZnO rods excluding KOH. This is due to the dense forest of 16 μm long ZnO rods on the Ti plate, whilst including KOH in the growth environment created dense large structures but does not extend as far out of the substrate. Thus, we can approximate the ZnO microstructure film thickness to be 8-10 μm, which is reasonable as the diameter of the ZnO gems have a similar size (4-7 μm).

The TiO_2 peak at 40.2° has a peak height almost three times larger than the TiO_2 formed under typical nanorod growth conditions, this indicates a thicker layer of TiO_2 has formed in the initial stage of growth, possibly due to the higher oxygen or OH^- content in the growth environment.

The Zn_2TiO_4 peak at 35.16° (311) has a peak height similar to that of ZnO rods, and is twice as narrow as the same peak of the ZnO nanorods crystal structure. The particle size calculated using the Scherrer equation for a K-value of 1 gives the value of the crystallite size as 24.4 nm, almost twice the crystallite size of Zn_2TiO_4 without KOH addition, 12.87 nm, shown in Table 5.2. A similar amount of zinc titanate is present compared with ZnO nanorods without KOH addition.

The photocurrent measurements carried out are shown in Fig 5.27, the xenon lamp utilised for illumination can be fitted with a ultraviolet transmitting, Hoya U-340 Filter, the spectrum of the illumination with filter in place is shown in Figure 2.10. The filter enables the UV energy conversion of the photoanode to be investigated, the intensity output of the xenon lamp with the filter fitted is 35 mW/cm^2. The filter has a maximum transmittance value of 75 %, and some UV intensity is lost compared to the full beam of the xenon lamp. The solid lines are the photocurrent densities measured against potential vs. Ag/AgCl, the values reach a maximum of 40 mA at 1.2 $V_{Ag/AgCl}$ with the full beam and 17 mA under UV irradiation. The onset potential can be considered as the flat band potential between the electrolyte and semiconductor, the onset potential is 0.056 V_{RHE} for the whole beam and 0.05 V_{RHE} under UV illumination. The value is very close to 0 V_{RHE}, close to the value

Material	(hkl)	2θ (°)	Peak height	Peak area	Crystallite size (nm)	d (Å)
ZnO	(100)	31.8	1608	410.8	38.27	2.814
	(002)	34.44	11831	2770.6	42.04	2.604
	(101)	36.28	3389	937.94	35.75	2.476
	(102)	47.54	1033	329.88	32.18	1.913
	(110)	56.66	678	274.25	26.41	1.624
Zn_2TiO_4	(311)	35.16	265.9	107.56	24.39	2.552
TiO_2	(004)a	38.4	811	362.58	22.27	2.344
	(111)r	40.2	1209	334.61	36.18	2.243
	(210)r	42.14	150	38.321	39.44	2.144
Ti	(004)	38.98	682.9	159.92	42.59	2.311
	(102)	52.98	639	190.45	35.25	1.728

Table 5.3: XRD analysis of ZnO structures grown with KOH addition. Average crystallite size of 32.61 nm. Lattice constants of ZnO are a = 3.2495 Å c = 5.2079 Å.

required to create an unassisted water splitting system. The near zero value of the flat band potential indicates the band edges of the material are higher (more negative) than the ZnO nanorods formed without KOH, and there is approximately a 50 mV difference between the Fermi level of the semiconductor microstructure and chemical potential of the electrolyte, i.e the redox potential.

The maximum output photopower density of the structure is 10.9 mW/cm^2 under full beam illumination and 7.4 mW/cm^2 under UV illumination, the maximum UV photoefficiency is 21.1 %. At 1.23 V_{RHE} the photocurrent density is 31.7 mA/cm^2 and 15.15 mA/cm^2 under full beam and UV illumination respectively. The 3.5 mW difference in photopower between the UV and full beam of the xenon lamp is due to the transmittance of the filter, cutting out a portion of the higher frequencies. The photocurrent of the material under full beam illumination at 1.2 $V_{Ag/AgCl}$ is over double the photocurrent of the material under UV illumination (filter fitted), the large difference suggests a small amount of sensitivity toward longer wavelengths of visible light, and not only just due to the reduced intensity of the lamp in the UV

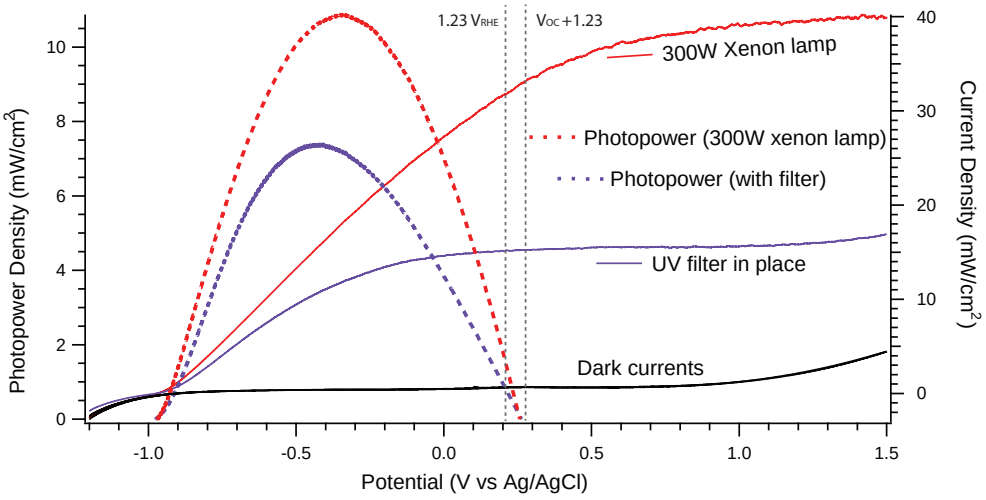

Figure 5.27: Photocurrent density plots (I-V curve, left axis) of the ZnO structures, red curve represents the photocurrent density of the material illuminated by a 300 W xenon lamp without filters; the purple curve represents the UV photoresponse, utilising a UV transmission filter in the xenon lamp beam.

spectrum.

Youn et al[255] created similar pyramid pits after etching a hydrothermally created ZnO bulk film, exposing Zn terminated faces. In the investigation of the pyramid pits, the PL spectra showed oxygen vacancy defects and Zn interstitial defects of the structure. If the morphology of the pits are indicative of the surface defects this would explain the improved photocatalytic behaviour. Electron paramagnetic resonance (EPR) measurements would provide experimental confirmation of oxygen vacancy defects in the structure.[256,257]

5.6 Conclusion

Vapour transport deposition is a direct route to create ZnO structures of varying morphologies, the growth temperature and carrier gas flow controls the diameter and structure of ZnO formed. Direct vapourisation of Zn powder consistently formed ZnO nanorods and are not inhibited by the seeding or substrate. ZnO rods formed on a Ti foil demonstrated high photopower densities and outperformed TiO_2 nanotubes with a larger surface area, which were expected to perform better than the ZnO structure. A Zn_2TiO_4 barrier layer is introduced at the roots of the ZnO rods, which encourage exciton separation and promote effective photocurrent flow.

With the introduction of KOH in the reaction conditions, microstructures of

ZnO formed. The doping of the ZnO effected the band structure of the material, enhancing the photoabsorption and electronic transport in the material. Unique multifaceted growth was exhibited in the formation of ZnO micro rods, either the encompassed potassium or increase in oxygen enhanced the growth rate of ZnO, and selective face growth with 6 fold symmetry.

Chapter 6

Zinc Oxide Nanotubes and Rods on Titanium Nanotubes

An improvement of photoelectrochemical properties by constructing a heterostructure photoanode composed of TiO_2-Zn_2TiO_4-ZnO is evident in Chapter 5. Further improvement is possible by increasing the surface area of this heterostructure; allowing a larger region of the photoanode to effectively separate charges after a photoexcitation. Here, the ambitious plan is to take advantage of the porous structure of vertically aligned TiO_2 nanotubes, which will serve as a substrate in conjunction with the effective vapour solid deposition technique to develop ZnO nanostructures. The unique vertical hollow heterostructure will have a large surface area to facilitate surface reactions. The large diameter channels allow transportation of the electrolyte close to the substrate, and a 3D interface layer of TiO_2/Zn_2TiO_4/ZnO encourages better charge separation. Figure 6.1 illustrates the steps of forming the TiO_2/Zn_2TiO_4/ZnO structure. Initially Zn condenses on the inner surface of the TiO_2 nanotubes creating a Zn_2TiO_4 coating following the topology of the TiO_2 nanotube substrate. ZnO oxide forms inside the coating as TiO_2 is limited, and the ZnO tubular structure grows as the vapour condenses inside and on the lips of the titania nanotubes.

Figure 6.2 (a)-(c) are the SEM micrographs showing the realisation of the tubular TiO_2/Zn_2TiO_4/ZnO structure, forming ZnO tubes contained in a Zn_2TiO_4 coated TiO_2 nanotubular array. Initially a TiO_2 nanotube array (a) is created *via* anodisation of a Ti foil, a brief VS reaction (b) fills the nanotubes with ZnO and

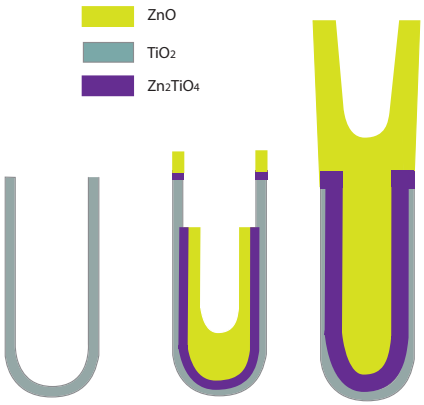

Figure 6.1: Concept illustration of the growth process mechanism during VS deposition of ZnO.

forms a Zn_2TiO_4 thin layer at the interface of the core/shell structure. A further 20 min VS deposition completely fills the TiO_2 nanotubes with rodular/tubular ZnO structures (c).

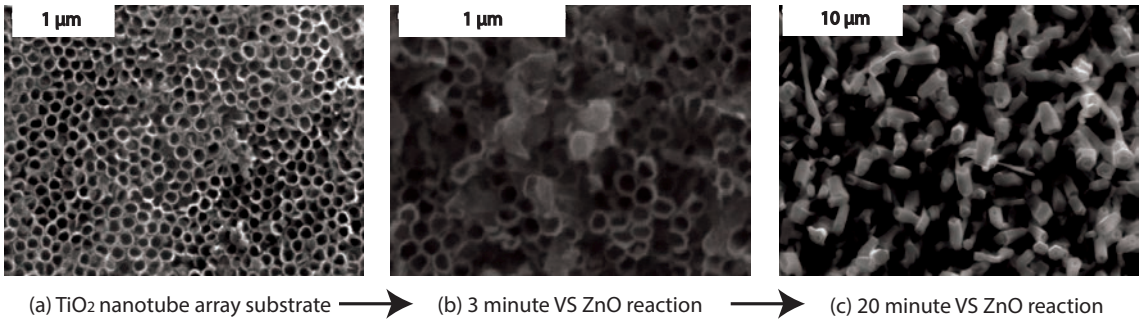

Figure 6.2: SEM micrographs of the series of steps taken to create a ZnO structure inside TiO_2 nanotubes. (a) the TiO_2 nanotubular array which serves as the substrate, (b) an initial vapour transport reaction fills the tubes with Zn_2TiO_4 and ZnO, and (c) a 20 mins VS reaction forms ZnO tubes.

Magnified SEM micrographs of the Zn_2TiO_4 coated titania nanotubes in Figure 6.3(a) shows that rodular growth of ZnO has yet to begin after an initial 3 min VS reaction at a reaction temperature of 650 °C. The inner lining of the tubes is brighter in the SEM micrograph, indicating a formation of an element with a different electronic structure than the titania tubes. Once rodular growth begins, the growth on the lips of the titania and in the bottom of titania occurs simultaneously; growth on the lips could be more dominant than at the centre. Either way, ZnO hexagonal tubes form on the surface, Figure 6.3(b), tubular growth is assisted by the titania nanotube framework and as the tubular ZnO grows, the diameter of the ZnO tubes enlarges due to the lateral growth of the ZnO.

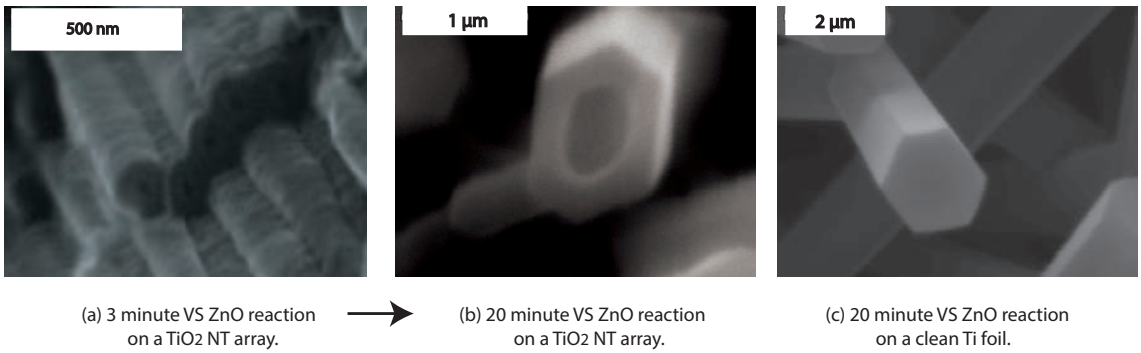

Figure 6.3: SEM micrographs of magnified sections of the two latter steps of the ZnO nanotube formation. (a) Shows the limited ZnO deposition and (b) shows the complete formation of ZnO. (c) Shows ZnO rods formed on a clean Ti foil.

Clear sharp edged hexagonal rods form if the same VS deposition conditions are applied to a clean Ti foil serving as substrate. Figure 6.3(c) shows ZnO deposited *via* VS on a polished Ti foil take the form of ZnO hexagonal rods and not tubular.

6.1 Material Synthesis

6.1.1 Titanium Dioxide Nanotubes

Initially a TiO_2 nanotubular array is created *via* anodisation; a polished titanium plate served as the anode and another Ti foil as a cathode. The electrolyte bath consisted of 2 % H_2O and 0.6 % NH_4F in ethylene glycol solution. A potential of 60 V is supplied between the electrodes (5 cm apart) through the electrolyte. The thickness of the titania nanotube array film depends on the length of time of the anodisation duration. An anodisation of one hour creates a thickness of 2 μm long tubes. Homogenous titanium dioxide nanotubes are highly ordered, SEM micrographs of the tubes are shown in Figure 6.4, the average outer diameter of the tubes are 133 nm $\pm$ 12.2 nm and inner diameter is 83.9 nm $\pm$ 15.9 nm.

The titanium dioxide nanotube array will serve as the substrate in the VS reaction, the TiO_2 nanotube array exposes a large surface area of TiO_2 where Zn_2TiO_4 can form during the introduction of Zn vapour.

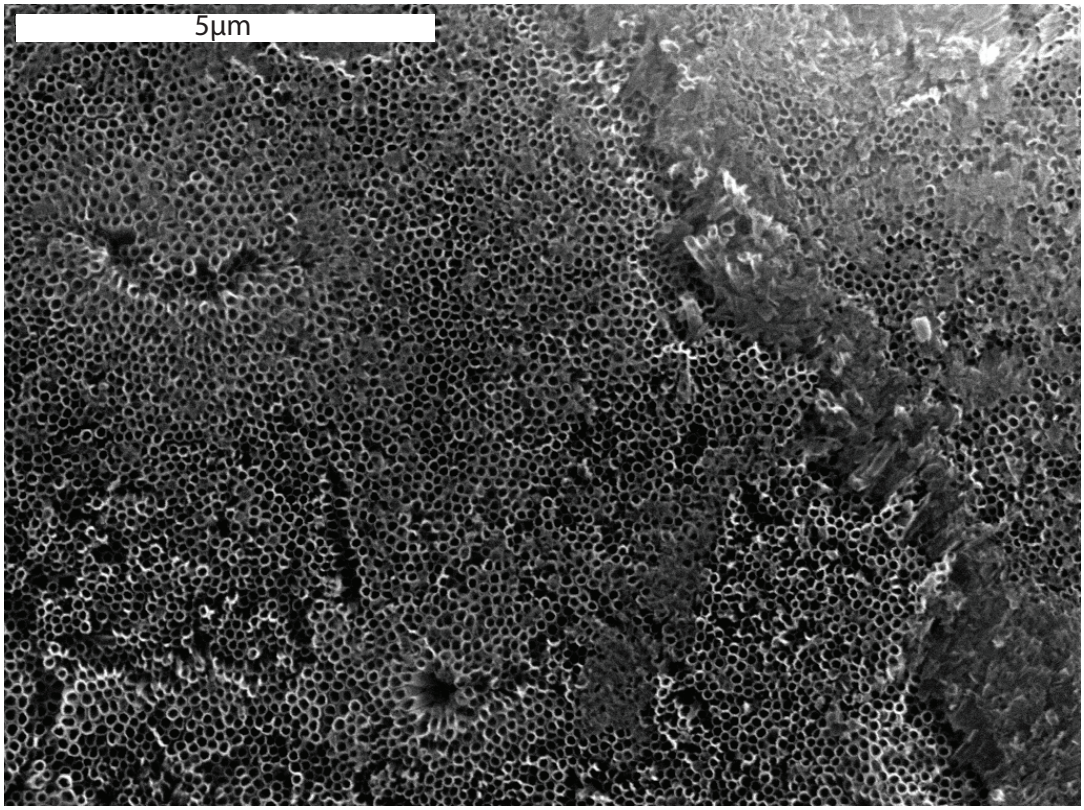

Figure 6.4: SEM micrographs of a high quality TiO_2 nanotube array formed *via* anodisation using 2 % H_2O and 0.6 % NH_4F in a solution of ethylene glycol.

6.1.2 Zinc Oxide Nanotubular Growth

Zinc Oxide VS growth is conducted in a quartz reactor within a tube furnace as described in chapter 3.

A TiO_2 NT array is placed on the top of an alumina (porous) crucible containing the Zn powder precursor. The crucible is placed toward the centre of the quartz reactor/furnace. The quartz reactor is evacuated to a pressure of 1.10^{-3} mbar. Ar is used as the carrier gas, with a flow rate of 120 SCCM. The temperature of the crucible is elevated to 650 °C, at a rate of 50 °C per min. This temperature is held until the condensation reaction is complete.

Initial Zinc Oxide Growth inside Tubes

A limited reaction helps elucidate the understanding of the initial formation of ZnO within the titania tubes. This is achieved through limiting the Zn precursor as well as maintaining the reaction temperature for a limited time. The growth is stunted if a carrier gas is not present (oxygen is carried by Ar), it is possible to quench the

reaction simply by eliminating the flow of Ar. 0.25 g of Zn precursor is placed in the crucible. The temperature of the reactor is ramped up to 650 °C and held for 3 mins. The Ar flow rate is eliminated and the reactor cools slowly.

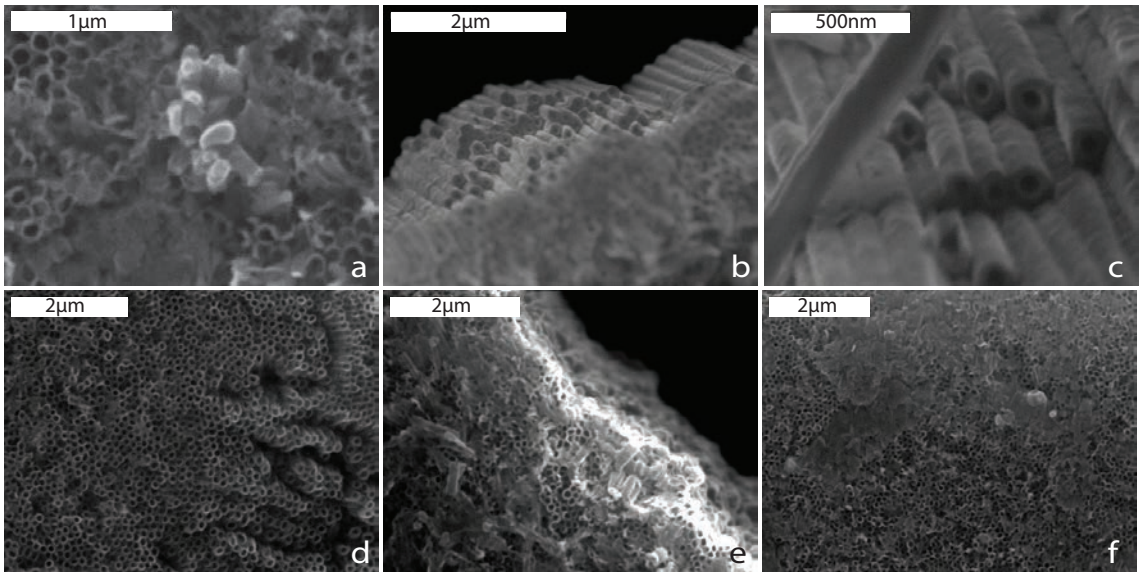

Figure 6.5: SEM micrographs of a TiO_2 nanotubular array coated with Zn_2TiO_4 during vapour deposition. A small amount of ZnO is formed at the bottom of the tubes by adopting a limited VS deposition. The various magnification of the micrographs are (a) ×20,000 (b) ×11,000 (c) ×35,000 (d) & (e) ×7500 and (f) ×6250.

From Figure 6.5, the TiO_2 NT array is still exposed; ZnO did not grow over the tubes. The ZnO must form within the tube or on the lips of the tubes. The energy dispersive X-ray (EDX) spectrum analysis shows a 50 % content of elemental titanium and zinc. In Figure 6.6 presence of Zn is clear from the peak at the K_α transition at 8.5 keV, whilst the ZnO structures are not visible in the SEM micrograph of the titania nanotubes after a limited deposition. The penetration depth of the electrons in the SEM is a few μm, the 50 % content of both metal elements implies that the TiO_2 is coated with Zn, and ZnO has formed within the tubular structure. It can be seen Figure 6.5(a) some growth of the ZnO has sprouted from the TiO_2 tubes; this accelerated growth could be due to the alignment of the ZnO initial seed growth. Preferential growth occurs in the [002] direction, if a considerable amount of ZnO attaches to the base of the titanium nanotube in this alignment, growth could be accelerated. Also from Figure 6.5(c) a contrast difference between the inner diameter of the tube and the outer diameter is clear. This could be due to the centre being coated with zinc titanate or zinc oxide, which will have

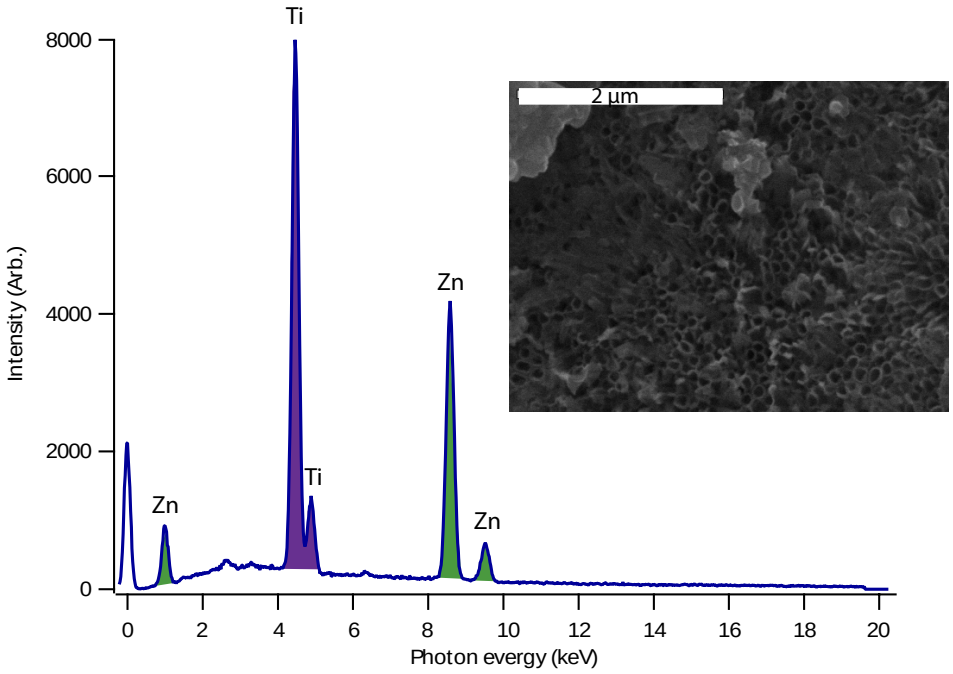

Figure 6.6: Energy dispersive X-ray spectrum of zinc titanate coated titania nanotubes containing a small amount of ZnO inside the tube. (inset is the SEM micrograph of the area sampled).

different electron scattering properties. An element resolved scan could not resolve the elemental structure at this magnification. The tubes exposed in the middle have a smaller inner diameter compared to the TiO_2 nanotubes imaged from above the film in Figure 6.5(d). Both outer diameters are very similar with a value of 130 nm ± 13 nm and the inner diameter of the exposed TiO_2 nanotube array is 80 nm ± 14 nm whilst the SEM micrograph exposing half the tube has an inner diameter of 47.7 nm ± 8.35 nm. The 30 nm difference suggests a 15 nm thick Zn_2TiO_4 film is present in the inner lining of the tube.

6.1.3 Growth of a Zinc Oxide Nanotubular Structure on a Titanium Dioxide Nanotube Framework

The reaction took place over 20 mins at a reaction temperature of 650 °C and 2 g of Zn precursor, the temperature was ramped up from room temperature to 650 °C at a rate of 50 °C/min. ZnO grown within the TiO_2 nanotubes formed novel morphologies. The Zinc oxide forms on the lip of the titanium dioxide nanotubes and from the bottom. As the ZnO tube/rod height becomes greater than the TiO_2 nanotube depth, the growth around the ZnO circumference is greater than in the

centre, forming a tubular hexagonal structure.

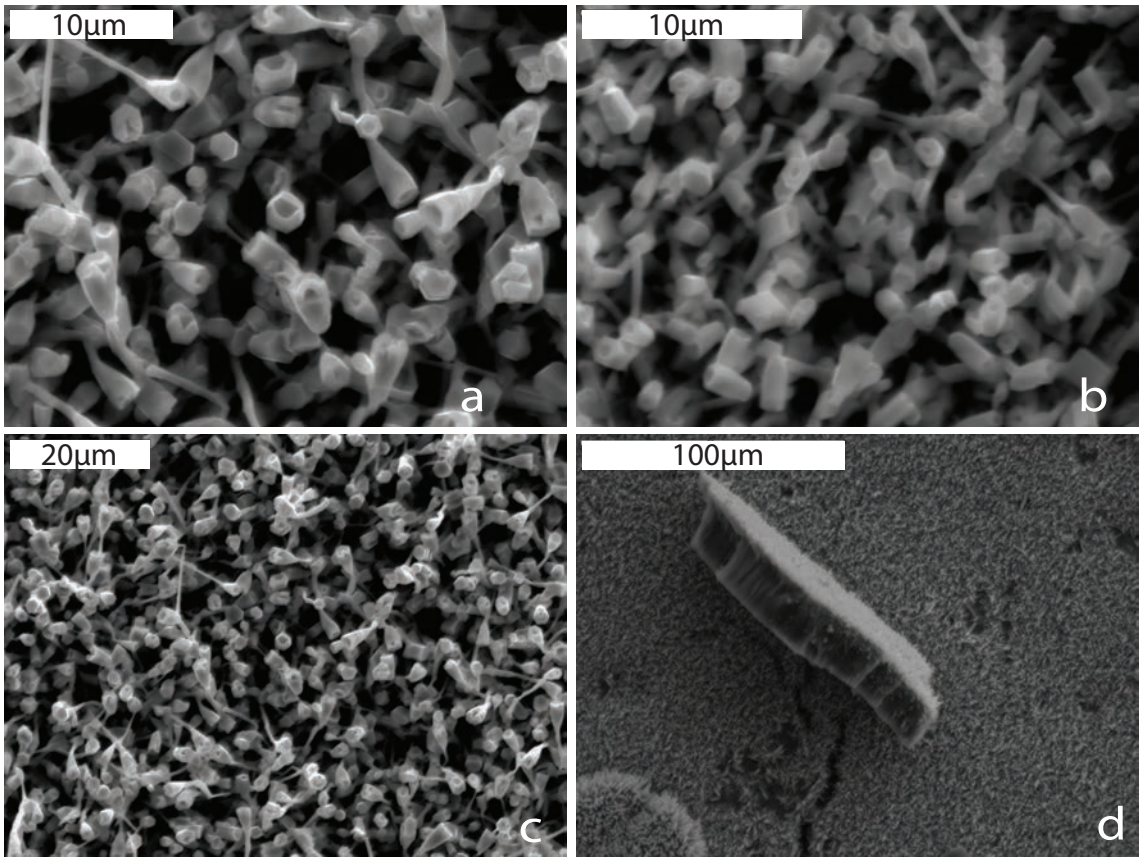

Figure 6.7: SEM micrographs of a ZnO tubular structures created *via* VS reaction at 650 °C, for a 20 min duration. (a) shows a ZnO nanotube at a high magnification (×2000) and (b) ×3000, coverage of ZnO tubes on the titania nanotube framework substrate is visible at lower magnifications (c) ×900 and (d) ×350 .

This is clearly seen from the high magnification SEM micrograph in Figure 6.7(a). The formation of ZnO tubular structures were unique and unexpected. The length of the ZnO structure is 19.36 μm ± 1.74 μm, and the diameter of the heads of the ZnO tubular structure is 1.75 μm ± 0.34 μm. The inner diameter is much smaller with a size of 368 nm ± 143 nm and varied significantly from one tube to another.

6.2 XRD analysis

X-ray diffraction (XRD) measurements were performed on three samples, one sample is a limited VS reaction on TiO_2 NT's, the second is the full VS reaction on TiO_2 NT's and the third is of ZnO rods formed on a Ti foil for comparison; these are shown in Figure 6.8. Figure 6.8(a) shows the XRD spectrum of a 3 min VS reaction in titania nanotubes, there is limited ZnO growth whilst a substantial amount of

Zn_2TiO_4 is present on the substrate. The TiO_2 (101) anatase phase is the prominent feature of the XRD spectrum. Increasing the growth duration and precursor material aligned ZnO nanotubular rods form in the (0001) direction, the spectrum is shown in Figure 6.8(b). The $\times 20$ magnified plot inset of the full spectrum shows that the Zn_2TiO_4 (220) content relative to the anatase (101) does not change as much as the ZnO (002). Table 6.1 shows the value of relative intensities of the Zn_2TiO_4 (220) and ZnO (002) planes with respect to the anatase (101) face, this indicates the formation of the Zn_2TiO_4 layer occurs in the early stages of growth, and that the Zn_2TiO_4 has formed on the inner surface of the TiO_2 nanotubes, limited by the available Ti cations on the surface. After further deposition (reaction duration) ZnO forms above the TiO_2/Zn_2TiO_4 heterostructure and Zn_2TiO_4 formation saturates.

The large intensity of the Ti (102) diffraction peak in the spectra (the peak at 53° with a peak height ranging from 300 counts to 1158 counts depending on the thickness of the nanostructure film) indicates the XRD sampling depth includes the substrate (penetration depth of X-rays). Due to the excellent penetration of X-rays through the materials, the concentration of each metal oxide component is directly proportional to the associated XRD peak intensities. The surface area of TiO_2 is related to the signal intensity of anatase and rutile in the XRD spectrum.

	TiO_2 (101) a	Zn_2TiO_4 (220)	ZnO (002)
3 min reaction	10	2.68	7.46
20 min reaction	10	4.26	200.37

Table 6.1: Ratio of relative intensities of peaks at a chosen face of three materials.

Tables 6.2 & 6.3 contain the XRD data of the ZnO nanotubular structures grown on TiO_2 nanotubes, for the initial reaction and the full reaction respectively. From this data we can assess the crystal properties of the structures created and compare with the data of ZnO rods formed on a Ti foil from Table 5.2 in Chapter 5. The crystallite size is calculated using the Scherrer equation (2.7), the crystallite size is the average size of a coherent scattering domain. Crystallite domain size could also be affected by the physical dimensions of the particles, if the dimensions of the particle are comparable to the crystallite size the calculated size will be a measure of the dimensions of the particle. For the 3 min growth the crystal sizes of ZnO

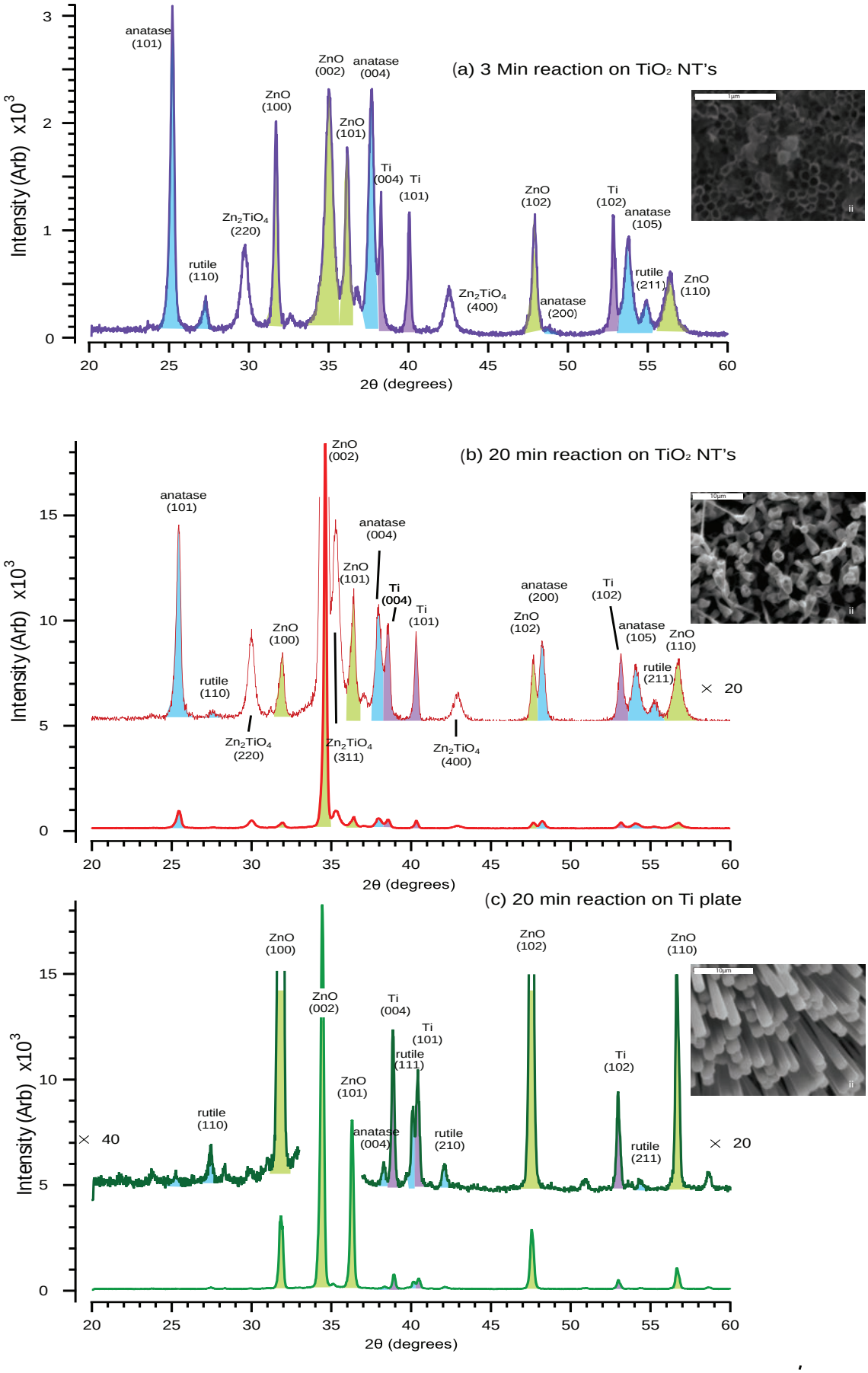

Figure 6.8: X-ray Diffraction pattern spectra for (a)i limited deposition of ZnO in a titania nanotube array, (b)i $TiO_2/Zn_2TiO_4/ZnO$ tubular structure and (c)i ZnO rods grown on a Ti foil (root heterostructure). Associated SEM micrographs of the materials are shown on the right.

at the 34.9° and 56.36° peaks are 14.9 nm and 13.9 nm respectively, and are much smaller than the crystal sizes of the surrounding peaks with an average of 30.7 nm. These peaks correspond to the (002) face and the {110} lateral faces. This indicates the growth in the [002] direction has begun, but the growth of the thin film has yet to reach the estimated crystallite size as the growth of the film is orientated in the [002] direction.

A ZnO thin film with a thickness of approximately 14 nm forms over the zinc titanate in the [002] direction determined by the crystallite size, matching closely to the inner diameter difference in the SEM micrographs of the 3 min growth reaction in Figure 6.5(a) compared to Figure 6.5(c).

Material	(hkl)	2θ (°)	Peak height	Peak area	Crystallite size (nm)	d (Å)
ZnO	(100)	31.6	2030	605.04	32.79	2.831
	(002)	34.9	2328	1536.41	14.94	2.571
	(101)	36.06	1788	609	29.0	2.491
	(102)	47.86	1166	397.17	30.2	1.901
	(110)	56.36	634	485.90	13.92	1.632
Zn_2TiO_4	(220)	29.66	884	526.95	16.32	3.012
	(311)	35.58	379.741	202.11	18.56	2.523
	(400)	42.46	500	340.63	14.81	2.129
TiO_2	[101)a	25.08	3102	990.59	30.17	3.551
	(110)r	27.18	406	207.44	18.93	3.2808
	(004)a	37.62	2330	1041.69	22.22	2.391
	(105)a	53.76	960	592.7	17.08	1.705
	(211)r	54.88	3644	252.04	15.55	1.673
Ti	(004)	38.2	1362	348.01	38.95	2.356
	(101)	39.98	1190	253.34	47.0	2.255
	(102)	52.76	1158	345.14	35.22	1.735

Table 6.2: XRD data of ZnO formed in nanotubes after a small reaction.

Under identical conditions, VS deposition of Zn vapour on a clean Ti foil results

in limited TiO_2 formation and accordingly less Zn_2TiO_4 formation. Figure 6.8(c) shows the XRD spectrum of aligned ZnO rods created *via* VS deposition on a Ti foil substrate for comparison. The peaks for TiO_2 and Zn_2TiO_4 are apparent at 40X magnification of the spectrum (left inset). The peak height for TiO_2 (004) anatase is 164 (counts) for ZnO rods on a thin film of TiO_2 on a Ti foil, whilst, for ZnO condensed in TiO_2 nanotubes the peak height increases by a factor of 14 to 2330 (counts), the volume (and therefore surface area) of TiO_2 present has increased significantly by utilising TiO_2 nanotubes as a framework for ZnO deposition. Since there is a larger surface area of TiO_2, there is consequently a larger volume of Zn_2TiO_4 formed at the interface between the condensed ZnO and TiO_2 nanotube framework. The Zn_2TiO_4 peak height has increases from 73 counts to 884 counts for the (220) peak at 29.7°, from ZnO forming on planar Ti foil to ZnO condensed in TiO_2 nanotubes.

Comparing these values to the intensities of the same peaks in full growth of ZnO nanotubes in TiO_2 nanotubes, it is evident the surface areas of TiO_2 and Zn_2TiO_4 have increased considerably compared to the Zn_2TiO_4 formed at the roots of ZnO rods grown on a planar thin film of TiO_2. Thus, a TiO_2 framework on which Zn_2TiO_4 forms at the initial stages of growth has increased the surface area of the TiO_2/Zn_2TiO_4/ZnO heterostructure interfaces

The ZnO (002) crystallite size is approximately 46 nm after a 20 min growth reaction. The large value of crystallite size for the ZnO nanotubes (46.3 nm) in the (002) compared to the surrounding peaks (average value of 24.3 nm) is indicative of long range crystallite domain order in the [002] direction. This is not true for ZnO nanorods formed on a Ti foil where crystal size is similar for each of the peaks with an average value of 37.3 nm, and crystallite domain size is equal in all directions whilst the growth of the crystal is preferential in the [002] direction, indicated by the high intensity peak in the (002) plane.

The relative intensity of the c-axis and lateral planes ($ZnO\frac{(002)}{(100)}$) corresponds to the aspect ratio of the rodular structures. Thus, a large relative intensity indicates longer rods and smaller diameter rods. The ZnO tubes formed in the TiO_2 nanotubes have a much higher $ZnO\frac{(002)}{(100)}$ intensity ratio ($ZnO\frac{(002)}{(100)} = 58$) compared to ZnO rods formed on a Ti foil ($ZnO\frac{(002)}{(100)} = 5.2$), this indicates the the aspect ratio of the

Material	(hkl)	2θ (°)	Peak height	Peak area	Crystallite size (nm)	d (Å)
ZnO	(100)	31.96	320	156.09	22.97	2.800
	(002)	34.62	18541	4525.16	46.26	2.591
	(101)	36.42	592.34	260.23	25.83	2.467
	(102)	47.68	284.65	104.21	32.19	1.907
	(110)	56.8	294.07	215.32	16.74	1.621
Zn_2TiO_4	(220)	30.02	422.63	247.56	19.05	2.977
	(311)	35.28	850	477.14	20.15	2.544
	(400)	42.94	147.42	115.14	14.83	2.106
TiO_2	(101)a	25.46	878.81	364.63	26.64	3.498
	(110)r	27.6	70.7	136.32	5.757	3.232
	(004)a	37.98	529.8	323.27	18.68	2.369
	(200)a	48.2	371.2	181.21	24.19	1.888
	(105)a	54.08	267.8	182.98	17.71	1.696
	(211)r	55.34	110.1	86	15.59	1.66
Ti	(004)	38.6	404.2	138.12	33.43	2.332
	(101)	40.32	411.1	120.41	39.21	2.237
	(102)	53.14	314.6	138.23	27.44	1.723

Table 6.3: XRD data of ZnO formed in nanotubes.

structure has increased by a factor of ten, and the ZnO tubes formed in TiO_2 nanotubes have a smaller diameter along the X-ray path (if length is assumed to be the same). From the SEM micrographs in Figure 6.7(b) the diameter of the tube closer to the TiO_2 nanotube array is 390 nm, this is consistent with the XRD peaks and the TiO_2 nanotubes restricted lateral growth of ZnO in the initial stages of the growth.

Still, the ZnO rods formed on a Ti foil ZnO$\frac{(002)}{(100)}$ intensity ratio is larger than the intensity ratio of ZnO powder ($\frac{(002)}{(100)} = 0.78$), the rods length to diameter aspect ratio is approximately 7, which is close to the dimensions measured (15.6 μm long with a diameter of 1.66 μm and aspect ratio of 9.4).

6.3 Photo-electrochemical Applications; the Splitting of Water

6.3.1 Experimental Analysis

The photoelectrochemical properties of the structures was experimentally examined in a photoelectrochemical cell (PEC) using a three electrode cell configuration as described in chapter 2.3.1. A potentiostat performs a potential scan (with respect to a saturated Ag/AgCl reference electrode) whilst measuring the photocurrent generated between the working (photoanode) and the counter electrode. The setup is shown in Figure 2.8. A reference electrode is used because the half-cell potential is well known.

6.3.2 Photoelectrochemical Performance of Photoanodes under different Illumination Sources

Photoanode Performance under Xenon light source Illumination

A light source, a 300 watt xenon lamp (Compact Illuminator 6000CI, ORC) with a focusing lens, acts as the solar simulator. The spectrum of a xenon light source is shown in Figure 2.9 in chapter 2.

1 M KOH in water serves as the electrolyte in the PEC cell; A basic electrolyte was chosen, instead of an acidic electrolyte, for the purpose of protecting the metal oxide nanomaterials such as ZnO which might suffer dissolution under acidic conditions. The oxidation reaction is the most demanding of the two reactions (OER and HER), as it's a 4 electron process. The advantage of shifting the O_2/OH^- potential upwards (more negative), by increasing the pH, is that it increases the overpotential of the photoanode, which will help to increase the rate of oxygen evolution. The optimum conditions for effective water splitting requires the fine balance of the reaction rate on both the anode and the cathode for the generation of H_2 and O_2 (HER and OER). The amount the O_2/OH^- potential is shifted is given by the Nernst equation, this is shown in equation 6.1, the same is true for the hydrogen H_2O/H^2 potential (equation 6.2).

$$E_{O_2/OH^-} = E^0_{O_2/OH^-} - 0.059 \times pH \quad (NHE) \tag{6.1}$$

$$E_{H_2O/H_2} = E^0_{H_2O/H_2} - 0.059 \times pH \quad (NHE) \tag{6.2}$$

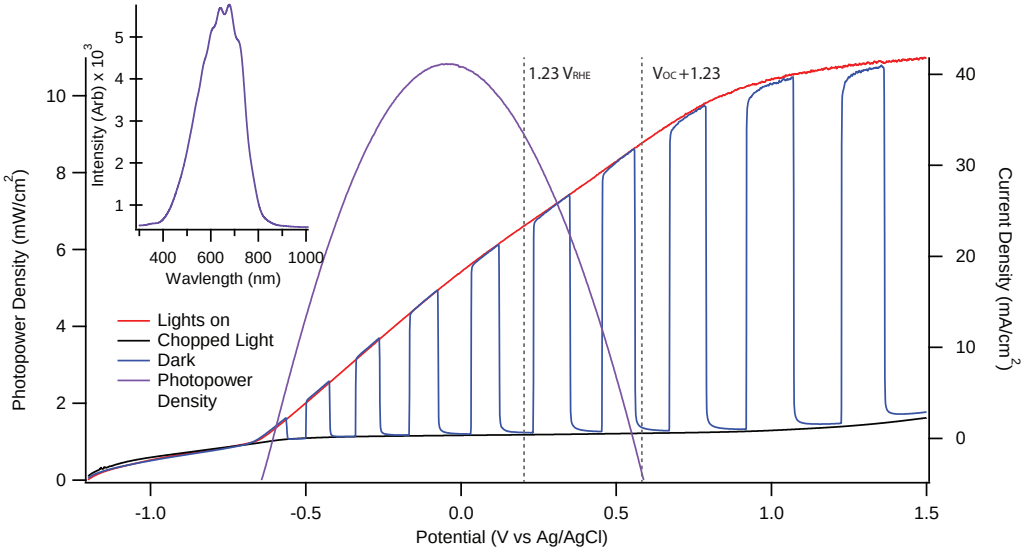

Figure 6.9: Current-Voltage (I-V) curve testing the properties of $TiO_2/Zn_2TiO_4/ZnO$ tubular structure, the red curve illustrates the photocurrent under illumination of a 300 W Xe lamp. The purple curve represent the power density. Inset: Spectrum of the xenon lamp.

A photocurrent density (I-V) plot is shown in 6.9 for the ZnO tubular heterostructure, with a photocurrent density of 32.6 mA/cm^2 at 1.23 V - V_{OC}, and a maximum power density of 10.8 mW/cm^2, significantly larger than materials reported thus far. The photocurrent density at 1.23 V_{RHE} is 25.4 mA/cm^2, and the onset potential is 0.59 V_{RHE}. The quality of the nanostructure film can be determined through the response time as it is indicative of electron and hole mobility within the material, and magnitude of the photocurrent density. The photoresponse is sharp, illustrated by the blue curve which represents the photocurrent under intermittently switched illumination. The xenon light source irradiance spectrum intensity is dominant in the visible light range and with the same overall intensity solar irradiance is 5 times more intense in the UV range, shown in Figure 2.9. Therefore, it is uninstructive to measure the efficiency of the photoanode with the intensity of the xenon light source. A UV transmission filter is employed to calculate the UV efficiency of

the photoanode material.

Photoanode Performance under Xenon Light Illumination with a UV Transmission Filter Fitted

The xenon light source is fitted with a transmission filter allowing only UV light to pass and is opaque to other wavelengths. The spectrum in Figure 2.10 shows the UV intensity peak, ranging from 300 nm to 400 nm, anything below 387.45 nm can be utilised in generating excitons (> 3.2 eV).

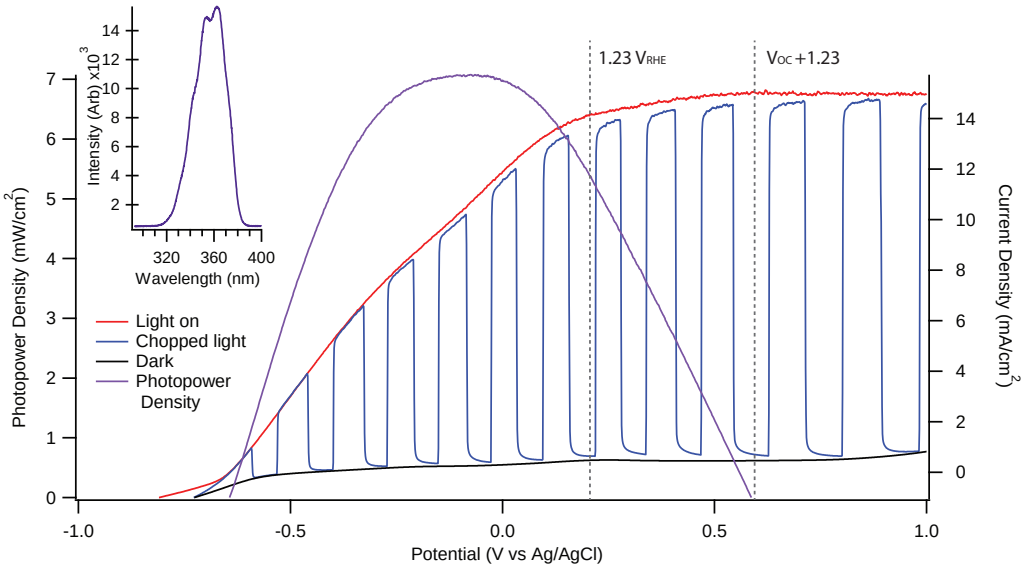

Figure 6.10: Photocurrent density and power density measurements of the TiO_2/ZnO tubular structure as a photoanode, under illumination of a xenon light source with UV filter (*Ultraviolet Transmitting, Visible Absorbing Filter, Hoya U-340*) in place. Inset: Spectrum of the illumination after passing the filter.

The photocurrent measurements are shown in Figure 6.10, where the red curve is the photocurrent density, the black curve is the dark current, and the blue curve represents the current under intermittent illumination. The short circuit photocurrent is 15 mA/cm^2 (1.23 V - V_{OC}), and 1.23 V_{RHE} is 14.2 mA/cm^2. The onset potential is the same as without the filter at 0.64 V_{RHE}. The purple curve is the power density output of the photoanode, and has a maximum photopower density of 7.077 mW/cm^2, which is only 30 % lower than the power density under full beam illumination.

The efficiency of the ZnO tubular heterostructure under the illumination of a xenon lamp with a UV transmitting filter (*Ultraviolet Transmitting, Visible Absorb-*

ing Filter, Hoya U-340) is significant, The ZnO tubular heterostructure demonstrates outstanding UV photoconversion, reaching a maximum photoefficiency of 20.22 %, under 35 mW/cm^2 UV illumination.

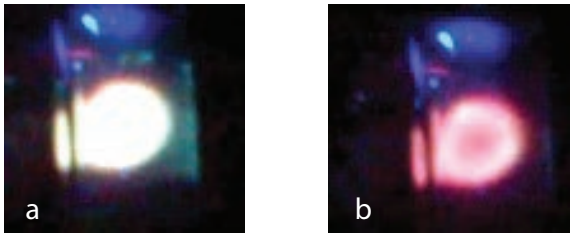

Figure 6.11: A voltage prevents a large portion of excitons created from recombining and re-emitting light. (a) is a photo of the beam spot on the photoanode surface under open circuit conditions and (b) shows that the beam spot dims drastically under applied potential (1.2 V_{RHE}).

The ZnO heterostructure is formally a 3D layered thin film structure with 3 different materials with the sequence of TiO_2, Zn_2TiO_4 and ZnO, the electrical field applied cross three films will depend on the film thickness, charge mobility and current flow within the films. ZnO is well know for its photoluminescence properties, with a large exciton binding energy. Under UV illumination white photoluminescence is observed, Figure 6.11(a) shows the beam spot on the substrate in electrolyte under open circuit conditions, and Figure 6.11(b) shows the same beam spot under a bias of 1.2 V, the beam spot wavelength has changed from white light to a near UV wavelength. With an applied potential across the three material heterostructure the electric field will drive charge movement and separation within the anode reducing exciton recombination therefore eliminating the white photoluminescence. The white light luminescence possibly originates from interfacial exciton transitions, ZnO white luminescence can also originate from radiative defects within the band gap emitting different colours to form white light. Without bias, native, defect free ZnO has a photoluminanscence peak with strong UV emission centred at 375 nm. Zinc oxide/zinc titanate composite materials produced by sol gel methods enhanced green emission in photoluminescence spectra as documented by Song et al.[258]

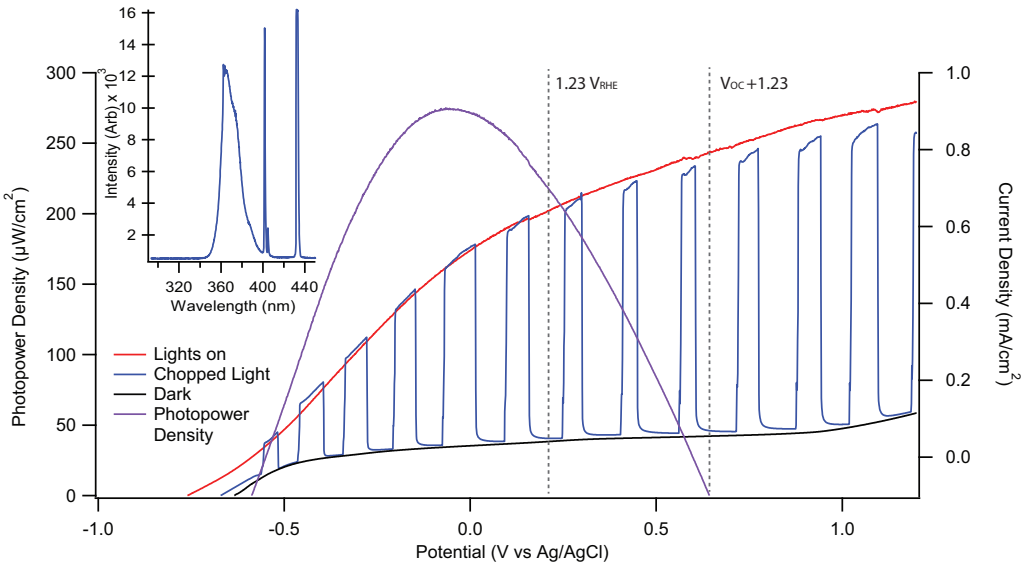

Figure 6.12: Photocurrent measurement (I-V curve) of the $TiO_2/Zn_2TiO_4/ZnO$ tubular structure under illumination of a low power (800 μW) UV lamp (CCFL). Inset: Spectrum of the CCFL lamp.

Photoanode Performance under Cold Cathode Fluorescent Light (CCFL) Illumination

The low power absorption of UV light can give further insight into the UV sensitivity of the photoanode material. For low power UV excitation analysis, I used a 36 W (4× 9 W) cold cathode fluorescent (CCFL) lamp enclosed light source with the PEC inserted in the light chamber. The light intensity measured in the chamber is approximately 800 $\mu W/cm^2$. A broad intense peak centred at 370 nm contributed to the major light output, and surpasses the wavelength required to excite an electron hole pair (3.35 eV) in all three materials of the heterostructure by ∼0.1 eV. The photoanode is immersed in the electrolyte, and the front and back surfaces are illuminated inside the light cavity. The photoelectrochemical measurements are conducted on a large surface area (2.5 cm^2 each side), illustrating the nanotubular structure is formed homogenously on the surface of the Ti foil substrate.

The photocurrent densities are plotted in Figure 6.12; the red line represents the photocurrent generated by the photoanode under illumination, the black line shows almost zero current under no illumination. The blue curve is the photocurrent of the photoanode under intermittent illumination, and the purple parabola represents the output photopower density ($\mu W/cm^2$) of the photoanode structure. A cold cathode fluorescent lamp light source (350-400 nm) showed 34.4 % (P_{max} = 275 $\mu W/cm^2$)

photoconversion efficiencies. The response time is fast, illustrated by the blue curve in the figure where lights are turned on and off in a fraction of a second. The photocurrent at 1.23 V_{RHE} is 0.65 mA/cm^2, the short circuit photocurrent is 0.79 mA/cm^2 and the onset potential is 0.59 V_{RHE}.

Comparison of Various Photoanodes

Figure 6.13 illustrates the I-V curve of the ZnO grown in TiO_2 nanotubes and compares between various materials serving as photoanodes. The photocurrent density achieved with the $TiO_2/Zn_2TiO_4/ZnO$ structure surpasses both TiO_2 nanotubes as well as ZnO nanorods formed on a Ti foil, with a value of 42 mA/cm^2 compared to 20.1 mA^2 and 31 mA^2 respectively at 1 $V_{Ag/AgCl}$.

The initial limited VS reaction showed a similar performance to that of titanium nanotubes, this implies the zinc titanate does not contribute much to the enhanced photocurrent exhibited by the $TiO_2/Zn_2TiO_4/ZnO$ heterostructure and that zinc oxide is the photoactive material of the photoanode. The three tier heterostructure is the reason for the better overall performance of the $TiO_2/Zn_2TiO_4/ZnO$ heterostructure due to improved charge carrier separation and mobility.

Inset of Figure 6.9 is the corresponding photopower output density plotted against potential (vs Ag/AgCl) and the photopower output density of the TiO_2-Zn_2TiO_4-ZnO heterostructure. Efficiency is clearly improved compared to both ZnO rods on a titanium plate as well as titania nanotubes. A comparison of photoelectrochemical data in Table 6.4 shows the $TiO_2/Zn_2TiO_4/ZnO$ heterostructure has enhanced properties compared to the other materials. The maximum power density of the ZnO in TiO_2 nanotubular heterostructure reaches 11.36 mW/cm^2 compared to 6.42 mW/cm^2 maximum power density of TiO_2 nanotubes.

An initial VS deposition of ZnO formed a thin film of Zn_2TiO_4 on the inner surface of titania nanotubes. Controlling the parameters and limiting the VS deposition creates a TiO_2-Zn_2TiO_4 structure with a 3 min ZnO growth reaction. The photoelectrochemical performance of the coated titania tubes is slightly less than the TiO_2 nanotubes, inferring the Zn_2TiO_4 is not the primary photoactive material generating large photocurrent densities. The surface area of the semiconductor increases the oxidation reaction area and area of absorption. The significant increase

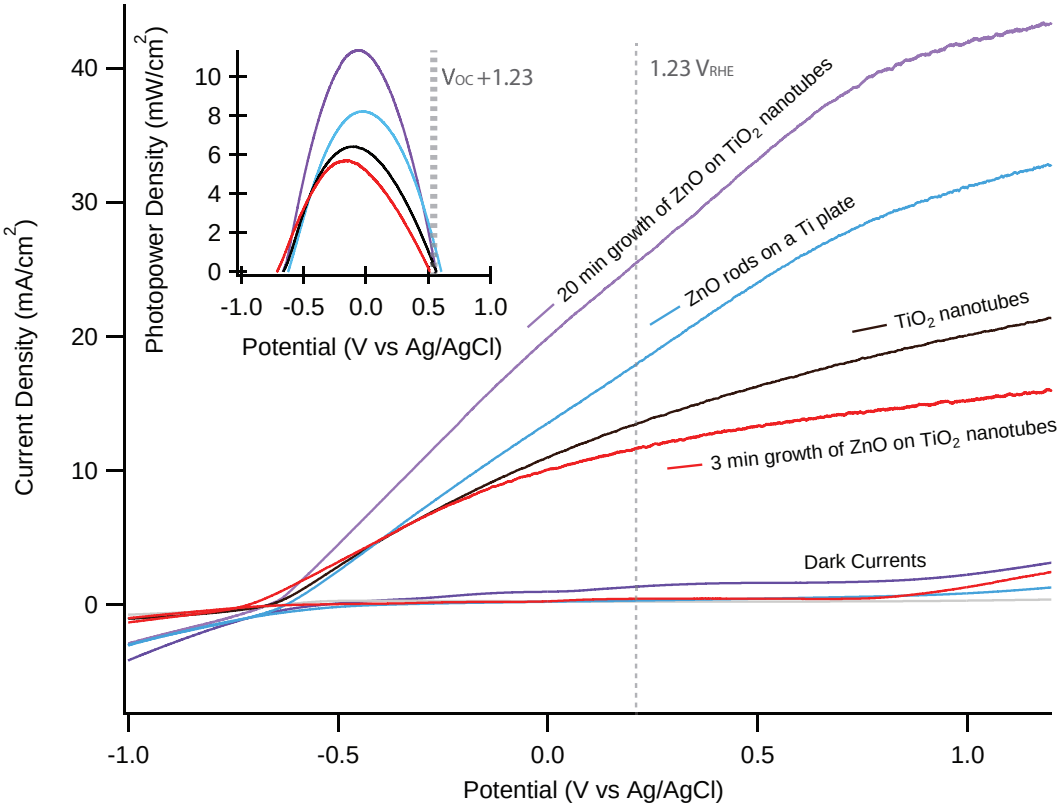

Figure 6.13: Photocurrent measurements, I-V Curves, of $TiO_2/Zn_2TiO_4/ZnO$ tubular structure, Zn_2TiO_4 coated titania nanotubes, ZnO rods formed on a polished plate and a TiO_2 nanotube array under illumination by a Xe light source. Inset is the power density output (vs. Ag/AgCl) of each of the materials.

in photocurrent and power density of the ZnO nanotubular rods formed over the Zn_2TiO_4-TiO_2, is due to a combination of increased surface area and reduced exciton recombination.

Material	P_{max} (mW/cm^2)	$I_{1.23V_{RHE}}$ (mA/cm^2)	$I_{1.23V-V_{OC}}$ (mA/cm^2)	V_{OC} (V)	$I_{1V_{Ag/AgCl}}$ (mA/cm^2)	V_{fb} (V)
ZnO nanorods on a Ti foil	8.23	17.83	26.04	-0.624	31.03	0.399
TiO_2 nanotubes	6.42	13.45	16.85	-0.664	20.09	0.359
3min reaction on TiO_2 NT's	5.72	11.61	13.33	-0.714	15.17	0.309
20min reaction on TiO_2 NT's	11.36	25.39	34.81	-0.666	41.91	0.357

Table 6.4: Photoelectrochemical data for the variety of photoanodes assessed. The $TiO_2/Zn_2TiO_4/ZnO$ tubular structure outperformed all others.

Photoelectrochemical water splitting efficiency of the $ZnO/Zn_2TiO_4/TiO_2$ heterostructure is higher compared to ZnO nanorods and TiO_2 nanotubes. High temperature synthesis of a ZnO nanostructure in a TiO_2 nanotubular array has formed a zinc titanate coating within the inner walls of the tubes, the ZnO nucleates on the zinc titanate and c-axis crystal growth dominates Zn condensation. The large surface area of the inner walls of the TiO_2 nanotubes results in the formation of a larger surface area of the $TiO_2/Zn_2TiO_4/ZnO$ heterostructure junction. The high crystallinity in the c-axis of the ZnO contributes largely to the high electron mobility, and also acts as a wave guide for incoming photons which can be absorbed closer to the heterostructure.

The barrier layer at the $ZnO/Zn_2TiO_4/TiO_2$ interfaces reduces the exciton recombination rate, thereby producing a larger flux of electrons, with energies capable of reducing the water that can travel to the platinum counter electrode. The electron and hole separate after an electron tunnels or is transported into the TiO_2 layer; the electron cannot overcome the potential barrier to recombine with the hole. The hole enters the electrolyte to efficiently oxidise the water.

The position of band gaps for the application of water splitting are advantageous. The conduction band edge of anatase is close to the reduction potential of water, whilst the conduction band and valence band of Zn_2TiO_4 are ideal for photoreduction of water, i.e. reduction potential for hydrogen generation is between the bands. Both anatase and Zn_2TiO_4 have a band gap of 3.2 eV and ZnO has a band gap of 3.3 eV respectively. Taking into account the peak energy of the solar spectrum is 2.5 eV and the requirement of 1.23 eV to split water, all three materials are suitable candidates as photoanodes for photocatalytic water splitting.

6.4 Conclusion

Here, I have demonstrated a 3D architecture of $TiO_2/Zn_2TiO_4/ZnO$ photoanode shows large photoefficiencies, and outperformed ZnO rods formed on a Ti foil as well as TiO_2 nanotubes. The increase in surface area of the Zn_2TiO_4 barrier layer sandwiched between the ZnO nanorod photoabsorber and TiO_2 thin film, discourages recombination of electron and hole pairs over a larger area. The higher density

of photoexcited electrons can then be utilised in the hydrogen evolution reaction on the Pt counter electrode. This is achieved by depositing ZnO *via* a vapour transport mechanism into a TiO_2 nanotubular array. At the junction of ZnO and TiO_2, Zn_2TiO_4 is formed unilaterally by thermal oxidation. The Zn_2TiO_4 barrier layer is composed of a thin film, small enough for electrons to tunnel from the ZnO CBM into the TiO_2 CBM under a bias, whilst the higher CBM of Zn_2TiO_4 restricts backflow of the electrons.

Chapter 7

Novel Deposition Methods - AACVD and CBD and the Formation of Novel Nanostructures

A deposition process is affected by the delivery of the nutrients for the growth of nanomaterials and there is a fine balance between delivery and the growth rate. Here, I have developed effective aerosol and aqueous solution deposition methods for achieving low temperature delivery of the growth particles through aerosol assisted CVD and chemical bath deposition, which allows us to grow nanomaterials either in ambient conditions or in a solution. An advantage of low temperature growth includes less restriction and a wide range of materials can be used as a substrate.

A sequential method of VS deposition followed by AACVD was developed to create hybrid metal oxide nanostructures, in order to develop interfaces with interesting electronic properties for improving light absorption and charge separation. A ZnO mesoporous thin film deposited by direct AACVD, illustrates the versatility of the technique and the possibility of depositing a variety of thin metal oxide films.

Chemical bath deposition produced unexpected results, creating ZnO tubular structures in addition to vertically aligned nanorods, depending on the properties of the seeding layer. The temperature of the substrate remain below 100 °C. Thus, substrate choice is larger; polymer, glass, paper and metal foil can all be adopted

as substrates.

7.1 Aerosol Assisted Chemical Vapour Deposition (AACVD)

The vapour deposition setup is altered to include the additional function of aerosol assisted vapour deposition. The principle and setup of AACVD are explained in chapter 2, in which an aerosol vapour is created *via* ultrasonic vibrations of a solution. The aerosol vapour is carried by inert gas to the reaction zone. The reaction zone is at a temperature such that the vapour will decompose and solidify onto the hot surface. There are two methods of heating to accomplish this; a cold walled horizontal bed configuration, and a hot wall reactor.

In a cold wall horizontal bed reactor configuration, the substrate is placed on a heating block which is maintained at the reaction temperature. In this case nucleation of the metal oxides is concentrated on the surface of the substrate, the solidification and growth occurs solely on the substrate surface. Since the vapour is a very fine particle mist ($\sim \mu$m's), the growth is homogenous and controllable.

The hot wall reactor configuration utilises a horizontal tube furnace, in which case the reaction zone is larger, but temperature control is of a higher accuracy. The drawback is that the quartz reactor is also at the temperature required to nucleate and oxidise the vapour; such that the inner surface of the quartz tube will be heavily coated by the reactants. The solution has a limited capacity, a substantial quantity of which will be wasted coating the quartz reactor.

AACVD is an emerging deposition technique; the versatility of the technique allows a variety of material, organic and non-organic, to serve as a precursor for deposition. Polymer precursors can create thin films, with hydrophobic properties,[167] and tungsten solutions can create tungsten oxide thin films,[259,260] $ZnFe_2O_4$ nanostructures[261] and ZnO nanowires doped *in situ* with VS deposition with aluminium.[262]

7.1.1 ZnO Nanorods Enhanced Photocatalytic Behaviour Attributed to TiO_2 Particulate Coverage

Hybrid materials have the following advantages over pure metal oxides, 1) It becomes possible to widen the wavelength of light absorption. Metal oxides with different band gaps can be designed and constructed within the 3D hybrid materials with the consequence of broad absorption and possibly full solar spectrum absorption. 2) It is possible to construct tandem structures with appropriately aligned Fermi levels and band edges that can result in a device with higher electrical potential than a pure metal oxide device. 3) within the hybrid materials, electronic junctions, such as p-n junctions normally exists at the interfaces between different materials. Such junctions facilitate a built-in electrical field which always helps for charge separation within the region. Careful design of heterostructures with precise control of the 3D metal oxide composition offers the possibility of a comprehensive optimisation of the materials for harvesting solar energy. Here, the deposition of TiO_2 nanoparticles on a ZnO nanorodular array through the use of a combination of AACVD and VS for creating hybrid heterostructures demonstrates the versatility of the technique described.

ZnO has a higher electron mobility than TiO_2, whilst TiO_2 is stable in a basic electrolyte solution. Using TiO_2 as a photoabsorber and an oxidant for water and the ZnO nanorod array as an ordered electron pathway; the performance of the photoanode is predicted to increase. Photogenerated electrons created in the TiO_2 nanoparticles are injected into the conduction band of ZnO under a bias. The performance could be reduced with increasing TiO_2 particle size, and denser coverage of ZnO rods. Due to an increase of the electrons path in the TiO_2 and an increase in the chance of recombination. The ZnO will also undergo photoabsorption and exciton creation. TiO_2 nanoparticles decorating ZnO rods can significantly increase the surface area at the semiconductor/electrolyte interface which will enhance the oxidation reaction on the surface of the photanode.

Surface modification of TiO_2 and ZnO nanostructures are heavily researched.[263–266] For DSSC applications, the reasons are two fold; 1) increased surface area improves dye loading which facilitates higher rates of redox reactions at the electrode surface, and 2) sensitisation by incorporating a semiconductor with a larger absorption band-

width that utilises visible light. A surface modified structure can improve the local charge separation if the surface modifier band edges are higher than the framework material, culminating in a favourable charge injection scenario, as well as spatial separation of excitons close to the surface of the two media. The charge lowers into the conduction band of the framework structure and will migrate the circuit to the counter electrode. A higher crystalline framework structure enhances electron transport properties.

Utilising TiO_2 NP's for surface modification of ZnO extends the surface area of the structure compared to that of an unmodified ZnO structure, either by filling tubular structure[265] or interstitially between rodular structures.[267] The absorption bandwidth is not an important factor in this case, since the TiO_2 and ZnO have almost identical band gaps with a slight difference in their Fermi levels. Covering the surface of ZnO rods with TiO_2 nanoparticles increases the surface area and improves local charge separation at the TiO_2/ZnO interface.[268,269] However it does not improve charge injection and light absorption.

Additionally a thin coating of TiO_2 can enhance the lifetime of the ZnO rods,[270] which is unstable in highly acidic solution. The photoelectrode lifetime is a key issue in the construction of a practical PEC cell. Photocorrosion of ZnO under UV illumination contributes further to the instability of ZnO rods.

7.1.2 Sample Preparation

ZnO rods were formed *via* VS deposition with a Ti foil serving as the substrate. The substrate is placed on the lips of a porous alumina crucible. The Zn powder precursor is positioned underneath the substrate. The alumina boat is inserted into the centre of the quartz reactor and tube furnace. The quartz tube is evacuated with a rotary pump and Ar flows through the reactor at a rate of 100 SCCM. The furnace achieved a temperature of 650 °C at a temperature ramp up rate of 50 °C/min. The temperature is held for 20 mins.

AACVD growth of TiO_2 particles on the ZnO rods was carried out under a controlled environment. The aerosol is created from a titanium solution in a beaker under the influence of ultrasonic vibration at room temperature. Ar (220 SCCM) carrier gas is used to drive the aerosol into the reaction zone, and maintain the system

pressure. The exhaust gas was purged through a liquid nitrogen trap before being released. The aerosol solution consisted of 0.6 ml to 6 ml titanium tetraisopropoxide (TTIP) dissolved in 50 ml methanol solvent depending on the coverage required.

ZnO rods on a Ti foil served as the substrate in this configuration, and a temperature of 550 °C is maintained until the precursor solution is exhausted.

7.1.3 Material Analysis, EDX and SEM

The samples of ZnO rods decorated by TiO_2 were investigated under the SEM in Figure 7.1. Figure 7.1(a) i-iii shows SEM micrographs of the ZnO rod array at different magnifications before the decoration of TiO_2. The average diameter of the ZnO rods are 1.11 μm ± 110 nm, the hexagonal morphology is an indication that the ZnO growth is preferentially aligned in the c-axis.

Controlling TTIP concentration in methanol alters the mass deposition of titania particles. 50ml of solution was used as a precursor, and the concentration of TTIP determined the TiO_2 particle coverage. The AACVD deposition was carried out until the precursor was exhausted. Figure 7.1(b) i-iii shows the SEM micrographs of ZnO rods (1.287 μm ± 0.12 μm in diameter) decorated lightly with TiO_2 nanoparticles (395 nm ± 41 nm in diameter) at three magnifications. The titania is faintly visible in the SEM micrographs, the ZnO rods have formed a well ordered array across the surface of the Ti foil, with a high density and vertical alignment (Figure 7.1(b) ii).

With increasing elemental titanium content (EDX quantitative analysis) NP aggregation occurs. Figure 7.1(c) i-iii show the titania decorated ZnO rods with a 4 % Ti content; the rods have a diameter of 1.063 μm ± 0.12 μm and the TiO_2 particles are clearer to observe in the micrograph. The TiO_2 NP's have a diameter of 416 nm ± 131 nm, which is consistent with previous Ti concentrations. The aerosol dispersed by the agitation of TTIP in methanol consists of $\sim$ 400 nm sized particles of TiO_2 once the reaction zone has been reached. The lower magnification SEM micrographs show that the rods are dense and evenly formed over a large area. For 8 % Ti content the ZnO rods have a diameter of 1.326 μm ± 83 nm with a TiO_2 average particle size of 460 nm ± 105 nm.

As the concentration of Ti content increases to 12 % coverage, shown in the SEM micrographs in Figure 7.1(d) i-iii, the NP's have aggregated at the top of rods

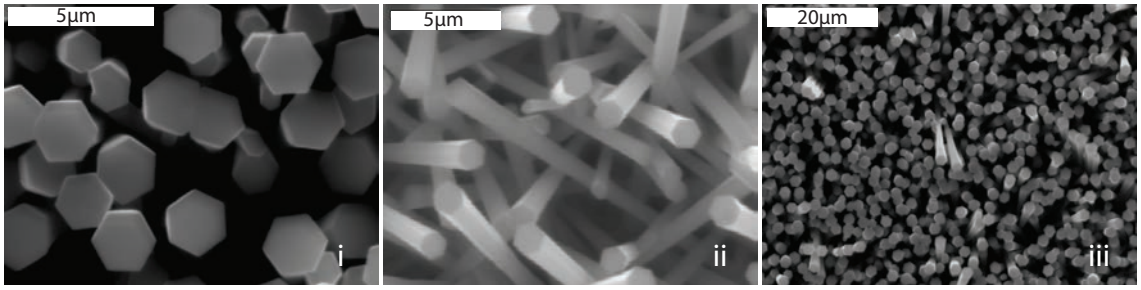

(a) ZnO rods.

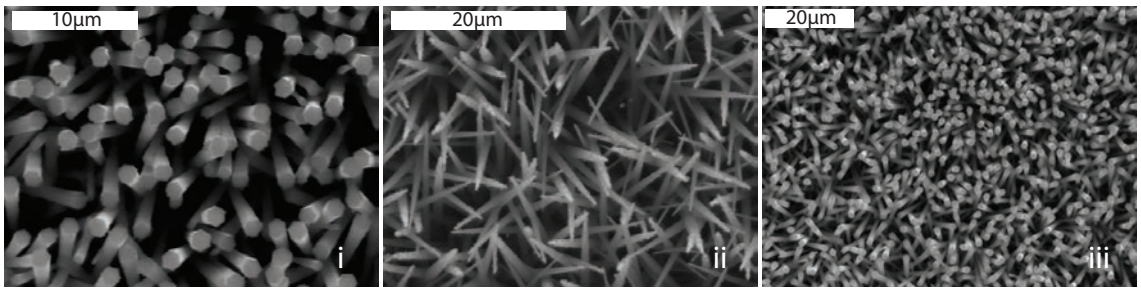

(b) ZnO rods with a 0.5% Ti content

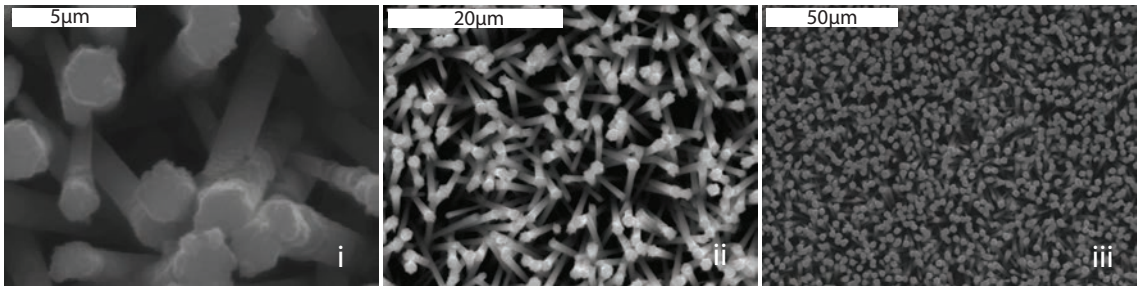

(c) ZnO rods with a 4% Ti content

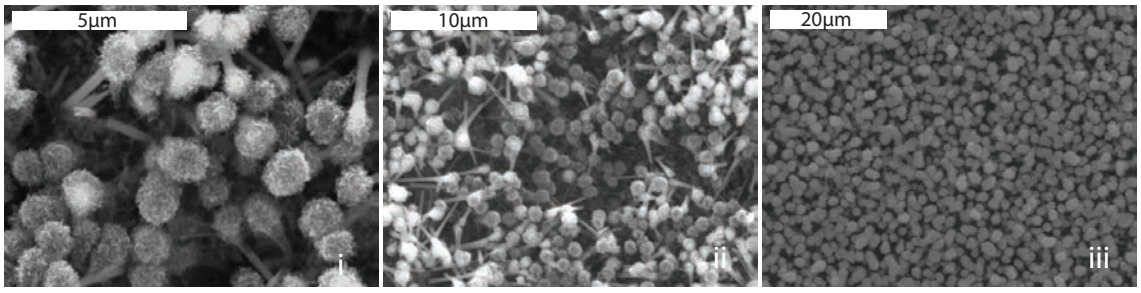

(d) ZnO rods with a 12% Ti content

Figure 7.1: SEM micrographs of ZnO rods grown *via* VS deposition (a) at various magnifications of i-×3,500, ii-×3,000, iii-×750, and with various AACVD depositions of TiO_2 particulates ranging from 0.5 % (b) i-×1,500, ii-×1,200, iii-×550, 4 % (c) i-×3,000, ii-×1,200, iii-×350, and 12 % (d) i-×4,500, ii-×1,750, iii-×750, Ti content overall. The titania is noticeable in the SEM micrographs, as concentration increases.

which is clearly seen in Figure 7.1(d) i. At lower magnification (ii-iii) the density of the rods show they are homogenously dispersed across the surface. The flow rate of Ar determines the occupation time of the aerosol in the condensation zone, with a high flow rate (220 SCCM) the aerosol has limited time to reach lower section of the rods and aggregate on the top, increasing the surface area of the top. Thus, the particles have a larger probability of condensing on the top of the rod. This has created a TiO_2 bulb on the top of the rod with a larger diameter of 1.037 μm $\pm$ 0.091 μm; the ZnO rods serving as the substrate have a smaller diameter initially compared to previous samples with a 367 nm $\pm$ 50 nm diameter. The associated EDX spectruma for each of these materials are plotted in Figure 7.2, the Ti and Zn peaks are labelled and show the increasing Ti $K_{\alpha,\beta}$ peak areas as Ti coverage increases. Inset of Figure 7.2 is an example of an area sampled by EDX,

Figure 7.3 shows an elemental map using EDX of an area of the sample where flowering ZnO rods are decorated with TiO_2 nanoparticles. Significant elemental Ti is adhered to the surface of the flowering ZnO rods. This shows the Ti detected by the EDX analysis is of the decorated Ti on the ZnO, rather than the substrate.

7.1.4 Photoelectrochemical Analysis of Structures Created

In order to investigate the effect of TiO_2 decoration of ZnO rods for the purpose of a photoanode, photoelecrochemical analysis was performed in a three electrode photoelectrochemical cell; the potential is controlled *via* a potentiostat simultaneously measuring the photocurrent generated at the Pt counter electrode. A saturated Ag/AgCl reference electrode is utilised during the current-voltage (I-V) measurements. The photocurrent is proportional to the hydrogen generated ($2e^-$ produces one hydrogen molecule). The photocurrent characteristics define the quality and efficiency of the photoanode material. A 1 M KOH in deionised water serves as the electrolyte. A 300 watt xenon light source (Compact Illuminator 6000CI, ORC) with a focusing lens acts as the solar simulator. The photoelectrochemical setup is discussed in Chapter 2.3.1, which shows the photoelectrochemical cell and positions of the electrodes.

I-V curves for the various concentrations of TiO_2 decorated ZnO rodular array photoanodes are shown in Figure 7.4, the black curve represents bare ZnO rods,

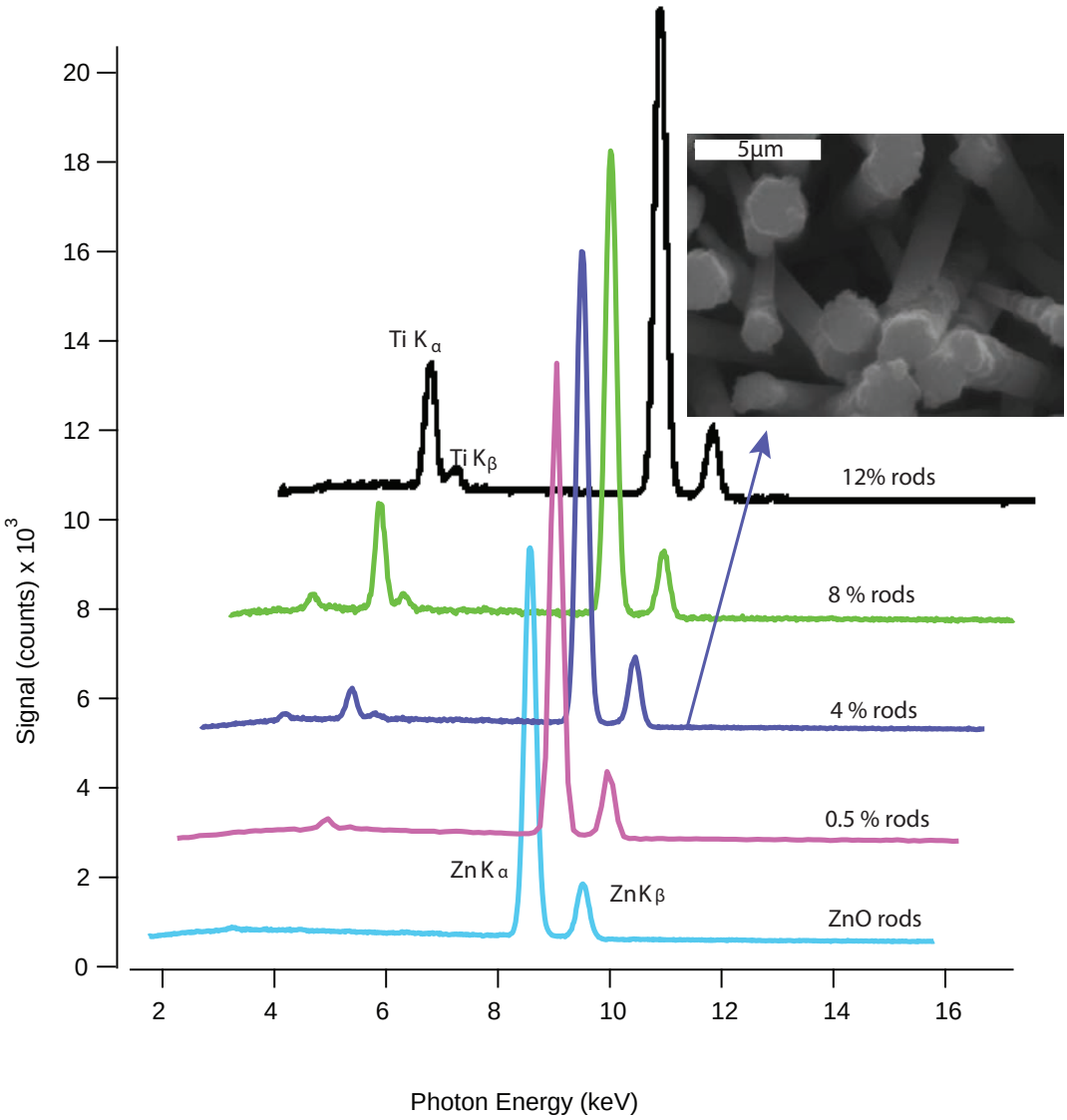

Figure 7.2: Energy dispersive X-ray spectra of ZnO rods coated by titania particles with a 0.5 % Ti content, 4 % Ti content, 8 % Ti content and 12 % Ti content. Inset is an SEM micrograph of ZnO rods coated with titania and a 4 % Ti content.

Figure 7.3: Element resolved SEM micrographs of ZnO rods with a 4 % Ti content coverage, (a) SEM micrograph images of area sampled, (b) is the Ti resolved micrograph, and (c) is the Zn resolved image. It can be seen that $Ti(O_2)$ coats the surface of ZnO rods.

and has a maximum power density output of 8.4 mW/cm^2 and reaches a photocurrent of 26 mA/cm^2 at a potential of 1 V vs Ag/AgCl. By decorating the ZnO rodular array with TiO_2 nanoparticles with an overall concentration of 0.5 % Ti content (black curve), the power density output is enhanced by 22 % and a maximum photopower density output of 10.3 mW/cm^2 is achieved. The photocurrent is considerably higher at 1 V vs Ag/AgCl at 34.26 mW/cm^2. Similar curvatures were found for ZnO nanorods with and without TiO_2 nanoparticles. This suggests that adding TiO_2 nanoparticles does not effect the chemistry of redox reactions at the anode-electrolyte interfaces. This is not surprising since TiO_2 and ZnO have similar electronic structures.

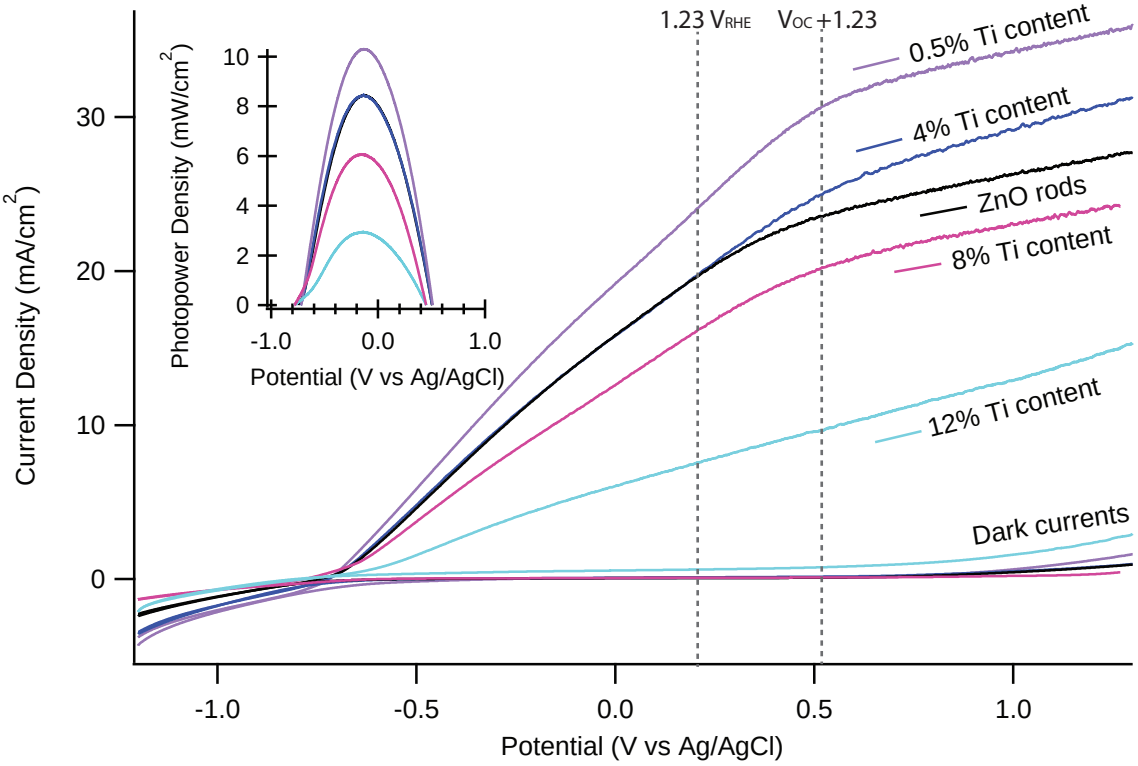

Figure 7.4: Photocurrent density (I-V) plots of titania sensitised ZnO rods of various concentrations of Ti.

The photopower density maximum of the TiO_2 decorated ZnO rod array with a 4 % Ti content (blue curve) reaches a value similar to bare ZnO rods of 8.45 mW/cm^2 and a photocurrent density of 29.15 mA/cm^2, 4 mA/cm^2 higher than bare rods. This is possibly due to the thickness of the congregated TiO_2 particles on the surface of the ZnO rods. At a certain thickness, spatial exciton separation enhancement no longer occurs. This is because the electrons path toward the ZnO rod becomes too

long within the amorphous TiO_2 structure. Consequently the electrons bombard multiple TiO_2 NP's during their passage in a random walk fashion. This passage is further than the diffusion length of electrons in amorphous TiO_2. Electrons also need to acquire a small additional energy to be injected into the higher ZnO conduction band which slightly inhibits electron transport to the Pt electrode, this is illustrated in Figure 7.5.

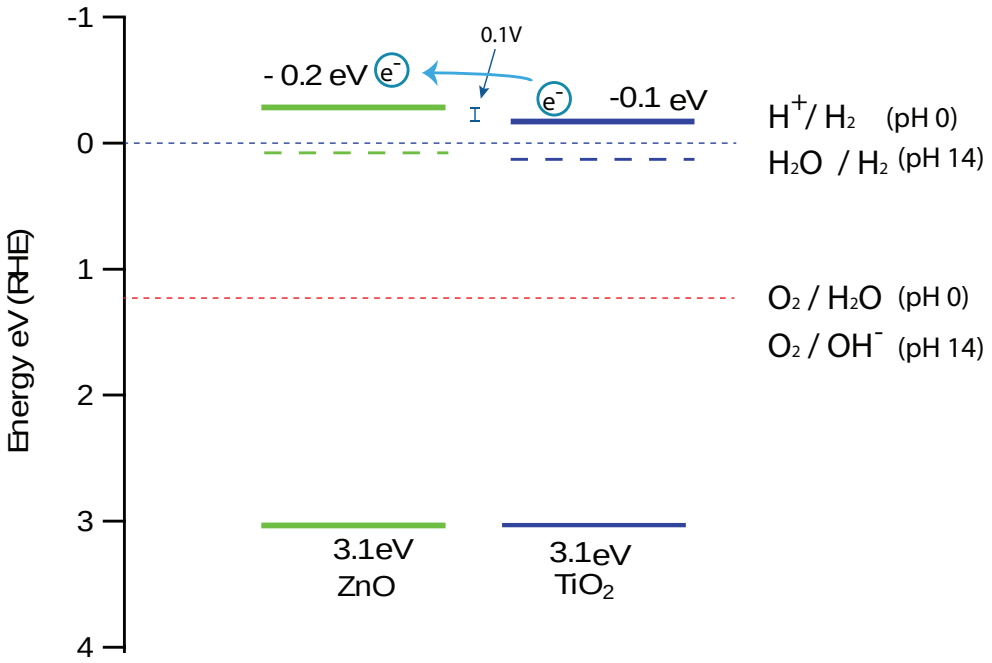

Figure 7.5: Energy levels of TiO_2 and ZnO relative to the redox reaction potentials. ZnO has slightly higher band edges, and require a small (0.1 V) bias for the electrons to traverse the TiO_2 into the ZnO framework.

With increasing Ti content the effects of the higher rates of recombination are evident in the photocurrent density, and with an 8 % Ti content (magenta curve) in the TiO_2 nanoparticle coating, the photopower density has reduced by 27 % to 6.07 mW/cm^2 compared to bare ZnO rods. Increasing the density of the coating further to 12 % Ti content (cyan curve) drop the photopower density maximum to 2.94 mW/cm^2. The photoelectrochemical data is summarised in Table 7.1.

The TiO_2 nanoparticles are advantageous with sparse coverage of ZnO rods, and photocurrent density is enhanced with Ti concentrations below 4 %. The low

Ti content	P_{max} (mW/cm^2)	$I_{1.23V_{RHE}}$ (mA/cm^2)	$I_{1.23V-V_{OC}}$ (mA/cm^2)	$V0_{mA/cm^2}$ ($V_{Ag/AgCl}$)	$I1V_{Ag/AgCl}$ (mA/cm^2)
0 %	8.44	19.69	23.33	-0.724	26.28
0.5 %	10.3	24.08	30.57	-0.719	34.26
4 %	8.46	19.71	24.89	-0.725	29.15
8 %	6.07	16.18	19.48	-0.781	22.7
12 %	2.94	7.55	19.258	-0.78	12.89

Table 7.1: Photoelectrochemical data for TiO_2 decorated ZnO rods, with varying Ti content.

coverage results in smaller distances between the photoabsorbtion sites and nanoparticle/rod interface. Increasing the coverage of ZnO rods with TiO_2 to a creation of a ZnO/TiO_2 core shell structure, will result in a mesopourous titania shell reducing the diffusion length of the electrons significantly. A large surface area increases the rate of oxygen evolution reaction and adversely a large volume also increases the rate of recombination.

Light coverage of titania nanoparticles on ZnO rods has improved the photoefficiency of the ZnO rod structures serving as a photoanode. Excitons created within the TiO_2 particles are more likely to escape the particle before recombining. This charge injection into the ZnO rods separates the excitons spatially, under a bias. The additional surface area of the structure increases the semiconductor/electrolyte surface contact, increasing the photoabsorbtion and effectiveness of oxidation reactions.

The photo efficiency of ZnO nanorod anode can be improved not only by modifying its surface with TiO_2 nanoparticles, but also by increasing its surface area. The overall efficiency is determined by the light absorption efficiency, charge recombination rate, charge mobility and charge potential for redox reactions. The light absorption is expected to improve by engineering the band gap and increasing the thickness of the film. Although a reduced band gap could improve the visible light sensitivity, it will sacrifice the charge potential for redox reactions. Meanwhile, simply increasing the thickness could restrict electrons pathways towards the cathode.

In the next sections, the fabrication of large surface area films is explored, which could improve the rate of surface reactions at the interfaces between the solid electrode and the liquid phase electrolyte. For such heterogeneous reactions, the reactant concentration of the solid that can affect the reaction kinetics, is specified by its effective surface area. The large surface corresponds to high solid concentration and offers faster reactions.

Firstly, a porous ZnO film is deposited using the direct AACVD method which yields a large surface area to facilitate oxidation evolution reactions. Secondly, a unique seeding method utilising chemical bath deposition is demonstrated, which can create vertically aligned tubular ZnO nanostructures that could double the effective surface area of the original ZnO nanorods.

7.2 Photocatalytic Properties of a ZnO Mesoporous Film

AACVD was originally developed for creating semiconductor thin films, the deposition of a homogenous ZnO thin film on a Ti substrate is demonstrated. The properties of the thin film as a photoanode is explored *via* photoelectrochemical analysis. The ZnO thin film was deposited using a precursor of zinc acetate (ZnAc) dissolved in water at a concentration of 0.1 M. The reaction temperature is 650 °C, and argon flow rate is 100 SCCM. A Ti foil is coated with gold using a gold sputterer; the thin film of gold is annealed at a temperature of 550 °C. A gold thin film layer prevents the formation of TiO_2 on the surface of the Ti foil, so that the properties of the ZnO film can be analysed without a heterostructure present. The AACVD deposition continued until precursor exhaustion, a thin ZnO mesopourous film forms on the surface of the substrate. These are shown in Figure 7.6, the particle size of the ZnO is 0.95 μm $\pm$ 0.2 μm, with a film thickness of 2.11 μm.

7.2.1 Photoelectrochemical Analysis

The thin film of ZnO shows significant photoelectrochemical performance, as seen in Figure 7.7. The surface area of the mesopourous film introduces a large surface area of solid/electrolyte contact. The large area of solid/electrolyte contact results in a

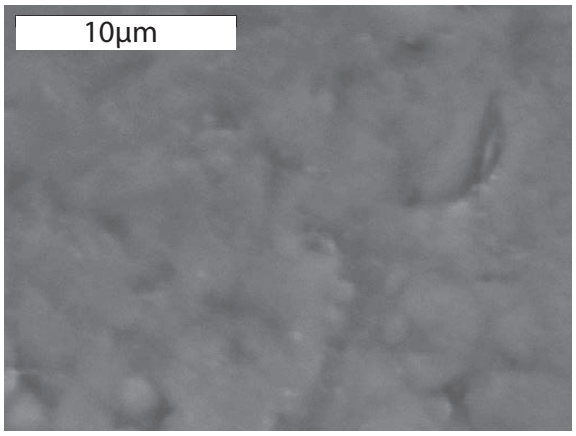

Figure 7.6: SEM micrograph of ZnO mesoporous film created *via* aerosol assisted chemical vapour deposition (AACVD).

higher number of photon absorptions close to the surface and the rate of oxidation of water is enhanced. Holes oxidise water and can be effectively separated from the respective electron which can migrate to the counter electrode and reduce the water, the mesopourous structure is disadvantageous compared to rods due to the poor electron transport and scattering properties of the disordered material, hence a greater opportunity for the electrons and holes to recombine after separation.

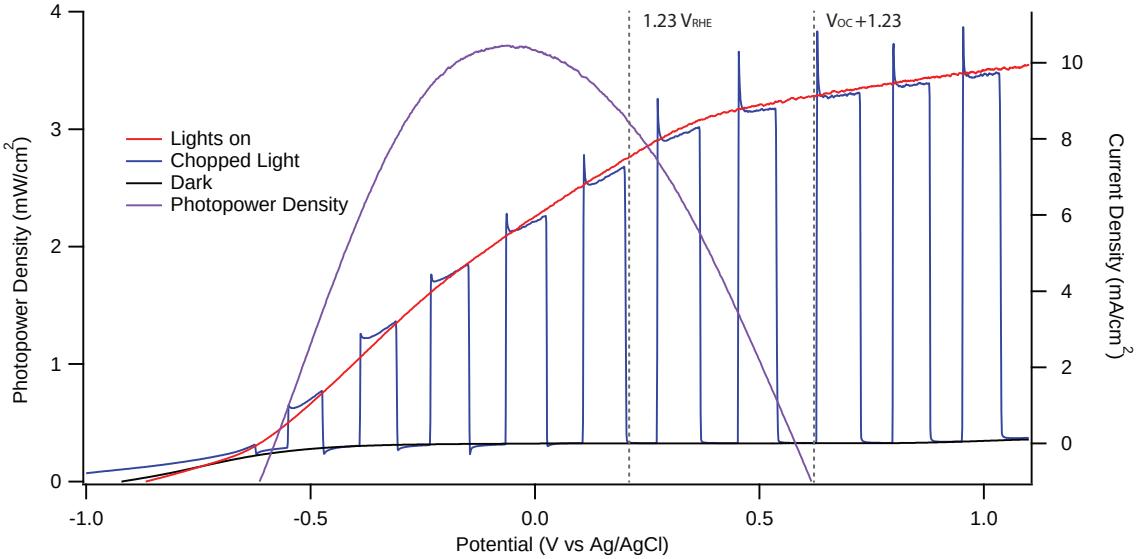

Figure 7.7: Photocurrent density I-V plot the ZnO thin film shows significant photoelectrochemical activity. The purple curve represents the power density output.

As it is possible to deposit thin films of ZnO, the distance between the conductive interface of the substrate and the sites of exciton creation is limited, reducing exciton recombination close to the surface. The electrons path will be that of a random walk across the mesopourous film. In the case of ZnO rods, the length dependency of the

photoefficiency is a competition between surface area, against recombination effects as the lengths of the rods increase.

A mesoporous ZnO films shows good photocatalytic behaviour, this is illustrative of the photoelectronic properties of unaligned ZnO. The photopower density peaks at 3.71 mW/cm^2, under half the photopower density of aligned ZnO rods on a Ti foil. Alignment and crystallinity is vital in creating fast pathways for electrons to achieve significant diffusion length. Charge carriers in the crystalline film have significant path lengths before recombination. The photocurrent profile could be used as a standard reference compared to other ZnO structures.

Here, the possibility of creating a porous metal oxide film with a photocurrent of 7.5 mA/cm^2 at 1.23V$_{\mathrm{RHE}}$ has been demonstrated. More importantly, with the AACVD method it is possible to develop other transition metal oxides and deposit the thin films in a layer by layer fashion. Enabling the ability to control the electronic structure of a 3D material with precise control of the band gap and optical properties. Future work utilising AACVD could be in the form of creating a perfect black 'leaf' for harvesting solar energy.

7.3 ZnO Nanorods and Nanotubes Formed *via* Chemical Bath Deposition (CBD)

Chemical bath deposition is a convenient low temperature aqueous synthesis method used to create nanostructures.[168] Growth Temperatures range from 50 °C to 100 °C in a water based solution, the low temperature allows freedom in the choice of substrate utilised for growth; from plastic to glass to metals. An expansion of the deposition method into printed metal oxide nanostructures is a viable route to low cost solar cells.[271]

ZnO undergoes a similar process of growth as in the vapour transport mechanisms. The deposition requires a seeding layer of ZnO, which initiates growth in the [0001] direction of the ZnO hexagonal wurtzite crystal structure. The Zn^{2+} exposed on the (0001) plane reacts with OH^- ions to form ZnO. The reaction continues in a consecutive fashion, forming ZnO nanorods aligned in the [0001] direction. The OH^- ions are supplied by the decomposition of hexamethylenetetramine (HMTA).

The aqueous method of ZnO crystal formation was first reported by Vergés et al in 1990,[272] demonstrating ZnO rodular crystals form in a solution of zinc nitrate (0.05 mol dm^{-3}) and HMTA (0.05 mol dm^{-3}) at a growth temperature of 100 °C for a duration of 30 mins.

The reaction taking place in the growth solution can be expressed as follows:[273,274]

$$(CH_2)_6N_4 + 6\,H_2O \rightarrow 6\,HCHO + 4\,NH_3$$
$$NH_3 + H_2O \rightleftharpoons NH_4^+ + OH^-$$
$$2\,OH^- + Zn^{2+} \rightarrow Zn(OH)_2 \rightarrow ZnO + H_2O$$

Literature is rich with applications of low temperature grown ZnO rods,[275,276] the mild temperature and versatility of the growth mechanism means that scalable growth is possible to produce large volume devices.[271]

ZnO rod arrays created by the CBD method are site specific, which opens up the possibility of creating devices *in situ* by growing rods directly on to electrodes. A piezogenerator has been demonstrated using this method.[277]

Nanotubes of ZnO are usually formed by a two step formation process *via* CBD and a dissolution process. The majority of articles presenting ZnO nanotubes have been reported using this chemical route.[278] Initially rods are created using normal synthesis conditions. The CBD nanorods are placed in a bath of alkaline or acidic solution for 1 hour at 80 °C, the basic solution causes dissolution of the centre of the rod. The dissolution rate is greater in the (0001) face direction, as a result of the higher reactivity of the high energy (0001) polar surface.

One step nanotube formation *via* chemical bath deposition frequently adopts an *in situ* etching of ZnO rods in either basic or acidic growth solutions.[279,280] In this work, a one step growth of ZnO nanotubes in a neutral growth environment is demonstrated. Since the ZnO growth is site specific, the ZnO seed layer on the substrate was manipulated to achieve a ZnO annulus, a tubular structure extends from the initial ZnO annulus, forming ZnO nanotubes through a bottom up growth approach.

7.3.1 Sample Preparation

Nanorod Preparation

Nanorods are formed on an FTO glass substrate, the substrate is coated with ZnO nanoparticles with an average diameter of 300 nm. A solution of 1 M ZnAc in deionised water served as the seeding solution, which is dispersed on the surface of the FTO *via* spin coating at a rate of 300 rpm which disperses an even coating. The FTO substrate and seed were then annealed at a temperature of 360°C for one hour to form ZnO crystals homogenously spread across the surface.

The substrate is placed into a beaker containing 100 ml of growth solution (10 mM zinc nitrate and 10 mM HMTA in deionised water), the beaker and substrate are inserted into a convection oven and a growth temperature of 85 °C is maintained, until the solution has evaporated (18 hours). The seed dictates the initial size and sites of the rods, and a further growth period enhances the diameter and length of the ZnO nanorods.

Figure 7.8(a) shows the morphology of a typical growth, where ZnO rods are well ordered with an average diameter of 335 nm ± 109 nm and a length of 3 μm. A less well ordered area of rods are shown in 7.8(b). The hexagonal features are clear, thus, it is expected the growth of the nanorods are aligned in the c-axis of the wurtzite crystal structure.

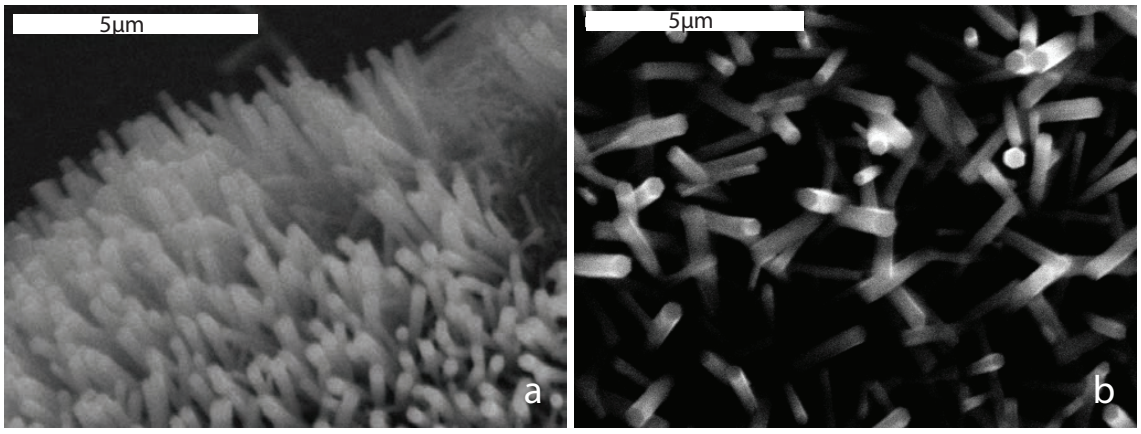

Figure 7.8: SEM micrograph of ZnO rods, utilising low temperature chemical bath deposition methods at magnifications of (a) ×4,000 and (b) ×3,500.

Nanotube Preparation

ZnO nanotubes are prepared by creating an initial annulus of ZnO crystals which serve as the seeding layer on the FTO glass substrate, on this ring, ZnO crystals precipitate and form tubes during the growth process. The seeding solution, containing 1 M zinc acetate (ZnAc) in deionised water, is adjusted with the addition of 0.6 g polyvinyl alcohol (PVA) in 10 ml of solution. The PVA is dissolved in the seeding solution overnight using a magnetic stirrer and heating plate. The solution is spin coated onto the FTO substrate using a higher spin rate (800 rpm) to take into account the higher viscosity of the solution as a consequence of adding PVA. The sample is coated several times to ensure a good coverage. The substrate is annealed in a convection oven at 360 °C for 1 hour.

The kinetics governing the evaporation of the water solution during annealing determines the morphology and size of the seed, and is a crucial step in the formation of the ZnO nanotubes reported here. To achieve the ZnO annulus seed, the droplet containing the PVA will experience contact line pinning, and as the outer edges evaporate at a faster rate than the rest of the droplet solution is drawn from the bulk to the edges *via* capillary flow replenishing the liquid evaporating from the edge.[281,282] With raising temperature the convective flow of the liquid increases, pronouncing the ring or annular formation. This process is known as the coffee-ring effect.

Unlike the ZnO rods seeding discussed in the previous section, where without PVA the 1 M ZnAc solution decomposes into spherical ZnO crystals. The droplet evaporates evenly as the radial contact lines of the droplet are not pinned to the surface. Thus, the droplet gradually reduces in size during evaporation and a spherical/circular ZnO crystal remains on the substrate after thermal decomposition.

The seeded substrate is placed in a beaker containing the growth solution (10 mM zinc nitrate ($ZnO(NO_3)_2$), 10 mM hexamine (HMTA) dissolved in water) at a temperature of 85 °C for 18 hours; the beaker is covered with foil to reduce loss of growth solution. Figure 7.9(a) shows a low magnification SEM micrograph of the ZnO nanotubular array after 18 hours in the growth solution, the average outer diameter is 267 nm ± 63 nm and in average inner diameter of 107 nm ± 62 nm. Figure 7.9(b) & (c) shows high magnification SEM micrographs of the nanotubular

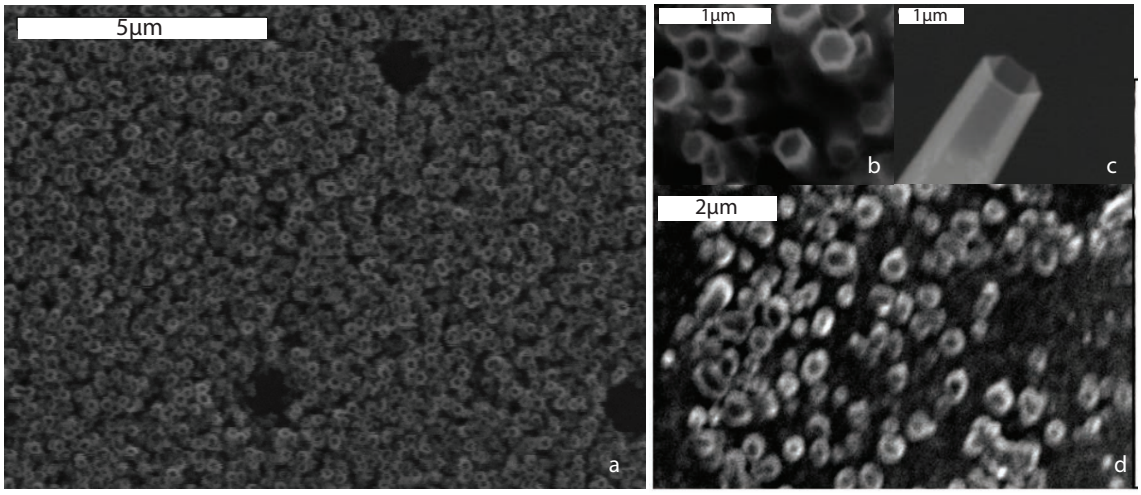

Figure 7.9: SEM micrograph of ZnO micro/nano tubes formed *via* chemical bath deposition at magnifications of (a) ×7,500 (b) ×23,000 and (c) ×13,000 whilst (d) is an SEM micrograph of the seeding layer at a magnification of ×10,000. *Images courtesy of Adward Lee and Teo Mertanen*

structures created on the conductive glass. The hollow structure is discernible from Figure 7.9(b), which shows an example of a large ZnO nanotube with an outer diameter of 1.05 μm and an inner diameter of 893 nm. Figure 7.9(d) is the SEM micrograph of the annulus ZnO crystal seeds before growth of the nanotubes, the outer and inner diameter of the ring can be clearly distinguished, with averages diameters of 375 nm ± 88 nm and 174 nm ± 58 nm, respectively.

7.3.2 Photoelectrochemical Analysis

In Figure 7.10 the red curve illustrates the photocurrent density, the blue is photocurrent density under chopped illumination and black is the dark current. The chopped illumination photocurrent density has anodic spikes present. These anodic spikes are due to electron and hole trapping in the structure. The photopower density is plotted as the purple curve, reaching a peak maximum of 1.275 mW/cm^2.

The low performance compared to other materials reported in this work could be due to the following factors; the crystallinity of the tubes are of a low quality or contact between the ZnO and the SnO coating of the FTO could be compromised. The low surface area and rod density contributes to the low photocurrent density. Further work in creating denser forests of ZnO tubes by this method could possibly improve the photoelectrochemical properties. Zn_2TiO_4 and TiO_2 are not present

in this structure. Creating a ZnO nanotube array *via* CBD with similar densities and dimensions to the ZnO nanotubes formed in Chapter 6 and comparing the photoelectrochemical behaviour may demonstrate the role of the heterostructure in the photocatalytic improvement of high temperature synthesised ZnO structures on a Ti foil.

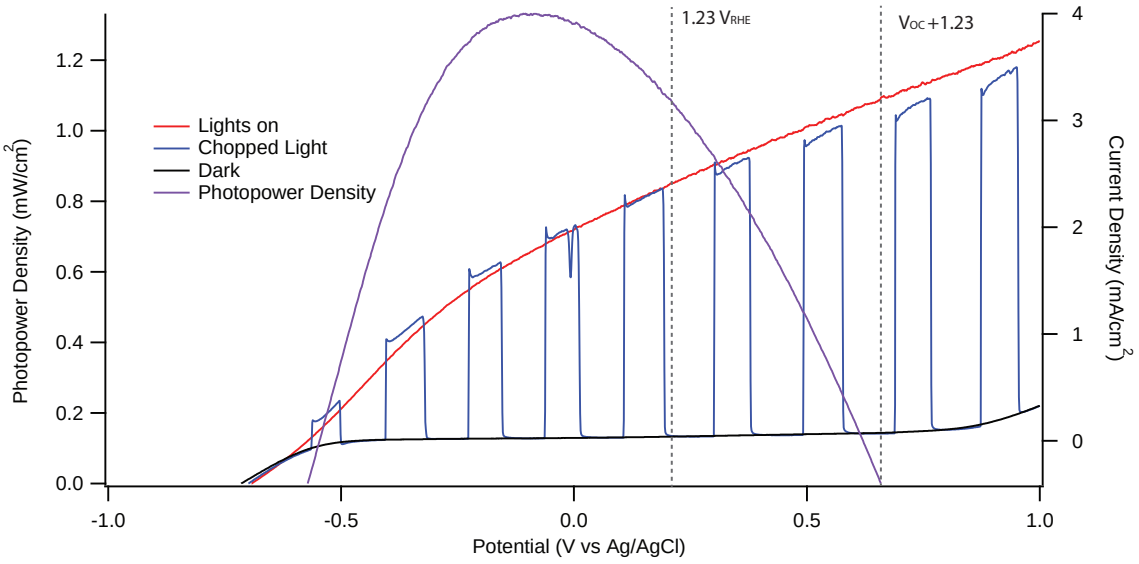

Figure 7.10: Photocurrent density (I-V) plots of ZnO tubes grown *via* CBD.

The lengths of the tubes change with time and the growth begins as a tubular template rather than a dissolution process (i.e. bottom up tubular growth). An annular ZnO crystal seed initially forms due to evaporation of the droplet and surface pinning of the edges of the solution droplet, and provides the nucleation sites for ZnO formation gradually building up the tubular structure.

7.3.3 Conclusion

Utilisation of novel deposition techniques opens up new possibilities for creating a 3D architecture of otherwise heat sensitive materials by aerosol assisted vapour deposition. The simple setup allows a precise control over the introduction of the deposition material in an ambient environment. The increase in photocurrent density of lightly decorated TiO_2 nanoparticles on a ZnO nanorodular array illustrates the vital role exciton separation plays. It was also demonstrated that AACVD can deposit homogenous thin films of ZnO which can be extended to almost any metal oxide, through the control of the ingredients of the solution fitted on the ultrasonic

transducer to create the aerosol. Temperature of the substrate is not a vital component in the formation of the thin film, and mild temperatures could facilitate thin film deposition.

Chemical bath deposition of ZnO nanostructures is a low temperature process which showed versatility in the formation of ZnO nanostructures. Importantly the growth process is site specific and control of the seed allowed a bottom up template growth process of ZnO nanotubes formed at a temperature below 100 °C. This method can be extended into creating devices through the control of the seeding density and structured profiles.

Chapter 8

Future Work

The work conducted herein has demonstrated the possibilities of band gap engineering and the manipulation of materials to create interfacially electronically favourable heterostructures. Firstly, by alloying Ti with Fe to form Fe-Ti-O nanotubes, and secondly, by forming a ZnO-Zn_2TiO_4-TiO_2 heterojunction. Both of which showed improvement of the output photopower density, one as a result of a larger absorption bandwidth and the other a result of improved charged separation close to the interfaces of the heterostructure.

At the time of synthesis of the Fe-Ti-O nanotubes XRD was unavailable for the analysis of the crystal structures formed. It would be beneficial to repeat the deposition and anodisation of varying iron content in the Fe-Ti-O nanotubes to assess whether iron titanates have formed during the anodisation process. Not only will this insight give completion to the studies performed herein, but will also be informative for the development of future experiments relating to iron oxide.

For all of the materials studied, experimental confirmation of band gap energies would be fruitful for the analysis of the materials. This can be achieved through the use of Diffuse Reflectance UV-Vis spectrometry (DR-UV-Vis) which measures the wavelength range at which the materials absorb light, the absorption profile can then be assessed to calculate the band gap energy.[283] The experimental characterisation of the flat band potential for the materials synthesised can be further elucidated *via* capacitance measurements; using the Mott-Schottky equation to determine the flat band potential.[62]

The next logical step in terms of material synthesis would be to combine zinc

and iron oxide, Zn-Fe-O, this could be achieved by AACVD, e-beam evaporation or chemical bath methods reported earlier. $ZnFe_2O$ has a band gap well within the visible range (2 eV - 620 nm) and the band edge positions are more favourable compared to Fe_2O_3, shown in Figure 1.9. Yet, the conduction band is approximately 0.05 V below the H^+ reduction potential which questions the stability of the material in an electrolyte. The conduction band can be shifted above the H^+ reduction potential, such that both band edges straddle the redox potentials, by introducing Ti to form $Zn_{1.5}FeTi_{0.5}O_4$.[284]

For example, iron, zinc and titanium can be deposited onto a substrate using the electron beam evaporators constructed in this work, which can then be anodised to form nanotubes. These nanotubes should be sensitive to visible light with the added benefit of multiple channels to facilitate oxidation reactions on the surface of the inner tubes. The thin film could also be composed of varying concentrations of Fe content, starting from $Zn_{1.5}FeTi_{0.5}O_4$ and ending in Zn_2TiO_4, whereby the CBM remains well above the H^+ reduction potential and the absorption range is broadened from UV to visible light from the tip to the roots of the nanotubes.

Another method could be to simultaneously deposit iron and titanium from precursors solution *via* AACVD whilst a vapour solid reaction of ZnO is performed. Hopefully forming $Zn_{1.5}FeTi_{0.5}O_4$ nanorods on a Ti foil thus increasing the surface area of the visible photosensitive material.

In conclusion, this work has demonstrated versatile methods to create nanostructures and the hybrid metal oxide nanomaterials synthesised have outperformed their single metal oxide counterparts. The insights drawn from these experiments can be utilised in the construction of new hybrid metal oxide photoanodes and spur further improvement for the photoelectrochemical decomposition of water.

Bibliography

[1] Energy strategy of europe. `https://www.ec.europa.eu`.

[2] UK renewable energy roadmap update 2012. *Department of Energy & Climate Change*, 2011.

[3] Energy trends march:2013. *Department of Energy & Climate Change*, 2013.

[4] Energy trends june:2011. *Department of Energy & Climate Change*, 2011.

[5] Göran Berndes, Monique Hoogwijk, and Richard van den Broek. The contribution of biomass in the future global energy supply: a review of 17 studies. *Biomass and Bioenergy*, 25(1):1–28, 2003.

[6] JS Reid, R Koppmann, TF Eck, and DP Eleuterio. A review of biomass burning emissions part ii: intensive physical properties of biomass burning particles. *Atmospheric Chemistry and Physics*, 5(3):799–825, 2005.

[7] JF Manwell, JG McGowan, and AL Rogers. Wind energy systems: Environmental aspects and impacts. *Wind Energy Explained: Theory, Design and Application*, pages 469–510, 2002.

[8] Oliver Paish. Small hydro power: technology and current status. *Renewable and sustainable energy reviews*, 6(6):537–556, 2002.

[9] Michael Grätzel. Photoelectrochemical cells. *Nature*, 414(6861):338–344, 2001.

[10] Jan F Kreider and Frank Kreith. Solar energy handbook. 1981.

[11] Sarah R Kurtz, Daryl Myers, Tim Townsend, Chuck Whitaker, Alex Maish, Roland Hulstrom, and K Emery. Outdoor rating conditions for photovoltaic modules and systems. *Solar Energy Materials and Solar Cells*, 62(4):379–391, 2000.

[12] Christian A Gueymard. The sun's total and spectral irradiance for solar energy applications and solar radiation models. *Solar energy*, 76(4):423–453, 2004.

[13] Richard E Bird, Roland L Hulstrom, and LJ Lewis. Terrestrial solar spectral data sets. *Solar Energy*, 30(6):563–573, 1983.

[14] CA Gueymard, D Myers, and K Emery. Proposed reference irradiance spectra for solar energy systems testing. *Solar Energy*, 73(6):443–467, 2002.

[15] Anthony D Owen. Environmental externalities, market distortions and the economics of renewable energy technologies. *Energy Journal-Cambridge MA*, 25(3):127–156, 2004.

[16] Parsons Brinckerhoff. Powering the nation. *Update*, 2010.

[17] Mott MacDonald. Review of the generation costs and deployment potential of renewable electricity technologies in the uk. *Department of Energy and Climate Change, ARUP*, 2011.

[18] J.R. Hook and H.E. Hall. *Solid state physics*. The Manchester physics series. Wiley, 1991.

[19] C. Kittel. *Introduction to Solid State Physics*. Wiley, 2004.

[20] W. Shockley. The theory of p-n junctions in semiconductors and p-n junction transistors. *Bell System Technical Journal*, 28(3):435–489, 1949.

[21] William Shockley and Hans J Queisser. Detailed balance limit of efficiency of p-n junction solar cells. *Journal of applied physics*, 32(3):510–519, 1961.

[22] KL Chopra, PD Paulson, and V Dutta. Thin-film solar cells: an overview. *Progress in Photovoltaics: Research and Applications*, 12(2-3):69–92, 2004.

[23] Martin A Green, Keith Emery, Yoshihiro Hishikawa, Wilhelm Warta, and Ewan D Dunlop. Solar cell efficiency tables (version 39). *Progress in photovoltaics: research and applications*, 20(1):12–20, 2011.

[24] I Kaiser, K Ernst, Ch-H Fischer, R Könenkamp, C Rost, I Sieber, and M Ch Lux-Steiner. The eta-solar cell with $CuInS_2$: A photovoltaic cell concept using an extremely thin absorber (eta). *Solar Energy Materials and Solar Cells*, 67(1):89–96, 2001.

[25] Ingrid Repins, Miguel A Contreras, Brian Egaas, Clay DeHart, John Scharf, Craig L Perkins, Bobby To, and Rommel Noufi. 19.9%-efficient $ZnO/CdS/CuInGaSe_2$ solar cell with 81.2% fill factor. *Progress in Photovoltaics: Research and applications*, 16(3):235–239, 2008.

[26] Matthew G Panthani, Vahid Akhavan, Brian Goodfellow, Johanna P Schmidtke, Lawrence Dunn, Ananth Dodabalapur, Paul F Barbara, and Brian A Korgel. Synthesis of $CuInS_2$, $CuInSe_2$, and $Cu(In_xGa_{1-x})$ Se_2 (CIGS) nanocrystal inks for printable photovoltaics. *Journal of the American Chemical Society*, 130(49):16770–16777, 2008.

[27] Jianhua Zhao, Aihua Wang, Martin A Green, and Francesca Ferrazza. 19.8% efficient honeycomb textured multicrystalline and 24.4% monocrystalline silicon solar cells. *Applied Physics Letters*, 73:1991, 1998.

[28] R Venkatasubramanian, BC O'Quinn, JS Hills, PR Sharps, ML Timmons, JA Hutchby, H Field, R Ahrenkiel, and B Keyes. 18.2%(AM1. 5) efficient gaas solar cell on optical-grade polycrystalline ge substrate. In *Photovoltaic Specialists Conference, 1996., Conference Record of the Twenty Fifth IEEE*, pages 31–36. IEEE, 1996.

[29] CJ Keavney, VE Haven, and SM Vernon. Emitter structures in MOCVD InP solar cells. In *Photovoltaic Specialists Conference, 1990., Conference Record of the Twenty First IEEE*, pages 141–144. IEEE, 1990.

[30] X Wu, JC Keane, RG Dhere, C DeHart, A Duda, TA Gessert, S Asher, DH Levi, and P Sheldon. 16.5%-efficient CdS/CdTe polycrystalline thin-film solar cell. In *Proceedings of the 17th European photovoltaic solar energy conference*, volume 995. James & James Ltd.: London, 2001.

[31] Jan Hendrik Petermann, Dimitri Zielke, Jan Schmidt, Felix Haase, Enrique Garralaga Rojas, and Rolf Brendel. 19%-efficient and 43μm-thick crystalline Si solar cell from layer transfer using porous silicon. *Progress in Photovoltaics: Research and Applications*, 20(1):1–5, 2012.

[32] O Schultz, SW Glunz, and GP Willeke. Short communication: Accelerated publication: Multicrystalline silicon solar cells exceeding 20% efficiency. *Progress in Photovoltaics: Research and Applications*, 12(7):553–558, 2004.

[33] Wei Liu, David B Mitzi, Min Yuan, Andrew J Kellock, S Jay Chey, and Oki Gunawan. 12% efficiency CuIn (Se, S)2 photovoltaic device prepared using a hydrazine solution process. *Chemistry of Materials*, 22(3):1010–1014, 2009.

[34] Robert F. Service. Outlook brightens for plastic solar cells, 2011.

[35] Kenji Yamamoto, Masashi Yoshimi, Y Tawada, Y Okamoto, A Nakajima, and S Igari. Thin-film poly-Si solar cells on glass substrate fabricated at low temperature. *Applied Physics A*, 69(2):179–185, 1999.

[36] Aswani Yella, Hsuan-Wei Lee, Hoi Nok Tsao, Chenyi Yi, Aravind Kumar Chandiran, Md Khaja Nazeeruddin, Eric Wei-Guang Diau, Chen-Yu Yeh, Shaik M Zakeeruddin, and Michael Grätzel. Porphyrin-sensitized solar cells with cobalt (ii/iii)–based redox electrolyte exceed 12 percent efficiency. *Science*, 334(6056):629–634, 2011.

[37] RR King, A Boca, W Hong, XQ Liu, D Bhusari, D Larrabee, KM Edmondson, DC Law, CM Fetzer, S Mesropian, et al. Band-gap-engineered architectures for high-efficiency multijunction concentrator solar cells. In *24th European Photovoltaic Solar Energy Conference and Exhibition, Hamburg, Germany*, volume 21, 2009.

[38] Tatsuo Saga. Advances in crystalline silicon solar cell technology for industrial mass production. *NPG Asia Materials*, 2(3):96–102, 2010.

[39] Michael. O'Regan, Brian. Gratzel. A low-cost, high-efficiency solar cell based on dye-sensitized colloidal TiO_2 films. *Nature*, 353(6346):737–740, 1991.

[40] M. K. Nazeeruddin, A. Kay, I. Rodicio, R. Humphry-Baker, E. Mueller, P. Liska, N. Vlachopoulos, and M. Graetzel. Conversion of light to electricity by cis-X2bis(2,2'-bipyridyl-4,4'-dicarboxylate)ruthenium(II) charge-transfer sensitizers (X = Cl-, Br-, I-, CN-, and SCN-) on nanocrystalline titanium dioxide electrodes. *Journal of the American Chemical Society*, 115(14):6382–6390, 1993.

[41] Laura L Tobin, Thomas O'Reilly, Dominic Zerulla, and John T Sheridan. Characterising dye-sensitised solar cells. *Optik-International Journal for Light and Electron Optics*, 122(14):1225–1230, 2011.

[42] Michael Faraday. Experimental researches in electricity.–third series. *Philosophical Transactions of the Royal Society of London*, 123:23–54, 1833.

[43] Alan E Jeffreys. *Michael Faraday: a list of his lectures and published writings*. Taylor & Francis, 1961.

[44] A Paets van Troostwijk and JR Deiman. Sur une manière de décomposer l'eau en air inflammable et en air vital. *J. Phys*, 35:369–378, 1789.

[45] R De Levie. The electrolysis of water. *Journal of Electroanalytical Chemistry*, 476(1):92–93, 1999.

[46] William Nicholson and Anthony Carlisle. Account of the new Electrical or Galvanic Apparatus of Alessandro Volta and Experiments performed with the same. *Chemistry and the Arts*, 4:179–187, 1801.

[47] Alexander Volta and Joseph Banks. I. on the electricity excited by the mere contact of conducting substances of different kinds. *The Philosophical Magazine: Comprehending the Various Branches of Science, the Liberal and Fine Arts, Agriculture, Manufactures, and Commerce*, 7(28):289–311, 1800.

[48] AE Becquerel. Mémoire sur les effets électriques produits sous l'influence des rayons solaires. *Comptes Rendus*, 9(567):1839, 1839.

[49] WH Brattain and CGB Garrett. Electrical properties of the interface between a germanium single crystal and an electrolyte. *Physical Review*, 94(3):750–750, 1954.

[50] Akira Fujishima. Electrochemical photolysis of water at a semiconductor electrode. *nature*, 238:37–38, 1972.

[51] Lionel Vayssieres. *On solar hydrogen and nanotechnology*. John Wiley & Sons, 2010.

[52] J. Augustyńnski, B.D. Alexander, and R. Solarska. Metal oxide photoanodes for water splitting. In Carlo Alberto Bignozzi, editor, *Photocatalysis*, volume 303 of *Topics in Current Chemistry*, pages 1–38. Springer Berlin Heidelberg, 2011.

[53] Sergio Trasatti. Electrocatalysis by oxides - attempt at a unifying approach. *Journal of Electroanalytical Chemistry and Interfacial Electrochemistry*, 111(1):125–131, 1980.

[54] Y Matsumoto and E Sato. Electrocatalytic properties of transition metal oxides for oxygen evolution reaction. *Materials chemistry and physics*, 14(5):397–426, 1986.

[55] Susanta K Mohapatra, Mano Misra, Vishal K Mahajan, and Krishnan S Raja. Design of a highly efficient photoelectrolytic cell for hydrogen generation by water splitting: Application of TiO_2-x C x nanotubes as a photoanode and Pt/TiO_2 nanotubes as a cathode. *The Journal of Physical Chemistry C*, 111(24):8677–8685, 2007.

[56] Gongming Wang, Hanyu Wang, Yichuan Ling, Yuechao Tang, Xunyu Yang, Robert C Fitzmorris, Changchun Wang, Jin Z Zhang, and Yat Li. Hydrogen-treated TiO_2 nanowire arrays for photoelectrochemical water splitting. *Nano letters*, 11(7):3026–3033, 2011.

[57] Amy L Linsebigler, Guangquan Lu, and John T Yates Jr. Photocatalysis on TiO_2 surfaces: principles, mechanisms, and selected results. *Chemical Reviews*, 95(3):735–758, 1995.

[58] R Dholam, N Patel, M Adami, and A Miotello. Hydrogen production by photocatalytic water-splitting using Cr-or Fe-doped TiO_2 composite thin films photocatalyst. *International Journal of Hydrogen Energy*, 34(13):5337–5346, 2009.

[59] Hideki Kato, Kiyotaka Asakura, and Akihiko Kudo. Highly efficient water splitting into H_2 and O_2 over lanthanum-doped $NaTaO_3$ photocatalysts with high crystallinity and surface nanostructure. *Journal of the American Chemical Society*, 125(10):3082–3089, 2003.

[60] VM Aroutiounian, VM Arakelyan, and GE Shahnazaryan. Metal oxide photoelectrodes for hydrogen generation using solar radiation-driven water splitting. *Solar Energy*, 78(5):581–592, 2005.

[61] A Di Paola, E Garcıa-López, S Ikeda, G Marcı, B Ohtani, and L Palmisano. Photocatalytic degradation of organic compounds in aqueous systems by transition metal doped polycrystalline TiO_2. *Catalysis Today*, 75(1):87–93, 2002.

[62] K Gelderman, L Lee, and SW Donne. Flat-band potential of a semiconductor: using the mott–schottky equation. *Journal of chemical education*, 84(4):685, 2007.

[63] Radim Beranek. (photo) electrochemical methods for the determination of the band edge positions of TiO_2-based nanomaterials. *Advances in Physical Chemistry*, 2011, 2012.

[64] Yasumichi Matsumoto. Energy positions of oxide semiconductors and photocatalysis with iron complex oxides. *Journal of solid state chemistry*, 126(2):227–234, 1996.

[65] CH Griffiths and HK Eastwood. Influence of stoichiometry on the metal-semiconductor transition in vanadium dioxide. *Journal of Applied Physics*, 45(5):2201–2206, 1974.

[66] LeRoy Eyring. Chemistry of non-stoichiometric compounds by k. kosuge. *Journal of the American Chemical Society*, 118(1):298–298, 1996.

[67] R. G. Rhodes. Oxide semiconductors by Z. M. Jarzebski. *Acta Crystallographica Section A*, 30(6):873, Nov 1974.

[68] Anlian Pan, Patricia L Nichols, and CZ Ning. Semiconductor alloy nanowires and nanobelts with tunable optical properties. *Selected Topics in Quantum Electronics, IEEE Journal of*, 17(4):808–818, 2011.

[69] Winfried Mönch. *Electronic properties of semiconductor interfaces*, volume 43. Springer, 2004.

[70] Andreas Züttel, Andreas Borgschulte, and Louis Schlapbach. *Hydrogen as a future energy carrier*. Wiley. com, 2011.

[71] Ghazi A Karim. Hydrogen as a spark ignition engine fuel. *International Journal of Hydrogen Energy*, 28(5):569–577, 2003.

[72] Carl-Jochen Winter and Joachim Nitsch. Hydrogen as an energy carrier. 1988.

[73] I.P. Jain. Hydrogen the fuel for 21st century. *International Journal of Hydrogen Energy*, 34(17):7368 – 7378, 2009.

[74] DK Ross. Hydrogen storage: the major technological barrier to the development of hydrogen fuel cell cars. *Vacuum*, 80(10):1084–1089, 2006.

[75] Jamie D Holladay, Jianli Hu, David L King, and Yong Wang. An overview of hydrogen production technologies. *Catalysis Today*, 139(4):244–260, 2009.

[76] Jianguo Xu and Gilbert F Froment. Methane steam reforming, methanation and water-gas shift: I. intrinsic kinetics. *AIChE Journal*, 35(1):88–96, 1989.

[77] Agus Haryanto, Sandun Fernando, Naveen Murali, and Sushil Adhikari. Current status of hydrogen production techniques by steam reforming of ethanol: a review. *Energy & Fuels*, 19(5):2098–2106, 2005.

[78] K Vasudeva, N Mitra, P Umasankar, and SC Dhingra. Steam reforming of ethanol for hydrogen production: thermodynamic analysis. *International Journal of Hydrogen Energy*, 21(1):13–18, 1996.

[79] Dimitris K Liguras, Dimitris I Kondarides, and Xenophon E Verykios. Production of hydrogen for fuel cells by steam reforming of ethanol over supported noble metal catalysts. *Applied Catalysis B: Environmental*, 43(4):345–354, 2003.

[80] Pamela L Spath and Margaret K Mann. *Life cycle assessment of hydrogen production via natural gas steam reforming*. National Renewable Energy Laboratory Golden, CO, 2000.

[81] R Pitchai and K Klier. Partial oxidation of methane. *Catalysis ReviewsâĂŤScience and Engineering*, 28(1):13–88, 1986.

[82] AT Ashcroft, AK Cheetham, and MrnLH Green. Partial oxidation of methane to synthesis gas using carbon dioxide. *Nature*, 352(6332):225–226, 1991.

[83] Patrick DF Vernon, Malcolm LH Green, Anthony K Cheetham, and Alexander T Ashcroft. Partial oxidation of methane to synthesis gas. *Catalysis Letters*, 6(2):181–186, 1990.

[84] PJ Dauenhauer, JR Salge, and LD Schmidt. Renewable hydrogen by autothermal steam reforming of volatile carbohydrates. *Journal of Catalysis*, 244(2):238–247, 2006.

[85] S Ayabe, H Omoto, T Utaka, R Kikuchi, K Sasaki, Y Teraoka, and K Eguchi. Catalytic autothermal reforming of methane and propane over supported metal catalysts. *Applied Catalysis A: General*, 241(1):261–269, 2003.

[86] TS Christensen and II Primdahl. Improve syngas production using autothermal reforming. *Hydrocarbon Processing;(United States)*, 73(3), 1994.

[87] GA Deluga, JR Salge, LD Schmidt, and XE Verykios. Renewable hydrogen from ethanol by autothermal reforming. *Science*, 303(5660):993–997, 2004.

[88] Harry Perry. Gasification of coal. *Sci. Amer., v. 230, no. 3, pp. 19-25*, 230(3), 1973.

[89] Shiying Lin, Michiaki Harada, Yoshizo Suzuki, and Hiroyuki Hatano. Hydrogen production from coal by separating carbon dioxide during gasification. *Fuel*, 81(16):2079–2085, 2002.

[90] William B Hauserman. High-yield hydrogen production by catalytic gasification of coal or biomass. *International journal of hydrogen energy*, 19(5):413–419, 1994.

[91] Calin-Cristian Cormos, Fred Starr, Evangelos Tzimas, and Stathis Peteves. Innovative concepts for hydrogen production processes based on coal gasification with CO_2 capture. *International Journal of Hydrogen Energy*, 33(4):1286–1294, 2008.

[92] Robert W Coughlin and Mohammad Farooque. Electrochemical gasification of coal-simultaneous production of hydrogen and carbon dioxide by a single reaction involving coal, water, and electrons. *Industrial & Engineering Chemistry Process Design and Development*, 19(2):211–219, 1980.

[93] Lorna Jeffery Minggu, Wan Ramli Wan Daud, and Mohammad B Kassim. An overview of photocells and photoreactors for photoelectrochemical water splitting. *International Journal of Hydrogen Energy*, 35(11):5233–5244, 2010.

[94] A. Djafour, M. Matoug, H. Bouras, B. Bouchekima, M.S. Aida, and B. Azoui. Photovoltaic-assisted alkaline water electrolysis: Basic principles. *International Journal of Hydrogen Energy*, 36(6):4117 – 4124, 2011.

[95] Bojan Tamburic, Fessehaye W. Zemichael, Geoffrey C. Maitland, and Klaus Hellgardt. A novel nutrient control method to deprive green algae of sulphur and initiate spontaneous hydrogen production. *International Journal of Hydrogen Energy*, 37(11):8988 – 9001, 2012.

[96] C.M. Perkins and University of Colorado at Boulder. *Solar Thermal Decomposition of Zinc Oxide in Aerosol Flow for Renewable Hydrogen Production*. University of Colorado at Boulder, 2006.

[97] Oscar Khaselev and John A Turner. A monolithic photovoltaic - photoelectrochemical device for hydrogen production via water splitting. *Science*, 280(5362):425–427, 1998.

[98] Ida Akkerman, Marcel Janssen, Jorge Rocha, and René H Wijffels. Photobiological hydrogen production: photochemical efficiency and bioreactor design. *International Journal of Hydrogen Energy*, 27(11):1195–1208, 2002.

[99] Paul F Weaver, Stephen Lien, and Michael Seibert. Photobiological production of hydrogen. *Solar Energy*, 24(1):3–45, 1980.

[100] Debajeet K. Bora, Elena A. Rozhkova, Krisztina Schrantz, Pradeep P. Wyss, Artur Braun, Thomas Graule, and Edwin C. Constable. Functionalization of nanostructured hematite thin-film electrodes with the light-harvesting membrane protein c-phycocyanin yields an enhanced photocurrent. *Advanced Functional Materials*, 22(3):490–502, 2012.

[101] Hiroaki Tagawa and Takayuki Endo. Catalytic decomposition of sulfuric acid using metal oxides as the oxygen generating reaction in thermochemical water splitting process. *International journal of hydrogen energy*, 14(1):11–17, 1989.

[102] CE Bamberger. Hydrogen production from water by thermochemical cycles; a 1977 update. *Cryogenics*, 18(3):170–183, 1978.

[103] Marc A Rosen. Advances in hydrogen production by thermochemical water decomposition: a review. *Energy*, 35(2):1068–1076, 2010.

[104] E Bilgen, M Ducarroir, M Foex, F Sibieude, and F Trombe. Use of solar energy for direct and two-step water decomposition cycles. *International Journal of Hydrogen Energy*, 2(3):251–257, 1977.

[105] Patrice Charvin, Stephane Abanades, Gilles Flamant, and Florent Lemort. Two-step water splitting thermochemical cycle based on iron oxide redox pair for solar hydrogen production. *Energy*, 32(7):1124–1133, 2007.

[106] Yumiko Nakamuro and Takayuki Mizuno. A two-step thermochemical water splitting by iron-oxide on stabilized zirconia. *Journal of solar energy engineering*, 128:3, 2006.

[107] M Hänchen, A Stiel, ZR Jovanovic, and A Steinfeld. Thermally driven copper oxide redox cycle for the separation of oxygen from gases. *Industrial & Engineering Chemistry Research*, 51(20):7013–7021, 2012.

[108] A Steinfeld. Solar hydrogen production via a two-step water-splitting thermochemical cycle based on Zn/ZnO redox reactions. *International Journal of Hydrogen Energy*, 27(6):611–619, 2002.

[109] Karsten Wegner, Hao C Ly, Rodrigo J Weiss, Sotiris E Pratsinis, and Aldo Steinfeld. In situ formation and hydrolysis of Zn nanoparticles for H_2 production by the 2-step ZnO/Zn water-splitting thermochemical cycle. *International Journal of Hydrogen Energy*, 31(1):55–61, 2006.

[110] A Weidenkaff, AW Reller, A Wokaun, and A Steinfeld. Thermogravimetric analysis of the zno/zn water splitting cycle. *Thermochimica Acta*, 359(1):69–75, 2000.

[111] RK Ahluwalia, TQ Hua, and JK Peng. On-board and off-board performance of hydrogen storage options for light-duty vehicles. *International Journal of Hydrogen Energy*, 37(3):2891–2910, 2012.

[112] Gavin Walker. *Solid-state hydrogen storage: materials and chemistry*. Woodhead Publishing, 2008.

[113] Tuan KA Hoang and David M Antonelli. Exploiting the kubas interaction in the design of hydrogen storage materials. *Advanced Materials*, 21(18):1787–1800, 2009.

[114] Georgios K Dimitrakakis, Emmanuel Tylianakis, and George E Froudakis. Pillared graphene: a new 3-d network nanostructure for enhanced hydrogen storage. *Nano letters*, 8(10):3166–3170, 2008.

[115] Mashkoor Ahmad, Caofeng Pan, and Jing Zhu. Investigation of hydrogen storage capabilities of ZnO-based nanostructures. *The Journal of Physical Chemistry C*, 114(6):2560–2565, 2010.

[116] Ping Chen, Zhitao Xiong, Jizhong Luo, Jianyi Lin, and Kuang Lee Tan. Interaction of hydrogen with metal nitrides and imides. *Nature*, 420(6913):302–304, 2002.

[117] Hoonkyung Lee, Woon Ih Choi, and Jisoon Ihm. Combinatorial search for optimal hydrogen-storage nanomaterials based on polymers. *Physical review letters*, 97(5):056104, 2006.

[118] Ki-Joon Jeon, Hoi Ri Moon, Anne M Ruminski, Bin Jiang, Christian Kisielowski, Rizia Bardhan, and Jeffrey J Urban. Air-stable magnesium nanocomposites provide rapid and high-capacity hydrogen storage without using heavy-metal catalysts. *Nature Materials*, 10(4):286–290, 2011.

[119] William Robert Grove. On the gas voltaic battery.–experiments made with a view of ascertaining the rationale of its action and its application to eudiometry. *Philosophical Transactions of the Royal Society of London*, 133:91–112, 1843.

[120] A John Appleby. Fuel cell handbook. 1988.

[121] Xuan Cheng, Zheng Shi, Nancy Glass, Lu Zhang, Jiujun Zhang, Datong Song, Zhong-Sheng Liu, Haijiang Wang, and Jun Shen. A review of PEM hydrogen fuel cell contamination: Impacts, mechanisms, and mitigation. *Journal of Power Sources*, 165(2):739–756, 2007.

[122] Lee F Brown. A comparative study of fuels for on-board hydrogen production for fuel-cell-powered automobiles. *International Journal of Hydrogen Energy*, 26(4):381–397, 2001.

[123] SC Singhal. Advances in solid oxide fuel cell technology. *Solid state ionics*, 135(1):305–313, 2000.

[124] Hans-Heinrich Möbius. On the history of solid electrolyte fuel cells. *Journal of solid state electrochemistry*, 1(1):2–16, 1997.

[125] P Padma Kumar and S Yashonath. Ionic conduction in the solid state. *Journal of Chemical Sciences*, 118(1):135–154, 2006.

[126] Thomas E Springer, TA Zawodzinski, and Shimshon Gottesfeld. Polymer electrolyte fuel cell model. *Journal of the Electrochemical Society*, 138(8):2334–2342, 1991.

[127] E Warburg. Sodium ions migration through glass. *Wiedemann Ann, Phys*, 21:622–24, 1884.

[128] Peter G Bruce. *Solid state electrochemistry*, volume 5. Cambridge University Press, 1997.

[129] Walther Nernst. Material for electric-lamp glowers, 1901. US Patent 685,730.

[130] Brian CH Steele and Angelika Heinzel. Materials for fuel-cell technologies. *Nature*, 414(6861):345–352, 2001.

[131] Akira Endo, Manabu Ihara, Hiroshi Komiyama, and Koichi Yamada. Cathodic reaction mechanism for dense Sr-doped lanthanum manganite electrodes. *Solid State Ionics*, 86:1191–1195, 1996.

[132] San Ping Jiang. Development of lanthanum strontium manganite perovskite cathode materials of solid oxide fuel cells: a review. *Journal of Materials Science*, 43:6799–6833, 2008.

[133] Max Knoll and Ernst Ruska. Das elektronenmikroskop. *Zeitschrift für physik*, 78(5-6):318–339, 1932.

[134] Conyers Herring and MH Nichols. Thermionic emission. *Reviews of Modern Physics*, 21(2):185, 1949.

[135] TE Everhart and RFM Thornley. Wide-band detector for micro-microampere low-energy electron currents. *Journal of scientific instruments*, 37(7):246, 1960.

[136] WH Zachariasen. A general theory of x-ray diffraction in crystals. *Acta Crystallographica*, 23(4):558–564, 1967.

[137] WH Bragg. The x-ray spectra given by crystals of sulphur and quartz. *Proceedings of the Royal Society of London. Series A*, 89(614):575–580, 1914.

[138] Marcin Wojdyr. *Fityk: a general-purpose peak fitting program. Journal of Applied Crystallography*, 43(5 Part 1):1126–1128, Oct 2010.

[139] P Scherrer. Bestimmung der grösse und der inneren struktur von kolloidteilchen mittels röntgenstrahlen. *Nachrichten von der Gesellschaft der Wissenschaften zu Göttingen, mathematisch-physikalische Klasse*, 1918:98–100, 1918.

[140] Carl H. Bates, William B. White, and Rustum Roy. New high-pressure polymorph of zinc oxide. *Science*, 137(3534):993, 1962.

[141] J Reichman. The current-voltage characteristics of semiconductor-electrolyte junction photovoltaic cells. *Applied Physics Letters*, 36(7):574–577, 1980.

[142] LM Peter, J Li, and R Peat. Surface recombination at semiconductor electrodes: Part i. transient and steady-state photocurrents. *Journal of electroanalytical chemistry and interfacial electrochemistry*, 165(1):29–40, 1984.

[143] A. B. Murphy, P. R. F. Barnes, L. K. Randeniya, I. C. Plumb, I. E. Grey, M. D. Horne, and J. A. Glasscock. Efficiency of solar water splitting using semiconductor electrodes. *International Journal of Hydrogen Energy*, 31(14):1999–2017, 2006.

[144] Heinrich Hertz. On the evaporation of liquids, especially of mercury, in a vacuum. *Ann. Phys*, 17:178–193, 1882.

[145] Martin Knudsen. *The kinetic theory of gases: some modern aspects*. Methuen London, 1934.

[146] I. Langmuir. The Vapor Pressure of Metallic Tungsten. *Physical Review*, 2:329–342, November 1913.

[147] Saul Dushman. *Scientific foundations of vacuum technique*. Wiley New York, 1949.

[148] KL Choy. Chemical vapour deposition of coatings. *Progress in materials science*, 48(2):57–170, 2003.

[149] Hari Singh Nalwa. *Handbook of Nanostructured Materials and Nanotechnology, Five-Volume Set*, volume 3. Academic Press, 1999.

[150] Jia Grace Lu, Paichun Chang, and Zhiyong Fan. Quasi-one-dimensional metal oxide materials - Synthesis, properties and applications. *Materials Science and Engineering: R: Reports*, 52(1):49–91, 2006.

[151] RS Wagner and WC Ellis. Vapor-liquid-solid mechanism of single crystal growth. *Applied Physics Letters*, 4(5):89–90, 1964.

[152] Xinyong Tao, Jun Du, Yingchao Yang, Yiping Li, Yang Xia, Yongping Gan, Hui Huang, Wenkui Zhang, and Xiaodong Li. TiC nanorods derived from cotton fibers: Chloride-assisted VLS growth, structure, and mechanical properties. *Crystal Growth & Design*, 11(10):4422–4426, 2011.

[153] S Kodambaka, J Tersoff, MC Reuter, and FM Ross. Diameter-independent kinetics in the vapor-liquid-solid growth of Si nanowires. *Physical review letters*, 96(9):096105, 2006.

[154] CL Hsin, JH He, CY Lee, WW Wu, PH Yeh, LJ Chen, and ZL Wang. Lateral self-aligned p-type In_2O_3 nanowire arrays epitaxially grown on Si substrates. *Nano letters*, 7(6):1799–1803, 2007.

[155] Kazuki Nagashima, Takeshi Yanagida, Hidekazu Tanaka, and Tomoji Kawai. Control of magnesium oxide nanowire morphologies by ambient temperature. *Applied physics letters*, 90(23):233103–233103, 2007.

[156] Jonathon Milam, Lincoln Lauhon, and Jonathan Allen. Photoconductivity of semiconducting CdS nanowires. *Northwestern University*, pages 43–47, 2005.

[157] Jung-Chul Lee, Wonjoo Lee, Sung-Hwan Han, Tae Geun Kim, and Yun-Mo Sung. Synthesis of hybrid solar cells using CdS nanowire array grown on conductive glass substrates. *Electrochemistry Communications*, 11(1):231–234, 2009.

[158] Bin Zhang, Yeonwoong Jung, Hee-Suk Chung, Lambert Van Vugt, and Ritesh Agarwal. Nanowire transformation by size-dependent cation exchange reactions. *Nano letters*, 10(1):149–155, 2009.

[159] Carl J Barrelet, Yue Wu, David C Bell, and Charles M Lieber. Synthesis of CdS and ZnS nanowires using single-source molecular precursors. *Journal of the American Chemical Society*, 125(38):11498–11499, 2003.

[160] Jyh-Ming Wu, Han C Shih, Wen-Ti Wu, Yung-Kuan Tseng, I Chen, et al. Thermal evaporation growth and the luminescence property of TiO_2 nanowires. *Journal of crystal Growth*, 281(2):384–390, 2005.

[161] Volker Schmidt and Ulrich Gösele. How nanowires grow. *Science(Washington)*, 316(5825):698–699, 2007.

[162] Hongzhou Zhang, Xuhui Luo, Jun Xu, Bin Xiang, and Dapeng Yu. Synthesis of TiO_2/SiO_2 core/shell nanocable arrays. *The Journal of Physical Chemistry B*, 108(39):14866–14869, 2004.

[163] George Biskos, Vincent Vons, Caner U Yurteri, and Andreas Schmidt-Ott. Generation and sizing of particles for aerosol-based nanotechnology. *KONA Powder Particle J*, 26:13–35, 2008.

[164] Russell Binions and Ivan P Parkin. Novel chemical vapour deposition routes to nanocomposite thin films. 2011.

[165] Cynthia Edusi, Gopinathan Sankar, and Ivan P Parkin. The effect of solvent on the phase of titanium dioxide deposited by aerosol-assisted CVD. *Chemical Vapor Deposition*, 18(4-6):126–132, 2012.

[166] B Krause, M Ritschel, Ch Täschner, S Oswald, W Gruner, A Leonhardt, and P Pötschke. Comparison of nanotubes produced by fixed bed and aerosol-CVD methods and their electrical percolation behaviour in melt mixed polyamide 6.6 composites. *Composites Science and Technology*, 70(1):151–160, 2010.

[167] Colin R Crick and Ivan P Parkin. Superhydrophobic polymer films via aerosol assisted deposition - Taking a leaf out of nature's book. *Thin Solid Films*, 518(15):4328–4335, 2010.

[168] Sheng Xu and Zhong Lin Wang. One-dimensional ZnO nanostructures: Solution growth and functional properties. *Nano Research*, 4(11):1013–1098, 2011.

[169] Lionel Vayssieres. Growth of arrayed nanorods and nanowires of ZnO from aqueous solutions. *Advanced Materials*, 15(5):464–466, 2003.

[170] Xiaobo Chen and Samuel S Mao. Titanium dioxide nanomaterials: synthesis, properties, modifications, and applications. *Chemical reviews*, 107(LBNL–59769), 2007.

[171] Vishal K. Mahajan, Susanta K. Mohapatra, and Mano Misra. Stability of TiO_2 nanotube arrays in photoelectrochemical studies. *International Journal of Hydrogen Energy*, 33(20):5369 – 5374, 2008.

[172] Meng Ni, Michael KH Leung, Dennis YC Leung, and K Sumathy. A review and recent developments in photocatalytic water-splitting using TiO_2 for hydrogen production. *Renewable and Sustainable Energy Reviews*, 11(3):401–425, 2007.

[173] PVV Jayaweera, AGU Perera, and K Tennakone. Why gratzel's cell works so well. *Inorganica Chimica Acta*, 361(3):707–711, 2008.

[174] Zhonghai Zhang, Md Faruk Hossain, and Takakazu Takahashi. Photoelectrochemical water splitting on highly smooth and ordered TiO_2 nanotube arrays for hydrogen generation. *International journal of hydrogen energy*, 35(16):8528–8535, 2010.

[175] Zhaoyue Liu, Batric Pesic, Krishnan S Raja, Raghu R Rangaraju, and Mano Misra. Hydrogen generation under sunlight by self ordered TiO_2 nanotube arrays. *International Journal of Hydrogen Energy*, 34(8):3250–3257, 2009.

[176] Karthik Shankar, James I Basham, Nageh K Allam, Oomman K Varghese, Gopal K Mor, Xinjian Feng, Maggie Paulose, Jason A Seabold, Kyoung-Shin Choi, and Craig A Grimes. Recent advances in the use of TiO_2 nanotube and nanowire arrays for oxidative photoelectrochemistry. *The Journal of Physical Chemistry C*, 113(16):6327–6359, 2009.

[177] Jong Hyeok Park, Sungwook Kim, and Allen J Bard. Novel carbon-doped TiO_2 nanotube arrays with high aspect ratios for efficient solar water splitting. *Nano letters*, 6(1):24–28, 2006.

[178] Chengkun Xu and Shahed UM Khan. Photoresponse of visible light active Carbon-Modified-n-TiO_2 thin films. *Electrochemical and solid-state letters*, 10(3):B56–B59, 2007.

[179] Rajesh Sharma, Prajna P Das, Mano Misra, Vishal Mahajan, Jacob P Bock, Steve Trigwell, Alexandru S Biris, and Malay K Mazumder. Enhancement of the photoelectrochemical conversion efficiency of nanotubular TiO_2 photoanodes using nitrogen plasma assisted surface modification. *Nanotechnology*, 20(7):075704, 2009.

[180] H Paul Maruska and Amal K Ghosh. Transition-metal dopants for extending the response of titanate photoelectrolysis anodes. *Solar Energy Materials*, 1(3):237–247, 1979.

[181] Anders Hagfeldt, B Didriksson, Henrik Lindström, Sven Södergren, Håkan Rensmo, and Sten-Eric Lindquist. Verification of high efficiencies for the gratzel cell : A 7% efficient solar cell based on dye-sensitized colloidal TiO_2 films. *Solar Energy Materials and Solar Cells*, 31(481), 1994.

[182] Damon A. Wheeler, Gongming Wang, Yichuan Ling, Yat Li, and Jin Z. Zhang. Nanostructured hematite: synthesis, characterization, charge carrier dynamics, and photoelectrochemical properties. *Energy Environ. Sci.*, 5:6682–6702, 2012.

[183] Kevin Sivula, Florian Le Formal, and Michael Grätzel. Solar water splitting: Progress using hematite (α-Fe_2O_3) photoelectrodes. *ChemSusChem*, 4(4):432–449, 2011.

[184] Florian Le Formal, Nicolas Tetreault, Maurin Cornuz, Thomas Moehl, Michael Gratzel, and Kevin Sivula. Passivating surface states on water splitting hematite photoanodes with alumina overlayers. *Chem. Sci.*, 2:737–743, 2011.

[185] AJ Bosman and HJ Van Daal. Small-polaron versus band conduction in some transition-metal oxides. *Advances in Physics*, 19(77):1–117, 1970.

[186] Marian Nanu, Joop Schoonman, and APLM Goossens. Inorganic nanocomposites of n-and p-type semiconductors: A new type of three-dimensional solar cell. *Advanced Materials*, 16(5):453–456, 2004.

[187] Susanta K Mohapatra, Subarna Banerjee, and Mano Misra. Synthesis of Fe_2O_3/TiO_2 nanorod–nanotube arrays by filling TiO_2 nanotubes with Fe. *Nanotechnology*, 19(31):315601, 2008.

[188] ST Hussain and A Siddiqa. Iron and chromium doped titanium dioxide nanotubes for the degradation of environmental and industrial pollutants. *International Journal of Environment Science and Technology*, 8(2):351–362, 2011.

[189] Zainab T. Y. Al-Abdullah, Yuyoung Shin, Rantej Kler, Christopher C. Perry, Wuzong Zhou, and Qiao Chen. The influence of hydroxide on the initial stages of anodic growth of tio2 nanotubular arrays. *Nanotechnology*, 21(50), 2010.

[190] Yoshikazu Suzuki and Susumu Yoshikawa. Synthesis and thermal analyses of TiO_2-derived nanotubes prepared by the hydrothermal method. *Journal of materials research*, 19(4):982–985, 2004.

[191] P Davide Cozzoli, Andreas Kornowski, and Horst Weller. Low-temperature synthesis of soluble and processable organic-capped anatase TiO_2 nanorods. *Journal of the American Chemical Society*, 125(47):14539–14548, 2003.

[192] Seong Mu Jo, Mi Yeon Song, Young Rack Ahn, Chong Rae Park, and Dong Young Kim. Nanofibril formation of electrospun TiO_2 fibers and its application to dye-sensitized solar cells. *Journal of Macromolecular Science Part A: Pure and Applied Chemistry*, 42(11):1529–1540, 2005.

[193] Surawut Chuangchote, Jaturong Jitputti, Takashi Sagawa, and Susumu Yoshikawa. Photocatalytic activity for hydrogen evolution of electrospun TiO_2 nanofibers. *ACS Applied Materials & Interfaces*, 1(5):1140–1143, 2009.

[194] Jyh-Ming Wu, Han C Shih, and Wen-Ti Wu. Electron field emission from single crystalline TiO_2 nanowires prepared by thermal evaporation. *Chemical physics letters*, 413(4):490–494, 2005.

[195] Dongjiang Yang, Hongwei Liu, Zhanfeng Zheng, Yong Yuan, Jin-cai Zhao, Eric R Waclawik, Xuebin Ke, and Huaiyong Zhu. An efficient photocatalyst structure: TiO_2 (b) nanofibers with a shell of anatase nanocrystals. *Journal of the American Chemical Society*, 131(49):17885–17893, 2009.

[196] Jih-Jen Wu and Chi-Chung Yu. Aligned TiO_2 nanorods and nanowalls. *The Journal of Physical Chemistry B*, 108(11):3377–3379, 2004.

[197] C Tekmen, A Suslu, and U Cocen. Titania nanofibers prepared by electrospinning. *Materials Letters*, 62(29):4470–4472, 2008.

[198] S Sreekantan, LM Hung, Z Lockman, ZA Ahmad, and AF Mohd Noor. The synthesis and characterization of titania nanotubes formed at various anodisation time. In *AIP Conference Proceedings*, volume 989, page 155, 2008.

[199] Xiaofeng Yu, Yongxiang Li, Wojtek Wlodarski, Sasikaran Kandasamy, and Kourosh Kalantar-Zadeh. Fabrication of nanostructured TiO_2 by anodization: A comparison between electrolytes and substrates. *Sensors and Actuators B: Chemical*, 130(1):25–31, 2008.

[200] Gopal K Mor, Karthik Shankar, Maggie Paulose, Oomman K Varghese, and Craig A Grimes. Use of highly-ordered TiO_2 nanotube arrays in dye-sensitized solar cells. *Nano letters*, 6(2):215–218, 2006.

[201] Beata Chertok, Bradford A Moffat, Allan E David, Faquan Yu, Christian Bergemann, Brian D Ross, and Victor C Yang. Iron oxide nanoparticles as a drug delivery vehicle for mri monitored magnetic targeting of brain tumors. *Biomaterials*, 29(4):487–496, 2008.

[202] Michael J Potter. Iron oxide pigments. *Journal, v*, 78(32):43–46, 1994.

[203] Chun-Jiang Jia, Ling-Dong Sun, Zheng-Guang Yan, Li-Ping You, Feng Luo, Xiao-Dong Han, Yu-Cheng Pang, Ze Zhang, and Chun-Hua Yan. Single-crystalline iron oxide nanotubes. *Angewandte Chemie*, 117(28):4402–4407, 2005.

[204] Lu Liu, Hui-Zhong Kou, Wenling Mo, Huajie Liu, and Yuqiu Wang. Surfactant-assisted synthesis of α-Fe_2O_3 nanotubes and nanorods with shape-dependent magnetic properties. *The Journal of Physical Chemistry B*, 110(31):15218–15223, 2006.

[205] Zhenyu Sun, Hanqiu Yuan, Zhimin Liu, Buxing Han, and Xinrong Zhang. A highly efficient chemical sensor material for H_2S: α-Fe_2O_3 nanotubes fabricated using carbon nanotube templates. *Advanced Materials*, 17(24):2993–2997, 2005.

[206] RR Rangaraju, A Panday, KS Raja, and M Misra. Nanostructured anodic iron oxide film as photoanode for water oxidation. *Journal of Physics D: Applied Physics*, 42(13):135303, 2009.

[207] Martinez J A G Cesar I, Kay A and Gratzel M. *J. Am. Chem. Soc.*, 128(14):4582, 2006.

[208] Ingler W B and Khan S U M. *Electrochem. Solid State Lett.*, 9(3):A144, 2006.

[209] Haripriya E Prakasam, Oomman K Varghese, Maggie Paulose, Gopal K Mor, and Craig A Grimes. Synthesis and photoelectrochemical properties of nanoporous iron (III) oxide by potentiostatic anodization. *Nanotechnology*, 17(17):4285, 2006.

[210] Susanta K Mohapatra, Shiny E John, Subarna Banerjee, and Mano Misra. Water photooxidation by smooth and ultrathin α-Fe_2O_3 nanotube arrays. *Chemistry of Materials*, 21(14):3048–3055, 2009.

[211] Raghu R Rangaraju, KS Raja, A Panday, and M Misra. An investigation on room temperature synthesis of vertically oriented arrays of iron oxide nanotubes by anodization of iron. *Electrochimica Acta*, 55(3):785–793, 2010.

[212] Yu-Xin Tang, Jie Tao, Yan-Yan Zhang, Tao Wu, Hai-Jun Tao, and Ya-Rong Zhu. Preparation of TiO_2 nanotube on glass by anodization of Ti films at room temperature. *Transactions of Nonferrous Metals Society of China*, 19(1):192–198, 2009.

[213] Haidong Zheng, Abu Z Sadek, Michael Breedon, David Yao, Kay Latham, Johan du Plessis, and Kourosh Kalantar-Zadeh. Fast formation of thick and transparent titania nanotubular films from sputtered Ti. *Electrochemistry Communications*, 11(6):1308–1311, 2009.

[214] Elijah Thimsen, Subhashis Biswas, Cynthia S. Lo, and Pratim Biswas. Predicting the band structure of mixed transition metal oxides: Theory and experiment. *The Journal of Physical Chemistry C*, 113(5):2014–2021, 2009.

[215] VA Coleman and C Jagadish. Basic properties and applications of ZnO. *Zinc Oxide Bulk, Thin films and Nanostructures, Processing, Properties and Applications*, pages 1–20, 2006.

[216] Anderson Janotti and Chris G Van de Walle. Fundamentals of zinc oxide as a semiconductor. *Reports on Progress in Physics*, 72(12):126501, 2009.

[217] Gyu-Chul Yi, Chunrui Wang, and Won Il Park. ZnO nanorods: synthesis, characterization and applications. *Semiconductor Science and Technology*, 20(4):S22, 2005.

[218] Lukas Schmidt-Mende and Judith L MacManus-Driscoll. ZnO–nanostructures, defects, and devices. *Materials today*, 10(5):40–48, 2007.

[219] Zhiyong Fan and Jia G Lu. Zinc oxide nanostructures: synthesis and properties. *Journal of nanoscience and nanotechnology*, 5(10):1561–1573, 2005.

[220] Chien-Yuan Lu, Sheng-Po Chang, Shoou-Jinn Chang, Ting-Jen Hsueh, Cheng-Liang Hsu, Yu-Zung Chiou, and I-Cherng Chen. ZnO nanowire-based oxygen gas sensor. *Sensors Journal, IEEE*, 9(4):485–489, 2009.

[221] P Mitra and AK Mukhopadhyay. ZnO thin film as methane sensor. *Bulletin of the Polish Academy of Sciences: Technical Sciences*, 55(3):281–285, 2007.

[222] Q Ahsanulhaq, JH Kim, JS Lee, and YB Hahn. Electrical and gas sensing properties of ZnO nanorod arrays directly grown on a four-probe electrode system. *Electrochemistry Communications*, 12(3):475–478, 2010.

[223] Zhiyong Fan and Jia G Lu. Electrical properties of ZnO nanowire field effect transistors characterized with scanning probes. *Applied Physics Letters*, 86(3):032111–032111, 2005.

[224] Seung Nam Cha, Ju-Seok Seo, Seong Min Kim, Hyun Jin Kim, Young Jun Park, Sang-Woo Kim, and Jong Min Kim. Sound-driven piezoelectric nanowire-based nanogenerators. *Advanced Materials*, 22(42):4726–4730, 2010.

[225] Basudev Pradhan, Sudip K Batabyal, and Amlan J Pal. Vertically aligned ZnO nanowire arrays in rose bengal-based dye-sensitized solar cells. *Solar energy materials and solar cells*, 91(9):769–773, 2007.

[226] Xunyu Yang, Abraham Wolcott, Gongming Wang, Alissa Sobo, Robert Carl Fitzmorris, Fang Qian, Jin Z Zhang, and Yat Li. Nitrogen-doped ZnO nanowire arrays for photoelectrochemical water splitting. *Nano letters*, 9(6):2331–2336, 2009.

[227] Hao Ming Chen, Chih Kai Chen, Chun Che Lin, Ru-Shi Liu, Heesun Yang, Wen-Sheng Chang, Kuei-Hsien Chen, Ting-Shan Chan, Jyh-Fu Lee, and Din Ping Tsai. Multi-bandgap-sensitized ZnO nanorod photoelectrode arrays for water splitting: an x-ray absorption spectroscopy approach for the electronic evolution under solar illumination. *The Journal of Physical Chemistry C*, 115(44):21971–21980, 2011.

[228] Sheng Chu, Guoping Wang, Weihang Zhou, Yuqing Lin, Leonid Chernyak, Jianze Zhao, Jieying Kong, Lin Li, Jingjian Ren, and Jianlin Liu. Electrically pumped waveguide lasing from ZnO nanowires. *Nature nanotechnology*, 6(8):506–510, 2011.

[229] Huijuan Zhou, Markus Wissinger, Johannes Fallert, Robert Hauschild, Felix Stelzl, Claus Klingshirn, and Heinz Kalt. Ordered, uniform-sized ZnO nanolaser arrays. *Applied Physics Letters*, 91(18):181112–181112, 2007.

[230] CZ Ning. Semiconductor nanolasers. *physica status solidi (b)*, 247(4):774–788, 2010.

[231] Yanjun Fang, Yewu Wang, Yuting Wan, Zongli Wang, and Jian Sha. Detailed study on photoluminescence property and growth mechanism of ZnO nanowire arrays grown by thermal evaporation. *The Journal of Physical Chemistry C*, 114(29):12469–12476, 2010.

[232] Seung Chul Lyu, Ye Zhang, Cheol Jin Lee, Hyun Ruh, and Hwack Joo Lee. Low-temperature growth of ZnO nanowire array by a simple physical vapor-deposition method. *Chemistry of materials*, 15(17):3294–3299, 2003.

[233] BD Yao, YF Chan, and N Wang. Formation of ZnO nanostructures by a simple way of thermal evaporation. *Applied Physics Letters*, 81(4):757–759, 2002.

[234] Chih-Han Chen, Shoou-Jinn Chang, Sheng-Po Chang, Meng-Ju Li, I Chen, Ting-Jen Hsueh, Cheng-Liang Hsu, et al. Novel fabrication of uv photodetector based on ZnO nanowire/p-GaN heterojunction. *Chemical Physics Letters*, 476(1):69–72, 2009.

[235] H Chik, J Liang, SG Cloutier, N Kouklin, and JM Xu. Periodic array of uniform ZnO nanorods by second-order self-assembly. *Applied physics letters*, 84(17):3376–3378, 2004.

[236] Xudong Wang, Jinhui Song, and Zhong Lin Wang. Nanowire and nanobelt arrays of zinc oxide from synthesis to properties and to novel devices. *J. Mater. Chem.*, 17:711–720, 2007.

[237] Chien-Lin Kuo, Ruey-Chi Wang, Chuan-Pu Liu, and Jow-Lay Huang. Composition fluctuation induced growth of al:zno rectangular nanorod arrays. *Nanotechnology*, 19(3):035605, 2008.

[238] Mingshui Yao, Peng Hu, Yuebin Cao, Weicheng Xiang, Xing Zhang, Fangli Yuan, and Yunfa Chen. Morphology-controlled ZnO spherical nanobelt-flower arrays and their sensing properties. *Sensors and Actuators B: Chemical*, 177(0):562 – 569, 2013.

[239] Seung Chul Lyu, Ye Zhang, Hyun Ruh, Hwack-Joo Lee, Hyun-Wook Shim, Eun-Kyung Suh, and Cheol Jin Lee. Low temperature growth and photoluminescence of well-aligned zinc oxide nanowires. *Chemical Physics Letters*, 363(1 - 2):134 – 138, 2002.

[240] C.C Tang, S.S Fan, Marc Lamy de la Chapelle, and P Li. Silica-assisted catalytic growth of oxide and nitride nanowires. *Chemical Physics Letters*, 333(1âĂŞ2):12 – 15, 2001.

[241] JX Wang, Xiao Wei Sun, A Wei, Y Lei, XP Cai, Chang Ming Li, and ZL Dong. Zinc oxide nanocomb biosensor for glucose detection. *Applied physics letters*, 88(23):233106–233106, 2006.

[242] Yaohua Zhang, Xubo Song, Jie Zheng, Haihua Liu, Xingguo Li, and Liping You. Symmetric and asymmetric growth of ZnO hierarchical nanostructures: nanocombs and their optical properties. *Nanotechnology*, 17(8):1916, 2006.

[243] Chang Shi Lao, Pu Xian Gao, Ru Sen Yang, Yue Zhang, Ying Dai, and Zhong L Wang. Formation of double-side teethed nanocombs of ZnO and self-catalysis of Zn-terminated polar surface. *Chemical physics letters*, 417(4):358–362, 2006.

[244] Zhong Lin Wang. Nanostructures of zinc oxide. *Materials today*, 7(6):26–33, 2004.

[245] Hua Wang, Benshou Yong, Yuting Wan, Bo Chen, Yanjun Fang, Yewu Wang, and Jian Sha. Structure analyses and growth mechanism of ZnO nanoladders. *Materials Letters*, 64(17):1925–1928, 2010.

[246] Min-Hua Zhao, Zhong-Lin Wang, and Scott X Mao. Piezoelectric characterization of individual zinc oxide nanobelt probed by piezoresponse force microscope. *Nano Letters*, 4(4):587–590, 2004.

[247] Scott X Mao, Minhua Zhao, and Zhong Lin Wang. Nanoscale mechanical behavior of individual semiconducting nanobelts. *Applied Physics Letters*, 83(5):993–995, 2003.

[248] Theerapong Santhaveesuk, Torranin Chairuangsri, Duangmanee Wongratanaphisan, and Supab Choopun. Optical band gap of $Zn_{1-x}Ti_xO$ tetrapods. *J. Microsc. Soc. Thai*, 23:70–74, 2009.

[249] H Iwanaga, M Fujii, and S Takeuchi. Growth model of tetrapod zinc oxide particles. *Journal of crystal growth*, 134(3):275–280, 1993.

[250] Junlin Li, Huizhao Zhuang, Jie Wang, and Peng Xu. Fabrication and characterization of novel ZnO tetrapods induced by polar surfaces. *Materials Letters*, 65(11):1659–1662, 2011.

[251] JS Tawale, KK Dey, R Pasricha, KN Sood, and AK Srivastava. Synthesis and characterization of ZnO tetrapods for optical and antibacterial applications. *Thin Solid Films*, 519(3):1244–1247, 2010.

[252] D Calestani, M Zha, R Mosca, A Zappettini, MC Carotta, V Di Natale, and L Zanotti. Growth of ZnO tetrapods for nanostructure-based gas sensors. *Sensors and Actuators B: Chemical*, 144(2):472–478, 2010.

[253] Jing Yu Lao, Jian Guo Wen, and Zhi Feng Ren. Hierarchical ZnO nanostructures. *Nano Letters*, 2(11):1287–1291, 2002.

[254] Jum Suk Jang, Pramod H Borse, Jae Sung Lee, Kwon Taek Lim, Ok Sang Jung, Euh Duck Jeong, Jong Seong Bae, Mi Sook Won, and Hyun Gyu Kim. Energy band structure and photocatalytic property of Fe-doped Zn_2TiO_4 material. *Bull. Korean Chem. Soc*, 30(12):3021, 2009.

[255] C.J Youn, T.S Jeong, M.S Han, and J.H Kim. Optical properties of Zn-terminated ZnO bulk. *Journal of Crystal Growth*, 261(4):526 – 532, 2004.

[256] K. Hoffmann and D. Hahn. Electron spin resonance of lattice defects in zinc oxide. *physica status solidi (a)*, 24(2):637–648, 1974.

[257] A. Hausmann. Ein "F-Zentru" als paramagnetischer donator in zinkoxid. *Zeitschrift für Physik*, 237(1):86–97, 1970.

[258] Chun Feng Song, Teng Qiu, Hong Fu Yuan, and Xiao Yu Li. Enhanced green emission in ZnO/zinc titanate composite materials. *Materials Science and Engineering: B*, 175(3):243–247, 2010.

[259] Sobia Ashraf, Christopher S Blackman, Robert G Palgrave, Simon C Naisbitt, and Ivan P Parkin. Aerosol assisted chemical vapour deposition of WO_3 thin films from tungsten hexacarbonyl and their gas sensing properties. *Journal of Materials Chemistry*, 17(35):3708–3713, 2007.

[260] T Stoycheva, S Vallejos, J Calderer, I Parkin, C Blackman, and X Correig. Characterization and gas sesing properties of intrinsic and Au-doped WO_3 nanostuctures deposited by AACVD technique. *Procedia Engineering*, 5:131–134, 2010.

[261] Asif Ali Tahir and KG Wijayantha. Photoelectrochemical water splitting at nanostructured $ZnFe_2O_4$ electrodes. *Journal of Photochemistry and Photobiology A: Chemistry*, 216(2):119–125, 2010.

[262] Swee-Yong Pung, Kwang-Leong Choy, Xianghui Hou, and Keith Dinsdale. In situ doping of ZnO nanowires using aerosol-assisted chemical vapour deposition. *Nanotechnology*, 21(34):345602, 2010.

[263] Hao Ming Chen, Chih Kai Chen, Yu-Chuan Chang, Chi-Wen Tsai, Ru-Shi Liu, Shu-Fen Hu, Wen-Sheng Chang, and Kuei-Hsien Chen. Quantum dot monolayer sensitized ZnO nanowire-array photoelectrodes: True efficiency for water splitting. *Angewandte Chemie*, 122(34):6102–6105, 2010.

[264] S Biswas, MF Hossain, and T Takahashi. Fabrication of gratzel solar cell with TiO_2/CdS bilayered photoelectrode. *Thin Solid Films*, 517(3):1284–1288, 2008.

[265] Xuan Pan, Changhong Chen, Kai Zhu, and Zhaoyang Fan. TiO_2 nanotubes infiltrated with nanoparticles for dye sensitized solar cells. *Nanotechnology*, 22(23):235402, 2011.

[266] Tetsuya Sasamura, Ken-ichi Okazaki, Akihiko Kudo, Susumu Kuwabata, and Tsukasa Torimoto. Photosensitization of ZnO rod electrodes with $AgInS_2$ nanoparticles and ZnS-$AgInS_2$ solid solution nanoparticles for solar cell applications. *RSC Advances*, 2(2):552–559, 2012.

[267] Xiaoyan Gan, Xiaomin Li, Xiangdong Gao, Fuwei Zhuge, and Weidong Yu. ZnO nanowire/TiO_2 nanoparticle photoanodes prepared by the ultrasonic irradiation assisted dip-coating method. *Thin Solid Films*, 518(17):4809–4812, 2010.

[268] Meili Wang, Changgang Huang, Yongge Cao, Qingjiang Yu, Zhonghua Deng, Yuan Liu, Zhi Huang, Jiquan Huang, Qiufeng Huang, Wang Guo, and Jingkui Liang. Dye-sensitized solar cells based on nanoparticle-decorated ZnO/TiO_2 core/shell nanorod arrays. *Journal of Physics D: Applied Physics*, 42(15):155104, 2009.

[269] CaiLu Wang, XiangDong Gao, XiaoMin Li, ZhengWu Jiang, ZhengHong Yang, ZhengYing Gu, and Peng He. Hybrid photoanode films based on sparse ZnO rod array-TiO_2 nanoparticles in dye-sensitized solar cells. *Science China Physics, Mechanics & Astronomy*, 55(7):1183(6), 2012-07-01.

[270] J.-H. Lee, M.-H. Hon, Y.-W. Chung, and I.-C. Leu. The effect of TiO_2 coating on the electrochemical performance of ZnO nanorod as the anode material for lithium-ion battery. *Applied Physics A: Materials Science & Processing*, 102:545–550, 2011.

[271] Gul Amin, MO Sandberg, Ahmed Zainelabdin, Siama Zaman, Omer Nur, and Magnus Willander. Scale-up synthesis of ZnO nanorods for printing inexpensive zno/polymer white light-emitting diode. *Journal of Materials Science*, 47(11):4726–4731, 2012.

[272] M. Andres Verges, A. Mifsud, and C. J. Serna. Formation of rod-like zinc oxide microcrystals in homogeneous solutions. *J. Chem. Soc., Faraday Trans.*, 86:959–963, 1990.

[273] Zhitao Chen and Lian Gao. A facile route to ZnO nanorod arrays using wet chemical method. *Journal of Crystal Growth*, 293(2):522 – 527, 2006.

[274] Quanchang Li, Vageesh Kumar, Yan Li, Haitao Zhang, Tobin J. Marks, and Robert P. H. Chang. Fabrication of ZnO nanorods and nanotubes in aqueous solutions. *Chemistry of Materials*, 17(5):1001–1006, 2005.

[275] Sheng Xu, Changshi Lao, Benjamin Weintraub, and Zhong Lin Wang. Density-controlled growth of aligned ZnO nanowire arrays by seedless chemical approach on smooth surfaces. *Journal of Materials Research*, 23(08):2072–2077, 2008.

[276] Rajaram S Mane, Won Joo Lee, Habib M Pathan, and Sung-Hwan Han. Nanocrystalline TiO_2/ZnO thin films: fabrication and application to dye-sensitized solar cells. *The Journal of Physical Chemistry B*, 109(51):24254–24259, 2005.

[277] Sheng Xu, Yong Qin, Chen Xu, Yaguang Wei, Rusen Yang, and Zhong Lin Wang. Self-powered nanowire devices. *Nature Nanotechnology*, 5(5):366–373, 2010.

[278] Dewei Chu, Yoshitake Masuda, Tatsuki Ohji, and Kazumi Kato. Formation and photocatalytic application of ZnO nanotubes using aqueous solution. *Langmuir*, 26(4):2811–2815, 2009.

[279] Dewei Chu, Yoshitake Masuda, Tatsuki Ohji, and Kazumi Kato. Formation and photocatalytic application of ZnO nanotubes using aqueous solution. *Langmuir*, 26(4):2811–2815, 2010. PMID: 20141215.

[280] Francisco Pola-Albores, Francisco Paraguay-Delgado, Wilber Antúnez-Flores, Patricia Amézaga-Madrid, Edna Ríos-Valdovinos, and Mario Miki-Yoshida. Microstructural study of ZnO nanostructures by rietveld analysis. *J. Nanomaterials*, 2011:27:1–27:11, January 2011.

[281] Hua Hu and Ronald G. Larson. Marangoni effect reverses coffee-ring depositions. *The Journal of Physical Chemistry B*, 110(14):7090–7094, 2006.

[282] Yueh-Feng Li, Yu-Jane Sheng, and Heng-Kwong Tsao. Evaporation stains: Suppressing the coffee-ring effect by contact angle hysteresis. *Langmuir*, 29(25):7802–7811, 2013.

[283] A.E. Morales, E.S. Mora, and U. Pal. Use of diffuse reflectance spectroscopy for optical characterization of un-supported nanostructures. *Revista Mexicana de Fisica S*, 53(5):18, 2007.

[284] Yasumichi Matsumoto, Masaru Omae, Itsuo Watanabe, and Ei-ichi Sato. Photoelectrochemical properties of the Zn-Ti-Fe spinel oxides. *Journal of The Electrochemical Society*, 133(4):711–716, 1986.